Doctoral theses at NTNU, 2017:230

Antoine R. M. Dalod

In situ synthesis of titania and titanium based organic-inorganic nanomaterials

ISBN 978-82-326-2532-1 (printed ver.)
ISBN 978-82-326-2533-8 (electronic ver.)
ISSN 1503-8181

NTNU
Norwegian University of
Science and Technology

Doctoral theses at NTNU, 2017:230

NTNU
Norwegian University of Science and Technology
Thesis for the Degree of
Philosophiae Doctor
Faculty of Natural Sciences
Department of Materials Science
and Engineering

NTNU
Norwegian University of
Science and Technology

Antoine R. M. Dalod

In situ synthesis of titania and titanium based organic-inorganic nanomaterials

Thesis for the Degree of Philosophiae Doctor

Trondheim, September 2017

Norwegian University of Science and Technology
Faculty of Natural Sciences
Department of Materials Science and Engineering

NTNU
Norwegian University of
Science and Technology

NTNU
Norwegian University of Science and Technology

Thesis for the Degree of Philosophiae Doctor

Faculty of Natural Sciences
Department of Materials Science and Engineering

ISBN 978-82-326-2532-1 (printed ver.)
ISBN 978-82-326-2533-8 (electronic ver.)
ISSN 1503-8181

Doctoral theses at NTNU, 2017:230

Printed by NTNU Grafisk senter

Preface

This thesis has been submitted to the NTNU, Norwegian University of Science and Technology in partial fulfillment of requirements for the academic degree of *Philosophiae Doctor*.

The doctoral studies were performed in the Inorganic Materials and Ceramics Research Group, Department of Materials Science and Engineering, NTNU, Trondheim, from August 2014 to July 2017. The work was supervised by Prof. Mari-Ann Einarsrud and the co-supervisors were Prof. Tor Grande and Dr. Lars Henriksen (poLight AS).

This work has been funded by the Research Council of Norway as part of the project "Beat the Human Eye" (grant number 235210).

Part of this thesis have been published (included in Appendix 8.5). The author of this thesis has been the main contributor and all the co-authors have been involved in the elaboration of the manuscripts.

Trondheim, July 2017
Antoine R. M. Dalod

Acknowledgements

I would like to express my gratitude to those who have encouraged and helped me throughout this journey.

First of all, to my main supervisor, Mari-Ann Einarsrud, many thanks for your continuous guidance and support. I am deeply grateful for everything I have learnt. To my co-supervisor, Tor Grande, thank you for your valuable advices, particularly during the writing processes. I would also like to thank Lars Henriksen, my co-supervisor, your inputs always brought new fruitful ideas.

All this work would have not been possible without the help from colleagues and friends. Thank you, Ola Grendal, for your contributions. It was very inspiring to work with you and I learnt a lot from our collaboration. Together with Susanne Skjærvø, many thanks for sharing this beamtime experience. To Katie Inzani and Sverre Selbach, thank you for the computational input to this work and for showing me a glimpse of the DFT field. Furthermore, I would like to express my sincere gratitude to Ragnhild Sæterli, Vedran Furtula, and Marie-Laure Léonard, for the help with TEM, ellipsometry, and DMA analysis, respectively, and for the discussion of the results. Also, many thanks to Anders Blichfeld and Ola Grendal for accepting to travel abroad to perform the SAXS analysis while I was writing this thesis. I would also like to express my sincere appreciation to Javier Pérez for giving us the chance to collect SAXS data and for considering my time limitation.

In our research group, I would like to thank all the technical and scientific staff for your help and your availability. Many thanks to everyone in the chemistry buildings, for all the things that make this place a great and peaceful working environment. I especially wish to thank Julian Tolchard for taking the time and the patience to share his knowledge on the Rietveld analysis. I have been lucky to share my office with Laura Rioja-Monllor, Mads Christensen, and Rokas Sažinas, forming a great international team. Thank you for the everyday life, for the discussions about work but also for all the non-scientific parts. Also to my longtime mentor, Nils Wagner, thank you.

To my family, thanks for your encouragements all along these years, and to my parents for always supporting my choices. Finally, to my dear wife, Xiao, many thanks for your love, your care, your patience.

Summary

The idea of combining the properties of inorganic and organic materials to produce new materials with unique and tunable properties has attracted a lot of interests to biologists, chemists, physicists, and materials scientists. Furthermore, to control and understand all the parameters of the synthesis and the elaboration of materials at nanoscale remains one of the main challenges in nanotechnology. Finally, for potential industrial use of these emerging technologies, key parameters are simplicity, cost efficiency, and environmental friendliness of the processes. In this work, low temperature and single-step synthesis routes were investigated to prepare titania and titanium based organic-inorganic nanomaterials. The project used a relatively wide range of methods both with respect to materials synthesis and materials characterization, but computational and modeling approaches were also included.

In the first part, surface-functionalized titanium dioxide (TiO_2) nanoparticles were prepared by a single-step hydrothermal synthesis, using titanium(IV) isopropoxide as precursor for the metal oxide nanoparticles. Three different silane coupling agents (3-aminopropyltriethoxysilane, 3-(2-aminoethylamino)propyldimethoxymethylsilane, and *n*-decyltriethoxysilane) were used to demonstrate the versatility of the synthesis and for tuning the surface properties of the nanoparticles. X-ray diffraction and electron microscopy demonstrated that for pure TiO_2 and TiO_2 nanoparticles synthesized with alkylsilane, spherical nanoparticles of about 10 nm were formed, with anatase as the main phase (about 75 wt.%) and brookite as secondary phase (about 25 wt.%). When aminosilanes were used, in addition to the spherical nanoparticles (also about 10 nm), larger rod-like nanoparticles were formed and these samples were phase pure anatase. The rod-like nanoparticles had a width similar to the spherical particles and a length varying in the range 50-200 nm. It was determined that the rod-like nanoparticles were elongated along the *c*-axis of the anatase unit cell (tetragonal) by combining refinement of diffraction patterns using an anisotropic peak broadening model and high resolution transmission electron microscopy. A combination of Fourier transform infrared spectroscopy, thermogravimetry, and nitrogen adsorption measurements confirmed the *in situ* functionalization of the TiO_2 nanoparticles by the formation of covalent bonds between the silane coupling agent and the nanoparticles, with surface coverages varying between 2.3 to 4.0 silane per square nanometer. Special efforts were employed in order to understand the role of each parameter and the mechanism of each

step of the synthesis on the formation of the rod-like nanoparticles. The pH and the precursors molar ratios were varied for the synthesis with 3-aminopropyltriethoxysilane and *in situ* synchrotron X-ray diffraction was revealed to be an efficient tool to investigate the growth and the kinetics of TiO_2 nanocrystals by oriented attachment mechanism. The synthesis was further developed into a two-step synthesis to TiO_2-SiO_2 core-shell nanoparticles. Heat treatment of the hybrid nanoparticles (up to 700 °C in air) resulted in the formation of TiO_2-SiO_2 core-shell nanoparticles, by the combustion of the silane coupling agents forming an amorphous silica layer, which inhibited further coarsening of the nanoparticles. The particles were dispersed in a silicone-based polymer provided by poLight AS. However, the transparency of the polymer was drastically reduced, especially when using nanoparticles with the lowest hydrophobicity. At a volume fraction of nanoparticles above 5 vol.%, the cross-linking of the polymer was inhibited and it was thus decided to redirect the focus to *in situ* synthesis of polymer nanocomposites.

The second part of the thesis was related to a non-aqueous sol-gel approach to prepare titanium-polydimethylsiloxane based nanocomposites *in situ*. Several synthesis parameters such as the precursor ratios (titanium(IV) isopropoxide and hydroxy-terminated polydimethylsiloxane) were varied and optimized to study the effect on the optical, mechanical, and structural properties of the resulting nanocomposites. Spectroscopy analysis showed that cross-linking was achieved by covalent bonding between polymer chains and the titanium alkoxide. Combined with small-angle X-ray scattering analysis, nanosized inhomogeneities (< 5 nm) that were attributed to titania-like amorphous nanodomains ($TiO_x(OH)_y$) were shown to be present in the nanocomposites. The simultaneous cross-linking and *in situ* formation of titania-like nanodomains allowed the synthesis of transparent materials up to approximately 15 vol.% of inorganic component, thus increasing the refractive index of the of the material from 1.40 (polymer matrix) to 1.56. The hydrophilicity of the hybrid materials and the shear storage modulus also increased as the amount of incorporated titanium was increased. The contact angle of water and the shear storage modulus at room temperature were measured from 126 to 91° and from 2 to 220 MPa, respectively.

Titanium dioxide and titanium-based materials were shown to be good candidates for potential use in many domains such as photocatalysis, photovoltaic, lithium-ion batteries, biomedical, and coatings applications. The synthesis methods used in this work are versatile and can be adjusted depending on the desired application.

Author contribution

All the experiments were performed by the author, at the Department of Materials Science and Engineering (DMSE), Norwegian University of Science and Technology (NTNU), Trondheim, except for the following. The *ex situ* synthesis and characterizations (except TEM, see below) of TiO_2 nanoparticles functionalized with APTES in which the pH, TIP/APTES molar ratio, and time of the synthesis were modified (Chapters 4.3 and 4.4) compared to the initial synthesis (Chapter 4.1), were performed by M.Sc. Ola G. Grendal (DMSE, NTNU), during his master project, under the supervision of the author. The TEM operations and EDS analysis were performed by Dr. Ragnhild Sæterli (Dept. of Physics, NTNU). The DFT calculations were performed by Dr. Katherine Inzani and Assoc. Prof. Sverre M. Selbach (DMSE, NTNU). The SAXS measurements were performed at the SWING beamline, SOLEIL synchrotron, Gif-sur-Yvette, France, by M.Sc. Ola G. Grendal, Dr. Anders B. Blichfeld (DMSE, NTNU), and Dr. Javier Pérez (SWING, SOLEIL).

The *in situ* XRD measurements were carried out at the Swiss-Norwegian Beamlines (SNBL), European Synchrotron Research Facility (ESRF), Grenoble, France. The measurements were performed with assistance from M.Sc. Ola G. Grendal, M.Sc. Susanne L. Skjærvø (DMSE, NTNU), and Dr. Wouter van Beek (SNBL, ESRF). The ellipsometry measurements were performed with assistance from Dr. Vedran Furtula (Dept. of Physics, NTNU). The DMA measurements were carried out at ESIREM, University of Burgundy, Dijon, France. The measurements were performed with assistance from Marie-Laure Léonard (ESIREM, University of Burgundy).

Table of content

List of common abbreviations

1. Acronyms

BET	Brunauer-Emmett-Teller theory
BJH	Barrett-Joyner-Halenda theory
DFT	Density functional theory
DMA	Dynamic mechanical analysis
EDS	Energy-dispersive X-ray spectroscopy
FTIR or IR	Fourier transform infrared spectroscopy
OA	Oriented attachment
OR	Ostwald ripening
SAXS	Small-angle X-ray scattering
SEM	Scanning electron microscope
TEM	Transmission electron microscope
TGA	Thermogravimetric analysis
UV-vis	Ultraviolet visible
XRD	X-ray diffraction

2. Chemicals

AEAPS	3-(2-aminoethylamino)propyldimethoxymethylsilane
APTES	3-aminopropyltriethoxysilane
DTES	*n*-decyltriethoxysilane
(A)IP	(Anhydrous) isopropanol or propan-2-ol
PDMS	Polydimethylsiloxane
PDMS-OH	Hydroxy-terminated polydimethylsiloxane
SiO_2	Silicon dioxide or silica
Ti-PDMS	Titanium-PDMS based nanocomposites
TIP	Titanium(IV) isopropoxide
TiO_2	Titanium dioxide or titania

3. Symbols

d_{BET}	Particle size estimated from BET measurements (nm)
d_{BJH}	Average pore diameter from BJH desorption (nm)
d_{SEM}	Average particle size from SEM observations (nm)
d_{XRD}	Average crystallite size from XRD refinements (nm)
d_{hkl}	Interplanar distance (Å) with *hkl* the Miller indices.
G' and G''	Shear storage and loss moduli (Pa)
m_{loss}	Organic mass loss from TGA measurements (g)
q	Scattering vector ($Å^{-1}$)
S_{BET}	Specific surface area from BET ($m^2\ g^{-1}$)
S_{cov}	Surface coverage (molecule nm^{-2})
tan δ	Loss factor or dumping factor (unitless), tan $\delta = G''/G'$
T_g	Glass transition temperature (°C or K)
ζ	Correlation length (nm)

1. Background and motivation

1.1. Description of the project

Voice coil motor (VCM) is the largest camera technology used today in the mobile devices market. It is based on an electromagnetic coil which allows to translate the lens and change the focus. During the last ten years, poLight AS has developed a new small lens, TLens® for which the main goal is to substitute VCM technology in mobile devices. The lens consists of a silicone-based polymer (300 µm thick) embedded between a glass substrate and a glass membrane (Figure 1.1a). The lens is equipped with a micro electro-mechanical system (MEMS) [1], based on lead zirconate titanate (PZT) piezoelectric materials. In this application, the converse piezoelectric effect is used *i.e.* an electric field is applied on the top and bottom electrodes of the piezoelectric material, inducing a deformation of the piezoelectric material. The curvature of the glass membrane and hence the polymer, can be increased and the focal length changed (Figure 1.1b-c). This design was inspired by the human eye. The lens itself is a technological evolution with respect to mobile photography. According to poLight, it is faster (response time < 1 ms) and less energy consuming (< 1 mW) than VCM technology and does not suffer from electromagnetic field interferences and field of view variation while focusing [2]. These properties allow for new

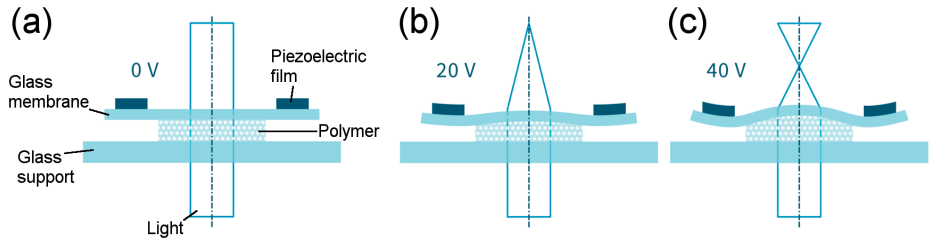

Figure 1.1. Simplified cross section scheme of the TLens® at different applied voltages (a) 0 V, (b) 20 V, (c) 40 V. Adapted from ref. [3].

features such as instant focus, all in focus imaging and easier implementation of dual camera systems, which has become a standard in the premium smartphone market during 2016-2017.

For the next TLens® generation, poLight AS plans are to increase the aperture of the lens from 1.55 mm to 2.2 mm and reduce the minimum focusing distance from 10 to 5 cm (or increasing the optical power from 10 to 20 diopters). Further possibilities for the developments of the lens include research on the design of the lens, investigating the possibility to use interdigitated electrodes instead of top and bottom electrodes [4-6] and replacing the PZT-based material of the piezoelectric electroceramic to lead-free and environmentally friendly alternatives [7, 8]. This is due to the temporary exemption from an European Union restriction of the use of hazardous substances in electrical and electronic equipment, until a sufficiently good alternative is found [9].

The polymer used in the TLens® today has a refractive index in the range between 1.40 and 1.53, a Young's modulus (E) lower than 100 kPa, and absorbs less than 10 % of the visible spectrum of light (400-800 nm) per millimeter thickness [10]. To reach the future goals for the TLens®, a polymer with a higher refractive index as high as possible (ideally above 1.65) while maintaining soft mechanical properties ($E < 100$ kPa) and a high transparency for visible light needs to be developed, in order to improve the overall optical power of the lens, without affecting its interactions with the piezoelectric MEMS. The present polymer matrix has a refractive index which is close to the limit of organic materials and can be classified as a high refractive index polymer [11] hence more complex material structures need to be developed.

The main motivation for this work is to explore the possibilities of enhancing the refractive index of the polymer system developing hybrid organic-inorganic materials [12]. Such organic-inorganic hybrid materials have already been demonstrated to be of large interest for optical applications [13]. As inorganic materials generally possess higher refractive index than organic materials [14], a first option consists of increasing the refractive index by incorporation of inorganic nanoparticles in the polymer matrix. Several challenges have to be solved like agglomeration of the nanoparticles inducing opacity, and the effect of the nanoparticles used as filler on the mechanical properties. A second possibility is to increase the refractive index of the polymer matrix itself by introduction of high refractive index organic groups [15]. The second option can be combined with the first.

However, these types of composites are industrially less attractive because of the number of steps required for their production: synthesis of the particles, synthesis of the polymer matrix, and their combination into a single material. A third route consists of *in situ* synthesis of the inorganic nanoparticles within the polymeric matrix [14]. This route is industrially the most interesting as it allows to synthesize the final material in a single step.

1.2. Objectives of the thesis

The main objective of this thesis is to provide new approaches for the synthesis of hybrid organic-inorganic materials with the focus on their use for high refractive index materials and their potential as substitute materials to the actual polymer in poLight's TLens®. A special attention was given to develop environmentally friendly synthesis routes and to achieve materials in the fewest number of steps as possible. The following two objectives were defined for the work.

In the first part, the goal was to achieve a new aqueous synthesis route to produce surface-functionalized nanoparticles, reducing the number of steps usually observed for the synthesis of such materials, synthesis of the particles and functionalization [16]. A hydrothermal synthesis to produce surface-functionalized titanium dioxide (TiO_2) nanoparticles with selected silane coupling agents is described. The influence of the silane coupling agents on the properties of the final materials and the growth mechanisms are discussed. The dispersion of the nanoparticles in silicone-based polymers was terminated due to dispersion and cross-linking challenges which thus led to the second part of the thesis.

The second part of the work aimed to simplify the synthesis of hybrid organic-inorganic materials further by preparation of the nanoparticles directly within the polymer matrix via an *in situ* route [14]. A non-aqueous sol-gel method using polydimethylsiloxane (PDMS) based materials and titanium alkoxides to produce high refractive index hybrid nanocomposites is reported. The correlations between the structure, the optical properties, and the mechanicals properties of the materials are described.

The two objectives of the thesis are linked by the fact that a common titanium precursor, titanium(IV) isopropoxide (TIP), and silanes and polysiloxanes types of organic materials were used for the study of titanium-silicon based organic-inorganic materials at nanoscale.

2. Introduction

In this chapter, a literature review on nanomaterials (and on titanium dioxide) and polymer materials (more specifically on polydimethylsiloxane) is first presented in order to introduce polymer nanocomposites and hybrid materials in a third part, including a dedicated sub-chapter on polymer nanocomposites with high refractive index (Chapter 2.3.3).

2.1. Nanomaterials

In 2011, the European Commission defined a nanomaterial as [17]:

> *"a natural, incidental or manufactured material containing particles, in an unbound state or as an aggregate or as an agglomerate and where, for 50 % or more of the particles in the number size distribution, one or more external dimensions is in the size range 1-100 nm".*

This definition differs from the International Organization for Standardization (ISO) which firstly defines nanoscale in the length range of 1-100 nm, and divides nanomaterials in two classes, nano-object (at least one dimension in the nanoscale) and nanostructured materials (internal structure or surface structure in the nanoscale) [18]. The divergence of these proposed definitions and their recent years of publication demonstrate the young age of nanotechnology. Nevertheless, since the end of the 20th century, nanomaterials have attracted a lot of interest from the industrial and academic fields. The increased interest in nanomaterials does not only come from their new and unique properties, but also because new synthesis methods and characterization techniques have drastically improved allowing resolution and better understanding of matter at nano- and subnanoscale [19]. A milestone was the invention of the probe microscopy (scanning tunneling microscope and atomic force microscope) in the beginning of the 1980s, by Binnig *et al*. [20-22], awarded Nobel Prize of physics in 1986.

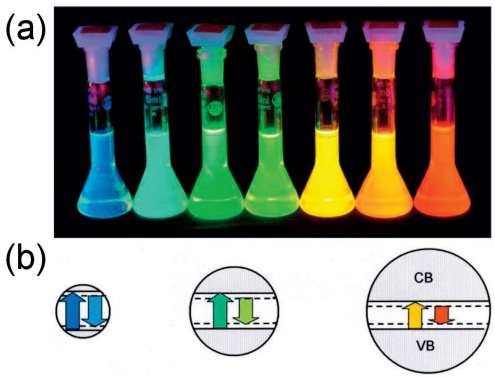

Figure 2.1. (a) Fluorescence of CdSe-CdS core-shell nanoparticles from 1.7 nm (blue) up to 6 nm (red), (b) representation of the gap between the conduction band (CB) and the valence band (VB) of the nanoparticles. (a-b) Adapted from ref. [23] with permission from The Royal Society of Chemistry.

At nanoscale, the surface to volume ratio of particles increases dramatically, and due to higher contribution of the surfaces, chemical and physical properties of nanoparticles are mostly governed by the properties and interactions at the surfaces. As an example, a 100 nm particle possesses about 1 % of its atoms located at the surface while a 5 nm particle possesses about 40 % of its atoms located at the surface [24]. In some cases, properties of a material become size dependent [19] *e.g.* the cell parameters [25]. This phenomenon is called the finite size effect. The most demonstrative cases are the finite size effects on the optical properties [26], and the band gap [27] also known as quantum size effect [23] (Figure 2.1a). In nanoparticles of selected metals and semiconductors, the density of states become more and more discrete as the particle size decreases and these discontinuities become size dependent (quantum confinement) influencing the absorption and fluorescence wavelengths (Figure 2.1b).

2.1.1. Synthesis of nanomaterials

Synthesis of nanomaterials can be separated in two main families, top-down and bottom-up processes [28]. For top-down processes, nanomaterials are synthesized from microscopic or macroscopic starting materials. For example, photolithography (UV, X-ray) is the most commercially used technique, as it is used in the silicon industry to produce microprocessors,

starting with silicon single crystal wafers, and finishing with nanostructures of about 14 nm (in 2017). Other examples of top-down processes are electron beam lithography (EBL) similar but more efficient and more expensive than photolithography, and focused ion beam (FIB) methods.

In bottom-up processes, nanomaterials are made from smaller building blocks such as atoms and molecules. The synthesis consists of designing paths for the building blocks to assemble in the desired manner. Example of bottom-up processes are depositions techniques such as pulse laser deposition (PLD), chemical vapor deposition (CVD), molecular beam epitaxy (MBD), atomic layer deposition (ALD), in which the initial materials are vaporized (or ablated from a target as a plasma, in the case of PLD) to be redeposited on a substrate with controlled thickness, phase, and crystallinity. Chemical solution methods (*e.g.* sol-gel, hydrothermal, precipitation, flame spray pyrolysis, *etc*.) are used for synthesis of nanomaterials starting with chemical solutions or colloids.

2.1.1.1. Metal alkoxides as precursors

Metal alkoxides are of general formula $M(OR)_z$ with a metal or metalloid M of valence or oxidation state z and OR an alkoxy group where R is a simple alkyl, substituted alkyl, or alkenyl group [29-31]. Metal alkoxides are widely used in solution chemistry processes where they react via hydrolysis and condensation mechanisms leading to the formation of the corresponding metal oxide, summarized as [31]:

$$M(OR)_z + \frac{z}{2} H_2O \xrightarrow[\text{condensation}]{\text{hydrolysis}} MO_{z/2} + z\,ROH \tag{2.1}$$

Intermediate steps involve formation of hydroxo-derivatives:

$$M(OR)_z + H_2O \xrightarrow{\text{hydrolysis}} M(OH)(OR)_{z-1} + ROH \tag{2.2}$$

The reaction thermodynamics is dependent on electrophilic character of the metal cation, the nucleophile specie, and the stability of the leaving group [29]. Kinetics can be assessed with the electronegativity (χ) of the metal and the degree unsaturation of the metal $N - z$ where N is the coordination number and z the valence of the metal [32, 33] (Table 2.1). The kinetics of hydrolysis is faster for high electrophilicity and high degree of unsaturation. For

Table 2.1. Electronegativity (χ), coordination number (N), oxidation state (z), and degree of unsaturation ($N-z$) of metals of selected alkoxides. Adapted with permission from ref. [32], Copyright 1996 American Chemical Society.

Alkoxide	χ	N	z	$N-z$
$Si(OR)_4$	1.90	4	4	0
$Sn(OR)_4$	1.96	6	4	2
$Ti(OR)_4$	1.54	6	4	2
$Zr(OR)_4$	1.33	7	4	3
$Al(OR)_3$	1.61	6	3	3

example, the hydrolysis rate of silicon ethoxide is five order of magnitude smaller than the one of $Ti(OR)_4$, at pH = 7 [29]. Hence, catalysts are often needed for silicon alkoxides while inhibitors are used in order to reduce the kinetics of reaction of titanium alkoxides [34]. Typical inhibitors are bidendate complexing ligands such as acetic acid or acetylacetone [35]. The relative reactivities of metal alkoxides listed in Table 2.1 follow the sequence:

$$\mathrm{Zr(OR)_4, Al(OR)_3 > Ti(OR)_4 > Sn(OR)_4 \gg Si(OR)_4} \tag{2.3}$$

The kinetics of reaction also decreases with increasing the size of the OR group, due to different partial charge distribution, and thus different M−OR bond polarity [36, 37]. The hydrolysis is then followed by formation of oxo bridges via condensation reaction. Several condensation mechanisms are possible depending on the hydrolysis ratio (H_2O/M) such as nucleophilic substitution (oxolation and alcoxolation, with production of water and alcohol, respectively) and nucleophilic addition (olation and alcoolation) which can occur if the metal cation coordination is not satisfied (*i.e.* $N - z > 0$) [29, 30, 33, 36]:

$$\mathrm{2\,M(OH)(OR)_{z-1} \xrightarrow{oxolation} (RO)_{z-1}M\text{–}O\text{–}M(OR)_{z-1} + H_2O} \tag{2.4}$$

$$\mathrm{M(OH)(OR)_{z-1} + M(OR)_z \xrightarrow{alcoxolation} (RO)_{z-1}M\text{–}O\text{–}M(OR)_{z-1} + ROH} \tag{2.5}$$

$$\mathrm{2\,M(OH)(OR)_{z-1} \xrightarrow{olation} (RO)_{z-1}M\text{–}(OH)_2\text{–}M(OR)_{z-1}} \tag{2.6}$$

$$\mathrm{2\,M(OR)_z \xrightarrow{alcoolation} (RO)_{z-1}M\text{–}(OR)_2\text{–}M(OR)_{z-1}} \tag{2.7}$$

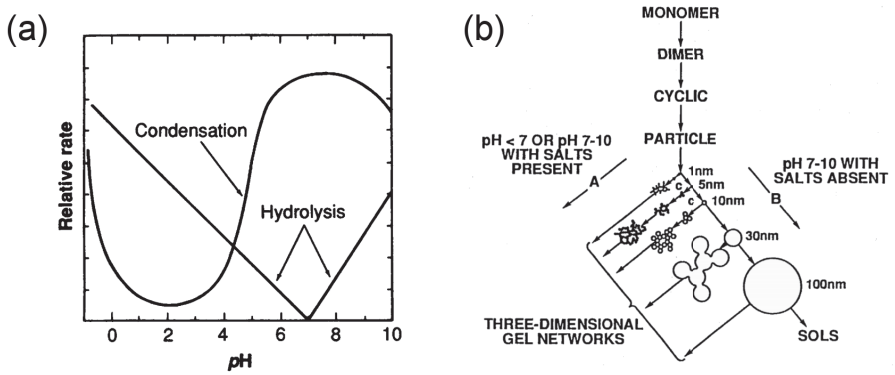

Figure 2.2. Schematic representations of the pH dependence of (a) the rates of hydrolysis and condensation, and (b) the polymerization behavior and morphology of silicon alkoxides. (a) From ref. [38], reprinted with permission from AAAS and (b) reprinted from ref. [29], Copyright 1990, with permission from Elsevier.

Both hydrolysis and condensation mechanisms can be catalyzed with the use of an acid or a base, and their use can influence the final morphology and structure of the obtained materials, as illustrated Figure 2.2 in the case of silicon alkoxides [29, 38].

In the case of titanium alkoxides, Blanchard *et al.* [39] showed via small-angle X-ray scattering (SAXS) and ^{17}O-nuclear magnetic resonance (NMR) that increasing the hydrolysis ratio (H_2O/Ti) or decreasing the inhibitor ratio (H^+/Ti) induce an increase of the fractal dimension of the titanium oxo-polymer (bushy polymers), while the size and the composition of the sub-units were not affected. Due to the coordination unsaturation and the Lewis acid properties, metal alkoxides can be oligomers in solution and in the solid state $[M(OR)_z]_n$. The formation of oligomers is increased with a large atomic size of the metal and decreases with the size of the alkoxy group, due to steric hindrance effect [31]. For example, $Ti(OR)_4$ with R = methyl, ethyl, or *n*-butyl exhibit oligomers while pure titanium(IV) isopropoxide (TIP) is a monomer due to the bulky isopropoxy groups [30, 35].

In an organic solvent, several types of reactions are possible, depending on the solvent and the type of alkoxides, such as C−C formation between benzyl alcohol and metal alkoxides, aldol condensation reaction, in the case of ketones [40-42]. In the case of highly valent metal ions, ether elimination reaction can occur between two metal alkoxides:

$$2\,\mathrm{M(OR)}_z \longrightarrow (\mathrm{RO})_{z-1}\mathrm{M{-}O{-}M(OR)}_{z-1} + \mathrm{ROR} \qquad (2.8)$$

2.1.1.2. Hydrothermal synthesis

Hydrothermal (from the Greek *hydros*, water and *thermos*, heat) synthesis is defined as a heterogeneous reaction in aqueous media above 100 °C and 1 bar [43]. It was initially used with precursors that were insoluble in normal conditions, in order to dissolve and recrystallize materials [44]. The specificity of hydrothermal synthesis resides by the changing properties of water at elevated temperatures and pressures, *e.g.* ionic product, viscosity, density, and dielectric constant [43, 45]. Above the critical point of water (374 °C, 221 bar), the difference between the liquid and the gas phases disappears, their densities become equal and dielectric constant of water drops, increasing the solubility of non-polar precursors [45]. It is thus important to distinct subcritical and supercritical conditions [46, 47]. Most works report synthesis performed under subcritical conditions and such synthesis still benefits of the characteristics of hydrothermal synthesis which are increased reactivity and solubility of the precursors. Hydrothermal synthesis is often performed in batch, using a PTFE-lined autoclave (Figure 2.3a) but also continuous hydrothermal synthesis has been developed [48, 49]. When the precursors are introduced in an autoclave, the resulting pressure conditions during synthesis are depending on the applied temperature and on the volume of the gas phase in the autoclave (Figure 2.3b). The ratio between the volume of precursors (including the solvent) and the total volume of the autoclave is called the filling factor [45].

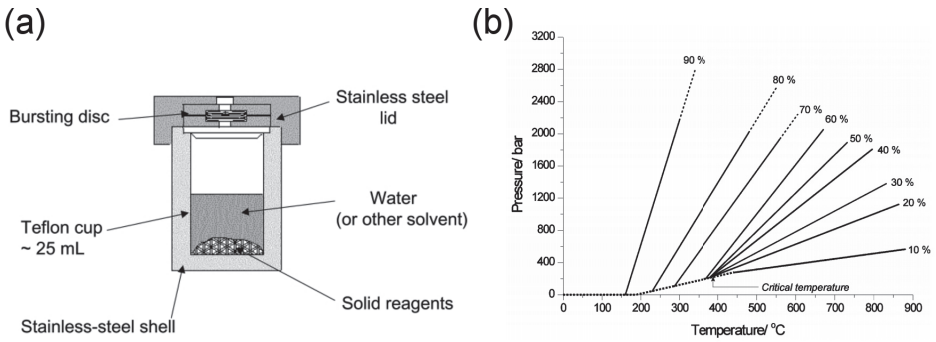

Figure 2.3. (a) Schematic of a PTFE-lined autoclave and (b) pressure as a function of temperature and filling factor of water in a sealed container. (a-b) Reproduced from ref. [50] with permission from The Royal Society of Chemistry.

By extension, the terms solvothermal and ionothermal synthesis define synthesis in organic solvent and ionic liquid, respectively [44, 51]. However, ionic liquids have negligible vapor pressure thus ionothermal synthesis are performed at ambient pressure, increasing the safety compare to the water and solvent counterparts [52].

In the case of production of oxide based materials, hydrothermal synthesis has several advantages compared to other methods such as sol-gel, solid state synthesis, or other physical methods. Among these advantages are a lower synthesis temperature, high control on the particle size and the particle size distribution, and a higher degree of crystallinity (for this temperature range) [50, 53]. The hydrothermal synthesis is in most cases a single-step method, and it is, however, harder to predict the outcome products of the synthesis.

With respect to applied temperatures, and depending on the precursors for producing desired materials, hydrothermal synthesis can be considered as environmentally friendly and a rather simple and cost efficient method [45].

2.1.1.3. Sol-gel synthesis

The term sol-gel comes from the different steps of the synthesis. *Sol* (for solution) refers to the initial step where a stable colloid suspension of particles is prepared from metal or metalloid elements based precursors such as salts, partially hydrolyzed alkoxides, and complexes [29, 54]. In a second step, via *e.g.* polycondensation mechanisms or destabilization of the colloidal suspension [54], the sol may form a *gel*, and the solvent is then removed. The sol-gel method can be used to prepare a wide range of final material structures like films, dense ceramics, powders, as well as aerogels (Figure 2.4). Processing conditions like pH, precursor concentration, mixing, oxidation state of the precursors are crucial in order to obtain the desired phases and morphologies of the final materials.

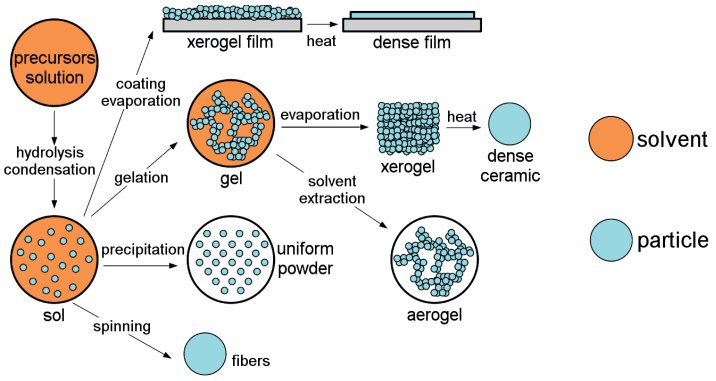

Figure 2.4. Flow chart of the different possibilities and steps involved in the sol-gel process. Adapted from ref. [55], CC BY 3.0.

In the case of the synthesis of multicationic oxides, the modified Pechini method and its variations were developed in order to increase the homogeneity of the cations in solution, a key parameter to obtain the desired phase and phase purity [56]. The method is based on the polyesterification of polycarboxilic acid (*e.g.* citric acid) and polyalcohol (*e.g.* ethylene glycol) around the metal cations to hinder their segregation. The choice of chelating agents depends on the nature and on the number of cations to produce stable solutions. Additional complexing agents such as ethylenediaminetetraacetic acid (EDTA) have been shown to increase phase purity, due to *e.g.* higher combustion temperature or degree of cross-linking [54]. Alternatively, water soluble polymers such as polyvinyl alcohol can be used, allowing to preserve high degree of porosity and nanosized primary particles after thermal treatments [57]. The sol-gel chemistry also allows for the synthesis of organic-inorganic hybrid network [32] (see Chapter 2.3.2).

Non-aqueous sol-gel processes involve organic solvent and allow for the use of a broader range of precursors [40]. Depending on the precursors and solvents used, different reactions pathways are possible for the formation of oxide nanoparticles such as haloalkane, ether, ester and amide eliminations and C−C bond formation between alkoxy groups [58].

2.1.2. Nucleation and growth mechanisms

From a thermodynamic point of view, homogeneous nucleation of nanoparticles in solution can be described by the total free energy (ΔG), the radius of the particle r, the surface energy between the solid-liquid interface (γ_{SL}), and the crystal free energy (ΔG_v) [59]:

$$\Delta G = 4\pi r^2 \gamma_{SL} + \frac{4}{3}\pi r^3 \Delta G_v \tag{2.9}$$

The crystal free energy ΔG_v is function of the temperature, the supersaturation of the solution (S_{sat}), and the molar volume (M / ρ, with M the molar mass and ρ the density) [59]:

$$\Delta G_v = \frac{-k_B T \ln(S_{sat})}{M / \rho} \tag{2.10}$$

with k_B, the Boltzmann constant. At very small r values, the surface energy term dominates, and when r increases, ΔG reaches a maximum value, ΔG_{crit} for which $r = r_{crit}$, the critical radius which is the minimum radius size for which a nucleated particle will not be redissolved in the solution (Figure 2.5a). Based on ΔG_{crit}, the rate of nucleation N can be modeled with an Arrhenius equation, where A is a constant:

$$\frac{dN}{dt} = A \exp\left(-\frac{\Delta G_{crit}}{k_B T}\right) \tag{2.11}$$

Heterogeneous nucleation differs from the homogeneous nucleation by the fact that the nuclei are in contact with another species that usually decreases the barrier for nucleation, often a surface, but also defects, impurities, bubbles, *etc*. [59, 60]. In these conditions, the nucleus does not have a spherical shape and the contact angle between the nucleus and the other specie must be taken in account.

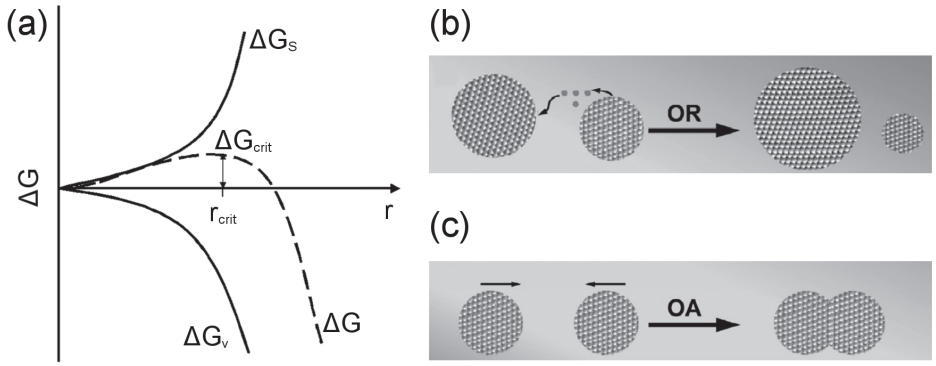

Figure 2.5. (a) Energy diagram of classical nucleation (ΔG_S represents the surface energy term) and schematic representation of (b) Oswald ripening (OR) and (c) oriented attachment (OA) growth mechanisms. Adapted from ref. (a) [61] and (b-c) [62] with permission from The Royal Society of Chemistry.

Classical growth occurs via surface reaction and surface diffusion and can be described using Fick's first law of diffusion [59]. This process is called Ostwald ripening (Figure 2.5b), where larger particles grow at the expense of the smaller ones due to variations in surface energies and chemical potentials as a function of the particle size [63]. Ostwald ripening kinetics can be followed with Lifshitz-Slyozov-Wagner (LSW) theory using:

$$d - d_0 = k_{OR} t^{1/n} \tag{2.12}$$

where d is the particle size at the time t, d_0 is the average size at $t = 0$, k_{OR} is a temperature-dependent rate constant, and n is an integer exponent which describes if the growth is controlled by diffusion of ions at the solution-particle boundary ($n = 2$), by volume diffusion of ions in the solution ($n = 3$), or by dissolution kinetics at the particle-solution interface ($n = 4$) [62, 64-67].

Oriented attachment (Figure 2.5c) is a non-classical growth mechanism in which crystalline nanoparticles self-organize spontaneously, sharing a common crystallographic plane resulting in monocrystalline particles [68-70]. The elongation direction is often directed so that oriented attachment occurs via the facets of highest energy. It has gained more attention since Penn and Banfield [70-72] described the phenomenon with high-resolution TEM analysis of titanium dioxide nanoparticles synthesized under hydrothermal

conditions. For oriented attachment, the first descriptions of the kinetics of growth were made during the synthesis of ZnS nanoparticles by Huang *et al*. [64, 73], and more recently in the case of CdS [74] and SnO_2 [75] quantum dots using:

$$d = \frac{d_0\left(\sqrt[3]{2}k_{OA}t + 1\right)}{k_{OA}t + 1} \tag{2.13}$$

where k_{OA} the rate constant for oriented attachment. Equation (2.13) was later modified in a more general formulation for the study of anatase nanoparticles by Zhan *et al*. [76]:

$$d = d_0 \frac{1 + mk_{OA}t}{1 + k_{OA}t} \tag{2.14}$$

where *m* was defined as the aggregation factor, representing a degree of aggregation of the nanoparticles being the building blocks of the oriented attachment.

Combined models (*i.e.* simultaneous Ostwald ripening and oriented attachment) and multistep oriented attachment models have also been described [62]. The size of the nanoparticles can be extracted by *e.g.* X-ray diffraction [64, 73, 76] and ultraviolet-visible optical spectroscopy [77]. Electron microscopy studies are also of importance for qualitative study of crystal growth via oriented attachment mechanisms but, however, do not allow *in situ* measurements [78].

Oriented attachment mechanism can be included in a larger family of non-classical growth mechanisms where, in intermediate steps, mesocrystals are formed and subsequently self-organize to the final material [79]. Different growth mechanisms can be observed and controlled with *e.g.* the use of surfactant and/or synthesis methods [80].

2.1.3. Titanium dioxide

With respect to its high abundance, low cost, nontoxicity, as well as physical and chemical properties, multiple applications of titanium dioxide or titania (TiO_2) has emerged. TiO_2 is a wide band gap semiconductor [81]. TiO_2 is used as a pigment and in cosmetics, food industry (labeled E171 in the European Union), sunscreens, and paints [82]. The discovery of water splitting on TiO_2 electrode under UV light [83] has brought lot of interests from the research community on TiO_2 for energy related applications. Based on surface [84] and nanosized properties [85], but also via doping [86], TiO_2 is used in a wide range of applications *e.g.* photocatalysis [87-91], photovoltaics [92-99], lithium-ion batteries [100, 101], but also in antimicrobial coatings [102], biomedical applications [103-109], memristive applications [110-112], optical enhancement [14, 113, 114], anti-corrosion, and self-cleaning properties [115].

However recent studies pointed out possibilities of toxicity [116-119] and neurotoxicity [120] of nanosized TiO_2. As precautions, standard HSE procedures and personal protective equipment must be used when manipulating nanoparticles.

2.1.3.1. Crystal structures of TiO_2

Eleven crystalline polymorphs of titania have been observed and/or obtained through different synthesis route (Table 2.2) [121]. Many experimental and computational works have been done to understand the thermodynamics of TiO_2 in order to be able to predict and synthesize the desired phases. Rutile, anatase, and brookite are the most common polymorphs since they occur naturally [122]. In addition, three other structures, TiO_2(B), TiO_2(H), TiO_2(R), are stable at ambient pressure. The five other structures (TiO_2(II), baddeleyite, OI, OII and cubic) are high pressure phases. Since all these structures are based on the same composition, lattice energies can be used to compare theoretical bulk stability of the structures (Table 2.2). Both rutile and anatase polymorphs are described by tetragonal systems, space groups $P4_2/mnm$ (136) and $I4_1/amd$ (141), respectively, while an orthorhombic space group *Pcab* (61) is used to describe the brookite structure. Rutile, brookite, and anatase are composed of TiO_6 octahedra and differ by the arrangement of the octahedra which share 2, 3, and 4 edges per polyhedron, respectively (Figure 2.6).

Table 2.2. Calculated lattice energies (at 0 K and 0 GPa) of the TiO_2 crystal structures, relative to that of rutile. Adapted with permission from ref. [121], Copyright 2014 American Chemical Society.

Phase	Crystal system	Space group (number)	Lattice energy (kJ mol^{-1})	Note
Rutile	Tetragonal	*$P4_2/mnm$* (136)	0	Ambient pressure phases
Anatase	Tetragonal	*$I4_1/amd$* (141)	24.75	
Brookite	Orthorhombic	*Pbca* (61)	18.53	
TiO_2(B)	Monoclinic	*C2/m* (12)	49.16	
TiO_2(H)	Tetragonal	*I4/m* (87)	73.05	
TiO_2(R)	Orthorhombic	*Pbnm* (62)	68.49	
TiO_2(II)	Orthorhombic	*Pbcn* (60)	8.86	High pressure phases
Baddeleyite	Monoclinic	*$P2_1/c$* (14)	155.55	
OI	Orthorhombic	*Pbca* (61)	141.07	
OII	Orthorhombic	*Pnma* (62)	141.97	
Cubic	Cubic	*Fm-3m* (225)	147.78	

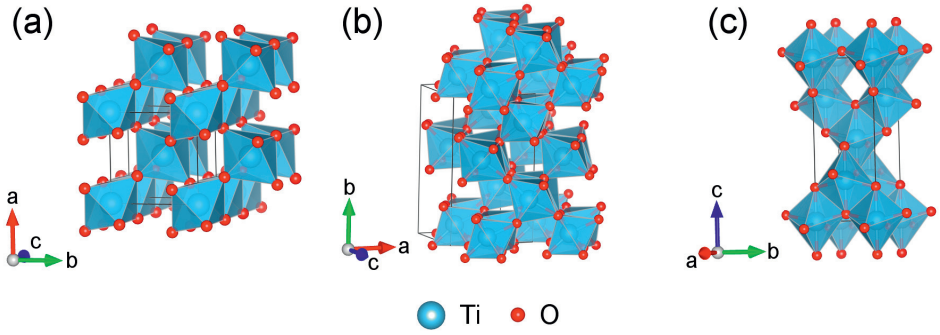

Figure 2.6. Polyhedra structures of (a) rutile, (b) brookite, and (c) anatase. Represented using VESTA [123] and data of anatase from ICDD card #00-021-1272, brookite from ICDD card #00-029-1360, and rutile from ICDD card #00-021-1276.

Rutile is the thermodynamically stable polymorph while brookite and anatase are metastable phases with lattice energy of 18.53 and 24.75 kJ mol^{-1}, respectively, relative to that of rutile. In addition, Gibbs free energy for the transition from anatase to rutile has been shown by Smith *et al*. [122] to remain negative at all temperature.

2.1.3.2. Finite size effect and phase equilibria of TiO_2

Surface free energy can be described as an excess energy relative to the bulk [63] being influenced by the number of bonds (more specifically, dangling bonds) per unit area, the strength of these bonds and, the surface chemistry. At the macroscopic scale, the crystal structure is mostly influenced by the bulk energy. As the particles are becoming smaller, the surface-volume ratio increases and the structure becomes more and more influenced by the surface free energy, also due to increased radius of curvature of the surfaces.

Most of the research on TiO_2 has been carried on the naturally occurring polymorphs, anatase, brookite, and rutile. Anatase and brookite have also been more observed for nanosized samples than rutile. Many different approaches have been used in order to estimate the influence of the size on the stability of rutile and anatase. Thermodynamically, stability of a nanoparticle system can be described by the general equation:

$$\mathrm{d}G = -\left(\sum_{i=1}^{N_S+N_F} \overline{S}_i n_i\right)\mathrm{d}T + \left(\sum_{i=1}^{N_S+N_F} \overline{V}_i n_i\right)\mathrm{d}\left(P + P_{\mathrm{exc}}\right) + \sum_{i=1}^{N_S+N_F} \overline{\mu}_i \mathrm{d}n_i + \sum_{j=1}^{J} \gamma_j \mathrm{d}A_j + \sum_{k=1}^{K} \sigma_k \mathrm{d}l_k + \sum_{l=1}^{L} \lambda_l \tag{2.15}$$

where G is the total free energy, N_s and N_F are the numbers of components in the nanoparticles and the number of species in the fluid phase, respectively; T, P, and P_{exc} are the temperature, external pressure, excess pressure induced by stress in the nanoparticles, respectively; $n_i, \overline{S}_i, \overline{V}_i, \overline{\mu}_i$ are the molar number, partial molar entropy, partial molar volume, and electrochemical potential of species i, respectively; γ_j is the interfacial free energy of interface j with area A_j formed by the solvent and one face of the nanoparticle; σ_k is the line energy of edge k with length l_k formed by two interfaces; and λ_l is the point energy of vertex l formed by two edges or three faces [19]. Equation (2.15) expresses the complexity of thermodynamics of titania at nanoscale with parameters which are keys to understand the stability of the nanoparticles *i.e.* temperature, pressure, surface pressure, surface free energy, solvent (environment), and morphology. Several computational and experimental studies have been carried out to reveal the influence of several of these parameters.

Computational methods are mostly based on molecular dynamics (MD) simulations and density functional theory (DFT) calculations. Oliver *et al*. [124] have calculated the surface free energies of different crystallographic surfaces of rutile and anatase. The energy of the

crystal is described via interatomic potentials. The surface free energy for a given *hkl* Miller plane (γ_{hkl}) was defined as the difference between surface block simulation energy (U_{surf}) and the energy of the same number of bulk ions (U_{bulk}), per unit area (A):

$$\gamma_{hkl} = \frac{U_{surf} - U_{bulk}}{A} \tag{2.16}$$

Using Wulff's theorem, and Equation (2.16) they obtained similar structures compared to experimental shapes, with {011} and {001} surfaces of surface energies of 1.40 and 1.28 J m^{-2}, respectively. Based on these results, Zhang and Banfield [125] modeled the stability crossover between anatase and rutile. Considering spherical particles, standard free energy of formation and surface stress (based on Young-Laplace equation for spherical shape), they obtained:

$$\Delta G^0 = \Delta_f G_R^0 - \Delta_f G_A^0 + (2x+3)\frac{M}{r}\left(\frac{\gamma_R}{\rho_R} - \frac{\gamma_A}{\rho_A}\right) \tag{2.17}$$

where ΔG^0 is the free energy of transition from rutile to anatase, $\Delta_f G^0$ is the standard free energy of formation, M is the molecular weight, r is the average radius of anatase particles, ρ is the density and γ is the surface free energy. Subscripts A and R represent anatase and rutile, respectively. Surface stress was assumed x times the surface free energy, as it was observed that the surface stress of metals is one to two times the surface energy. Using Equation (2.17), Zhang and Banfield calculated an anatase-rutile transition size of 14 nm, with negligible variations as a function of the temperature from 300 to 1000 K. The results were extrapolated and surface free energy of 1.91 J m^{-2} and 1.32 J m^{-2} for rutile and anatase at 298 K, respectively, were calculated [125]. For very small particles (2-6 nm), Naicker *et al*. [126] showed by MD simulations on spherical nanoparticles that the average coordination of the Ti atoms decreased from 6 to 5 or 4 with the diminution of the particle size, inducing change in surface free energy (Figure 2.7a). They also simulated phase stability of the different titania polymorphs relative to bulk rutile, as a function of the particle size (Figure 2.7b). According to Figure 2.7b, anatase to rutile transition size is about 2.5 nm (at 300 K), and brookite is not stable at any size, even though surface energy of brookite was calculated to be the lowest at diameters of 5 and 6 nm (Figure 2.7a).

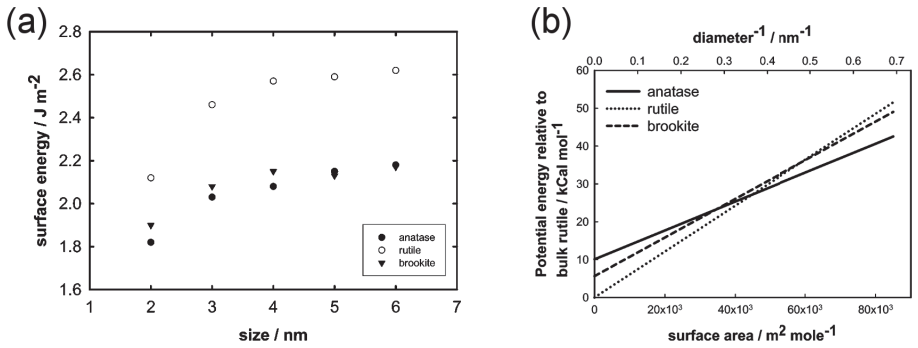

Figure 2.7. (a) Surface free energy at 300 K as a function of particle diameter and (b) energy of anatase, rutile, and brookite relative to the bulk rutile at 300 K as a function of surface area. (a-b) Reprinted with permission from ref. [126], Copyright 2005 American Chemical Society.

The difference between results from Zhang and Banfield [125] and Naicker *et al*. [126] can be explained by how the particles were modeled. Wulff's theorem was used in the first case, and isolated spherical particles were modeled in the second case. Zhou and Fichthorn [127] have also reported MD simulations on faceted titania nanoparticles based on Wulff's construction. An anatase-rutile transition size of 267 TiO_2 unit cells was calculated, corresponding to 2.1 nm along the (101) normal planes or 3.6 nm along the [001] direction, similar to that calculated by Naicker *et al.* [126]. The difference between these results and results from Zhang and Banfield [125] can be explained by contribution from edges and corners to the total surface free energies.

Many studies have been carried out using calorimetry in order to measure enthalpy of reactions and to calculate surface free enthalpy of the different titania polymorphs. Ranade *et al.* [128] reported experimental studies on the thermodynamics of titania transitions from nanoscale to bulk. The reaction from bulk rutile to nanosized anatase was described using:

$$\Delta H_{\text{trans}}\left(\text{bulk} \rightarrow \text{nano}\right) = \Delta H_{\text{trans}}\left(\text{bulk rutile} \rightarrow \text{bulk anatase}\right) + \gamma A \tag{2.18}$$

where ΔH_{trans} is the transformation enthalpy, γ is the surface free enthalpy and A is the surface area. Since the entropy for anatase and rutile are the same within experimental error, the enthalpy was used to describe the stability of nanosized TiO_2. The enthalpy change with respect to bulk rutile at 298 K was obtained after corrections for adsorbed water. Ranade *et al.* [128] reported a surface free enthalpy of 2.2 ± 0.2 J m^{-2} and 0.4 ± 0.1 J m^{-2} for rutile and

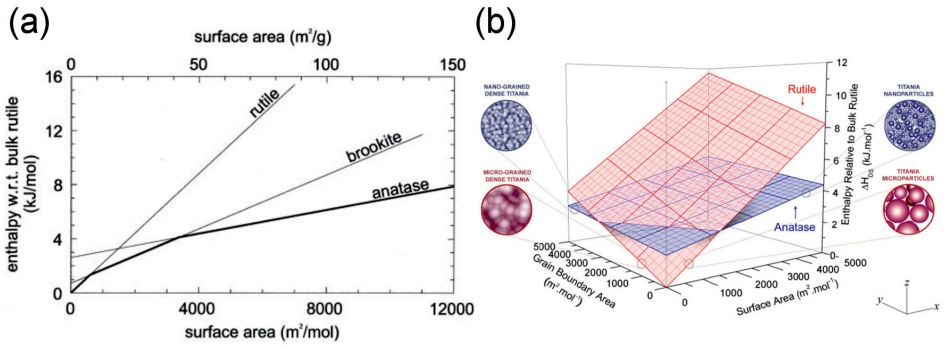

Figure 2.8. Enthalpy stability diagrams of titania as a function of (a) surface area, bold line shows stable structure and (b) both grain boundary and surface areas. (a) Reproduced with permission from ref. [128], Copyright 2002 National Academy of Sciences, U.S.A. and (b) reprinted from ref. [130], Copyright 2013, with permission from Elsevier.

anatase, respectively, crossing at a surface area of 1452 $m^2\ mol^{-1}$ (about 79 nm), as represented Figure 2.8a. However, Brookite was also included from previous literature values [129], and a size of 79 nm correspond to the stability region of brookite. Rutile and anatase were calculated to be the most stable phases, for a particle size above 201 nm and below 36 nm, respectively.

Levchenko *et al.* [131] additionally took into account the influence of the particle morphology and strongly bonded water. They calculated surface free enthalpy of 2.22 ± 0.07 J m^{-2} and 0.74 ± 0.04 J m^{-2} for rutile and anatase, respectively. The results from Levchenko *et al*. without corrections were in good agreement with results from Ranade *et al*. More recently, Castro *et al*. [132] have modified Equation (2.18), considering the influence from grain boundaries (solid-solid interfaces), in addition to solid-vapor interfaces:

$$\Delta H_{\text{trans}}\left(\text{bulk} \rightarrow \text{nano}\right) = \Delta H_{\text{trans}}\left(\text{bulk rutile} \rightarrow \text{bulk anatase}\right) + \gamma_{\text{SS}} A_{\text{SS}} + \gamma_{\text{SV}} A_{\text{SV}} \qquad (2.19)$$

where SS and SV subscripts represent solid-solid and solid-vapor interfaces, respectively. Figure 2.8b shows the influence of both grain boundary and surface area on energetic stability of titania.

Barnard *et al.* [133-135] have reported the influence of the pH and the surface chemistry on the anatase-rutile transition by DFT simulations and thermodynamic modeling. The influence of the surface chemistry on the surface energy (γ) was modeled using:

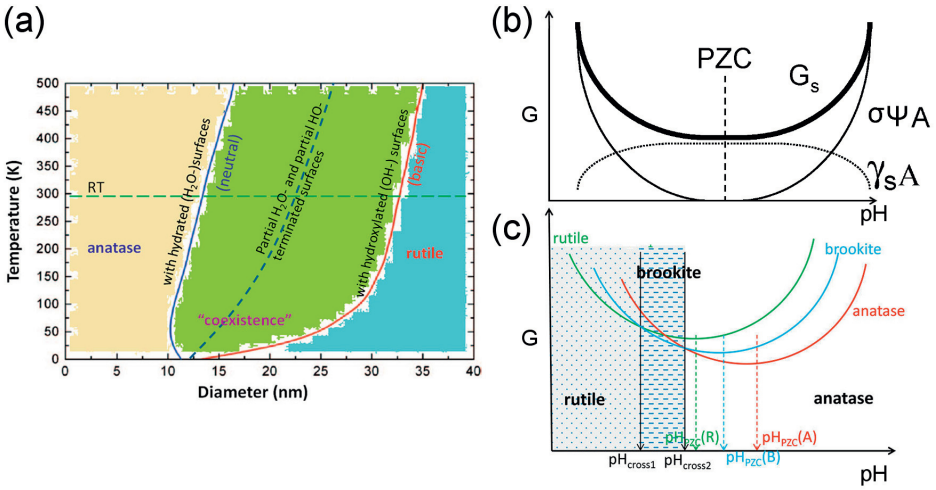

Figure 2.9. (a) Temperature-particle size phase diagram for nanosized TiO_2 with different surface terminations (hydrated, hydroxylated, or a mixture of the two), (b) schematic representation of Equation (2.21), showing contribution of surface electrostatic energy and interfacial free energy, (c) stability diagram of anatase, brookite and rutile as a function of pH. (a) Reprinted with permission from ref. [121], Copyright 2014 American Chemical Society, (b) adapted with permission from ref. [136], Copyright 2007 American Chemical Society, and (c) adapted with permission from ref. [121], Copyright 2014 American Chemical Society.

$$\gamma = \frac{1}{2A}(E_N^{\text{surface}} - NE^{\text{bulk}} - N_{\text{ad}}\mu_{\text{ad}}) \tag{2.20}$$

where A is the surface area, E_N^{surface} is the total energy of the surface, E^{bulk} is the energy per stoichiometric unit of the bulk, N is the number of TiO_2 units in the stoichiometric cell, N_{ad} is the total number of adsorbate units present, and μ_{ad} is the chemical potential of the adsorbates. The influence of pH was modeled using Equation (2.20) for −OH groups and water. Figure 2.9a shows that anatase is more stable when synthesized under basic conditions while rutile is more stable when synthesized under acidic conditions. A coexistence domain has been determined, giving an anatase-rutile transition size between 10 and 35 nm, depending on the temperature.

Electrochemical measurements have been carried out in order to measure environment and pH influences on phase stability of titania. Finnegan *et al*. [136] showed that the total surface free energy can be related to surface electrostatic energy and interfacial free energy:

$$G_S = \gamma A + \sigma \psi A \tag{2.21}$$

where G_S is the total surface energy, γ is the interfacial free energy, A is the surface area, σ is the surface charge per unit area, and ψ is the surface potential. Initial pH of the synthesis also influences phase stability, depending on precursor state and/or surface state. Figure 2.9b shows a schematic representation of Equation (2.21) as a function of pH.

At the point of zero charge (PZC), the contribution from the surface electrostatic energy can be neglected and surface free energy can be calculated. Far from the PZC, predominant contribution to phase stability is governed by surface electrostatic energy. Finnegan *et al*. were able to calculate the surface potential based on the measured surface charge density. Figure 2.9c shows a comparison plot of G_S curves from Equation (2.21) for anatase, brookite and rutile. The shapes of the curves were assumed similar due to similar composition and the relative position changes due to their respective PZC. PZC values of 5.9 and 6.3 for rutile and anatase, respectively, were taken from previously reported values by Bourikas *et al*. [137]. The PZC of brookite was assumed to be between those of anatase and rutile, based on the surfaces energies [121]. Figure 2.9c shows that anatase is more stable at high pH while rutile is more stable at low pH. The relative total surface energies of the polymorphs can cross and therefore their relative phase stabilities can reverse at a certain pH value. The stability crossover pH is also dependent on the particle size. Small particle size will favor anatase and shift the crossover pH towards lower values while large particles size will favor rutile and shift the crossover pH towards higher values (relative position of the G_S curves will be translated along the G axis). The effect of synthesis methods in solution, precursors, pH, and the processes of nucleation were extensively covered in a recent review by Kumar and Rao [138].

2.1.3.3. Hydrothermal synthesis of TiO_2 nanoparticles

Synthesis of titania nanoparticles via various hydro- and solvothermal synthesis routes using titanium precursors such as TIP, titanium(IV) butoxide (TIB), or titanium(IV) chloride ($TiCl_4$) were reported and depending on parameters and additives, different polymorphs and morphologies were obtained. A non-exhaustive summary of different reports is given in Table 2.3.

Table 2.3. Literature reports of hydro- and solvothermal routes to TiO_2 nanoparticles.

Precursor	Route[a] (solvent)	Conditions[b]	Results[c]	Note[c]	Ref.
$TiCl_4$	H	85-220 °C, 1-4 h, pH 0-8.2	A (10 nm) R rods	A favored at pH > 7 R favored with mineralizers	[139]
Anatase sols	H	100-250 °C, 1-255 h, pH 3-7	A elongated (10-50 nm)	Oriented attachment mechanism along [001]	[71]
TIP	H	250 °C, 26 h, pH 0.5 (HNO_3)	R (17.5 nm) A+R (28.6 nm)	Phase pure R obtained with stirring (with HNO_3)	[140]
$TiCl_4$	H	150-220 °C, 2-22 h, pH < 0-9	A (10 nm) R rods	A favored using HF, HCl, and HNO_3, R favored using citric and nitric acids	[141]
TIP	H	100-400 °C, 2-24 h	A+B (7-28 nm) A (11-115 nm)	B was formed as secondary phase at T < 200 °C	[46]
TIP	H/S (ethanol)	240 °C, 4 h, pH 0.7 (HNO_3)	A (15 nm) A+R (25 nm) A+B (7 nm)	Particle size was reduced by increasing ethanol/water vol. ratio	[142]
TIP	S (toluene)	250 °C, 20 h, OA	A (3-6 nm) A rods (3×20 nm)	[001] oriented rods at high precursor/surfactant ratio	[143]
$TiOSO_4$	H	150-250 °C, 10 min - 6 h	A (10-30 nm)	Increased size with higher temperature or longer reaction	[144]
TIP	H	200-250 °C, 12 h, pH 1-11	A (10-40 nm) A+R (15 nm)	Higher temperature gave R secondary phase, higher pH gave larger particles	[93]
TIP	H	1.5 M AA, 200 °C; 4 M HCl, 200 °C; 3 M HCl, 175 °C	A (3-6 nm) B+R (5-10 nm) R (5-15 nm)	At longer reaction time, rods (> 500 nm) were formed in the case of rutile.	[145]
TIB	H/S (ethanol)	140-180 °C 18 h, OA, OM	A spheres (13 nm) A tetragons (20 nm) A rod (20 nm)	The shape was highly dependent on TIB:OA:OM ratios.	[146]
TIB	S, H/S (cyclo-hexane)	150-250 °C 6 h, OA, OM	A+R wires A cubes (7 nm) A rods (5 nm)	The shape was highly dependent on solvent, and OA:OM ratios.	[147]

[a] H: hydrothermal, S: solvothermal, H/S: combination hydro- and solvothermal synthesis.
[b] AA: acetic acid, OA: oleic acid, OM: oleylamine.
[c] A: anatase, B: brookite, R: rutile.

2.2. Polymer materials

Polymer materials can be either natural such as proteins and cellulose or synthetic such as plastic materials *e.g.* polystyrene and poly(methyl methacrylate), also known as Plexiglas. Polymer materials are often divided in two main categories, thermoplastics and thermosets. The first category consists of polymers that keep their shape at room temperature and can be melted at elevated temperature to obtain a new shape. The second category corresponds to polymers that can be shaped while made but then keep their shape upon heating until degradation [148]. Polymers are macromolecules that consists of one (homopolymer) or several (copolymer) repeating subunits. They can be either linear, branched, or even cross-linked *i.e.* all linear chains are linked to each other via covalent bonds [148]. Most polymers do not have every chain of the same length, thus to describe polymers, the number average molecular weight (M_n) and weight average molecular weight (M_w) are defined as follow:

$$M_n = \frac{\sum_i N_i M_i}{\sum_i N_i} \tag{2.22}$$

and

$$M_w = \frac{\sum_i N_i M_i^2}{\sum_i N_i M_i} \tag{2.23}$$

where i is the degree of polymerization (*i.e.* number of repeating units), N_i is the total number of chains having the molar mass $M_i = i \times M_0$, with M_0 the molar mass of the repeating unit. Consequently, the dispersity ($Đ$) – previously known as polydispersity index and recently redefined by the IUPAC [149] – is defined as:

$$Đ = M_w / M_n \tag{2.24}$$

where a dispersity of 1 would describe a uniform polymer (*i.e.* all chains have the same number of repeating units, in the case of a homopolymer).

Properties of polymers are strongly related to the degree of polymerization and polymers exhibits unique properties *e.g.* amorphous or semi-crystalline structures and viscoelastic properties. Semi-crystalline and amorphous materials can exhibit glass-transition at a temperature, T_g, below the melting point. Above T_g the polymer chains acquire a relative mobility towards each other and the polymer becomes softer and flexible. The glass-transition is reversible and can be identified by a change of the volume slope as a function of the temperature (*i.e.* change of the thermal-expansion coefficient) and in the specific heat. The glass transition is similar to second-order phase transitions [150], and is related to the thermal history of the material [148].

2.2.1. Polysiloxanes

In today's society, polysiloxanes or silicones, are present in many fields such as electronics, aerospace, textile, food, and medical industries [151]. The organosilicon chemistry started in the 1940s, when the direct process (Rochow process) for production of chlorosilanes from metallic silicon and methyl chloride was developed [151, 152]. In this process around 80 wt.% dimethyldichlorosilane is formed together with other silanes:

$$x\,CH_3Cl + Si \xrightarrow[Cu\,catalyst]{300°C} (CH_3)_3SiCl + (CH_3)_2SiCl_2 + (CH_3)SiCl_3 + others \qquad (2.25)$$

The products can further be rearranged, hydrolyzed and condensed to form a variety of silicones [153, 154]. Polydimethylsiloxane (PDMS) is a homopolymer of general formula $H_3C\left[Si(CH_3)_2O\right]_n Si(CH_3)_3$ where n is the number of $\left[Si(CH_3)_2O\right]$ repeating units. PDMS can exhibit silanol end-groups −OH, also called hydroxy-terminated PDMS, which allow for further reaction via the active terminal hydroxy-groups.

Kataoka and Ueda showed trends between the room temperature viscosity (η, measured at 25 °C) and the mass-average molar mass (M_w) of PDMS by combining early studies (*e.g.* Barry [155] who showed a relationship between the intrinsic viscosity and molar mass of PDMS materials via the Mark-Houwink relation), as reproduced in Figure 2.10 [156]. The logarithm (base 10) of η as a function of M_w shows two linear regions, with different slopes, before and after a critical molar (M_c) which has been calculated for PDMS at 25 °C to be

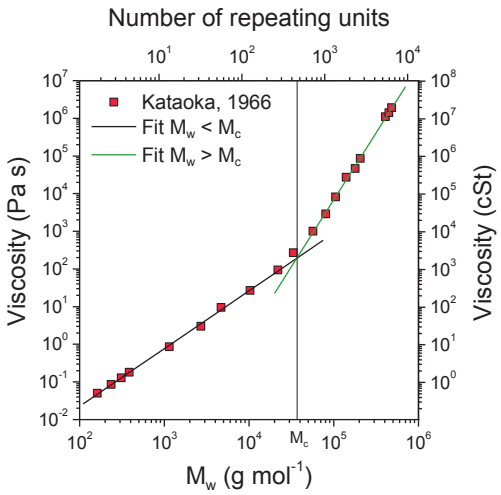

Figure 2.10. Relationship between viscosity (25 °C) and mass-average molar mass (M_w) of PDMS materials (replotted with data from ref. [156]). The number of repeating units corresponds to n in $HO\left[Si\left(CH_3\right)_2 O\right]_n H$ and is calculated from M_w, and the viscosity in centistokes (cSt) is calculated from the viscosity in Pa s and using a density of 0.97 g cm^{-3} [157].

M_c = 30 000 [156]. Regression of the linear regions before and after M_c (Figure 2.10), gives Equations (2.26) and (2.27), respectively:

$$\eta(\text{Pa s}) = 1.91146\times10^{-5} M_w^{1.53443} \tag{2.26}$$

$$\eta(\text{Pa s}) = 1.17115\times10^{-14} M_w^{3.55380} \tag{2.27}$$

The slope increase at M_c (22 000 < M_w < 60 000) results from chain entanglement effects, also called reptation [158], due to longer chains which are trapped into each other acting as obstacles, and reducing their mobility [148]. Data from Kataoka and Ueda were obtained in the case of unfractionated PDMS, Equations (2.26) and (2.27) can thus be used to estimate M_w (or M_n) or η of PDMS for monodisperse samples (*i.e.* $Đ$ = 1).

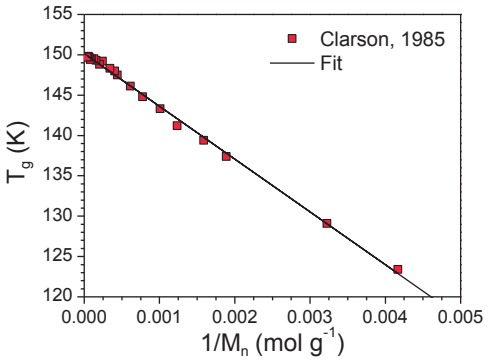

Figure 2.11. Relationship between glass transition temperature (T_g) and the number-average molar mass (M_n) of PDMS materials. Described by Equation (2.28), and replotted with data from ref. [159].

Clarson *et al.* [159] measured the glass transition temperature (T_g) of almost monodispersed (*i.e.* $Đ \approx 1$) linear trimethyl-terminated PDMS materials using differential scanning calorimetry (DSC). T_g was measured at about 123 K (−150 °C) for the polymer with the smallest chains containing around three repeating units. T_g showed a maximum value of 150 K (−123 °C) for longer chains, after extrapolation to infinite molar mass (Figure 2.11). A Flory-Fox relationship [150, 160] between T_g and the inverse of number-average molar mass (M_n) was observed:

$$T_g\,(\mathrm{K}) = \frac{-6543.8}{M_n} + 150.16 \tag{2.28}$$

2.2.2. Other polymers

Nearly every polymer can be used for the synthesis of nanocomposites, depending on the targeted application. In the case of optical applications, other commonly used polymer matrices are *e.g.* poly(methyl methacrylate), epoxy-based polymers, polyimide-based polymers, polyether-based polymers, polyol-based polymers, and polycarbonates [114, 161-172], as well as polymers containing high refractive index components such as sulfur and aromatic rings [11, 15, 173].

2.3. Hybrid materials and polymer nanocomposites

Composite materials are multiphase materials from which the properties are not necessarily the sum of the properties of the individual components, but can benefit from interactions, creating a synergetic effect. The term nanocomposite is used to describe a composite if one of the components is in the nanoscale [174]. Nanocomposites can thus have new, unique, and multifunctional properties.

Hybrids materials [12, 175] are part of the category of nanocomposites materials. The term hybrid refers to the fact that this class of materials are formed from both organic and inorganic components. New properties arise from the combination of these materials due to interactions [176]. Since organic and inorganic materials often exhibit opposite trends in properties, hybrid materials benefit from both kind of materials, and the possibilities of tuning the properties are greater than for traditional materials. Nanocomposites or hybrid materials are divided into two classes depending on the interaction type between the inorganic and organic components [33]. Class I corresponds to weak bonding between the inorganic and the organic phases, such as van der Waals, hydrogen, and ionic interactions. Class II materials contain strong covalent bonding such as alkoxy (M−O−C), organometallic (M−C) [175], or ionocovalent bond between the inorganic and the organic components (Figure 2.12). Some examples of class I and class II hybrids are intercalated polymer chains in clay-type materials [177], and metal-organic frameworks [178], respectively.

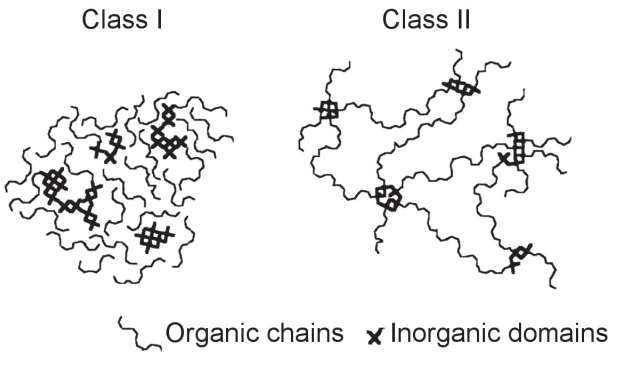

Figure 2.12. Schematic representation of class I and class II nanocomposites. Adapted from ref. [175] with permission of The Royal Society of Chemistry.

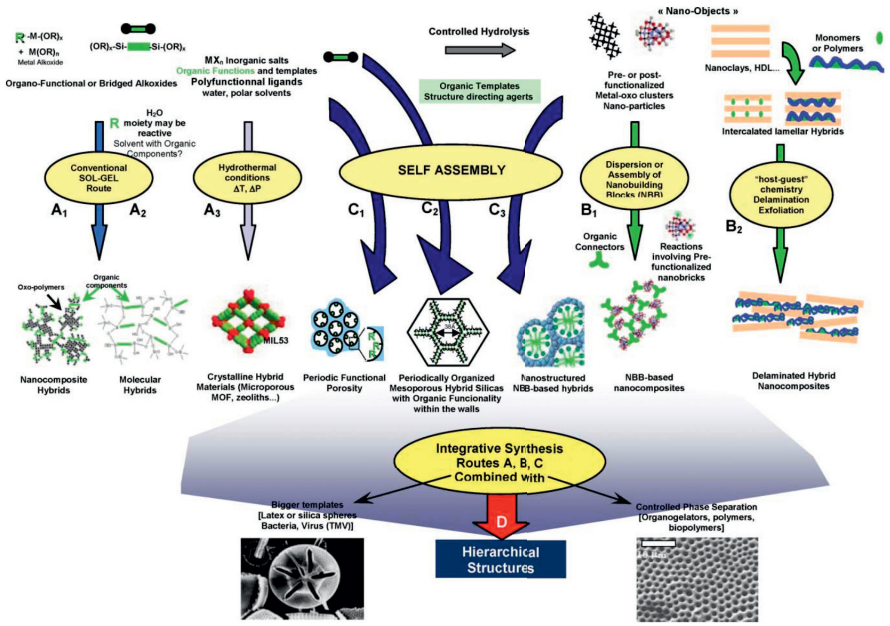

Figure 2.13. Scheme of the main chemical processes for the synthesis of organic-inorganic materials, A_1-A_2: sol-gel, A_3: hydrothermal, B_1: assembly of nano-building blocks, B_2: dispersion of nano-building blocks, C: self-assembling processes, D: combination of A, B, and/or C. Reproduced from ref. [179] with permission of The Royal Society of Chemistry.

Due to the multiplicity of the possible combinations of organic-inorganic materials, several synthesis processes have been developed depending on the targeted application. Figure 2.13 summarizes the different synthesis paths to obtain various types of hybrid organic-inorganic materials via sol-gel synthesis, hydrothermal synthesis, dispersion, self-assembly or a combination of these routes.

Using nanofillers in polymer matrices relative to larger sized fillers increases the interface between the polymer and the nanoparticles resulting in similar properties as the traditional composite for a significantly lower amount of particles [180]. Properties of the polymer nanocomposites are highly correlated with the amount of nanofillers, size and size distribution, dispersion state, and particle shape [180]. Polymer nanocomposites have emerged during the 1990s, when Toyota first reported the use of clay-based nanomaterials to increase thermal and mechanical strength of nylon-6 polymers [181]. Today these materials are used in many fields such as sports, automobile, electronic, medical, food and

aeronautical industries [182], as bio-compatible, flame-retardant, coating, and materials for optics. For the optical applications, the most studied properties are refractive index, transmittance and absorbance, fluorescence, polarization and non-linearity [114]. In an ideal case were spherical nanoparticles are dispersed in a polymer in a face centered cubic arrangement, the theoretical limit of particle incorporation is 74 vol.%, but in practice, this limit is lower [24].

2.3.1. *Ex situ* synthesis of polymer nanocomposites

In *ex situ* synthesis of transparent polymer nanocomposites, the particles are first synthesized. In a second step, the nanoparticles are then dispersed in either the polymer (blending route) or in the monomer or a solution containing the monomer which is then polymerized (*in situ* polymerization), as presented in Figure 2.14.

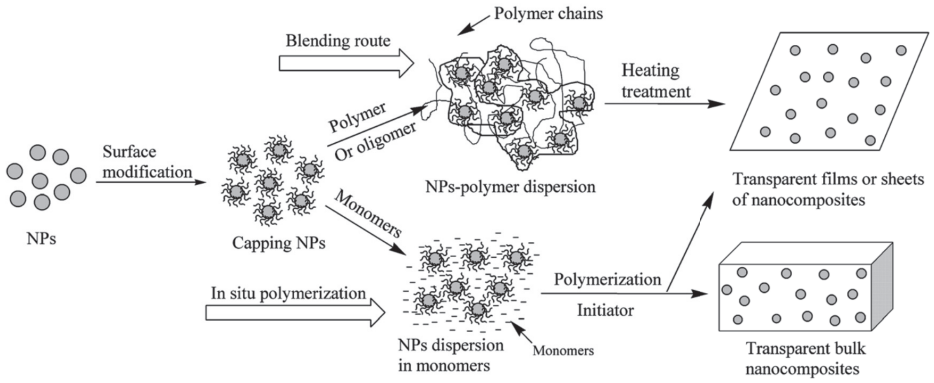

Figure 2.14. Scheme of the steps involved in *ex situ* synthesis of transparent polymer nanocomposites. Reproduced from ref. [14] with permission of The Royal Society of Chemistry.

2.3.1.1. Particle-matrix interface and surface functionalization

Due to high surface energy and energy difference between inorganic and organic materials (about 500-2000 mJ m^{-2} and about 20-50 mJ m^{-2}, respectively), the *ex situ* synthesis of homogeneously dispersed polymer nanocomposite is challenging because of the strong tendency of the nanoparticles to agglomerate [183]. In most nanoparticle systems, the dominating interparticle forces are van der Waals interactions, and nanoparticle stabilization in aqueous solutions can be approached using the DLVO theory [184, 185]. The agglomeration of nanoparticles reduces the interactions between inorganic materials and the polymeric matrix resulting in materials having similar properties to traditional composites.

One of the main strategies to overcome this mismatch of compatibility is to functionalize the inorganic nanoparticles with organic molecules or macromolecules (Figure 2.14) in order to reduce the hydrophilic behavior and obtain a better dispersibility in organic solvent and polymeric matrices [16]. Surface functionalization of inorganic nanoparticles also brings additional properties for multifunctional applications as for example, in biomedical application, with theranostic (combination of diagnostic and therapeutic capabilities) [186].

The characterization of nano-hybrid systems requires several complementary techniques in order to analyze the functionalization layer, the nature of the bond between the organic molecules and the nanoparticles, and the nanoparticles [187] (Figure 2.15).

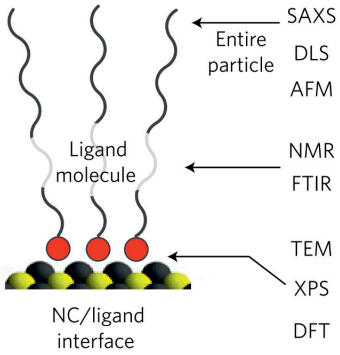

Figure 2.15. Commonly used techniques to characterize surface-functionalized nanoparticles (SAXS: small-angle X-ray scattering, DLS: dynamic light scattering, AFM: atomic force microscope, NMR: nuclear magnetic resonance, FTIR: Fourier transform infrared spectroscopy, TEM: transmission electron microscope, XPS: X-ray photoelectron spectroscopy, DFT: density functional theory, NC: nanocrystal). Adapted by permission from Macmillan Publishers Ltd: *Nature Materials*, ref. [187], Copyright 2016.

Classical synthesis routes of surface-functionalized nanoparticles are, in most cases, following two steps, particles synthesis and post-functionalization [16] (Figure 2.14). The main approach to surface functionalize metal or metal oxide surfaces is to take advantage of the presence of surface −OH groups [188]. Commonly used functionalization agents are silanes, phosphonates, carboxylates, and amines [188, 189]. Different types of structures and bonds (*e.g.* van der Waals or covalent bonding) can be obtained depending on the functionalization conditions and the targeted application. For example, Qu *et al*. [190] studied the effect of solvothermal treatments on TiO_2 nanoparticles functionalized with carboxylates and determined a bidentate chelating type of bonding, providing better stability of the functionalization than conventional routes. Sakeye *et al.* [191] compared functionalization of four oxide nanoparticles (SiO_2, TiO_2, ZrO_2, and SnO_2) with four types of functionalization agents (silane, phosphate, amine, and polyamine). Satisfactory functionalization was obtained on all oxides with silane, amine, and polyamine, but not with the phosphate functionalization agent, due to large phosphate anchoring group. Zeta potential values showed poor stability of the SnO_2 functionalized nanoparticles compared to the other oxides, and silano-modified samples at low pH show better long term stability of SiO_2 compared to ZrO_2 and TiO_2. Leroux *et al*. [192] functionalized layered double hydroxides (LDH) with different types of linear carboxylates and showed that the resulting interlayer spacing of the LDH and the rheological properties of polymer nanocomposites based on these functionalized LDH could directly be correlated to the length of the carboxylates.

Grafting molecule such as vinyltriethoxysilane (VTES), exhibiting $-CH=CH_2$ polymerizable group [193], allows for the synthesis of class II polymer nanocomposites [114] (Figure 2.16). Shirai *et al*. [194] reported several radical graft polymerizations of *e.g.* PMMA and polystyrene on pre-coated TiO_2 modified with hydroxyl groups or trichloroacetyl groups. The grafting efficiency was higher using trichloroacetyl group. PMMA-functionalized TiO_2 nanoparticles show better stability in THF and depending on the hydrophobicity of the grafted polymer, the wettability to water can be tuned.

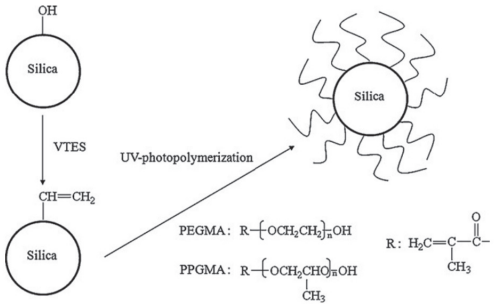

Figure 2.16. Process of UV-photopolymerization of SiO_2 nanoparticles functionalized with vinyltriethoxysilane. Reprinted from ref. [193], Copyright 2008, with permission from Elsevier.

Silane coupling agents

Silane coupling agents, of general formula R_ySiX_{4-y} (y = 1, 2, or 3) where X is a hydrolyzable group and R is an organofunctional group (*e.g.* an alkyl group), have been used for the surface functionalization of several types of materials such as metal oxides (*e.g.* SnO_2, TiO_2, Fe_xO_y), polymers, silica, and glass [188], but also as polysiloxane precursors [37, 195].

Chen *et al.* [196] investigated interactions of 3-aminopropyltrimethoxysilane (APTMS) and phenyltrimethoxysilane (PTMS) with commercially available TiO_2 nanoparticles (Degussa P-25). They concluded that the silane coupling agents bond onto the surface of TiO_2 nanoparticles via Ti−O−Si bonds. Milanesi *et al.* [197] especially focused on the structure of the grafted layer with X-ray photoelectron spectroscopy and solid state nuclear magnetic resonance, and proposed that cross-linking (via Si−O−Si bonds) and chemical bonding (via Ti−O−Si bonds) of silanes onto TiO_2 nanoparticles occurred. A contact angle of about 150° was measured for water on thin films prepared by drop-casting of suspension of the nanoparticles, demonstrating a hydrophobic behavior of the nanoparticles. Zhao *et al.* [198] detailed the cross-linking and chemical bonding reaction of APTMS and 3-isocyanatopropyltrimethoxysilane (IPTMS) on TiO_2 nanoparticles via hydrolysis and condensation mechanisms. The isoelectric point was shifted from about pH 6.4 to pH 9.4 and the photocatalytic properties of the nanoparticles were decreased as a function of the grafting efficiency. The functionalization mechanism of metal oxide with silane coupling agents is shown in Figure 2.17.

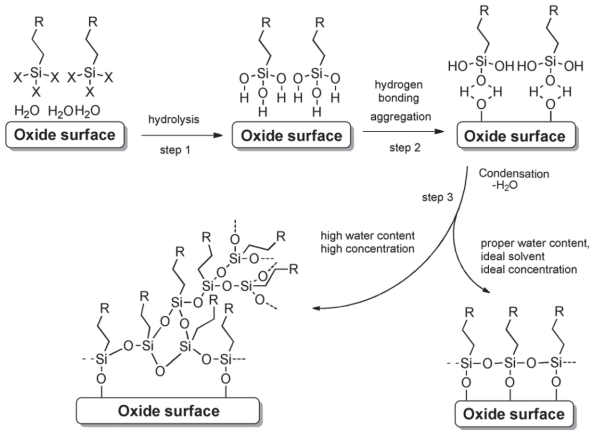

Figure 2.17. Chemical steps involved in the functionalization of metal oxide surfaces with silane coupling agents. Reproduced from ref. [188], Copyright 2014, with permission from Wiley-VCH.

Disordered or monolayer like organic layers can be obtained depending on the synthesis conditions (Figure 2.17). In the case of R being an alkyl group, Porter *et al*. [199] and later Fadeev and co-workers [200, 201] showed that by measuring the position of the CH_2 stretching modes in infrared spectroscopy, the ordering in the organic layer can be qualitatively obtained by comparison to crystalline materials (highly ordered) and liquid states (highly disordered) band positions. Liu *et al*. [202] studied the kinetics of APTES chemisorption on magnetic iron oxide nanoparticles (MNP) via direct mixing of the MNP with the aminosilane in selected solvents and temperatures. The kinetics of silanization was shown to depend mostly on the temperature (30-70 °C was used), but not on the solvent or the initial silane concentration. Longer reaction times (order of 10 h) were recommended by the authors to reach equilibrium and APTES formed a monolayer structure on the surface of the MNP, based on thermogravimetric analysis. Recently, Meroni *et al*. [203] investigated the geometrical configuration of APTES on the fully hydroxylated (101) anatase surface by a combined experimental and theoretical study, finding that single molecules or dimers could chemisorb with feasible geometries but high bond strain limited extensive cross-linking. Table 2.4 summarizes reports on post-functionalization of TiO_2 nanoparticles with silane coupling agents.

Table 2.4. Literature reports on post-surface functionalization of TiO_2 nanoparticles with different types of silane coupling agents.

Agent	Route (solvent)	Conditions	Ref.
APTMS[a] or PTMS[b]	Reflux (water or water/ethanol)	20 h, pH 9.8 (HCl)	[196]
APTMS or IPTMS[c]	Reflux (water)	2-16 h, 12.5-200 % silane	[198]
OTES[d] or OTMS[e]	Vigorous stirring (CH_2Cl_2) and rotoevaporation	0-33 wt.% silane, 90 min, 50 °C (30 min under vacuum)	[197]
DTMS[f] and APTMS	Vigorous stirring (CH_3OH)	16 h, 1.0-4.0 mmol per gram TiO_2	[204]
MPTMS[g]	Sonication (water)	pH 3-10 (NH_4OH and HCl), 0.10-0.35 mass fraction silane	[205]
APTES[h]	Sonication (water/acetone)	30 min, 10 wt.% silane	[206]
AHAPS[i]	Stirring (ethanol)	10 h, 0.05-9 mmol L^{-1} silane in 20 mL ethanol for 1 gram TiO_2	[207]
APTMS	Reflux under N_2 atmosphere (toluene)	5 h, 15-200 wt.% silane, 1.5 mL triethyl amine as catalyst	[208]
VTMS[j]	Reflux (ethanol)	pH 4 (acetic acid), 15 wt.% silane, 1 h at 60 °C	[209]

[a] 3-aminopropyltrimethoxysilane.
[b] Phenyltrimethoxysilane.
[c] 3-isocyanatopropyltrimethoxysilane.
[d] Octyltriethoxysilane.
[e] Octyltrimethoxysilane.
[f] Decyltrimethoxysilane.
[g] 3-(methacryloyloxy)propyltrimethoxysilane.
[h] 3-aminopropyltriethoxysilane.
[i] *n*-(6-aminohexyl)aminopropyltrimethoxysilane.
[j] Vinyltrimethoxysilane.

The biomedical field also benefit from using silano modified TiO_2 nanoparticles. Xie and co-workers synthesized functionalized TiO_2 with APTES from which the amino group was pre-functionalized with 2-(9H-fluoren-9-ylmethoxycarbonylamino) oxyacetic acid [105]. The functionalized nanoparticles showed good biocompatibility. Further functionalization with folic acid and N-hydroxysuccinimide maintained good dispersibility and gave photokilling properties to the nanoparticles, allowing potential use as photosensitizer for cancer targeting and photodynamic therapy [104]. Gold functionalized TiO_2 nanoparticles using APTES as coupling agent, and further modifications allowed to produced multi-functionalized nanomaterials increasing the electrochemical detection of specific proteins for cancer detection [107, 108].

In a few reports, *in situ* functionalization of TiO_2 nanoparticles with silane coupling agents is reported. Teleki *et al.* [210] developed a route for continuous production of surface-functionalized TiO_2 via flame spray pyrolysis in which the particles were directly functionalized after synthesis with OTES. Depending on the conditions, surface-functionalized TiO_2 nanoparticles with an average size of 40 nm and a maximum surface coverage of about 2.6 OTES nm^{-2} were obtained. However, to our knowledge, only one work has reported *in situ* functionalization of TiO_2 nanoparticles with silane coupling agents. Koziej *et al*. [211] used trimethoxy(7-octene-1-yl)silane (7-OTS) and MPTMS coupling agents during TiO_2 nanoparticle synthesis from TIP precursor in anhydrous benzyl alcohol via solvothermal synthesis. The particles where further successfully dispersed in PMMA-based materials

2.3.1.2. Dispersion in polymer matrices

Dispersion of nanoparticles in polymer matrices can be done mainly via two different routes, blending and *in situ* polymerization (Figure 2.14). In the case of blending routes, dispersion can be achieved via dispersion in a common solvent [162, 166, 206, 212, 213], or melt blending *i.e.* the polymer (thermoplastic) is heated above melting temperature and the dispersion is realized via *e.g.* extrusion [192, 214]. *In situ* polymerization routes mainly consist on mixing the nanoparticles in a monomer solution followed by the polymerization [163, 215, 216]. Polymerization can also be achieved through functional groups grafted onto the nanoparticles [193, 194] (Figure 2.16), or via ligand exchange [168, 170].

2.3.2. *In situ* synthesis of polymer nanocomposites

In situ synthesis methods consist of mixing precursors with a non-reactive solvent and the monomer, or with the polymer [14, 16, 32, 114, 183]. In the first case, chemical reaction of the precursors is initiated to synthesize the particles during the mixing and polymerization (or vice-versa). Then, the co-precipitation of the final nanocomposite is induced by solvent addition or solvent evaporation. In the second case, formation of the particles and polymerization are done in one step [217], and the nanoparticles are grown directly within

the polymeric matrix. One of the most common synthesis routes for *in situ* synthesis of nanocomposites is the sol-gel approach, where metal alkoxides and/or silane coupling agents are used [32, 218, 219]. Wei *et al*. [220] proposed a sol-gel synthesis of allyl methacrylate-*co*-methyl methacrylate-SiO_2 hybrid materials via hydrolysis and condensation reactions of tetraethoxysilane (TEOS) on the vinyl group of allyl methacrylate and methyl methacrylate copolymer.

Xiong *et al*. [221] prepared acrylic resin-TiO_2 hybrid materials via sol-gel synthesis of titanium(IV) butoxide and MPTMS-capped butyl acetate and methyl methacrylate copolymer precursors. The cross-linking of the organic and inorganic precursors was achieved via Ti−O−Si bonds. Small-angle X-ray scattering (SAXS) showed that an increasing amount theoretical TiO_2 from 5 wt.% to 20 wt.%, gave an increase in the radius of gyration from 4.0 to 9.2 nm, due to the formation of inorganic nanodomains. The hardness and the elastic modulus of hybrid films prepared from this material increased with increasing the amount of titanium precursor. Lowering the amount of water used during the synthesis decreased the phase separation and increased the elastic modulus (E) from 4.02 to 4.78 GPa.

Xiong *et al*. [222] also produced similar materials without the use of silane coupling agent, by both blending and *in situ* polymerization. E and the glass transition temperature (T_g) increased as a function of titanium incorporation due to higher cross-linking degree. The hybrid materials prepared by the blending route also had higher storage modulus (E') at 130 °C of 0.61, 0.79, and 1.65 MPa for blending, and 0.51, 0.78, and 1.14 MPa for *in situ* polymerization, for the same respective compositions.

Agag *et al*. [223] prepared polybenzoaxine-TiO_2 nanocomposites by co-reactions in tetrahydrofuran (THF). In this case, water was added to start the reaction of titanium(IV) isopropoxide (TIP) and films were prepared by casting on glass substrate and heating, to induce cross-linking of the monomer. The average size of the titania particles was less than 200 nm. The T_g, the thermal stability, and E' below T_g were increased with up to 7 wt.% incorporated TiO_2.

Müh *et al*. [224] used polyacrylate-based monomers exhibiting alkoxysilane groups after modification with 3-aminopropyltrimethoxysilane that were cross-linked with camphor quinone and ethyl 4-(dimethylamino)benzoate by a combination of sol-gel method and photopolymerization, in which steric hindrance favored the formation of nanoparticles, instead of a macroscopic network.

In several other studies, *in situ* polymerization of polymer and TIP using different type of polymers *e.g.* polymethyl methacrylate [225], polycaprolactone [226], modified polydimethylsiloxane diacrylate [227], and hydroxylated castor oil [228] was reported.

2.3.2.1. The case of PDMS–metal oxo nanocomposites

Contrary to class I hybrids, where weak interactions occur between the organic and the inorganic interfaces as in the case of dispersion of metal oxide nanoparticles in PDMS-based materials, PDMS-metal oxo (PDMS−O−M) types of materials, class II hybrids have chemical bonds between the siloxane backbone and the organometallic precursor [176]. Synthesis of polyorganometalosiloxanes was first introduced by Andrianov at the end of the 1950s [229], followed by several studies where Andrianov and co-workers described the synthesis of titanodimethylsiloxane oligomers precursors, $\mathrm{Ti}\left[\left(\mathrm{OSi}\left(\mathrm{CH_3}\right)_2\right)_n\mathrm{OH}\right]_4$ with n = 9, 18, 25, 34, 42, 52, 80, and 104 which were further polycondensed at 200 °C to form three-dimensional structures [230, 231]. The T_g of the oligomers was measured between −105 and −100 °C and the refractive indices (measured at 20 °C and 589.3 nm) was between 1.4049 and 1.4123, decreasing with higher number of repeating units (n). All oligomers and polymers have an amorphous structure at room temperature and only those with a value of $n \geq 42$ for oligomers, and $n \geq 36$ for polymers, crystallize upon cooling at −120 °C in a same crystalline structure as PDMS. Andrianov *et al.* [232] investigated the condensation reaction of titanium(IV) butoxide with hydroxy-terminated PDMS oligomers, $\mathrm{HO}\left[\mathrm{Si}\left(\mathrm{CH_3}\right)_2\mathrm{O}\right]_n\mathrm{H}$ with n = 2, 3, and 4. The precursors were mixed with in an equimolar ratio and reacted for several hours at 60 °C *in vacuo*. Infrared spectroscopy confirmed formation of Ti−O−Si bonds and formation of butan-1-ol. A secondary reaction was observed, in which butan-1-ol reacted with the terminal −OH groups of PDMS via esterification and production of water.

Silicon and metal alkoxides as precursors

More recently, synthesis of PDMS-based hybrid materials has been focused on the use of silicon and metal alkoxides, but because the different reactivity of high-valent metal alkoxides compared to their silicon counterparts (Table 2.1), the use of catalyst or inhibitor is often necessary [30, 36, 39]. Glaser and Wilkes [233] synthesized PDMS−O−Ti materials using TEOS, TIP, and poly(tetramethylene oxide) (PTMO) oligomer precursors via sol-gel synthesis in a mixture of isopropanol and THF. The synthesis time required one week, but gelation was observed after typically 24 h. With addition of 0 to 30 wt.% of TIP, the elongation at break of the materials were reduced from 104 % to 61 %, the Young's modulus was increased from 7 MPa to 71 MPa and the apparent T_g was decreased. SAXS analysis revealed no major structural change (similar correlation lengths of about 9 nm), but the scattering intensities were higher with higher amount of incorporated titanium.

Diré *et al*. [234] described the reaction of dimethyldiethoxysilane (DMDES) with TIP. DMDES was first dissolved in a mixture of absolute ethanol and water (1:1:1 molar ratio), and TIP was subsequently added in order to obtain Ti/Si molar ratio varying from 10:90 to 50:50. The solutions were stored in open containers for a few days until transparent bulk samples were obtained. ^{29}Si-NMR investigations showed the formation of Ti−O−Si containing intermediate species, but further structural rearrangement showed phase separation of the PDMS polymeric chains and TiO_2 based nanodomains, as schematically represented in Figure 2.18.

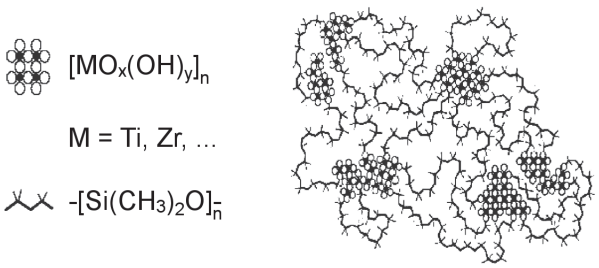

Figure 2.18. Schematic representation of PDMS−O−M materials with oxo-hydroxo nanodomains cross-linked with PDMS segments. Adapted from ref. [218] with permission of The Royal Society of Chemistry.

Guermeur *et al*. [235] synthesized PDMS−O−Zr materials using DMDES and zirconium(IV) isopropoxide as precursors. The synthesis was performed in a mixture of ethanol and acidic water (0.1 mol L^{-1} HCl), and the films were obtained after three weeks of slow drying at room temperature, similar to the method described by Diré *et al*. [234]. FTIR spectra showed that PDMS−O−Zr materials were obtained via Si−O−Si and Si−O−Zr bonding. Relative intensity of the Si−O−Zr band showed a good correlation with the zirconium precursor content. The effect of environment change after incorporation of Zr was observed on the chemical shift of Si in ^{29}Si-NMR. ^{17}O-NMR showed that the interface between inorganic and PDMS domains were mainly $(CH_3)_2$Si−O−Zr. SAXS showed that the nanocomposites where inhomogeneous, with zirconium oxo domains having a size of 1-2 nm, and a mean distance (correlation length) from 6 to 2 nm, when the Zr/Si ratio was increased. The structure of the materials was similar to schematic representation in Figure 2.18. The T_g was measured at around −117 °C. Depending on the samples heat treatment, an increase on the E' was observed (from 10 MPa to 60-70 MPa for Zr/Si = 0.17).

Julián *et al*. [236] synthesized PDMS−O−M (M = Al, Ge, Sn, Ti, Zr, Nb, and Ta), also by the method first described by Diré *et al*. [234] and later by Guermeur *et al*. [235], using DMDES and metal alkoxides as precursors, with a Si/M molar ratio of 80:20. Cross-linking was observed by FTIR where Si−O−Si and Si−O−M (M = Ge, Ta, Nb, and Zr) absorption bands were detected, but the Si−O−M band was not observed for samples with M = Sn, Al, and Ti. It was deduced that this was probably due to phase separation. Additionally, ^{29}Si-NMR showed broadening of the chemical shift assigned to Si in PDMS-type chains for all PDMS−O−M samples, demonstrating more constrained siloxane units, due to Si−O−M bonding. Increasing the coordination number of the metal cation resulted in higher T_g, due to more effective cross-linking of PDMS polymeric chains.

Alonso *et al*. [237] produced PDMS−O−V materials using DMDES and tri-*tert*-amyloxy vanadate or tris(trimethylsiloxy) vanadate as precursors. The structure of the products was analyzed via Raman and FTIR spectroscopy, thermogravimetry, DSC, ^{17}O-,^{29}Si-, and ^{51}V-NMR from which it was concluded the vanadate units were monomeric and linked with three segments of five to six repeating units. Similar structures were obtained by Matkovskii *et al*. [238] using methyltrietoxysilane with titanium(IV) chloride ($TiCl_4$) and zirconyl chloride ($ZrOCl_2$). However, using chloride precursors has the disadvantage of producing chloride ions.

Hydroxy-terminated PDMS and metal alkoxides as precursors

The synthesis of PDMS-based hybrid materials can also be done directly using PDMS precursors such as OH-terminated PDMS (PDMS-OH) [232]. In this case, the main advantage is that there is no need for silicon alkoxide precursors, and the main focus is thus the reaction of the metal precursors with PDMS materials. Using PDMS-OH as precursors allows for better control of the PDMS chains length and the final structure. For example, Foussaier *et al*. [239] showed that, in the case of cross-linking with TEOS, the structure and the opacity of the final materials is highly dependent on the average molecular weight of the PDMS-OH precursor and the amount of TEOS (Figure 2.19). Lower molecular weight PDMS-OH precursors lead to lower degree of phase separation.

Yamada *et al*. [240, 241] synthesized PDMS−O−M (M = Al, Ti, and Ta) hybrids films and studied the effect of the molecular mass and heat treatment on the structure and mechanical properties (Figure 2.20a). Ethyl acetoacetate (EAcAc) was used as hydrolysis inhibitor of the metal alkoxides. The films were transparent with yellow or brown colorization before heat treatment while heat-treated films at 150 °C were transparent with

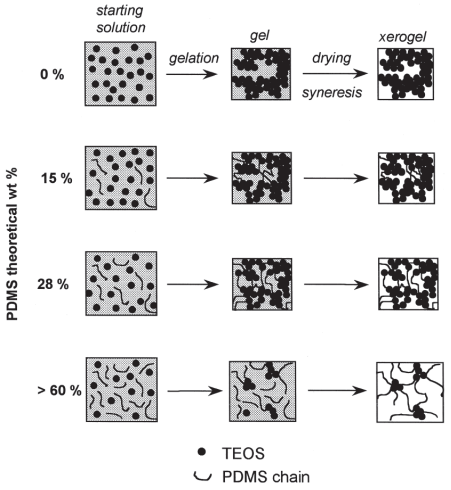

Figure 2.19. Schematic representation of PDMS−O−Si material structures as a function of the initial weight fraction of TEOS and PDMS (M_w = 550). Reprinted from ref. [239], Copyright 2000, with permission from Elsevier.

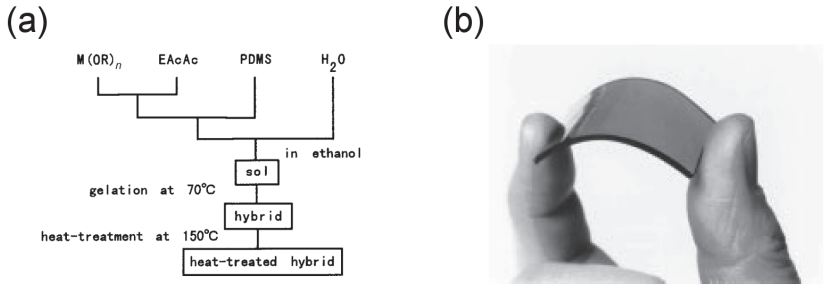

Figure 2.20. (a) Procedure of synthesis of PDMS−O−M hybrid films and (b) photograph of PDMS−O−Ti hybrid film. (a-b) Reproduced from ref. [240] with permission of The Royal Society of Chemistry.

brown or dark brown colorization (Figure 2.20b). M−O−Si absorption band in FTIR spectra was only observed after heat treatment, indicating further reaction at 150 °C. Lower M_w PDMS and/or heat-treated samples showed higher storage modulus (E') and the glass transition temperature (T_g) was calculated to be similar to the one for infinite M_w (−123 °C) (Figure 2.11), due to bonding with metal alkoxides, forming a cross-linked network and reducing the motion of the polymeric chains. E' increased and peak height of the loss factor (tan δ) decreased with the increase of the valence of the metal cation (Al^{3+}, Ti^{4+}, Ta^{5+}). Other work by Yamada and co-workers include the study of mechanical and surface properties of PDMS−O−M, and hybrid materials with phenyltriethoxysilane [242-246].

More recently, Almeida *et al.* [247] modified the synthesis developed by Yamada *et al*. [248] in which no ethyl acetoacetate was used. However, the pH was increased up to 13 (with ammonia), TEOS was also used, and a total reaction time of two weeks was necessary. The synthesis led to less colorized films. The effects of the addition of TEOS, increased pH, and increased water ratio were also studied [249, 250]. SiO_2 nanodomains were formed due to incorporation of TEOS and titanium oxo domains formed at the surface of the SiO_2 nanodomains, adopting a core-shell structure, which then prevented further growth. By using a combination of hybrid electrospinning and sol-gel methods, Kim *et al.* [251] fabricated hybrid PDMS-TiO_2 fibers, using TIP, PDMS (M_n = 46 000), and silicon ethoxide, ranging from pure TiO_2 to pure PDMS compositions range, for use as photocatalyst.

2.3.3. Polymer nanocomposites with high refractive index

2.3.3.1. Optical properties of polymer nanocomposites

Definitions of some optical constants

The refractive index (n) of a medium is defined as the ratio between the speed of light in vacuum ($c = 3\times10^8$ m s^{-1}) and the speed of light in the considered medium (v):

$$n = \frac{c}{v} \tag{2.29}$$

and is function of the temperature of the medium and the wavelength (λ) [252]. The refractive index of a medium is directly related to its dielectric properties with:

$$\varepsilon_r^{'} = n^2 - k^2 \tag{2.30}$$

and

$$\varepsilon_r^{''} = 2nk \tag{2.31}$$

where $\varepsilon_r^{'}$ and $\varepsilon_r^{''}$ are the real and the imaginary part of the dielectric constant, respectively, and k is the extinction coefficient [253].

Generally, the dielectric constant of a material can be estimated using the Clausius-Mossotti relation:

$$\frac{\varepsilon_r - 1}{\varepsilon_r + 2} = \frac{4\pi}{3} N\alpha \tag{2.32}$$

where α is the polarizability and N the number of molecules per unit volume [254]. The refractive index can be estimated from the Lorentz-Lorenz relation:

$$\left(\frac{n^2 - 1}{n^2 + 2}\right) V_{\mathrm{m}} = \frac{4\pi}{3} N_{\mathrm{A}}\alpha = \sum_i \left(R_{\mathrm{LL}}\right)_i \tag{2.33}$$

where V_m is the molar volume, N_A is the Avogadro's constant, and R_{LL} is the Lorentz-Lorenz molar refraction of the i functional group(s) in the case if the considered material is a polymer [255].

At an interface between two media of refractive indices n_1 and n_2, an incident ray of light forming an angle θ_1 with the normal to the interface is refracted with a direction forming an angle θ_2 with the normal to the interface, according to the Snell-Descartes law:

$$n_1 \sin\theta_1 = n_2 \sin\theta_2 \tag{2.34}$$

Snell-Descartes law is one the fundamental relations of geometrical optics with reflection, stating that a reflected light ray will form the same angle with the normal of the interface than the incident light ray with the normal.

For a plano-convex lens (Figure 2.21) and in the case of the thin lens approximation (the thickness of the lens is negligible compared to the distances associated with its optical properties), the optical power (P) can be defined as:

$$P = \frac{1}{f} = (n-1)\left(\frac{1}{R}\right) \tag{2.35}$$

where f is the focal length and R is the radius of curvature [252]. According to Equation (2.35), the optical power of a plano-convex lens can be increased by increasing the refractive index of the lens.

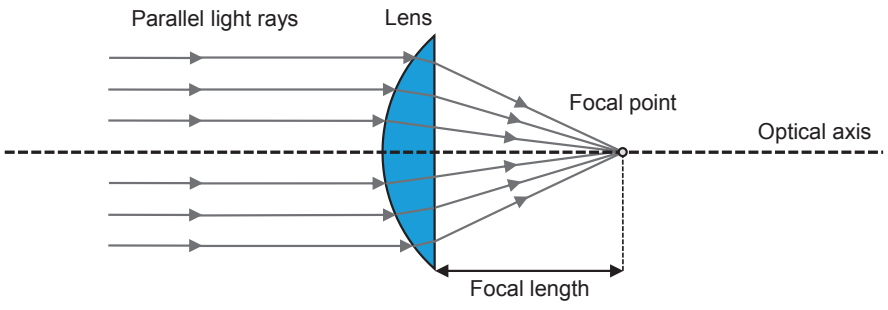

Figure 2.21. Simplified scheme of a plano-convex lens.

The refractive index of a medium varies with the wavelength. This phenomenon is called dispersion and, in the case of transparent materials, it can be described by Cauchy's law:

$$n = A + \frac{B}{\lambda^2} + \frac{C}{\lambda^4} \tag{2.36}$$

where A, B, and C are constants given for the considered medium [252]. The Abbe number (V_D) is commonly used to describe the dispersion of a material in the visible spectrum (400-800 nm), and is defined by:

$$V_D = \frac{n_D - 1}{n_F - n_C} \tag{2.37}$$

where n_D, n_F, and n_C, are the refractive indices at 589.3 nm, 486.1 nm, and 656.3 nm, respectively. A high value of the Abbe number corresponds to low dispersion properties.

In a case of a lens, highly dispersive materials lead to chromatic aberration *i.e.* the focal length (Figure 2.21) is highly dependent of the wavelength of the incident light and the focus of polychromatic light becomes impossible.

Refractive index of polymer nanocomposites

The development of high refractive index polymers (n > 1.50) has become an important part of research for electronic devices for optical applications where lightweight materials are required [15]. However, the value of the refractive index is a combined effect of molar volume, density, and molar refraction as described in Equation (2.33). Polymeric materials are then limited by their density and chemical composition and their refractive indices rarely exceed 1.70. A strategy to overcome this physical limit is to incorporate inorganic nanoparticles in the system [14, 113, 114, 183, 217, 256]. Commonly used nanoparticles are metals, metal oxides and metal sulfides [183], as the refractive indices of inorganic materials are generally higher than those of organic materials (Table 2.5) [257]. Zimmermann *et al.* [258] have shown that the refractive index of a nanocomposite can be estimated by:

$$n_{comp} = \phi_p n_p + \phi_m n_m \tag{2.38}$$

Table 2.5. Refractive indices (at 589 nm) and densities of inorganic materials commonly used as nanofillers for optical nanocomposites. Refractive index values are given for the three coordinate axes in the order of least, intermediate, and greatest index. Adapted with values from ref. [257].

Material	Density ($g\ cm^{-3}$)	Refractive index		
		n_α	n_β	n_γ
Al_2O_3 (corundum)	3.97	1.761	1.769	
SiO_2 (cristobalite)	2.33	1.484	1.487	
SiO_2 (quartz)	2.65	1.544	1.553	
TiO_2 (anatase)	3.89	2.488	2.561	
TiO_2 (brookite)	4.12	2.583	2.584	2.700
TiO_2 (rutile)	4.26	2.609	2.900	
ZnO (zincite)	5.6	2.013	2.029	
ZrO_2 (baddeleyite)	5.7	2.13	2.19	2.20
CdS (greenockite)	4.8	2.506	2.529	
PbS (galena)	7.60	3.91		
ZnS (sphalerite)	4.0	2.369		
ZnS (wurtzite)	4.09	2.356	2.378	

where n_{comp}, n_p, n_m are the refractive indices of the composite material, the particles, and the matrix, respectively, and ϕ_p, ϕ_m are the volume fractions of the particles and the matrix, respectively. Starting with a polymer having a low refractive index, the potential of the relative increase the refractive index with one type of inorganic material is then higher than with a polymer matrix having a higher refractive index.

Assuming a polymer refractive index of $n_m = 1.53$ and based on Equation (2.38), the refractive index of a hypothetical nanocomposites based on the refractive indices of the selected filler presented in Table 2.5 has been modeled in Figure 2.22.

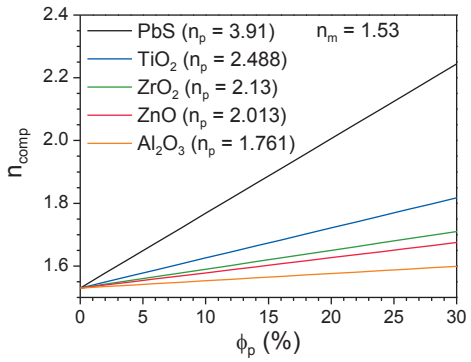

Figure 2.22. Modeling of the refractive index (at 589 nm) of the hypothetical nanocomposites based on a polymer with $n_m = 1.53$ and different type of nanoparticles, using Equation (2.38) and refractive indices from Table 2.5.

From Figure 2.22, lead sulfide stands out from the metal oxides, increasing the refractive index up to 2 for 20 vol.% of particles. However, with respect to environmental concerns, incorporating lead-based filler materials in the polymer would not be desirable. A reasonable choice would thus be titanium dioxide based fillers, here represented by anatase, being the expected polymorph of TiO_2 at nanoscale (see Chapter 2.1.3).

Transparency of polymer nanocomposites

Incorporation of nanoparticles into a polymer matrix affects the transparency of the resulting nanocomposite by inducing scattering, depending on the size of the particles and their distribution. When the size of the particles decreases well below the wavelength of the incident light (one tenth of the visible light wavelength and ideally below 10 nm), scattering induced by the particle is reduced [14] (Figure 2.23). If the particles are agglomerated, the nanocomposite appears opaque, unless the refractive indices of polymer and particles are equal. The intensity loss of a nanocomposite which does not absorb at the wavelength λ, with randomly dispersed spherical particles can be estimated by the Rayleigh scattering formula:

$$\frac{I}{I_0} = \exp\left(-\frac{32\phi_p x\pi^4 r^3 n_m^4}{\lambda^4} \left[\frac{\left(n_p / n_m\right)^2 - 1}{\left(n_p / n_m\right)^2 + 2} \right]^2 \right) \tag{2.39}$$

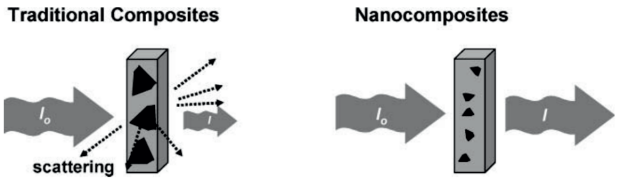

Figure 2.23. Using nanoparticles as filler reduces the scattering induced by the inorganic materials, resulting in higher transparent nanocomposites compared to traditional composites. Reproduced from ref. [217] with permission of The Royal Society of Chemistry.

where I is the intensity of transmitted light, I_0 the intensity of the incident light, x the thickness of the nanocomposite, and r the particle radius [256].

For a polymer with $n_m = 1.53$ and a thickness $x = 300$ µm with dispersed anatase nanoparticles (d is the particle diameter) the transmittance (I/I_0) as a function of the volume fraction and the refractive index of the nanoparticles was modeled using Equation (2.39) and is represented in Figure 2.24. At constant volume fraction of nanoparticles, the effect of the particle size on the nanocomposite transmittance is more important (Figure 2.24b) than the effect of the volume fraction at a given particle size (Figure 2.24a).

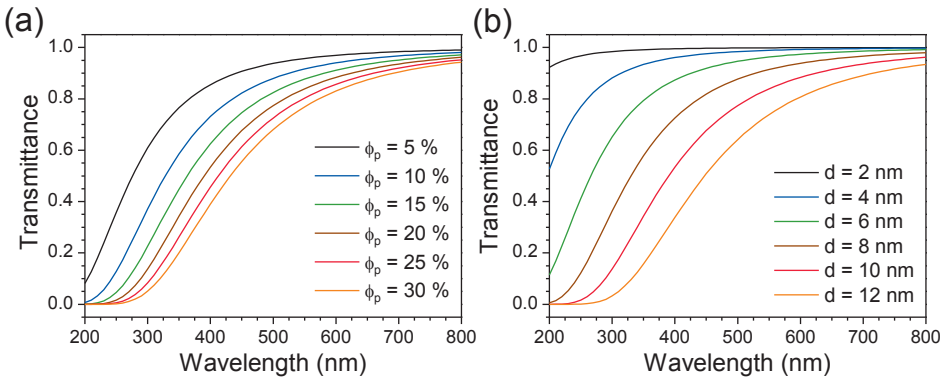

Figure 2.24. Modeling of the transmittance of a polymer nanocomposite based on anatase TiO_2 ($n_m = 1.53$, $n_p = 2.488$, $x = 300$ µm) versus the wavelength as a function of (a) the particle volume fraction ($d = 10$ nm) and (b) the particle diameter ($\phi_p = 20$ %), using Equation (2.39).

However, an experimental study showed that the transmittance reaches a plateau above 8 vol.% of nanoparticle incorporation [216]. A hypothesis which could explain this phenomenon is the contribution of the interparticle distance to the scattering effect. The average distance between two particles can be calculated from:

$$<D>=0.55396N^{-1/3} \tag{2.40}$$

where $<D>$ is the average distance between two particles and N the number of particles per unit volume [259]. In the case of monodispersed and uniform spherical particles, Equation (2.40) becomes [260]:

$$<D>=0.55396\left(\frac{4\pi}{3\phi_p}\right)^{1/3} r \tag{2.41}$$

Keeping the average distance between the particles as small as possible might be as relevant as the particle size to maintain the polymer transparent after incorporation of nanoparticles. Figure 2.25 represents modeling of the average distance between two particles for different particles volume fractions and particle diameter, using Equation (2.41).

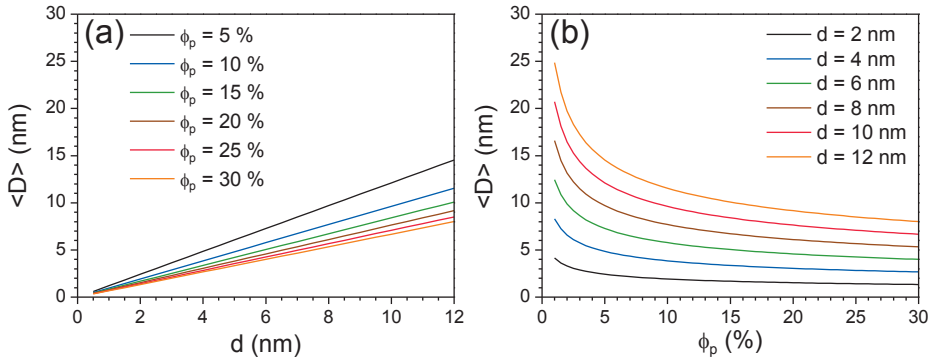

Figure 2.25. Modeling of the average distance between two particles in a homogeneously dispersed nanocomposite, considering monosized and spherical particles, as a function of (a) the particle diameter at different volume fractions and (b) the particle volume fraction with different particle diameters, using Equation (2.41).

2.3.3.2. *Ex situ* prepared polymer-TiO_2 nanocomposites

Several studies have reported successful incorporation of metal oxide nanoparticles in various polymer matrices. Table 2.6 summarizes recently reported studies of incorporation of TiO_2 nanoparticles in polymers for high refractive index applications.

The refractive indices of the nanocomposites increased linearly with the volume fraction of TiO_2 (Figure 2.26a) and extrapolations of the refractive indices to 100 vol.% TiO_2 were comprised between 2.33 and 2.68, similar to that of TiO_2 (Table 2.5). The results are consistent with predictions from Equation (2.38). It is challenging to quantitatively compare all these works since different polymer matrices were used and the refractive indices were often measured at different wavelength. Figure 2.26b shows the linear increase of the relative refractive index (%) as a function of the volume fraction of TiO_2 using polymer matrices with similar refractive index n_m.

Table 2.6. Characteristics *ex situ* prepared TiO_2 based nanocomposites for high refractive index application.

Polymer matrix[a]	Functionalized TiO_2	Dispersion route[b]	Max. TiO_2 incorporation	Refractive index (wavelength)	$\Delta n/n_m$[c] (%)	Ref.
PVA	No	Blending	10.5 vol.%	1.61 (589 nm)	5.9	[161]
PHE	Yes	Blending	80 wt.%	1.81 (589 nm)	14.6	[162]
Polysiloxane-based	No	ISP	55 wt.%	1.66 (633 nm)	10.7	[261]
Epoxy-based	Yes	ISP	70 wt.%	1.80 (n/a)	10.4	[262]
PC-based	Yes	Blending	30 vol.%	1.82 (633 nm)	15.6	[167]
PC-based	Yes	Blending	42 wt.%	1.72 (589 nm)	8.5	[166]
PGMA-based	Yes	ISP	30 vol.%	1.79 (500 nm)	17.8	[168]
PMMA	Yes	Blending	30 wt.%	1.58 (633 nm)	6.0	[169]
Polyacrylate-based	Yes	ISP	18 wt.%	1.70 (633 nm)	9.7	[171]
PVBA	Yes	ISP	19 wt.%	1.77 (633 nm)	9.9	[171]
PMMA	Yes	ISP	6.3 vol.%	1.57 (633 nm)	5.0	[172]

[a] PVA: polyvinyl alcohol, PHE: poly(bisphenol-A and epichlorohydrin), PC: polycarbonate, PEGMA: poly(glycidyl methacrylate), PMMA: poly(methyl methacrylate), PVBA: poly(vinyl benzyl alcohol).
[b] ISP: *in situ* polymerization.
[c] $\Delta n/n_m$ represents the relative increase of the refractive index from the initial polymer.

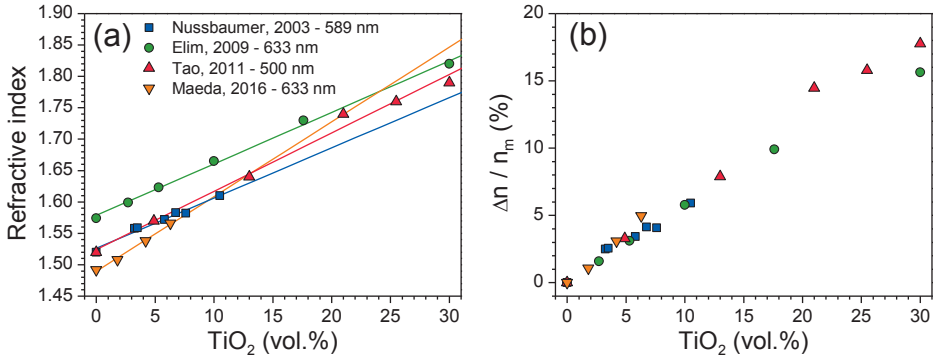

Figure 2.26. Linear increase of the (a) refractive index and (b) relative refractive index of *ex situ* synthesized nanocomposites as a function of TiO_2 vol.% described in previous works. The wavelengths used for the measurements are labelled in the legend. Replotted with data from ref. [161, 167, 168, 172].

Incorporation of TiO_2 nanoparticles can bring additional properties to the polymer matrix such as increased resistance towards long-term UV exposition [208, 209, 263]. Sullalti *et al*. [263] prepared TiO_2 based polyester microcomposites by mixing the particles in the molten polymer. It was demonstrated that the photooxidation of the polymer matrices was reduced when increasing the vol.% of incorporated nanoparticles, and that anatase was more efficient than rutile.

2.3.3.3. *In situ* prepared polymer-titanium based hybrid materials

In the recent years, the optical properties of polymer-titanium type of hybrid materials have been investigated. Yamada *et al*. [248], used the method described in Figure 2.20 in order to produce PDMS−O−M (M = Al, Ti, Zr, Nb, and Ta) materials with metal alkoxides and PDMS-OH (M = 3000) as starting materials. The precursors were mixed using metal alkoxides/PDMS-OH/ethyl acetoacetate/H_2O/ethanol molar ratio of 1:x:2:2:4 (with x = 0.1-1.0). The solution was heated at 70 °C for 2 days until gelation and subsequently heat-treated at 150 °C to obtain the hybrid film. The refractive index (at 589 nm) of the obtained films synthesized using titanium(IV) ethoxide showed an increase from 1.416 to 1.467 (3.6 % relative increase).

Chang and Chen [264] developed a synthesis route to aminoalkoxysilane-capped pyromellitic dianhydride-titania hybrid materials with high refractive index. Pyromellitic dianhydride (PMDA) monomers were firstly functionalized with 3-aminopropyltrimethoxysilane (APTMS), and after addition of TIP, the solutions (PMDA/APTMS/TIP/H_2O with 2:4:*x*:2 molar ratios, where *x* is varying between 0 and 8) were spin-coated on silicon wafers and cured resulting in cross-linked structures. The maximum incorporation of inorganic material was calculated to be 59.1 wt.% (SiO_2 and TiO_2). The refractive index (at 633 nm) of the hybrid films was increased from 1.567 to 1.780 (13.6 %) going from $x = 0$ to 8. They also described a similar route to polyimide-based-SiO_2 nanocomposites in which the refractive index decreased linearly as a function of SiO_2 vol.% due to its lower refractive index [265].

Xiong *et al*. [221] prepared acrylic resin-TiO_2 hybrid materials via sol-gel synthesis using titanium(IV) butoxide and MPTMS-capped butyl acetate and methyl methacrylate copolymer precursors. The refractive index (at 633 nm) increased from 1.525 to 1.761 (15.5 %) at theoretically 50 wt.% TiO_2.

In these cases, extrapolation to 100 vol.% TiO_2 gives a value of *n* of about 2.0, substantially lower than the expected value (about 2.5) and the reported values for *ex situ* synthesis (Figure 2.26). However, *in situ* methods allow for greater volume of incorporation of nanosized TiO_2, which could be a consequence of obtaining smaller TiO_2 domains (even at the molecular level). Smaller domains would thus reduce the opacity of the materials and allow higher volume fraction of inorganic materials, as described by Equation (2.39).

Su *et al*. [165] developed a synthesis route to polyimide-TiO_2 hybrid materials from 0 to 100 wt.% (pure titania). The films were cured up to 350 °C which induced crystallization of anatase nanodomains, observed via XRD and TEM analysis. Interestingly, the refractive index of pure titania was measured to be 1.993 at 633 nm, much lower than the theoretical value (Table 2.5).

More recently, Lu and Mullins [266] synthesized PDMS−O−Ti materials, using PDMS (M_n = 3500) and TIP as precursors and isopropanol as solvent. An increase of the refractive index (at 600 nm) was observed from 1.45 to 1.67 (15.2 %), using TIP/PDMS molar ratios from 5:1 to 20:1. The sample with the highest amount of incorporated titanium (30 mol.%) has a refractive index which decreased from around 1.75 at 500 nm to 1.52 at 1000 nm, while the refractive indices of the other samples did not show significant variation with the

wavelength. The refractive indices of the films reported by Lu and Mullins are higher than those of Yamada *et al*., probably because they only used isopropanol as solvent, which lead to films that are purer than those obtained by Yamada *et al*. In the latter case, the films might still contain ethyl acetoacetate. The highest curing temperature used was 150 °C while ethyl acetoacetate has a boiling temperature of 180 °C. The method by Lu and Mullins has several advantages. It is a single-step method, and no chemical stabilizer, catalyzer, nor water were used.

Zhan *et al*. [173] developed a two-step process in which titanium-doped oligosiloxanes were first prepared with vinyltrimethoxysilane (VTMS), dephenylsilanediol (DSPD), and TIP and the obtained oligomers were subsequently cross-linked with a cross-linking agent and a platinum catalyst. As the content of TIP was increased (0, 10, 20, and 30 mol.%), the amount of VTMS was decreased to keep a constant amount of DSPD. The refractive index (at 589 nm) was increased from 1.578 to 1.622 (2.8 %). The synthesis route by Zhan *et al*. gives higher refractive index at lower TIP amount, probably due to the phenyl groups of the cross-linker (DSPD).

Park *et al*. [267] proposed a synthesis route to triethylene glycol-titanium oxide via sol-gel reaction. The refractive index was shown to be dependent on the titanium amount, but also on the curing temperature where anatase was detected via XRD (for curing at 400 °C). The roughness of the samples was however increased and the authors did not comment on the final state of the polymer after curing at elevated temperature. It is however difficult to quantitatively compare these different synthesis methods, as the volume ratio of TiO_2 is in most cases not reported.

3. Experimental details

3.1. List of chemicals

The chemicals listed in Table 3.1 were used without further treatment and the chemical structures of the silane coupling agents used are given Figure 3.1.

Table 3.1. List of chemicals used in this work.

Name	Abbreviation	Provider	Grade
Titanium(IV) isopropoxide	TIP	Sigma-Aldrich	≥ 97 %
3-aminopropyltriethoxysilane	APTES	Sigma-Aldrich	99 %
3-(2-aminoethylamino)propyldimethoxymethylsilane	AEAPS	Fluka	≥ 95 %
n-decyltriethoxysilane	DTES	ABCR	97 %
Ammonium hydroxide solution	NH_4OH	Sigma-Aldrich	30-33 %
Nitric acid in water	HNO_3	Sigma-Aldrich	65 %
Hydroxy-terminated polydimethylsiloxane (25, 65, and 750 cSt)	PDMS-OH	Sigma-Aldrich	n/a
Anhydrous propan-2-ol	AIP	Sigma-Aldrich	99.5 %

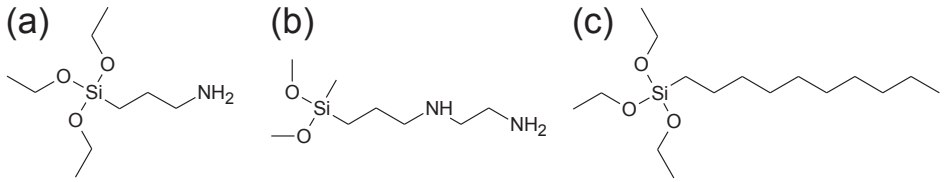

Figure 3.1. Chemical representations of (a) APTES, (b) AEAPS, and (c) DTES silane coupling agents.

3.2. Hydrothermal synthesis

The synthesis of pure TiO_2 nanoparticles was based on the work by Hayashi and Torii [46]. TIP (27.9 mmol or 8 mL) was mixed with 79.5 mL of distilled water in a beaker, which directly formed a white precipitate. The solution was stirred for 10 min prior to transfer into a 125 mL PFTE-lined autoclave (Parr). The filling factor in the autoclave was 70 %. The autoclave was then sealed and heated for 2 h at 200 °C. After cooling to room temperature, the product was centrifuged (10000 rpm, 10 min) and washed with distilled water. This process was repeated three times. The obtained slurries were dried for about 12 h at 100 °C for further analysis.

For the syntheses performed with silane coupling agents, the volume of water was substituted with the volume of silane, to keep the volume of TIP and the total volume constant. The silane were first mixed with water and TIP was then added. The solution was thereafter stirred for 10 min prior to transfer into a 125 mL PTFE-lined autoclave. The synthesis steps were then identical to those of pure TiO_2 described above. For the synthesis with silane coupling agent at titanium to silane molar ratio equal to 10, the samples are labelled Ti-APTES, Ti-AEAPS, and Ti-DTES when the synthesis was performed with APTES, AEAPS, and DTES, respectively (Chapter 4.1). The same samples heat-treated after thermogravimetric analysis (see Chapter 3.6.7) are labelled adding the suffix "-HT" to the original sample name *i.e.* TiO_2-HT, Ti-APTES-HT, Ti-AEAPS-HT, and Ti-DTES-HT (Chapter 4.2).

For the APTES functionalized samples, the time of the synthesis, precursor ratio, and pH were studied, and as reference, effect of the pH on pure TiO_2 was also investigated (Chapters 4.3 and 4.4). Ammonium hydroxide and nitric acid were used to change the pH to about 10 and 2, respectively, for the 120 min synthesis time. Some syntheses were also investigated via *in situ* synchrotron diffraction, their preparation is described in Chapter 3.3. Table 3.2 summarizes the synthesis parameters of the different samples.

Table 3.2. Sample names and synthesis parameters during the hydrothermal synthesis of TiO_2 and APTES *in situ* functionalized TiO_2 nanoparticles (Chapters 4.3 and 4.4).

Sample name	TIP/APTES (mol. ratio)	Duration of reaction (min)	pH	*In situ* XRD
TiO_2 (ref.)	n/a	120	4.5	Yes[c]
TiO_2-A			2.7	No
TiO_2-B			9.3	No
10:1-120[a,b]	10:1	120	6.3	Yes[c]
10:1-60		60		
10:1-30		30		
10:1-15		15		
10:1-1		1		
15:1-120[b]	15:1	120	6.3	No
15:1-60		60		
15:1-30		30		
15:1-15		15		
15:1-1		1		
10:1-A	10:1	120	2.2	No
10:1-B			10.1	Yes[d]
15:1-A	15:1		2.2	No
15:1-B			9.7	No

[a] Reproduction of Ti-APTES.
[b] The suffix "-120" is omitted in Chapter 4.3.
[c] pH was not measured and not modified.
[d] pH was increased to about 10 with ammonium hydroxide.

3.3. Samples for *in situ* synchrotron X-ray diffraction

The slurries used for *in situ* X-ray diffraction (XRD) measurements were prepared three times more concentrated than the synthesis in autoclave in order to obtain high signal during the acquisition. Typically, 9.55 mmol of TIP (2.74 mL) was added to distilled water to get a total volume of 10 mL. When the synthesis was performed in order to *in situ* functionalize TiO_2 with APTES, the necessary volume of water was substituted with APTES. The slurries were gently grinded in a mortar to facilitate injection in the sapphire capillary with a plastic syringe (see Chapter 3.6.2).

3.4. Non-aqueous sol-gel synthesis

The synthesis of the titanium-PDMS (Ti-PDMS) based hybrid films was based on the work by Lu and Mullins [266]. The polymeric precursors were OH-terminated PDMS (PDMS-OH) with viscosities (η) of 25 cSt, 65 cSt, and 750 cSt. The average molecular mass of the precursors was calculated using Equation (2.26), and assuming monodisperse polymers, the number of repeating units (n) and the concentration (C_{PDMS}) of each precursors were calculated (Table 3.3). For each PDMS-OH precursors, hybrid materials were prepared with titanium(IV) isopropoxide (TIP) using TIP/PDMS-OH molar ratio of 2:1, 5:1, 10:1, 15:1, and 20:1.

The synthesis route was optimized for all the synthesis as follow. In a first step, PDMS-OH (3 mL) were mixed with 8 mL anhydrous propan-2-ol (AIP, 8 mL) in a closed glass container. The solution was sonicated for 5 min at room temperature and subsequently stirred and heated at 70 °C during the preparation of the titanium precursors. In another closed glass container, the necessary volume of TIP was added to AIP (4 mL) and sonicated for 5 min at room temperature. The titanium precursors were then mixed with the PDMS-OH precursors and the obtained sols were vigorously stirred for 30 min at 70 °C while keeping the containers closed in order to avoid solvent evaporation. In the case of the 25 cSt series of samples, 15:1 and 20:1 samples, all the volumes were divided by two, to keep the same concentrations. In the case of the 750 cSt series, as the volume of TIP was small (*e.g.* 86 µL for 2:1 sample), the titanium precursor was prepared as a common solution for all samples and a micro-pipette was used to prepare each sample.

Table 3.3. Viscosity, density and calculated average molecular weight and number of repeating units of the PDMS-OH precursors.

η (cSt)	ρ (g cm^{-3})	η (Pa s)	M_n	n	C_{PDMS} (mol L^{-1})
25	0.95	2.425	2118	28	0.449
65	0.97	6.305	3948	53	0.246
750	0.97	72.75	19433	262	0.050

For the preparation of *thin* films, the sols were spin-coated on single crystal Si wafers (1×1 cm), for 1 min at 3000 rpm, including 15 s of acceleration and 15 s of deceleration. For the preparation of the thick films, the sols were mold-casted in PTFE molds. The films were dried at 50 °C for 24 h and cured at 100 °C for 24 h on a hot plate. For the 25 cSt series, bubbles and cracks formed during these steps and they were thus dried at room temperature and cured at 50 °C. The samples are labelled Ti-PDMS-X-Y:1, where X is the viscosity of the PDMS-OH precursor (in cSt) and Y is the molar ratio of TIP/PDMS-OH (Chapter 5).

3.5. Density functional theory calculations

3.5.1. Computational details

Density functional theory (DFT) calculations were performed using the Vienna *ab initio* Simulation Package (VASP) with the projector augmented wave (PAW) pseudopotentials Ti_sv ($3p^6 4s^2 3d^2$), O ($2s^2 2p^4$), Si ($3s^2 3p^2$), N ($2s^2 2p^3$), C ($2s^2 2p^2$) and H ($1s^1$) [268-271]. The exchange-correlation functional PBEsol [272] was used as it provided close to experimental values for the lattice parameters, based on full geometry optimization of the anatase unit cell (a = 3.776 Å, c = 9.584 Å). The residual forces for initial testing of the bulk and slab structures were less than 0.01 eV $Å^{-1}$. Energy convergence to < 1 meV was reached for an energy cut-off for the plane-wave basis set of 700 eV, and a Gamma centered 5×5×2 k-point mesh. These settings were applied to the slab models (Figure 3.2a) with equivalent k-point densities and a single k-point in the vacuum direction. For the slab model, 4 atomic layers were sufficient to relax the forces on the first and second layers of the (001) and (100) surfaces. In order to avoid a dipole, symmetric slabs were constructed with 11 atomic layers, holding the ion positions of the central 3 layers fixed to bulk values (Figure 3.2b). For the (101) surfaces twice the number of atomic layers were needed to relax the forces. As a compromise between computational cost and comparable scenarios, 12 atomic layers slabs were used with the bottom 4 layers held fixed and the top 8 layers allowed to relax (Figure 3.2c); this provided surface energies within 0.001 eV $Å^{-2}$ compared to the former method with twice the slab thickness. Single-sided adsorption of APTES on the top of the slab and

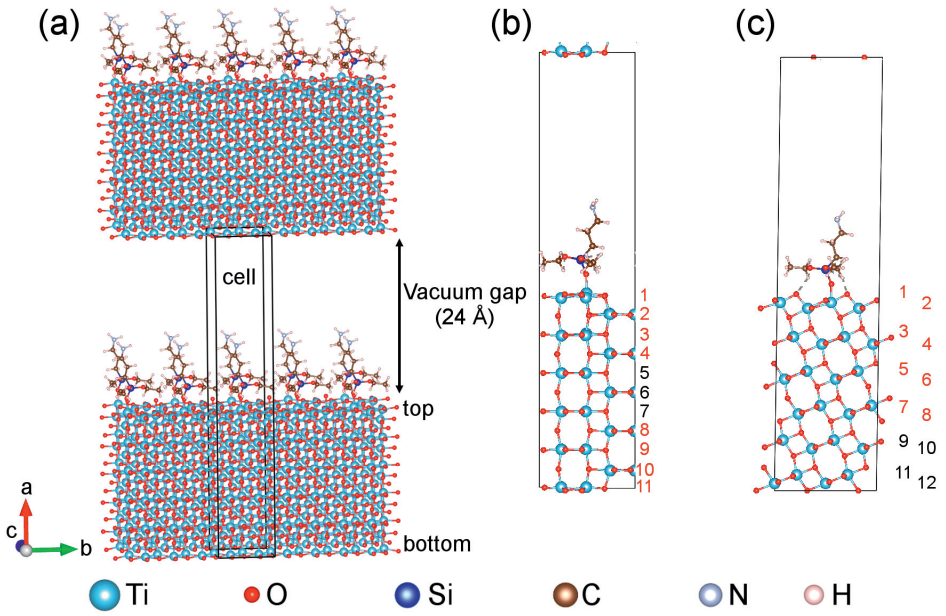

Figure 3.2. (a) Definition of the cell, (b) slab model for (001) and (100) surfaces, (c) slab model for (101) surface. Red and black numbers indicate the layers that are allowed to relax and the fixed layers, respectively. Represented using VESTA [123].

a vacuum gap of 24 Å provided a sufficient gap of 14 Å between the bottom of the slab and the top of the APTES molecule (Figure 3.2a). Slab models with adsorbed APTES were optimized until the residual forces on the ions were less than 0.05 eV $Å^{-1}$.

3.5.2. Calculations of surface energies

The APTES molecule consists of a Si atom with three ethoxy groups and one aminopropyl group. From one to three ethoxy groups may be removed in the formation of one to three Ti−O−Si bonds per APTES molecule. The relevant chemical reaction is hydrolysis of the silane:

$$\text{Ti–OH} + \text{R–O–Si} \longrightarrow \text{Ti–O–Si} + \text{R–OH} \qquad (3.1)$$

where R is an ethyl group, C_2H_5. Furthermore, the calculation is limited to the formation of one Ti−O−Si bond per APTES molecule. Meroni *et al*. [203] demonstrated in a combined

experimental and theoretical work that APTES chemisorption on TiO_2 takes place by only one or two Ti−O−Si bonds per molecule, whilst no converged energy minimum was found for the formation of three Ti−O−Si bonds. Although it is likely that all ethoxy groups are eventually removed from the molecule, cross-linking of APTES molecules (Si−O−Si) is neglected. This situation can be considered as an intermediate stage of the reaction as infrared spectroscopy data indicates at least partial cross-linking on the nanoparticles (see Chapter 4). In addition, Meroni *et al*. [203] also showed that high bond strains limit extensive cross-linking.

The surfaces considered are (001), (100) and (101). The bare, unfunctionalized TiO_2 surfaces are referred to as "bare TiO_2". For the functionalized surfaces, a Ti−OH bond is necessary for the hydrolysis reaction. There are two options for the type of bond which could be involved in the reaction – that of a surface Ti with attached −OH, or that of surface O with attached H. Here, only surface Ti with an −OH bond is considered, because this reduces the interactions between the surface and the remaining ethoxy branches. Such interactions are likely to be long-range in nature and require specific treatment by DFT, so limiting these interactions reduces this source of error. An −OH bond is introduced to 25 % of the surface Ti, which provides sites for one APTES molecule per four surface Ti (Figure 3.2).

Surface energies are calculated based on the 0 K DFT ground state energies, hence neglecting entropy and chemical potential terms. Solvent effects are also neglected, which are expected to reduce the adsorption energies substantially for polar solvents. The basis of these assumptions is that these effects are expected to be similar on each surface and not to affect the overall ratio of surface energies. The surface energy from a symmetric slab is given by:

$$\gamma_{\mathrm{hkl}} = \frac{E_{\mathrm{sym}} - N_{\mathrm{TiO_2}} E_{\mathrm{bulk}}}{2A} \tag{3.2}$$

where E_{sym} is the energy of the symmetric slab, $N_{\mathrm{TiO_2}}$ is the number of formula units in the slab, E_{bulk} is the energy per formula unit of TiO_2 from the bulk calculation, A is the slab surface area and the factor of ½ is used to account for the top and bottom slab surfaces.

Similarly, for the 101 surface, the surface energy of the upper surface from a slab with one-side fixed is:

$$\gamma_{top} = \frac{E_{slab} - N_{TiO_2} E_{bulk}}{A} - \gamma_{bottom} \tag{3.3}$$

where

$$\gamma_{bottom} = \frac{E_{unrelaxed\ slab} - N_{TiO_2} E_{bulk}}{2A} \tag{3.4}$$

The surface energy of the upper surface from a slab with one-sided absorption is:

$$\gamma_{hkl\_ads} = \frac{E_{sys} - N_{TiO_2} E_{bulk} - N_{ads} E_{ads}}{A} - \gamma_{hkl} \tag{3.5}$$

where E_{sys} is the energy of the slab with adsorbate, N_{ads} is the number of adsorbed molecules and E_{ads} is the energy of the isolated adsorbate.

The Wulff constructions were plotted using the software by Zucker *et al.* [273], with lattice parameters of anatase from ICDD card #00-021-1272.

The binding energies (B.E.) were calculated from:

$$\text{B.E.} = E_{slab} + E_{ads} - E_{sys} \tag{3.6}$$

where E_{slab} is the energy of the bare slab, E_{ads} is the energy of the isolated adsorbate and E_{sys} is the energy of the slab with adsorbate.

3.6. Characterization techniques

3.6.1. X-ray diffraction

Powder X-ray diffraction (XRD) were performed on a Bruker D8 Advance Da-Vinci working in Bragg-Brentano (θ/2θ) geometry and equipped with LynxEye detector. Diffractograms were recorded with CuK$_\alpha$ radiation (1.5406 Å), with a step size of 0.013°, an integration time of 0.4 s, and using variable divergent slits.

3.6.2. Synchrotron X-ray diffraction

The *in situ* XRD data were collected at the Swiss-Norwegian Beamlines (BM01A) at the European Synchrotron Radiation Facility (ESRF), Grenoble, France.

The experimental setup consisted of a single crystal sapphire capillary (1.15 ± 0.1 and 0.8 ± 0.08 mm outer and inner diameters, respectively) connected to a high-pressure liquid chromatography (HPLC) pump at one end and closed at the other end, as previously described [274-276]. A heat blower was placed above the capillary as heat source and it was pointed towards the sample once desired temperature and pressure were reached and data collection was started (Figure 3.3a).

The diffraction data were collected in transmission mode using the *PILATUS@SNBL* platform [277], with an exposure time of 10 s, and the interval between each scan was 12.72 s. After cooling the sample, 5 min exposure time diffractograms were collected for each sample. The distance between the sample and the detector was 150 mm and the monochromatic beam wavelength was set to 0.6999 Å (17.715 keV). The 2D diffraction patterns (Figure 3.3b) were integrated after masking the diffraction spots from the capillary and the beam stopper using the *SNBL Toolbox* [277].

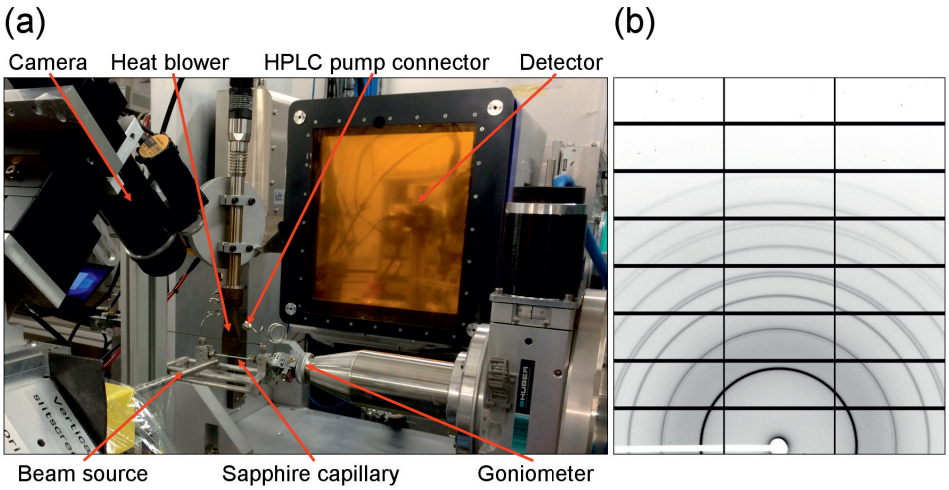

Figure 3.3. (a) Experimental setup for the *in situ* synchrotron diffraction analysis and (b) example of 2D diffraction pattern (anatase) obtained from this setup.

3.6.3. Diffraction data analysis

Rietveld refinements [278] were performed using TOPAS (Bruker AXS version 5). For the *in situ* XRD, batch refinement was achieved with TOPAS operating in launch mode, and jEdit with macros for TOPAS [279]. The instrumental parameters were initially refined using a NIST 660a LaB_6 standard (Pawley fitting, space group *Pm-3m*). Hexagonal boron nitride was used for temperature calibration using the thermal expansion of the *c* cell parameter, based on the equation derived by Pease [280]:

$$c\,(\text{Å}) = 6.6516 + 2.74\times10^{-4}T\,(°\text{C}) \tag{3.7}$$

The *c*-parameters were obtained after refinements of the diffractograms (based on ICDD card #01-073-2095, space group $P6_3/mmc$) taken from room temperature to 500 °C, by steps of 50 °C (Figure 3.4). For all the *in situ* experiments, the temperature and the pressure were 213 °C and 250 bar, respectively.

Refinement of anatase was based on ICDD card #00-021-1272, space group $I4_1/amd$. For each frame, the cell parameters, scale factor, and Chebychev background parameters were refined. For selected samples, an anisotropic peak broadening model was implemented in order to refine *hkl* dependent crystallite sizes (integral breadth) [281], allowing to extract the

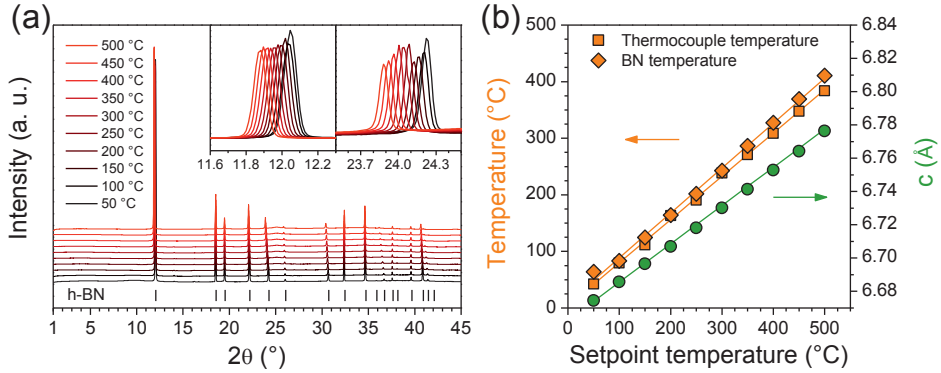

Figure 3.4. (a) Diffractograms of hexagonal boron nitride collected at different setpoint temperatures (λ = 0.6999 Å, vertical lines show diffraction lines of hexagonal boron nitride from ICDD card #01-073-2095) and (b) temperature calibration curves (thermocouple and boron nitride calculated temperatures from the *c*-parameter of boron nitride).

Table 3.4. Unit cell parameters of anatase at room temperature and at 213 °C.

Temperature (°C)	a (Å)	c (Å)	c/a	V (Å^3)
25[a]	3.7852	9.5139	2.5134	136.31
213	3.7884	9.5290	2.5153	136.76

[a] Values at 25 °C are from ICDD card #00-021-1272

average crystallite size (avg. size or d_{XRD}) as well as the crystallite sizes along a- and c-axes of anatase ($size_a$ and $size_c$, respectively). The size anisotropy (expressed as a percentage) was calculated using [282]:

$$\text{Size anisotropy} = \frac{\text{Size}_c - \text{Size}_a}{\text{Size}_c} \tag{3.8}$$

All atomic positions and displacements were kept constant. An example of TOPAS code used for refinement of *in situ* synchrotron data and comparison of the Rietveld refinements with and without the anisotropic peak broadening model can be found in Appendices 8.1 and 8.2, respectively. For references, bulk lattice parameters at 213 °C were calculated using the thermal expansion coefficient of anatase [283] ($\alpha_a = 4.46943\times10^{-6}$ K^{-1} and $\alpha_c = 8.4283\times10^{-6}$ K^{-1}), based on lattice parameters from ICDD card #00-021-1272 (Table 3.4). The interplanar distances (d_{hkl}) at 213 °C were calculated with VESTA [123] based on the calculated cell parameters at 213 °C.

For pure TiO_2 and Ti-DTES, refinement of brookite was also implemented, based on ICDD card #00-029-1360, space group *Pcab*; and in the case of heat-treated TiO_2 nanoparticles, refinement of rutile was implemented based on ICDD card #00-021-1276, space group $P4_2/mnm$, for which only the scale factors and the crystallite sizes were refined.

3.6.4. Scanning electron microscopy

Scanning electron microscope (SEM) images were recorded on an in-lens cold field emission S(T)EM Hitachi S-5500. The acceleration voltage was 7 kV and secondary electrons were detected. Samples were prepared by dropping an aqueous suspension of the

particles obtained after the centrifugation on an aluminium sample holder, which was set to dry overnight. The linear intercept method was used to calculate average particle sizes (d_{SEM}) using more than 100 particle intercepts.

3.6.5. Transmission electron microscopy

Transmission electron microscope (TEM) images were recorded on a JEOL 2100 equipped with Oxford X-Max 80 SDD detector for energy-dispersive X-ray spectroscopy (EDS) analysis. The acceleration voltage was 200 kV. For the preparation of the TEM samples, the nanoparticles were dispersed in anhydrous propan-2-ol dropped on a carbon coated copper TEM grid (Lacey). The interplanar distances (d_{hkl}) were measured by extracting area of interest from the high resolution TEM (HR-TEM) images with fast Fourier transform analysis, and calculating the average distance over more than 10 consecutive *hkl* planes, using DigitalMicrograph (Gatan Inc. version 3.01).

3.6.6. Nitrogen adsorption measurements

Specific surface area (Brunauer-Emmett-Teller (BET) method [284]) and pore size distribution (Barrett-Joyner-Halenda (BJH) method [285]) were measured by nitrogen adsorption on a Micrometrics Tristar 3000, at 77 K. Samples were degassed for 12 h at 180 °C in vacuum prior to analysis. Particle sizes were calculated from the specific surface area assuming non-porous and spherical particles using [286]:

$$d_{BET} = \frac{6000}{S_{BET}\rho_{TiO_2}} \tag{3.9}$$

where d_{BET} is the particles diameter estimated from BET measurements (nm), S_{BET} the measured specific surface area ($m^2\ g^{-1}$), and ρ_{TiO_2} is the density of the anatase nanoparticles (3.89 g cm^{-3}). The average pore diameter from BJH desorption calculations is labeled d_{BJH}.

3.6.7. Thermogravimetry

Thermogravimetric analysis (TGA) were acquired on a Netzsch Jupiter STA 449 C using an alumina crucible.

For the nanoparticles (Chapter 4), the samples were firstly heated from 25 to 150 °C (10 °C min^{-1}), maintained at 150 °C for 30 min, cooled down to room temperature, and heated again from 25 to 200 °C (2 °C min^{-1}) in order to remove adsorbed water. The samples were finally heated from 100 to 700 °C (2 °C min^{-1}). All treatments were performed in synthetic air.

Combined with nitrogen adsorption measurement, and considering loss of C, H, and N of the silanes during the heat treatment of the functionalized nanoparticles, the average surface coverages (S_{cov}, in molecules per square nm or nm^{-2}) of the nanoparticles were calculated using:

$$S_{cov} = \frac{\left(M_{org}/m_{loss}\right) N_A}{S_{BET} \times 10^{18}} \tag{3.10}$$

where M_{org} (g mol^{-1}) is the molar mass of C, H, and N of the considered silane, m_{loss} (g) is the mass loss for 1 g of material, measured from TGA between 230 and 460 °C, and N_A the Avogadro constant.

For the hybrid films (Chapter 5), the samples were first heated from 25 to 120 °C (5 °C min^{-1}), maintained at 120 °C for 30 min, cooled to 25 °C (5 °C min^{-1}) and finally heated to 800 °C (2 °C min^{-1}). All analyses were performed in synthetic air.

3.6.8. Fourier transform infrared spectroscopy

Fourier transform infrared (FTIR) spectra were acquired on a Bruker Vertex 80v spectrophotometer equipped with Bruker Platinum ATR diamond system from 400 to 4000 cm^{-1}. A background was collected, without sample and the ATR diamond was cleaned with isopropanol between each analysis.

For surface-functionalized nanoparticles (Chapter 4), at least 32 scans were acquired for each sample at a resolution of 1 cm^{-1} while for the heat-treated nanoparticles (Chapter 4), a total of 128 scans were acquired for each sample at a resolution of 1 cm^{-1}, at 280 Pa.

For the hybrid films and the polymers (Chapter 5), a total of 64 scans were acquired for each sample at a resolution of 1 cm^{-1}. For the *in situ* analysis of the hybrid formation reaction, 16 scans were acquired per spectrum, at a resolution of 1 cm^{-1} (analysis time of about 45 s), at ambient conditions. The time between each spectrum was 1 min.

3.6.9. Ultraviolet-visible spectroscopy

Ultraviolet-visible (UV-vis) spectra were recorded with an Evo220 Thermo Fisher Scientific spectrophotometer from 1000 to 200 nm with a step size of 1 nm and an integration time of 0.1 s. A background was collected at room temperature in air and the hybrid thick films were measured without substrate.

3.6.10. Micro-Raman spectroscopy

Raman spectra were recorded on a Renishaw InVia Reflex spectrometer using a monochromatic diode laser (λ = 785 nm) as an exciting light source, and a 1200 L mm^{-1} (633/780) grating. The spectra were measured on the thick films, from 400 to 1500 cm^{-1}, with a resolution of 1 cm^{-1}. A total of 20 scans were collected for 1 s each and were averaged for every sample.

3.6.11. Small-angle X-ray scattering

Small-angle X-ray scattering (SAXS) data were collected at the SWING beamline, SOLEIL synchrotron, Gif-sur-Yvette, France [287]. The acquisitions were performed in transmission mode, at sample-to-detector distances of 6.072 m and 0.997 m, for accessing q-ranges (scattering vector) from 0.002 to 0.2 $Å^{-1}$ and from 0.015 to 1.2 $Å^{-1}$, respectively, using a monochromatic beam with a wavelength of 1.0332 Å (12.000 keV). For each sample, the acquisition time was optimized in order to obtain high signal without saturating the

detector. Once desired acquisition time was selected, 10 backgrounds (air and, in some cases, Kapton) were collected, masked, integrated, and averaged. The same number of acquisitions and treatments were performed for the sample data. All the data treatments were performed at the beamline using FOXTROT [288]. The final data correspond to the averaged sample acquisition from which the averaged background was subtracted. Due to overlapping q-ranges, $q = 0.15$ Å^{-1} was selected as point of merging and the values given below and above this value are from the data collected at sample-to-detector distances of 6.072 m and 0.997 m, respectively.

3.6.12. Ellipsometry

Ellipsometry analysis were performed on a J.A. Woollam RC2 vertical ellipsometer. Calibration was achieved using a single crystal silicon wafer with a 25 nm SiO_2 layer, at a position of 65° (source-sample angle, corresponding to 130° source-detector angle). Spin-coated films were analyzed with a polychromatic light (210 to 1690 nm) using focusing probes. Three points per sample were recorded and for each point, measurements were done at five angles (50, 55, 60, 65, and 70° source-sample angles, corresponding to 100, 110, 120, 130, and 140° source-detector angles, respectively) with an analysis time of 20 s per position. The refinement of the data was performed using CompleteEASE (J.A. Woollam, version 5.13). The Cauchy model, represented in Equation (2.36), was used from 400 to 1600 nm on the hybrid film layer, and the substrate was modeled with a 2 nm SiO_2 layer on metallic silicon. The calculated parameters for each sample were A, B, and C Cauchy coefficients, thus $n(\lambda)$, and the thickness of the spin-coated film. Two refinement examples are shown in Appendix 8.4.1.

3.6.13. Contact angle measurements

Contact angle measurements (sessile test) were performed using a Krüss Drop Shape Analyzer – DSA 100. The measurements were performed on the spin-coated films, using a distilled water drop of 8 µL, at room temperature. The first image was taken 5 s after the water drop was deposited and a picture was collected every 2 s. A total of 11 pictures were captured. The Young-Laplace fitting was used on every image and the reported values are the average of the 11 images (± 1°).

3.6.14. Dynamic mechanical analysis

Dynamic mechanical analysis (DMA) were carried out at with a TA instrument DMA Q800 instrument (ESIREM, University of Burgundy, Dijon, France), using a shear-sandwich geometry. The acquisition was performed from −100 °C to 150 °C, at 3 °C min^{-1}, using a constant amplitude of 1 µm and a constant frequency of 10 Hz. Prior to the acquisition, an isotherm of 15 min at −100 °C was performed on all the samples.

4. *In situ* surface-functionalized titanium dioxide nanoparticles

The following content is based on ref. [289, 290] (available in Appendix 8.5) and ref. [291, 292].

4.1. Pure titanium dioxide and *in situ* functionalization

In this chapter, the synthesis of *in situ* surface-functionalized TiO_2 nanoparticles with different silane coupling agents (3-aminopropyltriethoxysilane (APTES), 3-(2-aminoethylamino)propyldimethoxymethylsilane (AEAPS), and *n*-decyltriethoxysilane (DTES), Figure 3.1) is described. Titanium(IV) isopropoxide (TIP) was used as titanium precursor. The influence of the type of silane coupling agent on the nanoparticles final structure and properties is discussed.

Before producing *in situ* functionalized nanoparticles, initial tests were performed in which TIP/DTES molar ratios of 1:1 and 2:1 were used. However, this synthesis lead to the formation of a yellowish gel-like materials where TiO_2 nanoparticles were embedded in a polysiloxane based structure (see Appendix 8.3). Based on the synthesis of pure TiO_2 and the calculated specific surface area, the molar ratio of 10:1 was thus calculated to be close to the optimum ratio to provide functionalization of TiO_2 nanoparticles with a diameter of about 10 nm. Each synthesis produced about 2 grams of materials that could easily be retrieved after the centrifugation steps, as a slurry. The nanoparticles could then be kept in distilled water for health and security purposes or dried for analysis. Typically, about half of the synthesis product was dried and the other half was kept in distilled water.

4.1.1. Results

4.1.1.1. Structure and morphology

XRD patterns of pure TiO_2 and surface-functionalized TiO_2 nanoparticles, displayed in Figure 4.1, shows anatase as the main polymorph. The reflection at 30.8° demonstrates that brookite is present as secondary phase in the case of TiO_2 and Ti-DTES. The samples functionalized with aminosilane are pure anatase. Broad diffraction lines demonstrate small crystallite size for all the samples.

The average crystallite sizes (d_{XRD}) calculated from Rietveld refinements of the XRD patterns (Figure 4.2) are given Table 4.1. For all samples, the crystallite size of anatase are smaller than 10 nm. Both pure TiO_2 and Ti-DTES samples consist of about 25 wt.% of brookite.

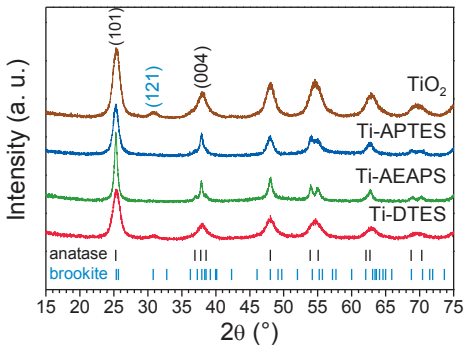

Figure 4.1. XRD patterns (λ = 1.5406 Å) of TiO_2 and *in situ* surface-functionalized TiO_2 nanoparticles. The vertical bars show diffraction lines of anatase from ICDD card #00-021-1272 and brookite from ICDD card #00-029-1360.

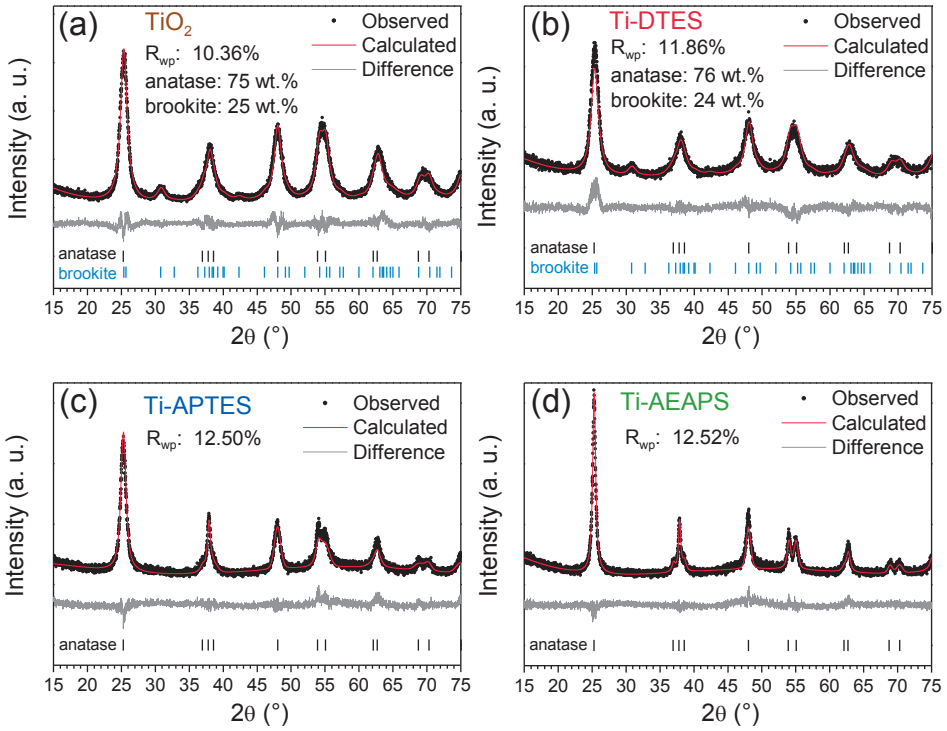

Figure 4.2. Rietveld refinement profiles ($\lambda = 1.5406$ Å) of TiO_2 and *in situ* surface-functionalized TiO_2 nanoparticles. Refinement of (c) Ti-APTES and (d) Ti-AEAPS included the correction for anisotropic peak broadening. The vertical bars show diffraction lines of anatase from ICDD card #00-021-1272 and brookite from ICDD card #00-029-1360.

Table 4.1. Characteristics of TiO_2 and *in situ* surface-functionalized TiO_2 nanoparticles from nitrogen adsorption, XRD, SEM, and TGA analysis.

Sample	S_{BET}[a] ($m^2\ g^{-1}$)	d_{BET}[b] (nm)	d_{BJH}[c] (nm)	d_{XRD}[d] (nm)	d_{SEM}[e] (nm)	m_{loss}[f] (%)	S_{cov}[g] (nm^{-2})
TiO_2	195 ± 1	7.9 ± 0.1	7.9 ± 0.1	5.7 ± 0.1	9.0 ± 0.6	n/a	n/a
Ti-DTES	114 ± 1	13.5 ± 0.1	9.7 ± 0.1	4.7 ± 0.1	9.2 ± 0.9	10.8 ± 0.5	4.0 ± 0.5
Ti-APTES	178 ± 1	8.7 ± 0.1	9.2 ± 0.1	6.0 ± 0.1	16.4 ± 1.4	5.8 ± 0.5	3.4 ± 0.3
Ti-AEAPS	149 ± 1	10.3 ± 0.1	11.8 ± 0.1	9.1 ± 0.1	20.9 ± 3.2	6.7 ± 0.5	2.3 ± 0.4

[a] BET specific surface area from nitrogen adsorption measurements.
[b] Particle size estimated from BET specific surface area.
[c] Average pore diameter from BJH desorption calculations.
[d] Average crystallite size from Rietveld refinement of XRD measurements.
[e] Particle size from SEM observations.
[f] Organic mass loss from TGA measurements.
[g] Surface coverage calculated from TGA and nitrogen adsorption measurements.

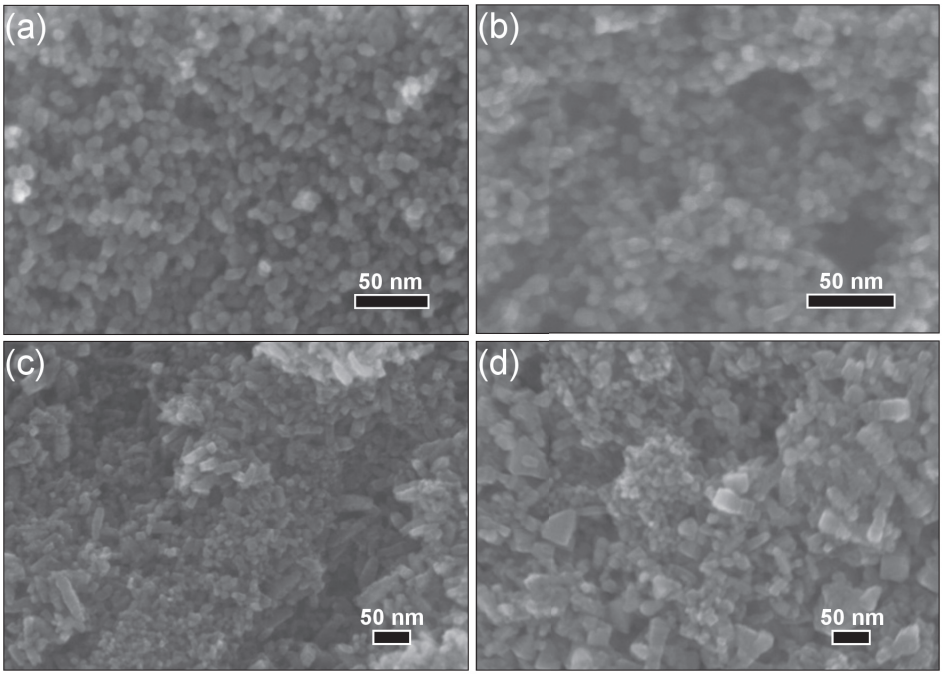

Figure 4.3. SEM images of (a) TiO_2 and *in situ* surface-functionalized TiO_2 nanoparticles, (b) Ti-DTES, (c) Ti-APTES, and (d) Ti-AEAPS.

SEM images of pure TiO_2 and samples synthesized with DTES, APTES, and AEAPS are displayed in Figure 4.3. For all the samples, spheres of about 10 nm of diameter and a narrow size distribution can be observed. In the case of aminosilane functionalized samples (Figure 4.3c-d), additional rod-like nanoparticles (50-200 nm in length) are observed, and are generally larger when the synthesis was performed with AEAPS. The average size of the particles from SEM analysis (d_{SEM}) are listed Table 4.1.

The HR-TEM images of pure TiO_2 (Figure 4.4a) demonstrates that single crystalline nanoparticles of anatase and brookite were formed. The electron diffraction pattern (Figure 4.4b) also confirms that both anatase and brookite were obtained as the (121) line of brookite is visible, in addition to the anatase diffraction pattern. Figure 4.4c shows a single crystal rod-like nanoparticle from Ti-APTES sample. The {004} planes are perpendicularly oriented to the elongation direction, indicating that the elongation is along the [001] crystallographic direction of anatase. In this case, no brookite is observed (Figure 4.4d). For

Ti-APTES and Ti-AEAPS the XRD patterns also points toward anisotropy along the [001] (Figure 4.1 and Figure 4.2). The full width at half maximum (FWHM) of the (004) diffraction line at 37.80° is narrower compared to other reflections, and the best fits were obtained when including the anisotropic peak broadening model. The size anisotropy was calculated to be 36 % and 42 % for Ti-APTES and Ti-AEAPS, respectively, coherently with the SEM analysis. The orientation of elongated anatase nanoparticles along the [001] direction was previously observed for hydrothermally synthesized titanium dioxide [71, 293].

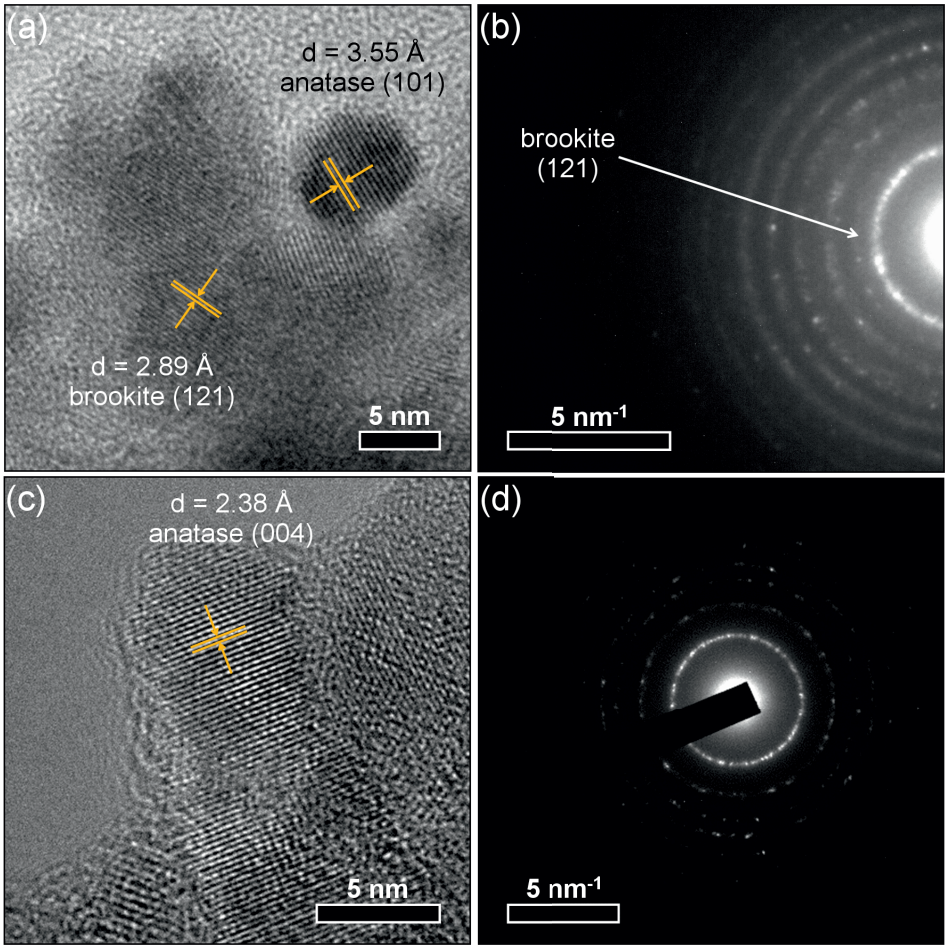

Figure 4.4. (a) HR-TEM image showing two individual nanoparticles of brookite and anatase and (b) electron diffraction pattern of pure TiO_2 (top); (c) HR-TEM image of a rod-like nanoparticle and (d) electron diffraction pattern of Ti-APTES (bottom).

The measured specific surface area (S_{BET}) and the corresponding calculated size (d_{BET}) of the nanoparticles are included Table 4.1. The particle size is consistent with the SEM and TEM analysis and the crystallite size determined by XRD, which suggest only weak agglomeration of the particles after drying. The nitrogen adsorption and desorption isotherms of TiO_2 and *in situ* surface-functionalized TiO_2 nanoparticles (Figure 4.5a) show hysteresis profiles similar to mesoporous materials. Since the particle sizes from SEM and surface area are similar (Table 4.1), the measured porosity is associated with the interparticle volume of the agglomerates and can be correlated with the particle size [294]. Figure 4.5b displays the BJH pore size distribution from the desorption isotherm of TiO_2 and *in situ* surface-functionalized TiO_2 nanoparticles. The pore size distribution is centered between 4 and 7 nm for TiO_2 and Ti-DTES, while for the aminosilane functionalized samples, the size distribution is broader and shifted towards larger pores and two features are observed. The first feature, centered between 4 and 7 nm, is assigned to the spherical nanoparticles and the second broader feature is assigned to the rod-like particles. Coherent with SEM analysis, as less spherical nanoparticles are observed in Ti-AEAPS, the volume of the feature between 4 and 7 nm is decreasing (by relative comparison to Ti-APTES), and as rod-like particles are larger, the feature at around 10 nm is shifted towards larger values. The average pore diameters from desorption curves (d_{BJH}) are included in Table 4.1.

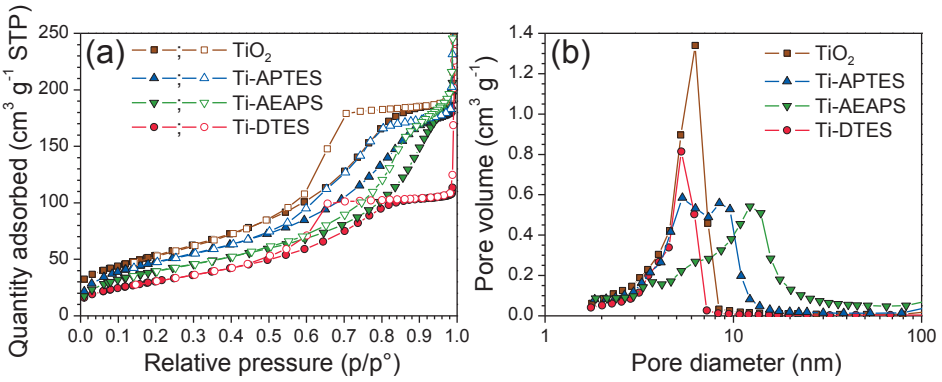

Figure 4.5. (a) Adsorption (solid symbols) and desorption (open symbols) isotherms and (b) BJH pore size distribution, from nitrogen adsorption measurements, of TiO_2 and *in situ* surface-functionalized TiO_2 nanoparticles.

4.1.1.2. Functionalization and hydrophobicity

Figure 4.6a shows mass loss from thermogravimetric analysis of TiO_2 and *in situ* functionalized TiO_2 nanoparticles. In the case of pure TiO_2 the mass loss is attributed to adsorbed water and hydroxy groups. In the case of the functionalized samples, the mass loss observed between 230 and 460 °C is assigned to the combustion of the organic part of the silane coupling agents (m_{loss}). Using Equation (3.10), the surface coverage (S_{cov}) was calculated to be between 2.3 and 4.0 silanes per square nanometer (Table 4.1). The FTIR spectra of TiO_2 and *in situ* functionalized TiO_2 nanoparticles are displayed Figure 4.6b and the assignments of the absorption bands are available in Table 4.2. Absorption bands due to the functional groups of the silane and to TiO_2 (below 900 cm^{-1}) are clearly present. In addition, Ti−O−Si (shoulder at 910 cm^{-1}) and Si−O−Si (at 1020 and 1120 cm^{-1}) bands confirmed the *in situ* functionalization of the particles through covalent bonding on the surface of the TiO_2 nanoparticles and cross-linking between the silanes, in line with previous reports [196-198, 200]. For Ti-DTES, the CH_2 stretching bands at 2852 and 2921 cm^{-1} are close to those measured for 1-decanethiol adsorbed on gold [199], corresponding to a well-ordered organic monolayer. For aminosilane functionalized samples, the low signal-to-noise ratios did not allow for an accurate measurement of the band positions. Additionally, because of possible carbon contamination and/or optical aberration, HR-TEM images of Ti-APTES (Figure 4.4c) do not provide clear evidence of an organic layer, confirming the nanometric nature of the organic layer.

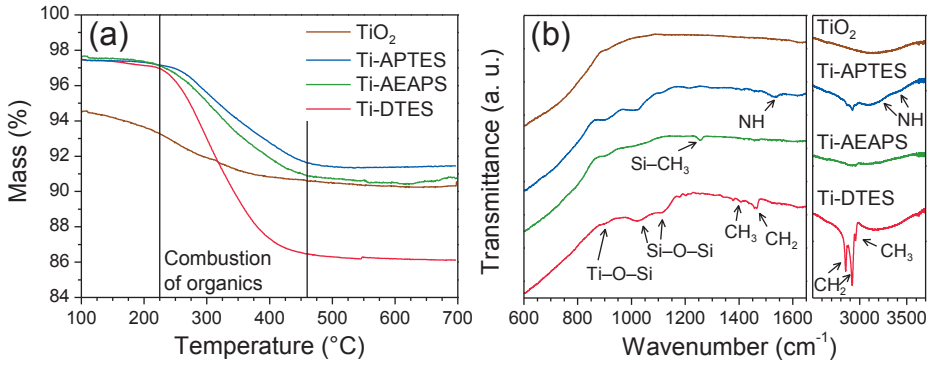

Figure 4.6. (a) TGA curves and (b) FTIR spectra of TiO_2 and *in situ* surface-functionalized TiO_2 nanoparticles.

Table 4.2. Assignments of characteristic IR bands of TiO_2 and *in situ* surface-functionalized TiO_2 nanoparticles.

Wavenumber (cm^{-1})	Assignment	Sample	Reference
< 900	Ti−O−Ti	All	[198, 205, 211, 295, 296]
910	Ti−O−Si	All functionalized samples	[197, 198, 205, 211, 295, 297]
1020 and 1120	Si−O−Si	All functionalized samples	[196-198, 205, 211, 295, 297, 298]
1220	Si−CH_2R	All functionalized samples	[295, 297, 298]
1260	Si−CH_3	Ti-AEAPS	[295, 297, 299]
1380	CH_3 (bend)	Ti-DTES	[295]
1460	CH_2 (bend)	All functionalized samples	[204, 295, 298]
1530 and 3200-3500	N−H	Ti-APTES, Ti-AEAPS	[198, 204, 295, 298]
1640 and 2500-3600	Adsorbed H_2O and −OH groups	All	[196, 198, 295, 298]
2850 and 2920	CH_2 (stretch)	All functionalized samples	[198, 199, 205, 295, 298]
2870 and 2960	CH_3 (stretch)	Ti-DTES	[199, 295]

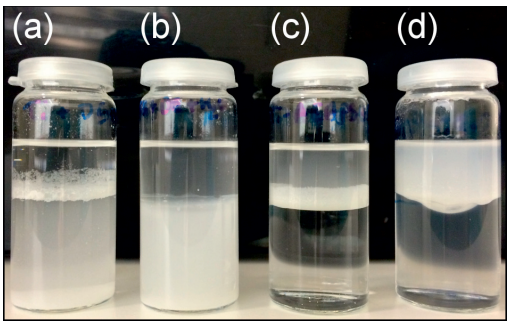

Figure 4.7. Photograph showing the behavior of (a) TiO_2 and *in situ* surface-functionalized TiO_2 nanoparticles, (b) Ti-APTES, (c) Ti-AEAPS, and (d) Ti-DTES in mixed solutions of diethyl ether (top) and water (bottom).

A photography of a dispersion of the nanoparticles in a mixture of diethyl ether and water is displayed Figure 4.7. Pure TiO_2 nanoparticles entirely dispersed in water, indicating a hydrophobic behavior. Nanoparticles from Ti-APTES dispersed in both phases, showing a partial hydrophobic behavior. Ti-AEAPS and Ti-DTES nanoparticles dispersed in the diethyl ether phase, demonstrating a hydrophobic behavior. These observations are consistent with the nature of the silane coupling agents (polarity and length of the organic chains), and also depends on the surface coverage [205]. Moreover, these results are comparable with the results obtained by Iijima *et al.* [204] on TiO_2 nanoparticles post-modified with decyltrimethoxysilane and aminopropyltrimethoxysilane mixed in solutions of methanol and toluene.

4.1.2. Discussion

From the XRD analysis (Figure 4.1), the formation of TiO_2 particles occurred through hydrolysis and condensation mechanisms of the titanium alkoxide (see Chapter 2.1.1.1) and the total reaction can be summarized as:

$$\mathrm{Ti}\left(\mathrm{OCH}\left(\mathrm{CH_3}\right)_2\right)_4 + 2\mathrm{H_2O} \xrightarrow[2\,\mathrm{h}]{200\,^{\circ}\mathrm{C}} \mathrm{TiO_2} + 4\left(\mathrm{CH_3}\right)_2\mathrm{CHOH} \qquad (4.1)$$

where isopropanol is removed during the cleaning, centrifugation, and/or drying steps. For the functionalized samples, the nucleation of the nanoparticles is most likely to occur first,

due to much higher reactivity of titanium alkoxides compared to their silicon counterparts [30]. Spectroscopy analysis (Figure 4.6b) confirms *in situ* functionalization of the nanoparticles through hydrolysis and condensation of the silane coupling agent on the surface of the growing nanoparticles. Furthermore, FTIR points to high purity of the nanoparticles. A surface coverage ranging from 2.7 to 4.0 silane nm^{-2} was obtained. Pure TiO_2 and Ti-DTES exhibit similar nanoparticle shape, with spheres of about 10 nm with a narrow size distribution and about 25 wt.% of brookite as secondary phase. When functionalized with aminosilanes larger rod-like nanoparticles are observed in addition to the spherical nanoparticles and the samples are phase pure anatase. The average size or the rod-like nanoparticles is larger in the case of *in situ* functionalization with AEAPS than with APTES. From HR-TEM imaging (Figure 4.4) and via crystal anisotropy measured by XRD (Figure 4.1 and Figure 4.2), the rod-like nanoparticles are elongated along the [001] direction of anatase. Elongated particles are only observed in the case of functionalization with aminosilane, demonstrating the role of the silane coupling agent in order to control the morphology of the nanoparticles. The relative roughness of the rod-like nanoparticles (Figure 4.3c-d) and their monocrystallinity suggest that an oriented attachment mechanism is occurring, as previously described during hydrothermal synthesis of TiO_2 nanoparticles [71, 76, 147, 293, 300, 301]. Figure 4.8 summarizes the hydrothermal reaction of TIP with silane coupling agents to *in situ* surface-functionalized TiO_2 nanoparticles.

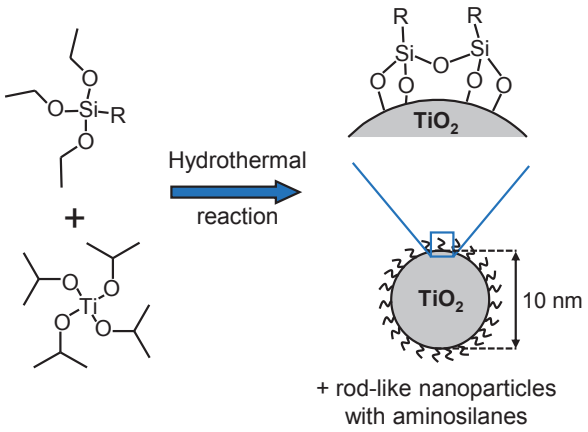

Figure 4.8. Scheme of the hydrothermal synthesis of *in situ* surface-functionalized TiO_2 nanoparticles with silane coupling agents.

This synthesis developed here is robust and versatile. The main advantage of this synthesis is the single-step route to functionalized TiO_2 nanoparticles, similar to the one developed by Koziej *et al.* [211], but using a non-organic solvent. The surface properties of the TiO_2 nanoparticles can be tuned depending on the type of silane coupling agent used during the synthesis (*e.g.* the hydrophobicity in Figure 4.7), which could enhance the dispersion in polymers, and thereby enable the synthesis of polymer nanocomposites [16, 256]. Further functionalization can be done depending on the final application of the nanoparticles, *e.g.* for biosensors in the case of TiO_2 nanoparticles functionalized with APTES [107, 108, 302].

The morphology and the polymorphism is however dependent on the chosen functionalization agent, and has to be controlled. The effect of the precursors molar ratio, the pH of the synthesis, and the growth processes are investigated in Chapters 4.3 and 4.4, in the case of *in situ* functionalization with APTES.

4.2. Effect of heat treatment

In this chapter, the effects of heat treatment at 700 °C in air on the structure, morphology, and chemical composition of the *in situ* functionalized nanoparticles described in Chapter 4.1 are presented. The samples are labelled adding the suffix "-HT" to the original sample name *i.e.* TiO_2-HT, Ti-APTES-HT, Ti-AEAPS-HT, and Ti-DTES-HT. Potential applications for the obtained materials are finally discussed.

4.2.1. Results

Diffractograms of heat-treated nanoparticles at 700 °C in synthetic air are displayed in Figure 4.9. The diffraction patterns of the heat-treated surface-functionalized nanoparticles are similar to those before the heat treatment (Figure 4.1). For pure TiO_2, the reflections are narrower indicating coarsening of the nanoparticles. In addition, partial transition to rutile, the thermodynamically stable polymorph of TiO_2 [122], can be observed with *e.g.* the (110) reflection at 27.5°.

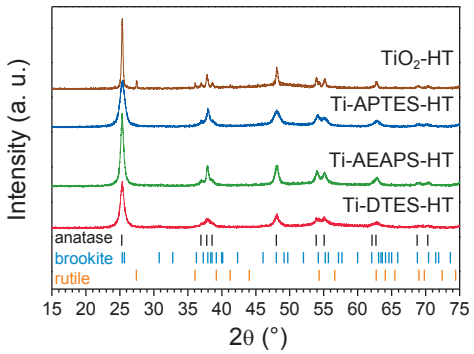

Figure 4.9. XRD patterns (λ = 1.5406 Å) of TiO_2 and *in situ* surface-functionalized TiO_2 nanoparticles after heat treatment at 700 °C. The vertical bars show diffraction lines of anatase from ICDD card #00-021-1272, brookite from ICDD card #00-029-1360, and rutile from ICDD card #00-021-1276.

Rietveld refinement of the diffractograms from the heat-treated nanoparticles are presented in Figure 4.10. For Ti-APTES-HT and Ti-AEAPS, the best fits were obtained with addition of the anisotropic size broadening model, as for the non-heat-treated samples. The size anisotropies are 46 % and 31 % for Ti-APTES-HT and Ti-AEAPS-HT, respectively. The average crystallite size from the Rietveld refinements (d_{XRD}) are given in Table 4.3. The quantitative analysis demonstrates that 8 wt.% of rutile were formed in pure TiO_2 after the heat treatment, and the brookite phase disappeared. For the functionalized nanoparticles, the phase composition is similar to that before heat treatment (Figure 4.2), and the brookite is still present in Ti-DTES-HT.

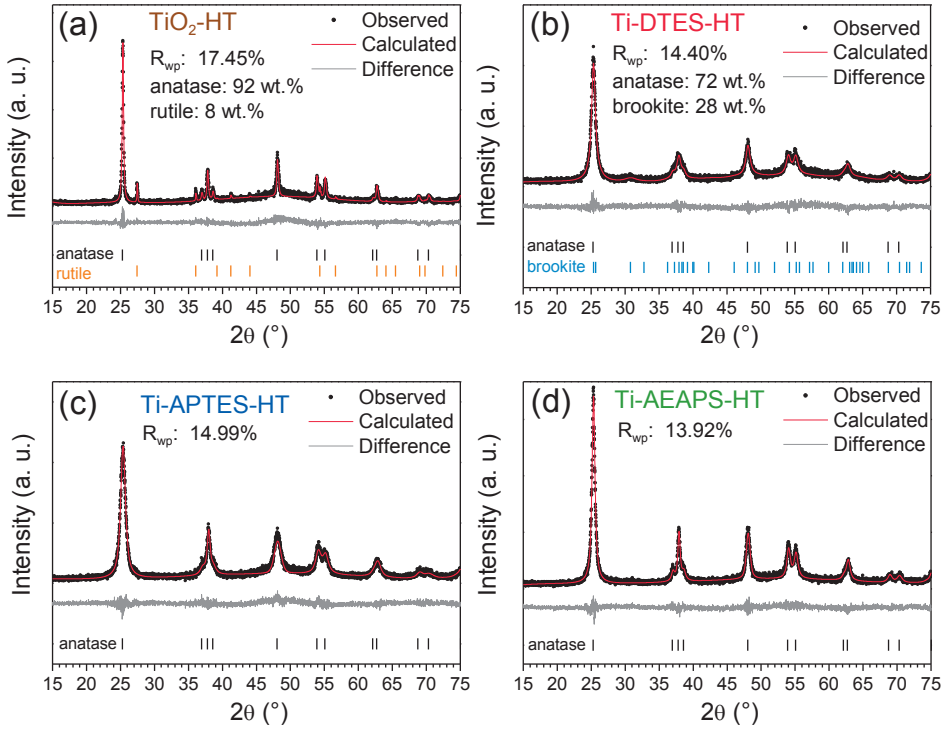

Figure 4.10. Rietveld refinement profiles (λ = 1.5406 Å) of heat-treated (700 °C) TiO_2 and *in situ* surface-functionalized TiO_2 nanoparticles. Refinement of (c) Ti-APTES-HT and (d) Ti-AEAPS-HT included the correction for anisotropic peak broadening. The vertical bars show diffraction lines of anatase from ICDD card #00-021-1272, brookite from ICDD card #00-029-1360, and rutile from ICDD card #00-021-1276.

Table 4.3. Sizes of TiO_2 and *in situ* surface-functionalized TiO_2 nanoparticles before and after heat treatment (HT) at 700 °C, from XRD and SEM analysis.

Sample	d_{XRD}[a] (nm)		d_{SEM}[b] (nm)	
	Before HT	After HT	Before HT	After HT
TiO_2-HT	5.7 ± 0.1	28.8 ± 0.4	9.0 ± 0.6	30.0 ± 2.9
Ti-DTES-HT	4.7 ± 0.1	8.9 ± 0.1	9.2 ± 0.9	12.0 ± 0.6
Ti-APTES-HT	6.0 ± 0.1	7.8 ± 0.1	16.4 ± 1.4	15.5 ± 2.1
Ti-AEAPS-HT	9.1 ± 0.1	10.4 ± 0.2	20.9 ± 3.2	23.7 ± 2.2

[a] Average crystallite size from Rietveld refinement of XRD measurements.
[b] Particle size from SEM observations.

SEM images of heat-treated samples are displayed Figure 4.11. Similar to the XRD analysis, negligible growth is observed for the *in situ* surface-functionalized nanoparticles while the average particle size (d_{SEM}) of pure TiO_2 increased from 9 to 30 nm (Table 4.3). The spherical and rod-like nanoparticles are still visible in the case of the heat-treated functionalized samples.

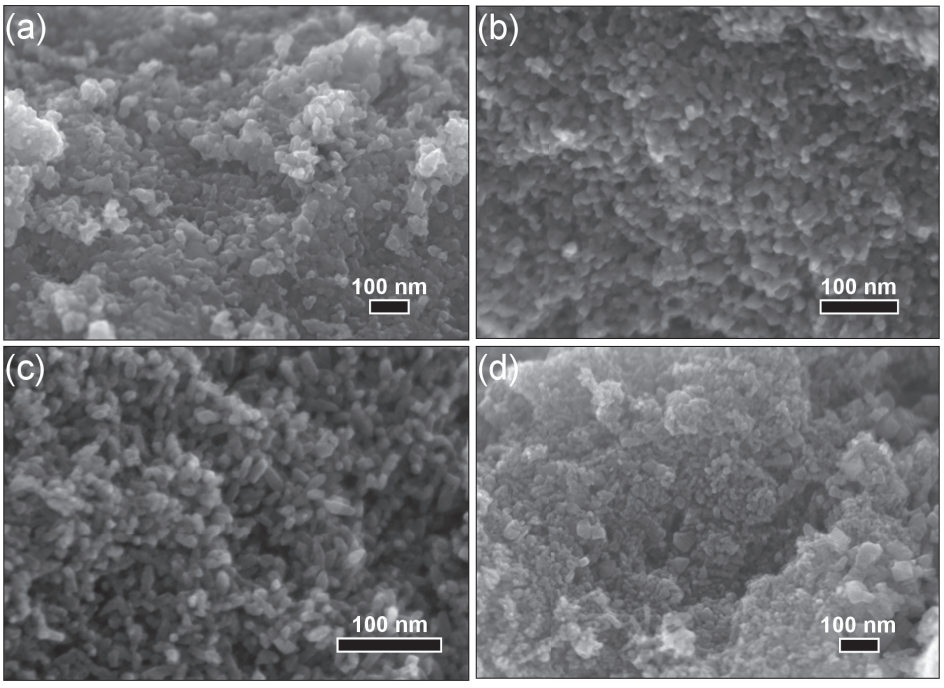

Figure 4.11. SEM images of (a) TiO_2-HT and heat-treated *in situ* surface-functionalized TiO_2 nanoparticles, (b) Ti-DTES-HT, (c) Ti-APTES-HT, and (d) Ti-AEAPS-HT.

From HR-TEM images of Ti-APTES-HT sample (Figure 4.12), similar spherical and rod-like nanoparticles as before heat treatment are present, and they exhibited negligible growth. Possible carbon contamination and/or optical aberrations do not allow to clearly distinguish any coating. However, EDS mapping of the Ti-APTES-HT sample (Figure 4.13) indicates that silicon is present, and that Si is homogeneously distributed over the particles. EDS spectra recorded on larger agglomerates (Figure 4.14) confirm the absence and the presence of silicon in pure TiO_2 and heat-treated *in situ* functionalized samples.

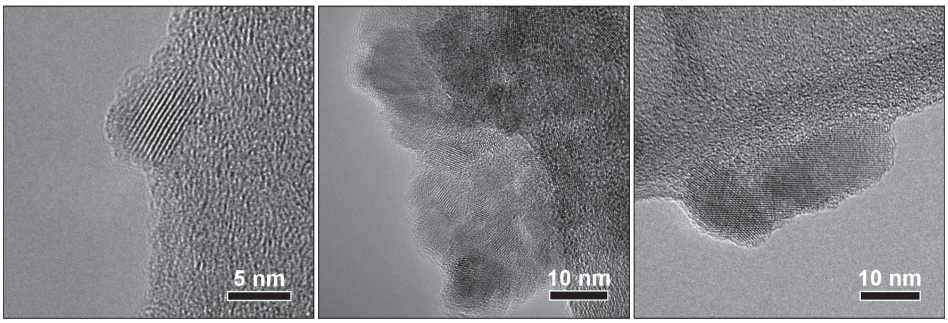

Figure 4.12. HR-TEM images of Ti-APTES-HT nanoparticles (anatase).

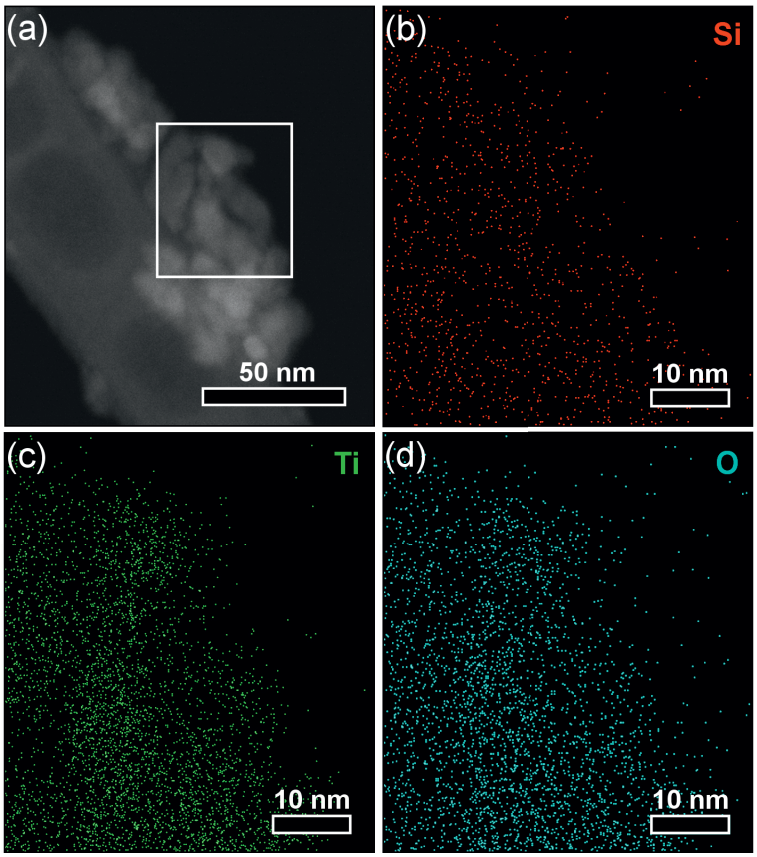

Figure 4.13. (a) Scanning electron image of Ti-APTES-HT with localization of the mapping (white rectangle) and EDS maps of (b) Si $K_{\alpha 1}$, (c) Ti $K_{\alpha 1}$, and (d) O $K_{\alpha 1}$ signals.

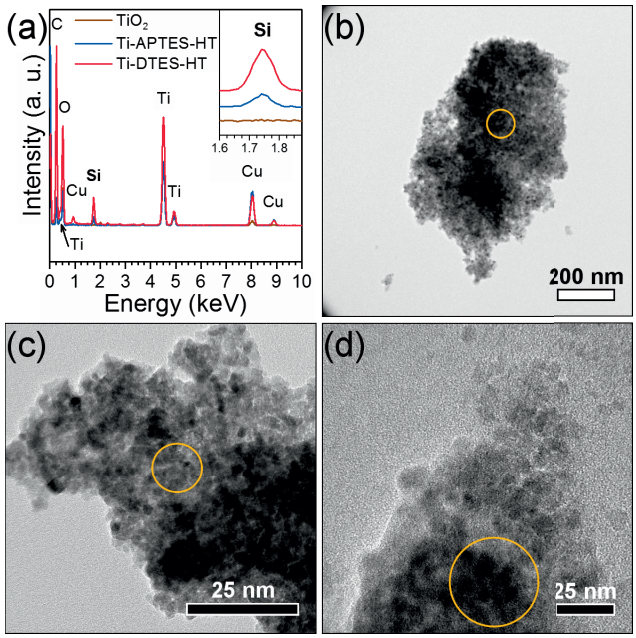

Figure 4.14. (a) EDS spectra from samples area (yellow circles) shown on TEM images of (b) TiO_2, (c) Ti-APTES-HT, and (d) Ti-DTES-HT.

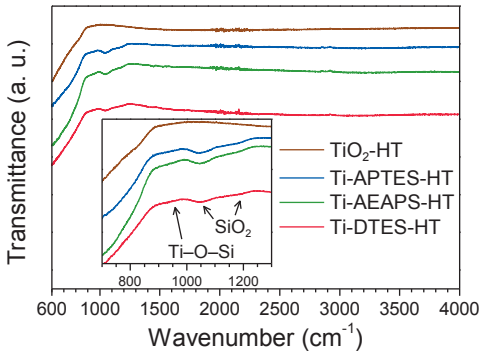

Figure 4.15. FTIR spectra of heat-treated (700 °C) TiO_2 and *in situ* surface-functionalized TiO_2 nanoparticles.

The infrared spectra of the heat-treated samples (Figure 4.15) show strong absorption band below 900 cm^{-1} due to Ti−O−Ti bond in TiO_2. All the heat-treated functionalized samples exhibit two additional bands located at about 1050 and 1150 cm^{-1} which are assigned to Si−O−Si in silica [303] and a weak shoulder centered at about 930 cm^{-1} assigned to Ti−O−Si absorption band.

4.2.2. Discussion

The entire loss of the organic parts of the silane coupling agents after the heat treatment at 700 °C in air of the *in situ* functionalized nanoparticles was confirmed by TGA analysis, FTIR spectroscopy (Figure 4.6a and Figure 4.15), and from the fact that the final materials were white powder. From XRD (Figure 4.9 and Figure 4.10), the crystallite sizes, as well as the structural changes were negligible after the heat treatment. Heat-treated samples initially functionalized with aminosilane are pure anatase and Ti-DTES-HT consists of anatase and about 28 wt.% of brookite, similarly as before the heat treatment, while pure TiO_2 shows partial phase transition to rutile. From SEM and TEM (Figure 4.11 and Figure 4.12), the particle sizes and the morphology of the heat-treated functionalized nanoparticles were not as increased as in the case of pure TiO_2, and no shell could be observed. However, FTIR combined with EDS (Figure 4.13-4.15) reveal the formation of an amorphous and nanometric SiO_2 layer on the surface of the particles, as summarized in Figure 4.16. The

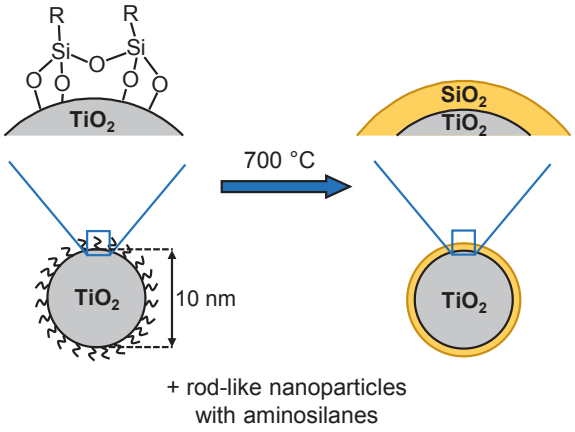

Figure 4.16. Scheme of the formation of TiO_2-SiO_2 core-shell nanoparticles by combustion of *in situ* functionalized TiO_2 nanoparticles with silane coupling agents.

SiO_2 layer was formed due to the combustion of the silane coupling agents resulting in TiO_2-SiO_2 core-shell nanoparticles. The TiO_2-SiO_2 system does not form solid solution at any composition below 700 °C [304, 305] thus the SiO_2 layer inhibits the surface diffusion of titanium during the heat treatment, as pure TiO_2 showed coarsening and partial phase transition from mixture of brookite and anatase to rutile and anatase. Because the growth of the particles is inhibited, the anatase to rutile phase transition does not take place. Inhibited and retarded phase transition by reduced crystallite growth in mixtures of TiO_2 and SiO_2 have previously been observed [306, 307].

SiO_2-TiO_2 mixtures can be used for tuning the photocatalytic properties of TiO_2 based materials [308-314] or for wastewater treatment [315]. In the case described here, a thin amorphous SiO_2 layer was formed at the surface of the anatase nanoparticles. This type of structures have been shown to be of interest for potential application for dye-sensitized solar cells [316, 317] or for photocatalytic degradation [318, 319]. This two-step process has the advantage of maintaining nanosized samples (thus high specific surface area), anatase polymorph, and high crystallinity, which have been shown to be of interest for good photocatalytic properties of TiO_2 [87, 88, 320].

4.3. Effect of pH and precursor ratios

In this chapter, the conditions that favor or suppress the formation of the rod-like nanoparticles and the *in situ* functionalization of the TiO_2 nanoparticles with 3-aminopropyltriethoxysilane (APTES) are investigated. The initial pH and the precursor ratios were varied during the synthesis, and the time of the synthesis was kept constant (120 min). The samples TiO_2 and 10:1 are reproductions of the synthesis of TiO_2 and Ti-APTES, respectively, described in Chapter 4.1.

Samples labelled 10:1 and 15:1 were synthesized with TIP/APTES molar ratios of 10:1 and 15:1, respectively, and samples labelled with "-A" and "-B" suffix were synthesized under acidic (pH ≈ 2) and basic (pH ≈ 10) conditions, respectively. The pH of the synthesis of references samples (TiO_2, 10:1, and 15:1) was not changed.

4.3.1. Results

XRD patterns and Rietveld refinements of pure TiO_2 synthesized at different pH are displayed in Figure 4.17a. The pH has negligible effect on the crystallite sizes, and the crystallite sizes calculated from the diffractograms (d_{XRD}) were about 5-6 nm (Table 4.4). However, the pH has an effect on the phase composition. The three samples are mainly anatase with 28, 22 and 14 wt.% of brookite under acidic, neutral, and basic reaction conditions, respectively. In the case of the *in situ* functionalized nanoparticles, for all pH and both TIP/APTES molar ratios, the samples are all pure anatase (Figure 4.17b-c). The XRD patterns of the functionalized samples show narrower Bragg reflections compared to pure TiO_2 samples, especially for basic reaction conditions, resulting in larger average crystallite sizes as the pH was increased (Table 4.4). For these samples, implementing the correction for the anisotropic peak broadening was necessary in order to obtain the best fits.

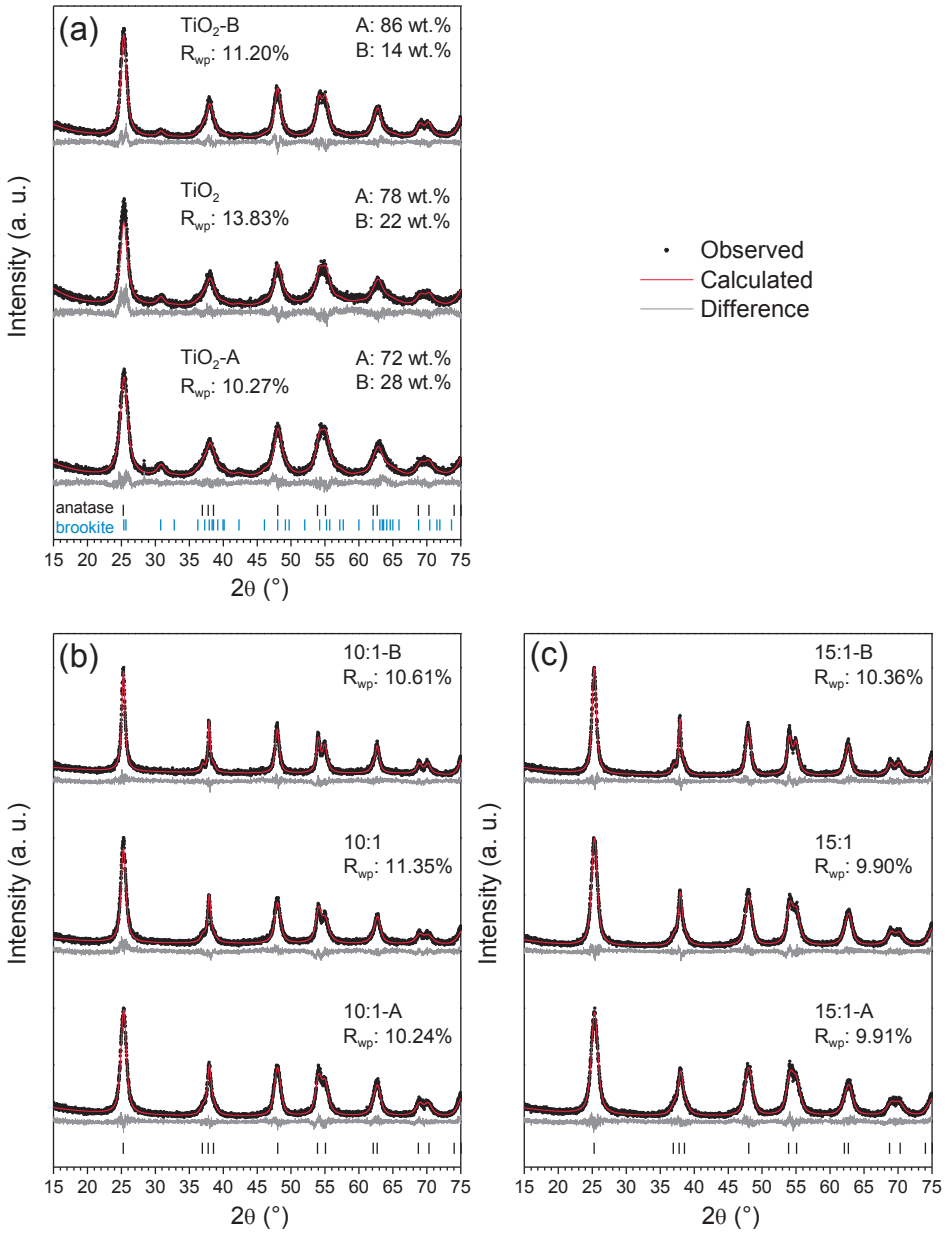

Figure 4.17. Normalized XRD patterns (λ = 1.5406 Å) and Rietveld profiles of (a) TiO_2 (A: anatase, B: brookite), (b) 10:1, and (c) 15:1 samples synthesized at different pH. Refinement of the diffractograms in (b) and (c) included the correction for anisotropic peak broadening. The vertical bars show diffraction lines of anatase from ICDD card #00-021-1272 and brookite from ICDD card #00-029-1360.

Table 4.4. Characteristics of TiO_2 and *in situ* surface-functionalized TiO_2 nanoparticles with APTES, synthesized at different pH; from nitrogen adsorption, XRD, SEM, and TGA analysis.

Sample	S_{BET}[a] ($m^2\ g^{-1}$)	d_{BET}[b] (nm)	d_{BJH}[c] (nm)	d_{XRD}[d] (nm)	d_{SEM}[e] (nm)	m_{loss}[f] (%)	S_{cov}[g] (nm^{-2})
TiO_2-A	203 ± 1	7.6 ± 0.1	7.3 ± 0.1	4.6 ± 0.1	7.9 ± 0.6	n/a	n/a
TiO_2	171 ± 1	9.0 ± 0.1	7.3 ± 0.1	4.8 ± 0.1	9.3 ± 0.1	n/a	n/a
TiO_2-B	158 ± 1	9.7 ± 0.1	5.7 ± 0.1	6.1 ± 0.1	9.1 ± 0.6	n/a	n/a
10:1-A	177 ± 1	8.7 ± 0.1	14.6 ± 0.1	5.9 ± 0.2	8.3 ± 0.5	5.0 ± 0.5	2.9 ± 0.3
10:1	213 ± 1	7.2 ± 0.1	11.3 ± 0.1	5.4 ± 0.1	11.6 ± 1.0	8.2 ± 0.5	4.0 ± 0.3
10:1-B	243 ± 1	6.3 ± 0.1	6.6 ± 0.1	8.4 ± 0.1	13.7 ± 3.0	7.0 ± 0.5	3.0 ± 0.2
15:1-A	190 ± 1	8.1 ± 0.1	6.6 ± 0.1	4.9 ± 0.1	10.0 ± 0.9	3.4 ± 0.5	1.9 ± 0.3
15:1	182 ± 1	8.5 ± 0.1	5.5 ± 0.1	5.5 ± 0.1	12.2 ± 1.2	6.0 ± 0.5	3.4 ± 0.3
15:1-B	183 ± 1	8.4 ± 0.1	8.0 ± 0.1	7.4 ± 0.1	10.5 ± 0.7	5.1 ± 0.5	2.9 ± 0.3

[a] BET specific surface area from nitrogen adsorption measurements.
[b] Particle size estimated from BET specific surface area.
[c] Average pore diameter from BJH desorption calculations.
[d] Average crystallite size from Rietveld refinement of XRD measurements.
[e] Particle size from SEM observations.
[f] Organic mass loss from TGA measurements.
[g] Surface coverage calculated from TGA and nitrogen adsorption measurements.

Figure 4.18 shows the pH dependence of the crystallite size from the Rietveld refinements along the *a*- and *c*-axes of anatase and the size anisotropy of the samples *in situ* functionalized with APTES. For both TIP/APTES ratios, the crystallite sizes in both directions as well as the size anisotropy increase as the pH of reaction was increased. The crystallite sizes and the size anisotropy of the 10:1 samples are larger than for the 15:1 samples, at any pH condition. The large uncertainty of the size anisotropy for the 15:1-A samples is due the similar values of $size_a$ and $size_c$, in addition to uncertainty of $size_c$ value.

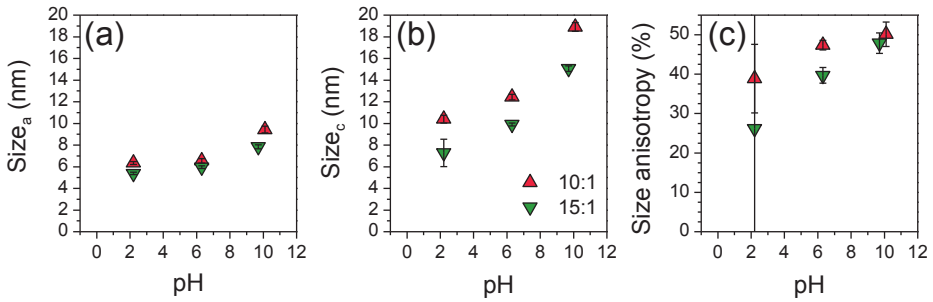

Figure 4.18. Crystallite sizes along the (a) *a*-axis and (b) *c*-axis, and (c) size anisotropy (defined as ($size_c$ − $size_a$) / $size_c$) evolution as a function of the pH of the synthesis of 10:1 and 15:1 samples.

SEM images of the samples are displayed in Figure 4.19 and the average particle sizes measured from these images (d_{SEM}) are included in Table 4.4. The non-functionalized samples consist of particles with a size of about 10 nm. Significantly larger rod-like particles with lengths from 50 to 200 nm were formed for samples functionalized with APTES, in addition to spherical nanoparticles, resulting in an average size larger than for pure TiO_2, at the same pH conditions. As a general trend, higher amount of APTES (10:1 samples) and higher values of pH resulted in the formation of more and larger rod-like nanoparticles. Oppositely, the lowest anisotropy was obtained when lowering the pH and reducing the amount of APTES. Sample 10:1-B consists of the largest and highest number of rod-like nanoparticles (Figure 4.19f), which was further investigated by TEM (Figure 4.20).

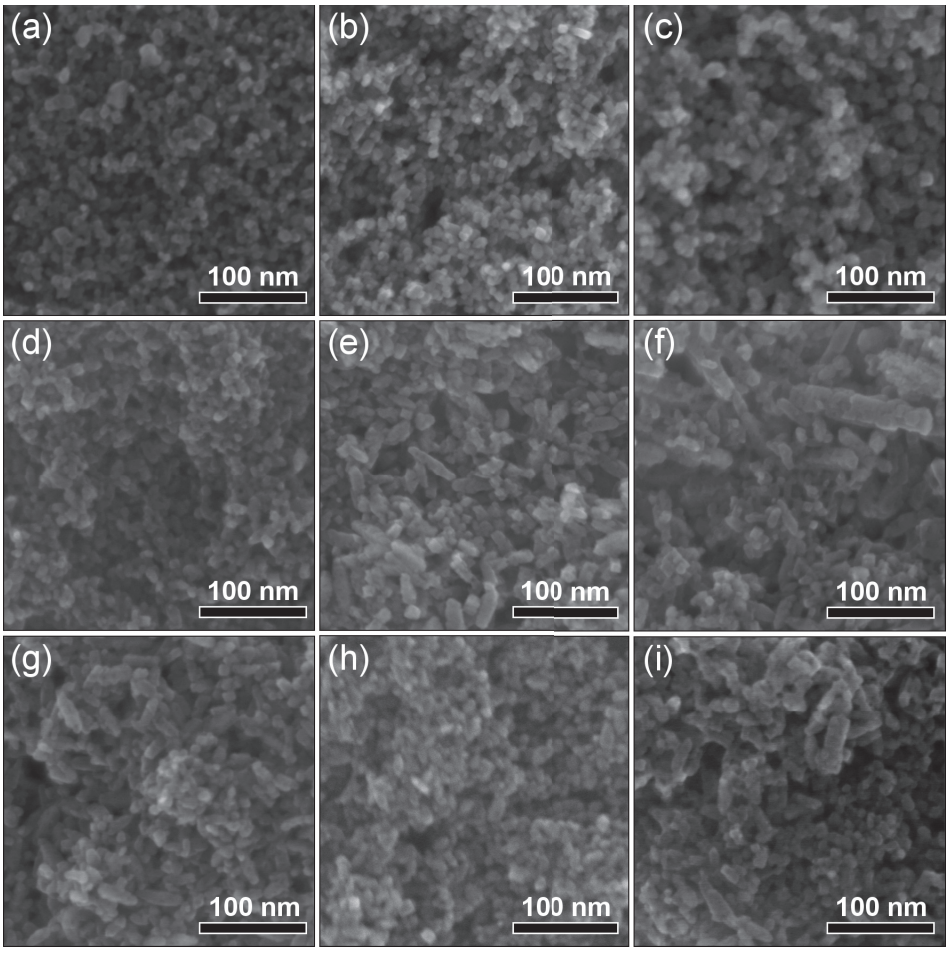

Figure 4.19. SEM images of (a) TiO_2-A, (b) TiO_2, (c) TiO_2-B, (d) 10:1-A, (e) 10:1, (f) 10:1-B, (g) 15:1-A, (h) 15:1, and (i) 15:1-B samples.

Figure 4.20a shows a TEM image of the 10:1-B sample, confirming the large number of rod-like nanoparticles and Figure 4.20b displays electron diffraction pattern of the sample which is pure anatase. HR-TEM images of selected rod-like nanoparticles from the 10:1-B sample are displayed in Figure 4.20c-d. The rod-like nanoparticles are single crystals and from the fast Fourier transform analysis (insets), the nanoparticles are elongated along the [001] direction of anatase. From the shape of the particle shown Figure 4.20c, it is likely that at least two individual crystals have merged via oriented attachment mechanism, since the curved surface at the center of the particle would be energetically unfavored by conventional growth mechanism. The rod-like nanoparticles exhibit partial faceting where {101} facets

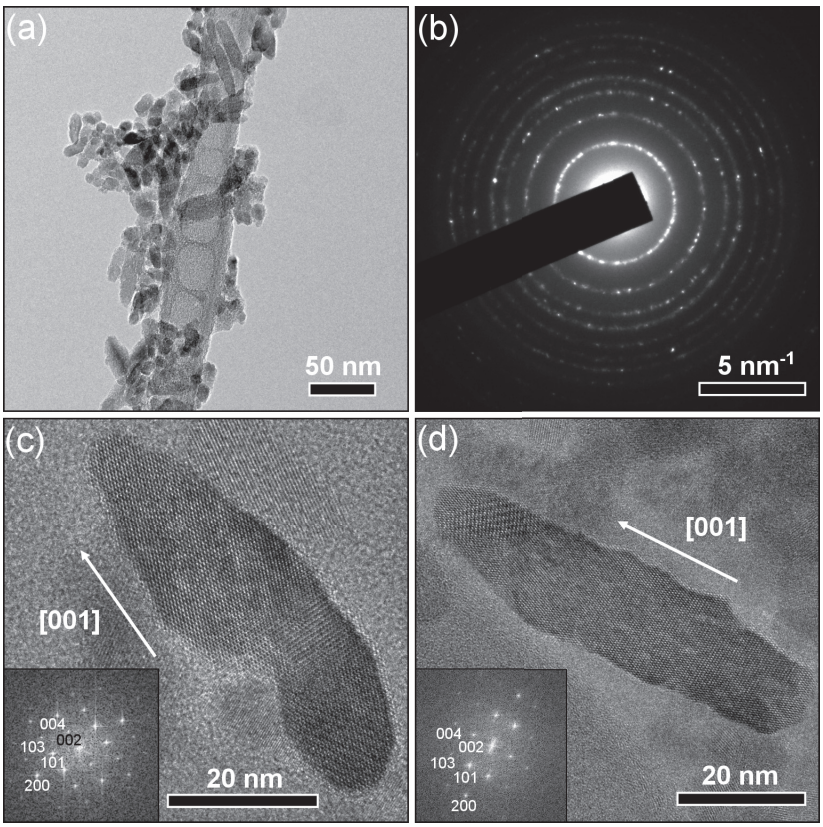

Figure 4.20. TEM images of 10:1-B sample: (a) overview, (b) electron diffraction pattern assigned to anatase, (c) a rod-like nanoparticle formed from attached nanoparticles, and (d) a rod-like nanoparticle. Insets show fast Fourier transform of a selected area within the particle.

can be distinguished at the extremities of the particles, but much more rough surfaces at the center of the particles are also visible (Figure 4.20d).

Adsorption and desorption isotherms and pore size distribution from nitrogen adsorption analysis are presented in Figure 4.21a and b, respectively. Specific surface area (S_{BET}) and particle size calculated from BET specific surface area (d_{BET}), as well as average pore size distribution from the desorption curve (d_{BJH}) are included in Table 4.4. As described in Chapter 4.1, hysteresis in the adsorption-desorption isotherms similar to mesoporous materials are visible for all samples and the porosity is correlated with the particle sizes. For pure TiO_2, the maximum of the pore volume is slightly shifted toward higher pore sizes when the pH was increased (from 4 to 6 nm) and the profile of the pore size distribution is similar,

indicating similar particles, as observed in the SEM images (Figure 4.19a-c). For the functionalized nanoparticles, the maximum of the pore volume broadens and shifts toward larger pores sizes (about 15 nm and 10 nm for 10:1-B and 15:1-B samples, respectively) with increasing pH. Similar to the SEM observations, this analysis also shows an increase in the size of the nanoparticles and a direct effect of the pH.

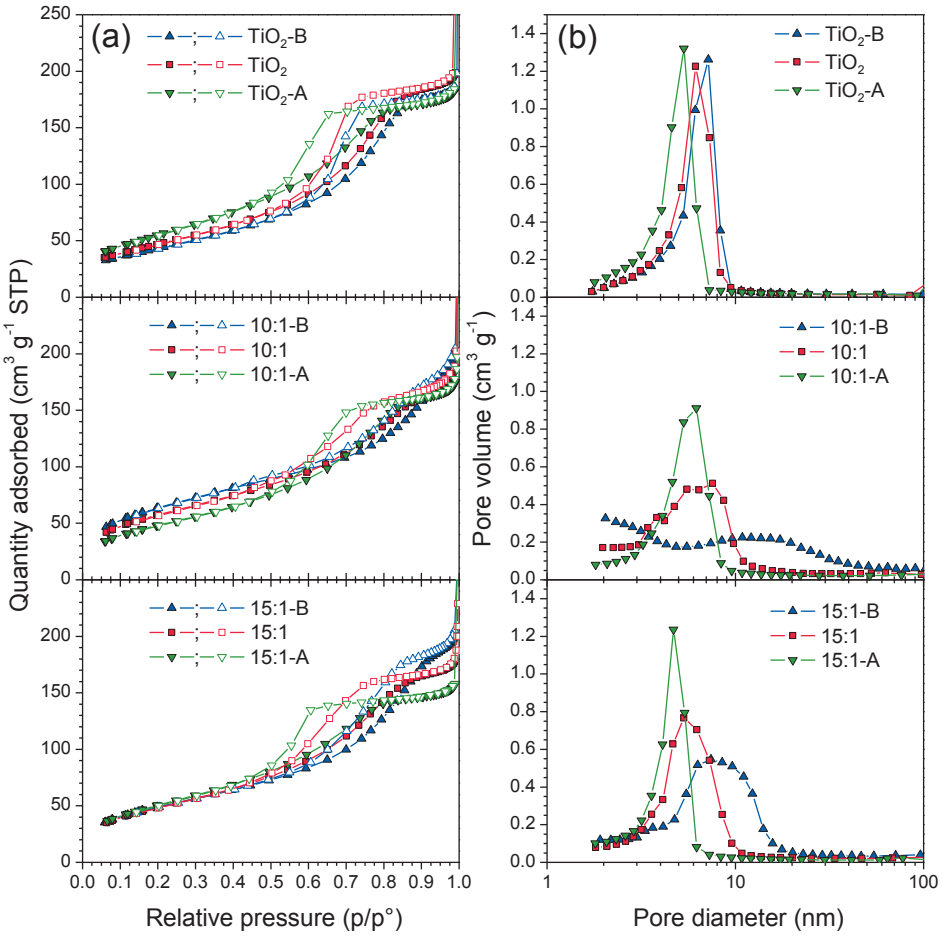

Figure 4.21. (a) Adsorption (solid symbols) and desorption (open symbols) isotherms and (b) BJH pore size distribution, from nitrogen adsorption measurements, of TiO_2 and *in situ* surface-functionalized TiO_2 nanoparticles with APTES, synthesized at different pH and TIP/APTES molar ratios.

The increased mass loss during TGA analysis from 230 to 460 °C (Figure 4.22a) is assigned to the combustion of the organics (m_{loss}) from the surface of the nanoparticles (Table 4.4). The estimated surface coverage (S_{cov}) based on the mass loss and the specific surface area, included Table 4.4, is ranging from 1.9 to 4.0 silane nm^{-2}. The mass loss is lower for the samples with 15:1 compared to 10:1 molar ratio (TIP/APTES), as expected from the initial formulations. The samples prepared under acidic reaction conditions show a smaller mass loss, while basic reaction conditions give a mass loss similar to the one of the samples for which the pH was not altered. From the FTIR spectra (Figure 4.22b), the presence of Si−O−Si bonds, due to hydrolysis and condensation of APTES on the surface of the nanoparticles is confirmed by the absorption at 1020 and 1120 cm^{-1}. Covalent bonding of APTES to the surface of the nanoparticles is demonstrated by the formation of Ti−O−Si bonds (900 cm^{-1}). In addition, the other absorptions due to APTES and TiO_2 are also present and are listed in Table 4.5. No amorphous coating was observed from the TEM analysis (Figure 4.20c-d and Figure 4.23a-c) because of carbon contamination from the TEM grid and/or optical aberrations, confirming the nanometric nature of the functionalization layer in the case of the 10:1-B sample. Additionally, EDS analysis (Figure 4.23d) also confirms the presence of APTES, mainly by the silicon signal at about 1.75 keV.

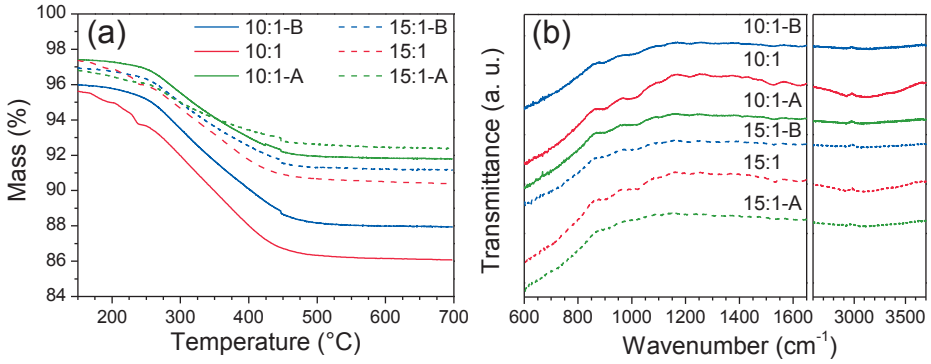

Figure 4.22. (a) TGA curves and (b) FTIR spectra of *in situ* surface-functionalized TiO_2 nanoparticles with APTES, synthesized at different pH and TIP/APTES molar ratios.

Table 4.5. Assignments of characteristic IR bands of *in situ* surface-functionalized TiO_2 nanoparticles with APTES, synthesized at different pH and TIP/APTES molar ratios.

Wavenumber (cm^{-1})	Assignment	Reference
< 900	Ti−O−Ti	[198, 205, 211, 295, 296]
900	Ti−O−Si	[197, 198, 205, 211, 295, 297]
1020 and 1120	Si−O−Si	[196-198, 205, 211, 297, 298]
1220	$Si-CH_2R$	[295, 297, 298]
1460 (very weak)	CH_2 (bend)	[204, 295, 298]
1530 and 3200-3500 (very weak)	N−H	[198, 204, 295, 298]
1640 and 2500-3600	Adsorbed H_2O and −OH groups	[196, 198, 295, 298]
2850 and 2920 (very weak)	CH_2 (stretch)	[198, 199, 205, 295, 298]

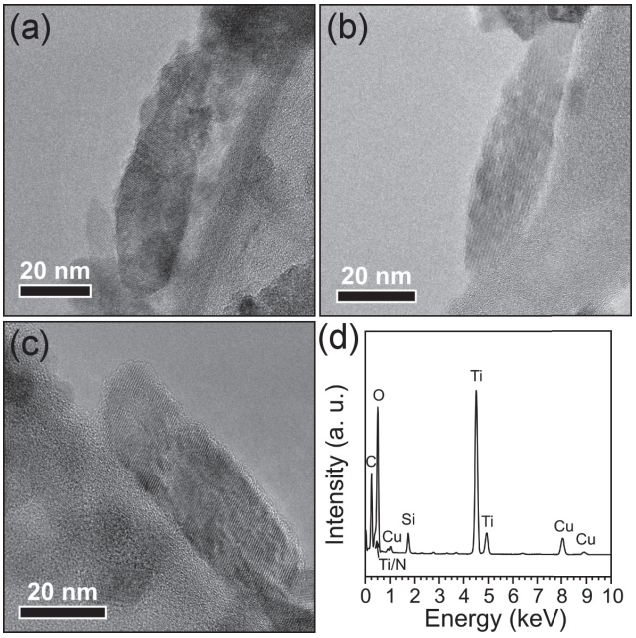

Figure 4.23. TEM images of the 10:1-B sample (a-c) HR-TEM images of [001] oriented rod-like nanoparticles and (d) EDS spectrum over a representative area.

4.3.2. Discussion

4.3.2.1. Pure TiO_2

For pure TiO_2 the amount of brookite is reduced with increased pH, as previously observed [121, 145]. From the SEM images and the pore size distribution profiles (Figure 4.19a-c and Figure 4.21b) the morphology and the size of the nanoparticles was almost unaffected by the variations of pH (Table 4.4), in contrast to previous hydrothermal studies where a strong dependence of the particle morphologies with the pH was reported [93, 293]. In these reports, increased pH led to elongated nanoparticles, perhaps because different synthesis procedures (titanium precursor and/or additive) were used.

4.3.2.2. *In situ* functionalized TiO_2 with APTES

All the *in situ* functionalized nanoparticles with APTES are pure anatase. An increased amount of silane coupling agent and increased pH result in more and larger rod-like nanoparticles. From the TEM analysis (Figure 4.20 and Figure 4.23), correction for anisotropic peak broadening of the XRD profiles (Figure 4.17), and the refined crystallite sizes (Figure 4.18), the elongation of the particles is confirmed in majority along the [001] direction of anatase. The particle size from BET shows the opposite trend compared to particle size from SEM images (Table 4.4). Since a sample with proportionally more rod-like nanoparticles would be expected to have a lower specific surface area (larger average particle size), this observation could be assigned to a different degree of agglomeration of the particles in these samples.

From the samples synthesized under acidic conditions (10:1-A and 15:1-A), significantly lower mass loss was measured and a lower surface coverage was calculated (Table 4.4), as well as a lower relative intensity of the bands attributed to APTES in the IR spectra (Figure 4.22b). These results show that grafting of the nanoparticles is less efficient under acidic conditions. At elevated pH and after hydrolysis, the APTES molecules are more likely to be deprotonated [29] and would thus repulse each other and react more easily on the surface of the growing titanium dioxide nanoparticles, resulting in higher surface coverage at pH close to neutral conditions and under basic conditions. Under acidic conditions, APTES molecules

are more likely to self-condensate in higher proportions than under neutral and basic conditions, resulting in siloxane or silica-like nanoparticles that are probably eliminated during the nanoparticles separation steps. The self-condensation results in lower grafting efficiency of the TiO_2 nanoparticles. As the grafting efficiency is reduced, the number of rod-like nanoparticles is also reduced, demonstrating the role of APTES in the formation of the elongated nanoparticles. This is also confirmed by the effect of reducing the APTES amount (15:1 samples), where smaller crystallite size and anisotropy were measured (Table 4.3 and Figure 4.18), as well as via SEM and nitrogen adsorption analysis (Figure 4.19 and Figure 4.21).

To summarize, a high APTES amount and a high pH will lead towards a larger fraction and longer rod-like nanoparticles. Lowering the pH of the synthesis reduces the grafting efficiency, leading to more spherically shaped nanoparticles. The initial amount of APTES and pH are key parameters to control surface coverage and morphology of the nanoparticles, and by adjusting these values, one could design synthesis of organic-functionalized inorganic nanoparticles with desired morphology, size distribution, and surface coverage.

The anisotropic size broadening of the XRD patterns is an efficient way to follow the formation of the [001] oriented rod-like nanostructures which can allow for *in situ* studies of the anisotropic growth, and is described further in Chapter 4.4.

4.4. *In situ* synchrotron XRD and growth kinetics

In this chapter, the effect of the time on the synthesis of TiO_2 nanoparticles *in situ* functionalized with 3-aminopropyltriethoxysilane (APTES) is investigated. The study is performed via the same *ex situ* techniques as previously used, and *in situ* X-ray diffraction. The goal was to determine the growth mechanism of the [001] oriented rod-like nanoparticles. The experimental studies are complemented by density functional theory (DFT) calculations to reveal the growth mechanism.

For the *ex situ* analysis, samples are labelled according to the TIP/APTES molar ratios and the suffix "-X" were X indicates the duration of the synthesis in minutes (1, 15, 30, 60, and 120 min). For example, for 10:1-120 and 15:1-120 the duration of the synthesis was 120 min and the TIP/APTES molar ratios were 10:1 and 15:1, respectively. These two samples are the same samples as 10:1 and 15:1 described in Chapter 4.3, respectively.

For the *in situ* analysis, three samples were selected. Pure TiO_2 was chosen as the reference sample. Ti-APTES (TIP/APTES molar ratio 10:1, labeled 10:1) was selected for studying the growth of the rod-like nanoparticles, and as the condition of the synthesis are the same as in pure TiO_2, they can be directly compared. The last sample is also with TIP/APTES molar ratio equal to 10:1, but the synthesis was performed under basic conditions ($pH \approx 10$, labeled 10:1-B), as it is the sample in which the largest rod-like nanoparticles were obtained *ex situ* (see Chapter 4.3), and can be compared with sample 10:1.

4.4.1. Results

4.4.1.1. *Ex situ* analysis

X-ray diffractograms and Rietveld profiles of 10:1 and 15:1 samples synthesized for different duration are displayed in Figure 4.24a and b, respectively. All the samples are pure anatase, as observed previously (see Chapters 4.1 and 4.3). The average crystallite sizes (d_{XRD}, Table 4.6) increase with the reaction time, from 2.6 to 5.4 nm and from 3.5 to 5.5 nm, for the 10:1 and the 15:1 series, respectively. The low signal-to-noise ratio in the XRD patterns recorded for the samples synthesized for 1 and 15 min implies that these samples are less crystalline than the samples synthesized for longer time.

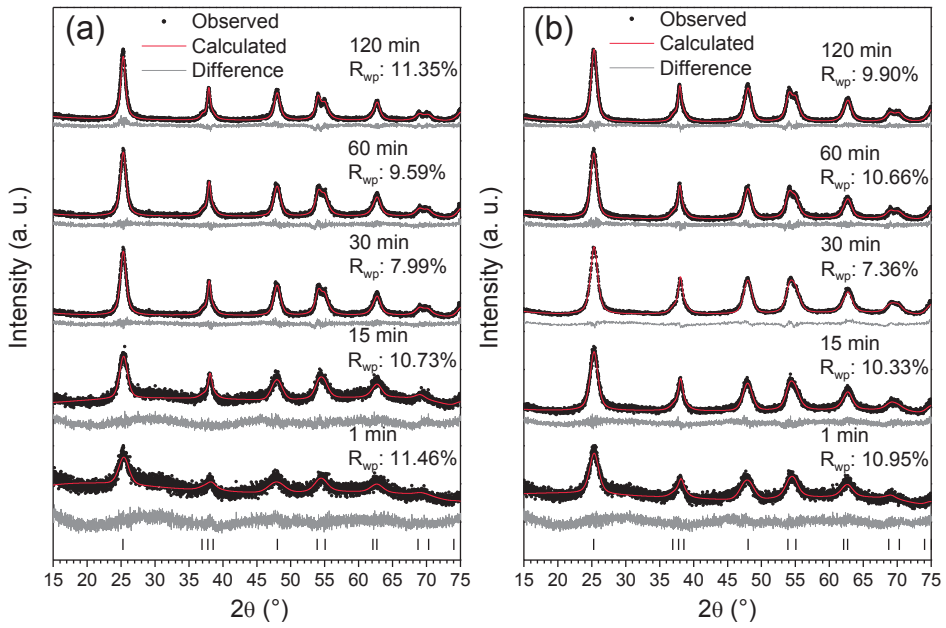

Figure 4.24. Normalized XRD patterns (λ = 1.5406 Å) and Rietveld profiles of *in situ* surface-functionalized TiO_2 nanoparticles with TIP/APTES molar ratio of (a) 10:1 and (b) 15:1, synthesized for different duration of time. All refinements included the correction for anisotropic peak broadening. The vertical bars show diffraction lines of anatase from ICDD card #00-021-1272.

Table 4.6. Characteristics of *in situ* surface-functionalized TiO_2 nanoparticles with TIP/APTES molar ratio of 10:1 and 15:1, synthesized for different duration of time, from nitrogen adsorption, XRD, SEM, and TGA analysis.

Sample	S_{BET}[a] ($m^2\ g^{-1}$)	d_{BET}[b] (nm)	d_{BJH}[c] (nm)	d_{XRD}[d] (nm)	d_{SEM}[e] (nm)	m_{loss}[f] (%)	S_{cov}[g] (nm^{-2})
10:1-1	314 ± 2	4.9 ± 0.1	11.7 ± 0.1	2.6 ± 0.1	7.2 ± 0.2	6.7 ± 0.5	2.2 ± 0.2
10:1-15	319 ± 1	4.8 ± 0.1	6.8 ± 0.1	4.4 ± 0.5	9.2 ± 0.8	8.7 ± 0.5	2.8 ± 0.2
10:1-30	284 ± 1	5.4 ± 0.1	9.3 ± 0.1	4.5 ± 0.4	9.9 ± 0.5	8.2 ± 0.5	3.0 ± 0.2
10:1-60	248 ± 1	6.2 ± 0.1	11.8 ± 0.1	5.3 ± 0.2	11.2 ± 0.5	9.0 ± 0.5	3.8 ± 0.2
10:1-120[h]	213 ± 1	7.2 ± 0.1	11.3 ± 0.1	5.4 ± 0.1	11.6 ± 1.0	8.2 ± 0.5	4.0 ± 0.3
15:1-1	328 ± 1	4.7 ± 0.1	9.1 ± 0.1	3.5 ± 0.2	7.3 ± 0.6	5.4 ± 0.5	1.7 ± 0.2
15:1-15	264 ± 1	5.8 ± 0.1	5.8 ± 0.1	4.1 ± 0.2	9.4 ± 0.3	6.6 ± 0.5	2.6 ± 0.2
15:1-30	235 ± 1	6.5 ± 0.1	8.1 ± 0.1	4.6 ± 0.2	10.6 ± 0.3	6.7 ± 0.5	3.0 ± 0.2
15:1-60	208 ± 1	7.4 ± 0.1	5.2 ± 0.1	4.8 ± 0.2	11.3 ± 0.7	5.8 ± 0.5	2.9 ± 0.3
15:1-120[i]	182 ± 1	8.5 ± 0.1	5.5 ± 0.1	5.5 ± 0.1	12.2 ± 1.2	6.0 ± 0.5	3.4 ± 0.3

[a] BET specific surface area from nitrogen adsorption measurements.
[b] Particle size estimated from BET specific surface area.
[c] Average pore diameter from BJH desorption calculations.
[d] Average crystallite size from Rietveld refinement of XRD measurements.
[e] Particle size from SEM observations.
[f] Organic mass loss from TGA measurements.
[g] Surface coverage calculated from TGA and nitrogen adsorption measurements.
[h] Sample 10:1 from Chapter 4.3.
[i] Sample 15:1 from Chapter 4.3.

SEM images of the samples and the measured particles size (d_{SEM}) are given in Figure 4.25 and Table 4.6, respectively. Similar to the previous trend observed for the crystallite sizes, the average measured size increases as a function of the increasing synthesis time, from 7.2 to 11.6 nm and from 7.3 to 12.2 nm, for 10:1 and the 15:1 series, respectively. At longer reaction time, as the samples are mixtures of spheres and rods, the average size does not represent the proportion and the size of the rod-like nanoparticles, and the measured sizes are similar. However, from the SEM images, the rods are about twice as long in the 10:1 series as in the 15:1 series after 120 min of synthesis (Figure 4.25.5).

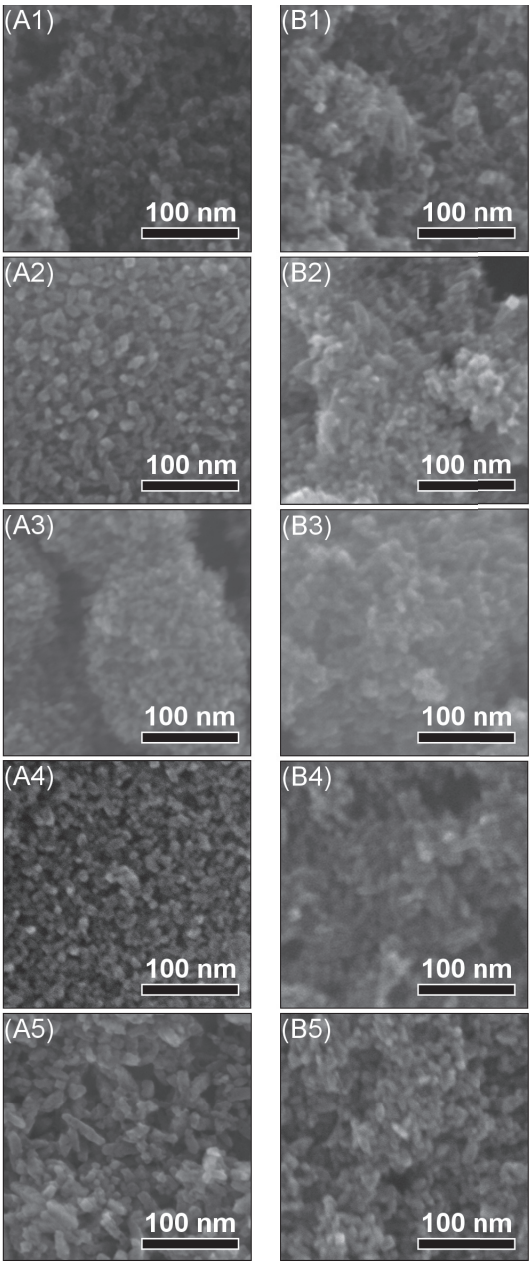

Figure 4.25. SEM images of *in situ* surface-functionalized TiO_2 nanoparticles with TIP/APTES molar ratio (A) 10:1 and (B) 15:1, synthesized for (1) 1 min, (2) 15 min, (3) 30 min, (4) 60 min, and (5) 120 min.

Adsorption and desorption isotherms (Figure 4.26a) of the functionalized nanoparticles synthesized for different reaction times show hysteresis behavior, and the pore volume revealed from the isotherms is correlated with the particle size. The specific surface area (S_{BET}), the particle size calculated from the specific surface area (d_{BET}), and the average pore diameter calculated from the desorption curves (d_{BJH}) are included in Table 4.6. For the 10:1 series, the calculated sizes are consistent with the average particle sizes obtained from the SEM images. For the 15:1 series, the average pore diameters are smaller than the particles sizes obtained from the SEM images. This could result from a larger degree of agglomeration in these samples as the amount of APTES is reduced. For both series, the pore size distribution (Figure 4.26b and d) of the nanoparticles prepared for 1 min shows a maximum at 4 nm. The maximum increases up to 8 nm and becomes broader with increasing reaction time. The pore volume at larger pore sizes (20-100 nm) decreases as the reaction time is increased. This is a different behavior compared to the previous samples, synthesized with different silane coupling agent or with APTES at different pH, where the pore volume in this pore size range was systematically negligible (see Chapters 4.1 and 4.3, respectively). This effect might result from different agglomeration states as the syntheses have reached different stages for each duration.

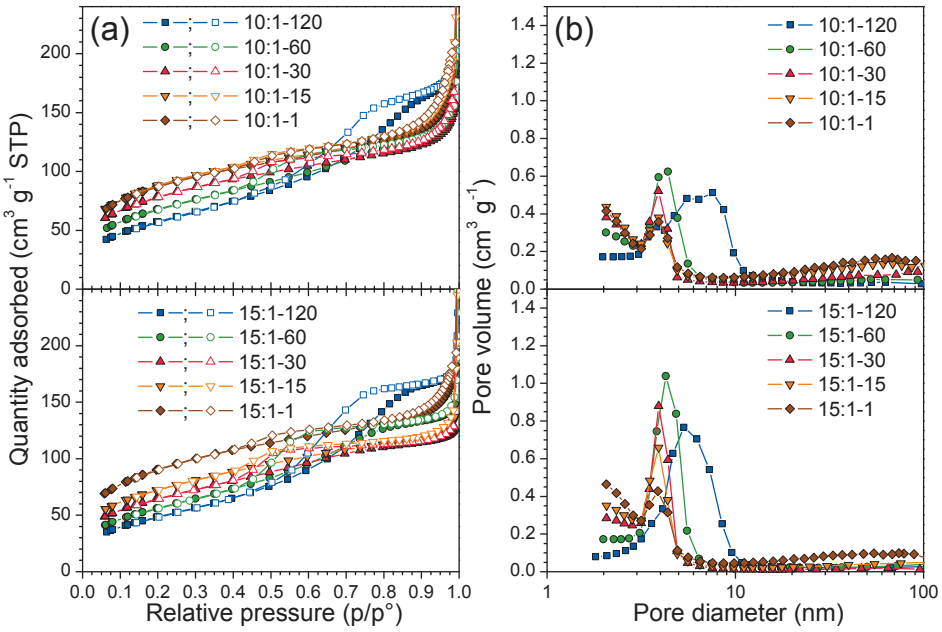

Figure 4.26. (a) Adsorption (solid symbols) and desorption (open symbols) isotherms and (b) BJH pore size distribution, from nitrogen adsorption measurements, of *in situ* surface-functionalized TiO_2 nanoparticles with TIP/APTES molar ratio of 10:1 (top) and 15:1 (bottom), synthesized for different durations of time.

TGA data for the *in situ* surface-functionalized TiO_2 nanoparticles with TIP/APTES molar ratio of 10:1 (Figure 4.27a) demonstrates larger mass loss than the 15:1 series (Figure 4.27b), as expected from the amount of organic material initially incorporated. The values of organic mass loss from 230 to 460 °C (m_{loss}) and the surface coverage (S_{cov}) are available in Table 4.6. The surface coverage is ranging from 2.2 to 4.0 silane nm^{-2} and 1.7 to 3.4 silane nm^{-2} for TIP/APTES molar ratio of 10:1 and 15:1, respectively. For both series, the surface coverage increases as the reaction time is increased. The difference in the onset of mass losses in the TGA curves (Figure 4.27a) could be due to an increased surface coverage of the nanoparticles as a function of the increasing synthesis time, resulting in a lower amount of adsorbed water initially removed during the initial heating cycles. This is also visible from the infrared spectra (Figure 4.27b and d), where the relative intensity of the bands attributed to APTES (Table 4.7) increases with longer reaction time, as well as the Ti−O−Si and Si−O−Si bands which confirm covalent bonding and cross-linking of APTES on the surface of the TiO_2 nanoparticles.

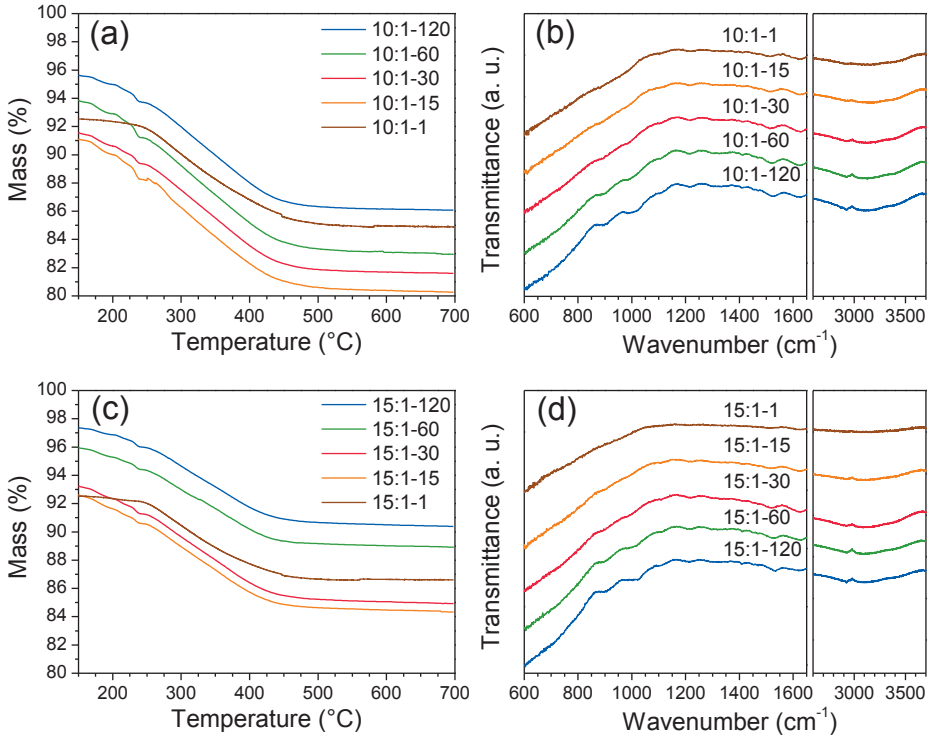

Figure 4.27. (a) TGA curves and (b) FTIR spectra of *in situ* surface-functionalized TiO_2 nanoparticles with TIP/APTES molar ratio of 10:1 (top) and 15:1 (bottom), synthesized for different durations of time.

Table 4.7. Assignments of characteristic IR bands of *in situ* surface-functionalized TiO_2 nanoparticles with APTES, synthesized for different durations of time.

Wavenumber (cm^{-1})	Assignment	Reference
< 900	Ti−O−Ti	[198, 205, 211, 295, 296]
900	Ti−O−Si	[197, 198, 205, 211, 295, 297]
1020 and 1120	Si−O−Si	[196-198, 205, 211, 297, 298]
1220	Si−CH_2R	[295, 297, 298]
1460	CH_2 (bend)	[204, 295, 298]
1530 and 3200-3500 (weak)	N−H	[198, 204, 295, 298]
1640 and 2500-3600	Adsorbed H_2O and −OH groups	[196, 198, 295, 298]
2850 and 2920 (very weak)	CH_2 (stretch)	[198, 199, 205, 295, 298]

4.4.1.2. *In situ* X-ray diffraction

Diffraction patterns and Rietveld profiles of the end-reaction products from the *in situ* XRD are displayed in Figure 4.28. The broad diffuse background (5-25°) is due to the aqueous solution in the capillary, and is more pronounced in the case of pure TiO_2 due to the relative intensity of the Bragg reflections. Both samples synthesized with APTES (Figure 4.28a-b) are pure anatase while pure TiO_2 consist of 87 wt.% of anatase and 13 wt.% of brookite, however, this value must be taken cautiously because of overlap with the solution background. The (121) diffraction line of brookite at 13.86° is slightly distinguishable. Table 4.8 summarizes the results of the Rietveld refinements of these three samples. Because of the higher resolution of the synchrotron diffraction data, the correction for the anisotropic broadening was also implemented for pure TiO_2. Similar to the *ex situ* analysis, the crystallite size and the size anisotropy calculated from the Rietveld refinements increase in the order TiO_2, 10:1, and 10:1-B. The increase in the crystallite size is also qualitatively visible from the narrower FWHM of the diffraction lines with *e.g.* the separation of (105) and (211) reflections at 23.76° and 24.24°, respectively. The higher uncertainty of the size anisotropy for pure TiO_2 is due to the similar values of the crystallite sizes along the *a*- and *c*-axes, as well as the relatively high uncertainty of the refined values.

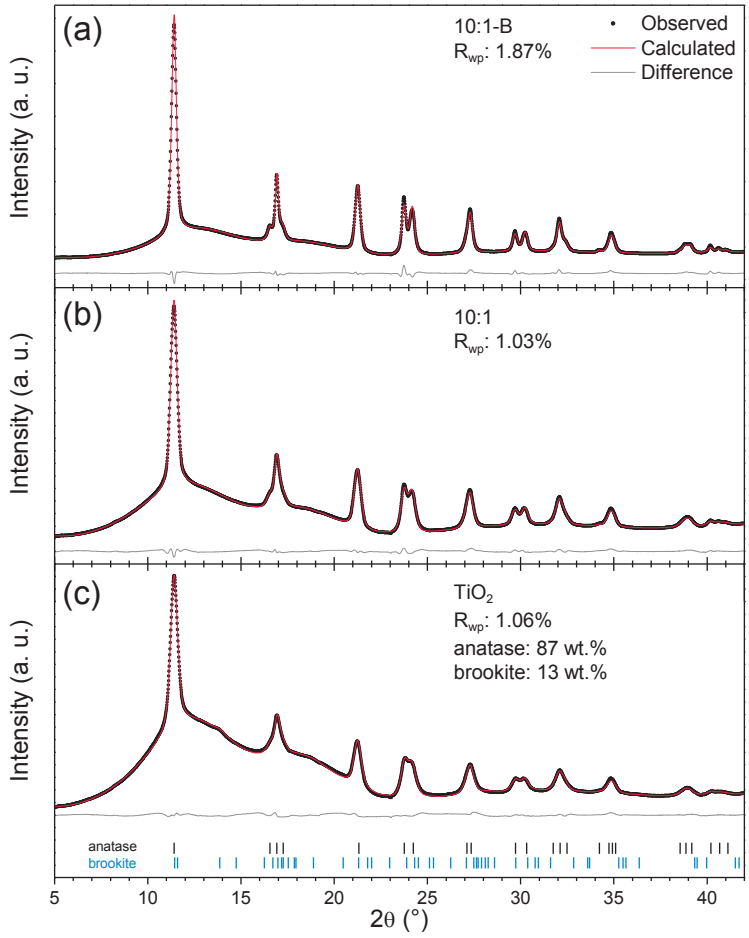

Figure 4.28. XRD patterns (λ = 0.6999 Å) and Rietveld profiles of (a) 10:1-B, (b) 10:1, and (c) TiO_2 samples collected *in situ* and at room temperature, after the reaction was completed. All refinements included the correction for anisotropic peak broadening. The vertical bars show diffraction lines of anatase from ICDD card #00-021-1272 and brookite from ICDD card #00-029-1360.

Table 4.8. Results of Rietveld refinements of long exposure diffractograms of the end-reaction products (anatase TiO_2) collected *in situ* at room temperature (Figure 4.28).

Sample	Duration of reaction (h)	R_{wp} (%)	Lattice parameters (Å)		Crystallite sizes (nm)			Size anisotropy (%)
			a	*c*	Avg. size	$Size_a$	$Size_c$	
TiO_2	1.75	1.06	3.7991(3)	9.5130(9)	6.28(15)	6.29(12)	7.29(22)	14 ± 7
10:1	1.58	1.03	3.7977(2)	9.5204(5)	7.44(11)	7.22(9)	9.11(17)	21 ± 2
10:1-B	9[a]	1.87	3.7969(1)	9.5236(4)	10.20(14)	9.52(12)	14.11(27)	32 ± 1

[a] Limited evolution after about 100 min of reaction.

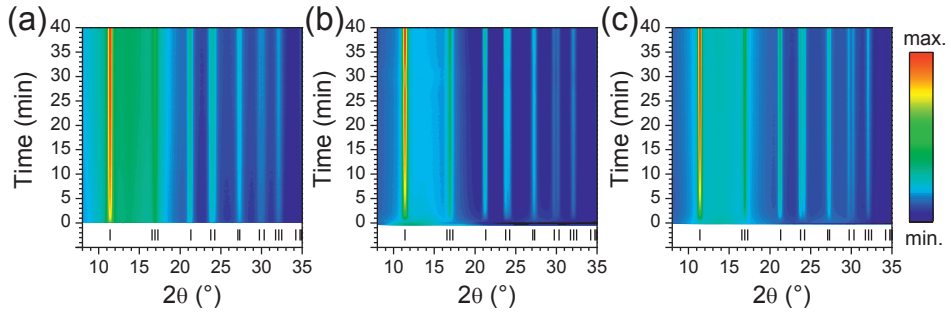

Figure 4.29. Time-resolved XRD contour plot (λ = 0.6999 Å) of (a) TiO_2, (b) 10:1, and (c) 10:1-B samples collected during the syntheses at 213 °C and 250 bar. The color scale represents the intensity and the vertical bars show diffraction lines of anatase from ICDD card #00-021-1272.

The XRD contour plots of the first 40 min of the reactions of pure TiO_2, 10:1, and 10:1-B are displayed Figure 4.29. The nucleation of anatase occurs within tens of second after the initial heating, and without the formation of any intermediate phase. The peak broadening is the largest for pure TiO_2 indicating the smallest crystallite sizes (Figure 4.29a), then follows 10:1 (Figure 4.29b), and the narrowest peaks are observed for 10:1-B (Figure 4.29c).

The reduction of the peak broadening is easier to visualize in Figure 4.30 which displays the initial 15 min evolutions of the (004) and (200) reflections of anatase for the three experiments. Figure 4.30 also shows the anisotropic growth of the nanocrystals when APTES was introduced. The FWHM of the (200) and (004) reflections are linked to the *a*- and *c*-directions, respectively. The relative FWHM of the (004) diffraction line (Figure 4.30a) becomes much smaller when the synthesis are performed with APTES, and even narrower under basic conditions (samples 10:1 and 10:1-B) compared to the (200) (Figure 4.30b), indicating increased anisotropy along the [001] direction in the 10:1, and even more in the 10:1-B samples. This is consistent with previous *ex situ* HR-TEM analysis, where the formation of [001] oriented rod-like nanoparticles was observed in both cases, with larger rod-like nanoparticles under basic conditions (see Figure 4.4c in Chapter 4.1 and Figure 4.23 in Chapter 4.3, for HR-TEM images of 10:1 and 10:1-B samples, respectively).

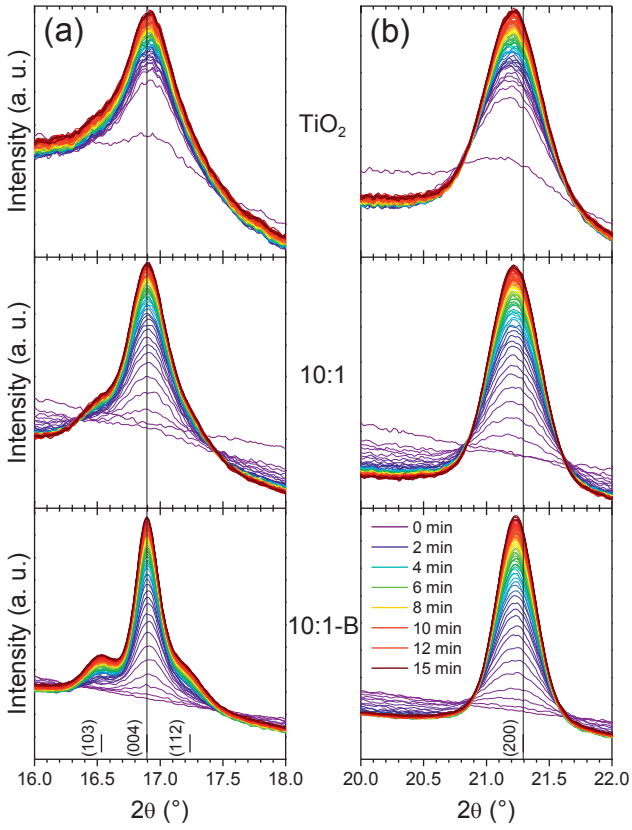

Figure 4.30. (a) (004) and (b) (200) diffraction lines ($\lambda = 0.6999$ Å) evolution during the first 15 min of the hydrothermal synthesis of TiO_2 (top), 10:1 (middle), and 10:1-B (bottom) samples. The vertical bars show calculated diffraction line positions of anatase at 213 °C.

In order to quantify the size anisotropy and its time dependence, batch Rietveld refinement was performed on all the frames from the *in situ* synchrotron XRD data, including the model that takes into account the anisotropic peak broadening. Selected diffractograms and Rietveld profiles at different synthesis time are represented in Figure 4.31, showing good fitting of the data, for any given sample and/or synthesis time.

According to *ex situ* analysis (see Chapters 4.1 and 4.3), the samples synthesized with APTES contain both spherical and elongated nanoparticles, thus it must be noted that the refined crystallite sizes and the size anisotropy reflect their average contributions.

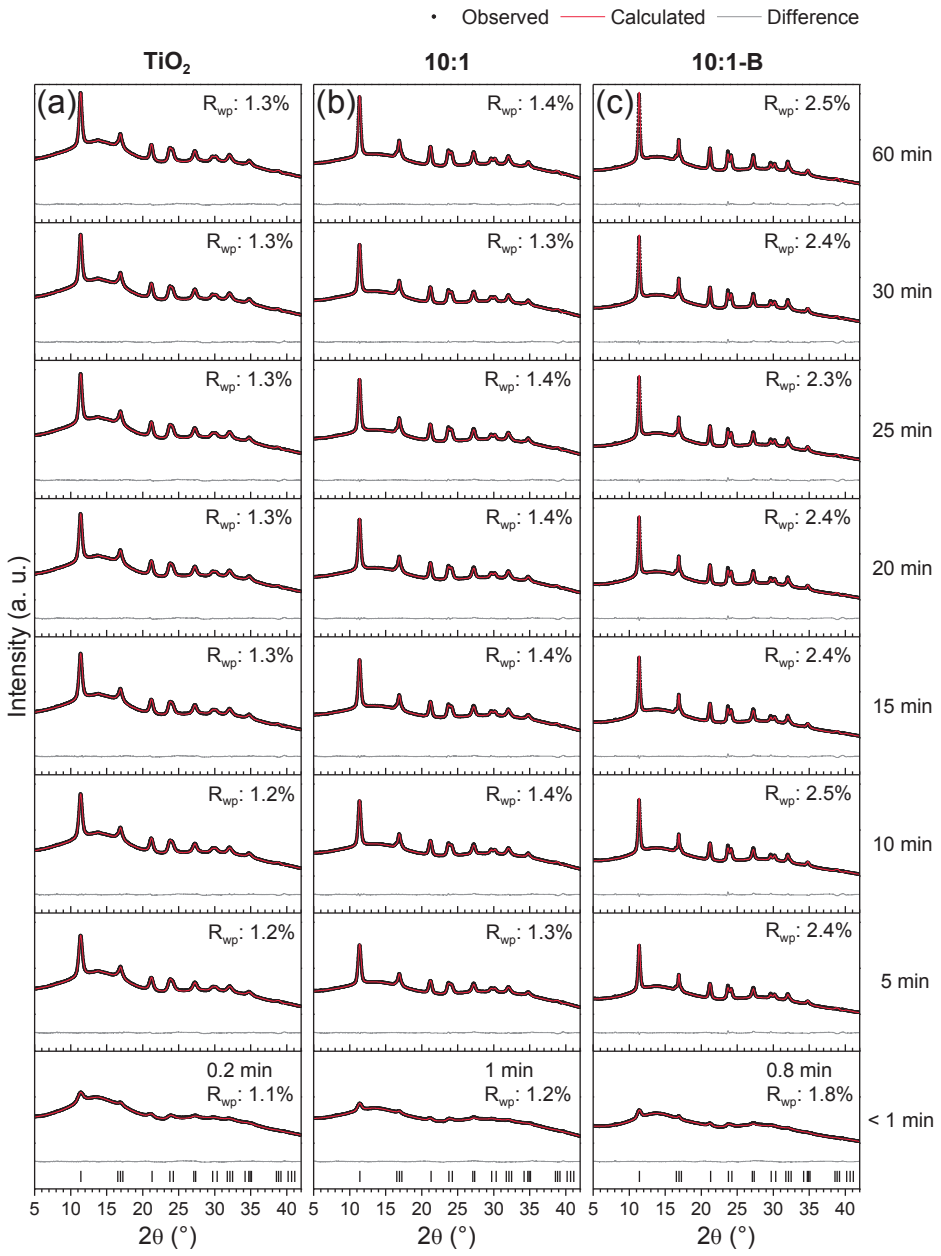

Figure 4.31. Examples of Rietveld refinement profiles (λ = 0.6999 Å) of (a) TiO_2, (b) 10:1, and (c) 10:1-B samples obtained from *in situ* XRD, at different duration of the synthesis. All the *in situ* XRD refinements included the correction for anisotropic peak broadening. The vertical bars show diffraction lines of anatase from ICDD card #00-021-1272.

4.4.1.3. Refined crystal parameters

Figure 4.32 shows the anatase crystallite sizes along the *a*- and *c*-axes and the size anisotropy from the Rietveld refinement of *in situ* and *ex situ* XRD, as a function of the time of the synthesis. Along the *a*-axis (Figure 4.32a and d), the crystal nucleation occurs rapidly and the crystallite size increases rapidly during the first few minutes. The initial crystallite size is about 4-5 nm for all samples, and increases more in the case of functionalization with APTES, especially under basic conditions. Then, the crystallite size increase with a lower and similar rate all along the rest of the experiments. The size difference is more noticeable along the *c*-axis (Figure 4.32b and e), where APTES and basic conditions give the highest crystallite sizes. The crystallite size along the *c*-axis increases steadily for pure TiO_2. However, when APTES was introduced (Figure 4.32b) slower growth is observed after about 5 min of reaction, defining two different growth regimes. Thus, the size anisotropy (Figure 4.32c) is evident from the initial moment of the reaction, reaches a maximum of 38 and 26 % for 10:1-B and 10:1, respectively, and decreases constantly to the values reported in Table 4.8, at the end of the recorded time. Similar trends are observed for the *ex situ* analysis (Figure 4.32d-f), but the anisotropy is larger (up to 48 %) even though the pH was not modified. The size anisotropy is more pronounced in the case of the 10:1 series than for the 15:1 series, as observed in Chapter 4.3.

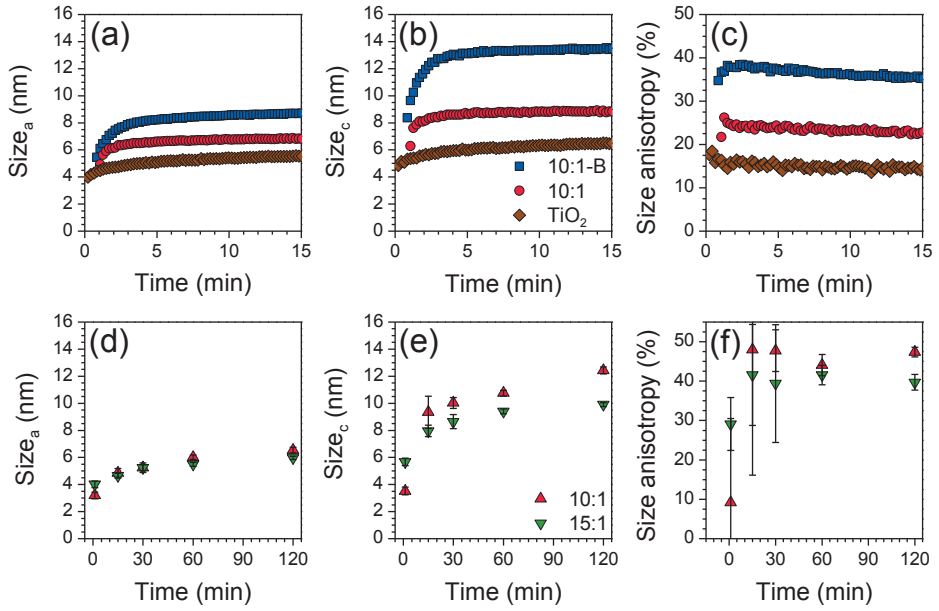

Figure 4.32. Time evolution of the anatase crystallite sizes along the (a) *a*- and (b) *c*-axes, and (c) size anisotropy (defined as ($size_c - size_a$) / $size_c$) from *in situ* XRD; time evolution of the anatase crystallites sizes along the (d) *a*-axis and (e) *c*-axis, and (f) size anisotropy from *ex situ* XRD.

The time evolution of the anatase cell parameters is reported Figure 4.33. For the *in situ* analysis, the *a*-parameter (Figure 4.33a) converges rapidly to 3.802 Å (slightly above for pure TiO_2), via expansion (10:1 sample) and contraction (TiO_2 and 10:1-B samples). For all samples, the *c*-parameter (Figure 4.33b) increases, but remains well below the calculated bulk value at 213 °C for pure TiO_2, and it converges rapidly to values above the reference for *in situ* functionalized samples (9.535 Å and 9.539 Å for 10:1 and 10:1-B samples, respectively). The divergence of the cell parameters from the calculated bulk values is also visible from the shifting of the positions of the (004) and (200) Bragg reflections (Figure 4.30), being directly related to the *c*-parameter and the *a*-parameter of anatase, respectively. Similar evolution were also observed in previous *in situ* hydrothermal study of pure TiO_2, where the *a*-parameter showed either increase or decrease, and the *c*-parameter often showed increase, during the initial period of the synthesis [321, 322]. These observations are different from the *ex situ* measurements where the *a*-parameter (Figure 4.33d) converges

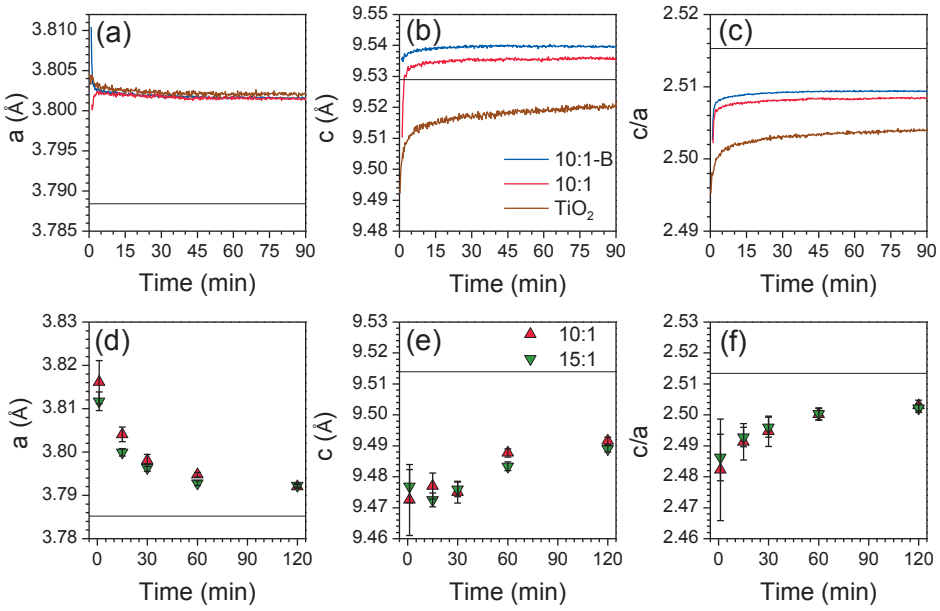

Figure 4.33. Time evolution of the anatase (a) *a*-parameter, (b) *c*-parameter, and (c) *c*/*a* from *in situ* XRD; time evolution of the anatase (d) *a*-parameter, (e) *c*-parameter, and (f) *c*/*a* from *ex situ* XRD. Horizontal lines show bulk references of anatase, calculated at 213 °C in the case of *in situ* XRD.

slowly to the bulk value (at room temperature) via contraction. The unit cell along the *c*-parameter (Figure 4.33e) expands as well, but remains well below the bulk value, for both TIP/APTES molar ratios. Previous *ex situ* studies have shown both expansion [323] and contraction [25] along the *a*-parameter, and, in both cases, expansion along the *c*-parameter, as a function of the crystallite size. However, in both *in situ* and *ex situ* analysis, the *c*/*a* ratios (Figure 4.33c and f) show similar trend, increasing and stabilizing at values below the values of the bulk phase.

4.4.1.4. Density functional theory

In order to study the effect on APTES functionalization on the particle equilibrium shape, density functional theory (DFT) calculations were performed on the common surfaces of anatase TiO_2, to calculate the difference in surface energies with and without APTES. Adsorption of APTES molecules was modeled via Ti−O−Si bonding to 25 % hydroxylated titanium on the (001), (100), and (101) anatase surfaces with removal of one C_2H_5 branch from the APTES molecule (Figure 4.34). This situation can be considered as an intermediate stage of the reaction, as the IR spectra show the formation of Si−O−Si (Figure 4.27). The hydroxylation of the surfaces is likely due to the hydrothermal conditions of the synthesis, and calculations by Barnard *et al*. [324] which show that the dissociative adsorption of water is energetically favorable on anatase surfaces. Barnard *et al*. found that the adsorption energy of H_2O is lowest for dissociative adsorption on (001) and (100) surfaces, and molecular adsorption on the (101) surface. However, both dissociative and molecular adsorption have a negative adsorption energy in all cases. In addition, the –OH groups could remain from the

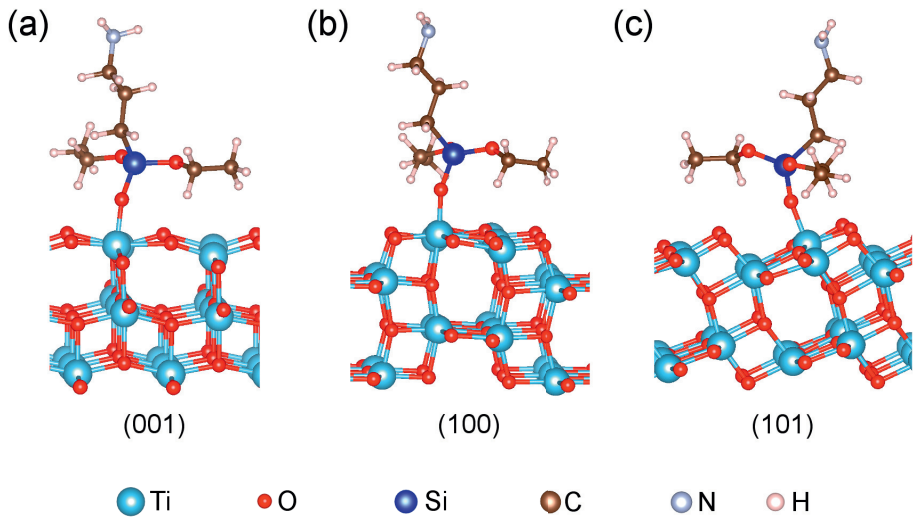

Figure 4.34. Relaxed anatase surface structures with APTES adsorption on (a) (001), (b) (100), and (c) (101) facets. Represented using VESTA [123].

TIP precursor. The calculated surface coverages were 1.75, 1.38, and 1.29 APTES nm^{-2} on (001), (100), and (101) surfaces, respectively (Figure 4.34), and are close to the measured values at short reaction time (Table 4.6).

Surface energies calculated by DFT are given in Table 4.9. The bare surface energies are in agreement with previously calculated values [325, 326], and result in a square truncated bipyramid Wulff construction, replicating the well-known equilibrium shape of anatase [134] (Figure 4.35a). When APTES adsorption was added to the model, all the surfaces energies were lowered, but the ratio of the surface energies remains similar, such that the Wulff construction is not strongly changed (Figure 4.35b). The calculated *c*/*a* ratios without and with APTES adsorption are 1.79 (Figure 4.35a) and 1.57 (Figure 4.35b), respectively. The equilibrium shape of anatase is not strongly affected by the adsorption of APTES. The (100) surfaces are not predicted to appear in either of the Wulff constructions, with or without APTES surface functionalization.

Table 4.9. Bare and APTES adsorbed surface energies, and binding energies of APTES to (001), (100), and (101) of anatase TiO_2, from DFT calculations.

	(001)	(100)	(101)
Bare surface energy (J m^{-2})	1.170	0.712	0.609
APTES adsorbed surface energy (J m^{-2})	0.567	0.400	0.338
Binding energy (eV)	2.145	1.413	1.315

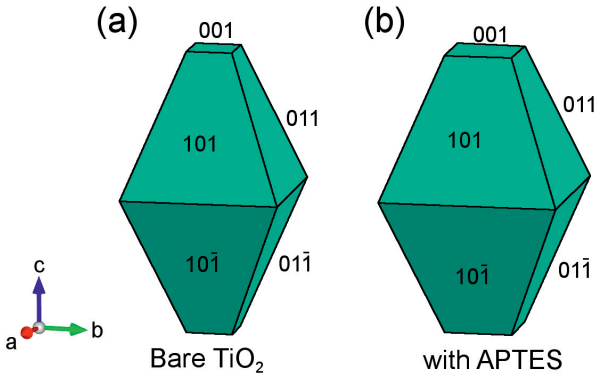

Figure 4.35. Wulff constructions of anatase equilibrium shapes with (a) bare surfaces and (b) APTES adsorption, based on DFT calculated surface energies (Table 4.9). Represented using WulffMaker [273].

4.4.2. Discussion

4.4.2.1. *In situ* reproducibility

The similarity between the *ex situ* and *in situ* diffraction patterns of TiO_2, 10:1, and 10:1-B samples (Figure 4.36) provides solid evidence for the robustness and the reproducibility of the synthesis conditions which can be reliably reproduced *in situ*. From the *ex situ* analysis (Figure 4.24) all the samples are pure anatase demonstrating that no intermediate phase was formed. The same was observed by the *in situ* analysis, when the synthesis was performed with APTES (Figure 4.29). *In situ* synthesis of pure TiO_2 resulted in the formation of both anatase (83 wt.%) and brookite (13 wt.%), similar to previous *ex situ* studies (Figure 4.36). The difference from the *ex situ* and the *in situ* studies (Figure 4.32 and Figure 4.33) could come from the fact that the *ex situ* XRD were recorded after synthesis, and correspond to the *final* properties of the product while the *in situ* data are snapshots at a given moment during the synthesis. Also, the quality of the data from synchrotron radiation, and after integration of 2D patterns, is significantly higher than traditional Bragg-Brentano setups. Nevertheless, the crystallite sizes, the anisotropy measured in both cases are within similar range of values, and follow similar trends (Figure 4.32). The difference is larger for the cell parameters (Figure 4.33), but different pressure and could explain these differences. The *c*/*a* ratios follow similar trends in both cases. The *in situ* analysis are hence considered as representative for the reaction pathways.

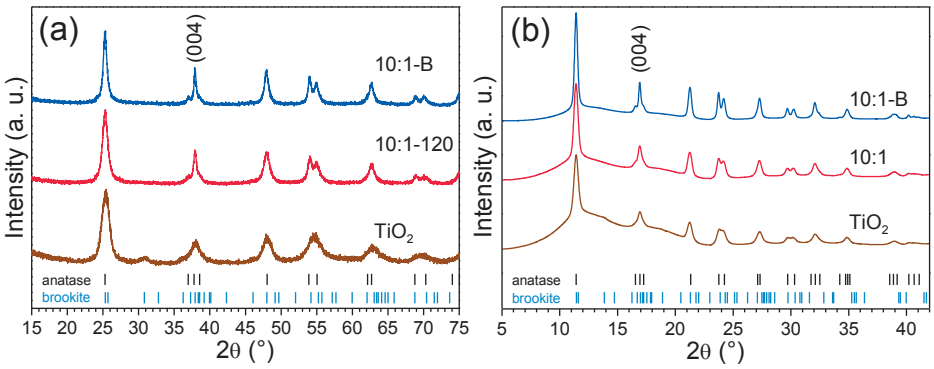

Figure 4.36. Diffractograms of TiO_2, 10:1, and 10:1-B samples collected (a) *ex situ* (λ = 1.5406 Å) and (b) *in situ* (λ = 0.6999 Å) and at room temperature, after reaction. The vertical bars show diffraction lines of anatase from ICDD card #00-021-1272 and brookite from ICDD card #00-029-1360.

4.4.2.2. Kinetics and growth mechanism

For pure TiO_2, the refined cell parameters and crystallite sizes follow the trend from previously reported *in situ* studies of hydrothermal synthesis of TiO_2 at different temperatures [322]. *Ex situ* SEM analysis on pure TiO_2 showed isotropic morphology, with particle size of about 9 nm (see Chapter 4.1). The isotropy is reflected with similar crystallite sizes along the *a*- and *c*-axes (6.29 ± 0.12 nm and 7.29 ± 0.22 nm, respectively, as final values), as the nanoparticles were shown to be single crystals. Thus, the anisotropy measured for pure TiO_2 is relatively small and associated with a significant uncertainty (14 ± 7 %). The evolution of the crystallite sizes as a function of the time (Figure 4.32a-b) follow Equation (2.12), power-law type of function describing an Ostwald ripening (OR) model, where the best fits were obtained for $n = 4$, indicating that the growth is controlled by dissolution kinetics at the particle-matrix interface [64]. The fitted plots and parameters are available in Figure 4.37a and Table 4.10, respectively. The initial crystallite sizes (d_0) and the rate constant for OR (k_{OR}) are similar for both crystallite sizes evolution, confirming no preferential direction of the growth in the case of pure TiO_2.

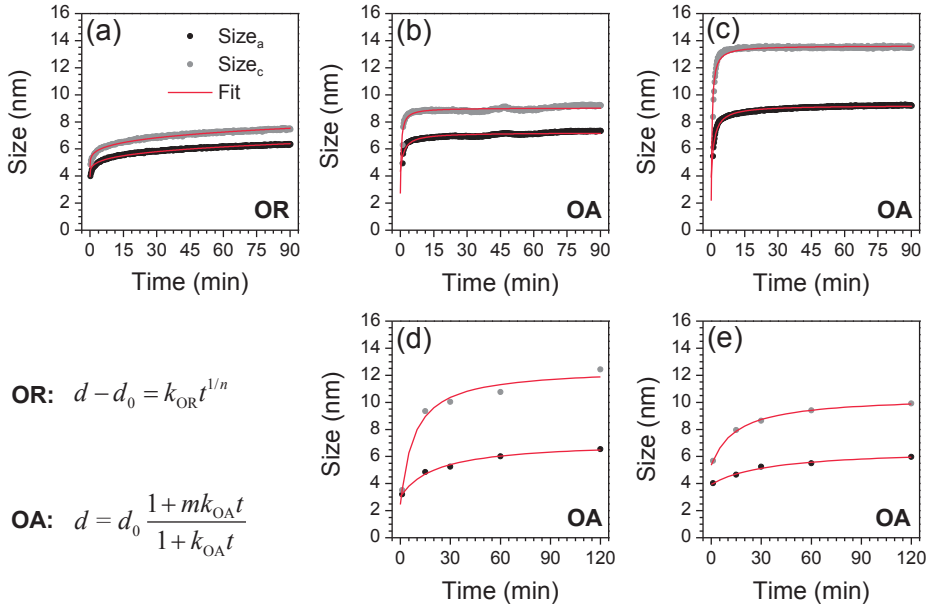

Figure 4.37. Fitted plots from the kinetic models of the crystallite growth from (top) *in situ* XRD data: (a) TiO_2, (b) 10:1, (c) 10:1-B, and (bottom) *ex situ* XRD data: (d) 10:1, (e) 15:1 (OR: Ostwald ripening, OA: oriented attachment).

Table 4.10. Fitted parameters for the kinetics of the crystallite growth along the *a*- and *c*-axes, from *in situ* and *ex situ* XRD data.

Sample	Variable	d_0[a] (nm)	k_{OR}[b] (nm min$^{-1/n}$)	k_{OA}[c] (min^{-1})	m[d]	R^2[e]
TiO_2 (*in situ*)	Size$_a$	3.9	0.80	n/a	n/a	0.98
	Size$_c$	4.6	0.95	n/a	n/a	0.98
10:1 (*in situ*)	Size$_a$	4.3	n/a	0.65	1.7	0.81
	Size$_c$	2.7	n/a	2.55	3.3	0.66
10:1-B (*in situ*)	Size$_a$	3.9	n/a	0.77	2.4	0.97
	Size$_c$	2.2	n/a	2.56	6.3	0.88
10:1 (*ex situ*)	Size$_a$	3.0	n/a	0.05	2.3	0.99
	Size$_c$	2.5	n/a	0.12	5.1	0.98
15:1 (*ex situ*)	Size$_a$	3.9	n/a	0.03	1.7	0.99
	Size$_c$	5.4	n/a	0.07	1.9	0.99

[a] Initial crystallite size (at $t = 0$ min).
[b] Rate constant for Ostwald ripening ($n = 4$).
[c] Rate constant for oriented attachment.
[d] Aggregation factor.
[e] Coefficient of determination.

When the particles were *in situ* functionalized with APTES, the difference in phase purity, morphology, and growth mechanism are attributed to APTES, as the growth and functionalization occur simultaneously and the conditions of synthesis were the same as the synthesis of pure TiO_2. From previous analysis, the hypothesis of an oriented attachment (OA) mechanism was formulated, especially from the HR-TEM analysis of single crystal rod-like nanoparticles, which seems to originate from at least two attached nanoparticles (Figure 4.20c). The kinetics of the crystallite growth for both *in situ* (Figure 4.32a-b) and *ex situ* (Figure 4.32d-e) experiments could not be fitted the OR model. However, the fitting could be done using Equation (2.14), which describes an OA mechanism. The fitted plots for *in situ* and *ex situ* data, as well as the fitted parameters are available in Figure 4.37b-e and Table 4.10, respectively. The rate of growth for OA (k_{OA}) along the *c*-axis, equivalent to the [001] direction of anatase, is two to four times higher than along the *a*-axis, depending on the synthesis conditions. Additionally, the aggregation factor (*m*) is larger along the *c*-axis and increases when the pH of the synthesis and/or the amount of APTES are increased. These observations are consistent with the previous particle size analysis, such as electron microscope analysis (Figure 4.19 and Figure 4.25).

After nucleation, aminosilanes probably adsorb regardless of facet because the binding energy of APTES is large and positive (> 1.3 eV) for all surfaces (Table 4.9). The similarity in the equilibrium shapes predicted by DFT with and without APTES adsorption (Figure 4.35), and the fact the *c*/*a* ratio is also smaller with APTES adsorption supports the fact that an OA mechanisms is occurring, as an elongated shape is not shown to be stable with functionalization of the nanoparticles. The surface energy of the (100) surfaces remains too high to be stable, thus partially faceted nanorods are obtained where one can distinguish {101} facets at the extremity of the rod-like nanoparticles, but rough surfaces at the center. The phenomenon is easier to visualize for the synthesis performed under basic conditions (Figure 4.23). The adsorption of APTES provides the building blocks for OA along the [001] direction of anatase, within the first minutes of the synthesis (Figure 4.32). Yet, the highest binding energy is on the (001) surfaces, which are also the faces with the highest surface energy (Table 4.9), thus the (001) surfaces are the locations where OA is most likely to occur. So, if there is preferential adsorption of APTES on the (001) surfaces, then this would likely attract the nanoparticles in this direction due to polarity effect (*e.g.* hydrogen bonding of the amino group), causing OA. The attraction of the building blocks facing (001) surfaces

could desorb APTES molecules, increasing the total entropy of the system and providing the alignment of the nanoblocks for OA. Thus, the anisotropy of the particles, preferentially along the *c*-axis or [001] direction of anatase is observed (*e.g.* Figure 4.4c, Figure 4.20, and Figure 4.32).

The increased intensity of the bands assigned to APTES in the IR spectra with longer reaction time confirms the slow kinetics of the APTES functionalization of the nanoparticles, as previously measured by Liu *et al*. [202], in the case of APTES post-functionalization of iron oxide nanoparticles. A lower functionalization efficiency could explain the observations on the different pore size distribution profiles at larger pore sizes (20-100 nm, Figure 4.26b and d), as different surface properties resulting from different functionalization degree would lead to different agglomeration state. During the second phase of the reaction, a slower evolution of the crystallite sizes and the cell parameters are observed (Figure 4.32 and Figure 4.33). The ongoing cross-linking of APTES on the surface of the nanoparticles does not allow for more drastic change in the nanoparticles morphology or further growth along the *c*-axis of the nanoparticles. However, surface diffusion might still occur to reach an equilibrium morphology (Figure 4.35c), thus the slow increase of the crystallite size along the *a*-axis and the slow decrease of the anisotropy (Figure 4.32a and c). These competing phenomena (growth and functionalization) results in a mixture of spheres and rods. To confirm the reduced growth at longer reaction time, the *in situ* diffractogram of 10:1-B (Figure 4.36b) was recorded after a total reaction time of 9 h and limited evolution was observed after about 100 min of reaction.

For the *ex situ* data, the sizes given in the Table 4.6 do not seem to be TIP/APTES molar ratio dependent, however, these values are averages, and the samples contain both spheres and rods (and less rods for shorter reaction time). The difference between the two series is more visible when looking at specific particles in the SEM images (Figure 4.25) or the axis dependent crystallite sizes (Figure 4.32d-f). The role of APTES to the attraction forces and oriented attachment is also demonstrated when the amount is reduced (15:1 series), leading to reduced amount and size of the rod-like nanoparticles.

The functionalization of TiO_2 with APTES increases the stability of the nanoparticles by reducing the deviation from the bulk of the cell parameters of anatase (Figure 4.33), and results in phase pure anatase (Figure 4.24 and Figure 4.28a-b). By creating covalent bonds (Figure 4.27), APTES reduces the surface stress and the surface energies (Table 4.9), thus

the finite size effect of the TiO_2 nanoparticles, which is usually observed [25, 323]. By changing the pH of the synthesis, the variations of cell parameters are relatively small thus the difference in the particle sizes does not seem to be at the origin of the variation of the cell parameters between pure TiO_2 and the APTES functionalized samples. However, the anisotropy is strongly influenced by the pH, but also by the type of silane coupling agent (see Chapters 4.1 and 4.3). The reactivity of silane coupling agents and titanium alkoxides, the surface state of TiO_2, and the attractive forces between the functionalized particles are all affected by the variation of pH. A kinetically faster functionalization (increasing the extent of cross-linking that can be achieved before OA takes place) and a more homogeneous system would lead towards more spherically shaped nanoparticles, thus *in situ* functionalization with DTES (non-polar) and AEAPS (two amino groups) resulted in only spheres, and a mixture of spheres and larger rods (compared to *in situ* functionalization with APTES), respectively (see Chapter 4.1).

To summarize, in the case of the hydrothermal synthesis of pure TiO_2, a classical Ostwald ripening (OR) was observed (Figure 4.38a). When APTES was introduced to *in situ* functionalize TiO_2, the adsorption of the aminosilane favors the anatase polymorph and an OA mechanism takes place (Figure 4.38b). OA was observed via anisotropic broadening of

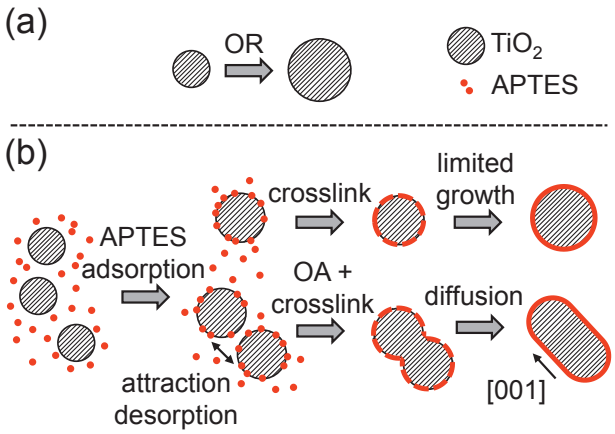

Figure 4.38. Schematics of the proposed growth processes during the hydrothermal synthesis of (a) TiO_2 and (b) TiO_2 *in situ* functionalized with APTES (OR: Ostwald ripening, OA: oriented attachment).

the Bragg reflections, HR-TEM imaging, kinetics modeling, and supported by DFT calculations. At longer reaction times, functionalization and cross-linking of APTES on the surface of the TiO_2 nanoparticles contribute to reduced growth rate.

Further work may include *in situ* small-angle X-ray scattering and/or *in situ* pair distribution function (PDF) analysis of the synthesis in order to also investigate the time evolution of the non-crystalline phases and precursors evolutions at the initial state of the reaction and during the functionalization [282, 327, 328]. Combining the results of different *in situ* techniques would allow for greater understanding on the formation processes.

4.5. Conclusions

A robust and versatile *in situ* hydrothermal route to synthesize surface-functionalized TiO_2 nanoparticles was developed. By selecting the appropriate silane coupling agent, the surface properties of the TiO_2 nanoparticles can be tuned. While spherical nanoparticles were obtained for pure TiO_2 and DTES functionalized TiO_2 nanoparticles, additional [001] oriented rod-like nanoparticles were formed via oriented attachment mechanism by choosing silane coupling agents containing amino groups (APTES and AEAPS). The amount and the size of the rod-like nanoparticles were shown to increase with increasing pH, and to decrease with a lower pH and/or a lower amount of APTES, resulting in a lower grafting efficiency. *In situ* synchrotron XRD was demonstrated to be an efficient tool in order to follow the kinetics of oriented attachment during hydrothermal synthesis, despite the extreme conditions of the synthesis (213 °C and 250 bar). The developed synthesis route to *in situ* surface-functionalized nanoparticles is single-step and has thus a great potential for industrial application with *e.g.* the development of a setup for continuous hydrothermal synthesis. This synthesis could also be feasible for other types of metal oxide nanoparticles for different applications. Understanding the phenomena and reaction processes are essential in order to have more control of the production of hybrid organic-inorganic nanoparticles. This method opens further possibilities for green and single-step synthesis of surface-functionalized nano oxides with controlled size, shape, crystalline phase, and surface properties.

Further analysis after heat treatment of surface-functionalized nanoparticles showed that combustion of the silane coupling agent leads to the formation of an amorphous silica layer, resulting in TiO_2-SiO_2 core-shell nanoparticles, for which further study could consist of evaluating the efficiency of these materials in dye-sensitized solar cells or for photocatalytic degradation devices.

4.5.1. Remark on the *ex situ* synthesis of nanocomposites

In order to prepare TiO_2 polysiloxane-based nanocomposites, several approaches have been investigated such as solvent extraction of the nanoparticles from the water, after the synthesis or direct mixing of the dried nanoparticles with the polysiloxane precursors, followed by *in situ* polymerization (see master thesis by Ola G. Grendal, ref. [292]). But sufficiently good dispersion and transparency were not obtained. The materials were similar to that obtained when using large excess of DTES (see Appendix 8.3), but less colorized. Additionally, at high loads of nanoparticles (> 5 vol.%), cross-linking of the polymer was not occurring. However, other types of applications might still benefit from the nanoscale of the samples, as well as the high surface areas, and surface functionalization.

To overcome the dispersion challenge, and because of the cross-linking issues, we then decided to terminate the work on the *ex situ* route to titanium dioxide based nanocomposites, and decided to go even further, by synthesizing the nanoparticles directly within the polymeric matrix. For this purpose, we chose polydimethylsiloxane (PDMS) as a model system, and kept titanium(IV) isopropoxide as a titanium precursor, to produce hybrid nanocomposites via an *in situ* route. This is described in Chapter 5.

5. Titanium-PDMS based nanocomposites

In this chapter, the synthesis of titanium-PDMS (Ti-PDMS) based hybrid nanocomposites is described. The effect of the PDMS precursor (average molecular mass) and amount of incorporated titanium (TIP/PDMS-OH molar ratio) on the structure, optical, and mechanical properties is discussed. Both mold-casted thick films and spin-coated films were produced. The series of samples are labelled by the viscosity of the PDMS-OH precursor (*i.e.* 25, 65, or 750 cSt), and by the TIP/PDMS-OH molar ratio. Each sample is labelled Ti-PDMS-X-Y:1, where X is the viscosity of the PDMS-OH precursor (in cSt) and Y is the molar ratio of TIP/PDMS-OH.

Prior to using the synthesis method described in Chapter 3.4 (dispersion of both precursors in anhydrous isopropanol and mixing) several preparation methods were investigated. The most challenging part was to promote higher stability of the titanium alkoxide precursor. If TIP is directly mixed with PDMS-OH, a gel is instantaneously formed, making the shaping and the homogeneity of the sample difficult to optimize. The first tests were performed using ethyl acetoacetate as titanium(IV) isopropoxide (TIP) stabilizer, as previously described [240, 242, 244, 245, 247-250, 266, 329, 330]. The resulting complexes and films were however significantly more colored (orange), similar to previously reported works [247, 248], and the quality of the films was mediocre. However, using anhydrous isopropanol (AIP), according to Le Chatelier's principle, allows to stabilize TIP as isopropanol (IP) is also to product of reaction of TIP, as ideally represented in reaction:

$$\mathrm{Ti}\left(\mathrm{OCH}\left(\mathrm{CH_3}\right)_2\right)_4 + 2\mathrm{H_2O} \rightleftharpoons \mathrm{TiO_2} + 4\left(\mathrm{CH_3}\right)_2\mathrm{CHOH} \qquad (5.1)$$

but also via isolation of the precursors surrounded by the solvent. The utilization of AIP allowed to prepare sols that were stable until the solvent was evaporated (after spin-coating or mold-casting), initiating the reaction between the precursors. The temperature of drying and curing are detrimental in order to synthesize films of good quality, without cracks or bubble formation and needed to be optimized for every composition.

5.1. Results

5.1.1. Structure

Photographs of the thick films between 1 and 2 mm thick are displayed Figure 5.1. All the films are transparent with a yellow tint, which increases as a function of increasing volume fraction of TIP. Increasing the volume fraction of titanium precursor led to more brittle samples which were partially damaged during the demolding process. The circular and rectangle samples of Ti-PDMS-750-20:1 (Figure 5.1.C1) had merged. However, these samples were substantially more viscous than the PDMS-OH precursor and the sample could be held with a pair of tweezers, indicating that a partial cross-linking had occurred. The merging of the samples by viscous flow was observed after a few days.

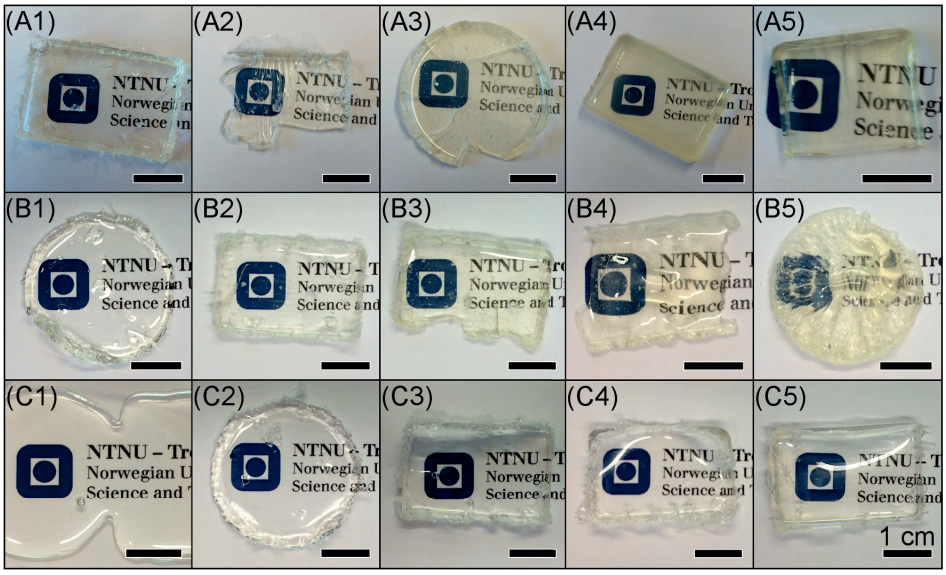

Figure 5.1. Photographs of Ti-PDMS hybrid thick films prepared using PDMS-OH with viscosities of (A) 25 cSt, (B) 65 cSt, and (C) 750 cSt; and TIP/PDMS-OH molar ratios of (1) 2:1, (2) 5:1, (3) 10:1, (4) 15:1, and (5) 20:1. The scale bar for all images is 1 cm.

Infrared spectra of the all the samples and the PDMS-OH precursors are displayed Figure 5.2. The spectra were all normalized to the Si−CH_3 band at 1260 cm^{-1}. The absorption bands of PDMS are observed for all samples (Table 5.1). Additionally, the broad band centered at 3300 cm^{-1} (−OH groups) present in the PDMS-OH precursors is not visible for the hybrid films. The band is mostly visible for 25 cSt and slightly visible for 65 cSt precursors, due to the reduced volume fraction of −OH terminal group as the PDMS chain length increases. In the 920-980 cm^{-1} region, additional absorption assigned to Ti−O−Si appeared with a maximum absorption shifting from 925 to 960 cm^{-1} as the amount of titanium was increased. An increasing absorption below 700 cm^{-1} can be observed as a function of increasing the volume fraction of TIP. This broad absorption is attributed to Ti−O−Ti, due to the alkoxide hydrolysis and condensation.

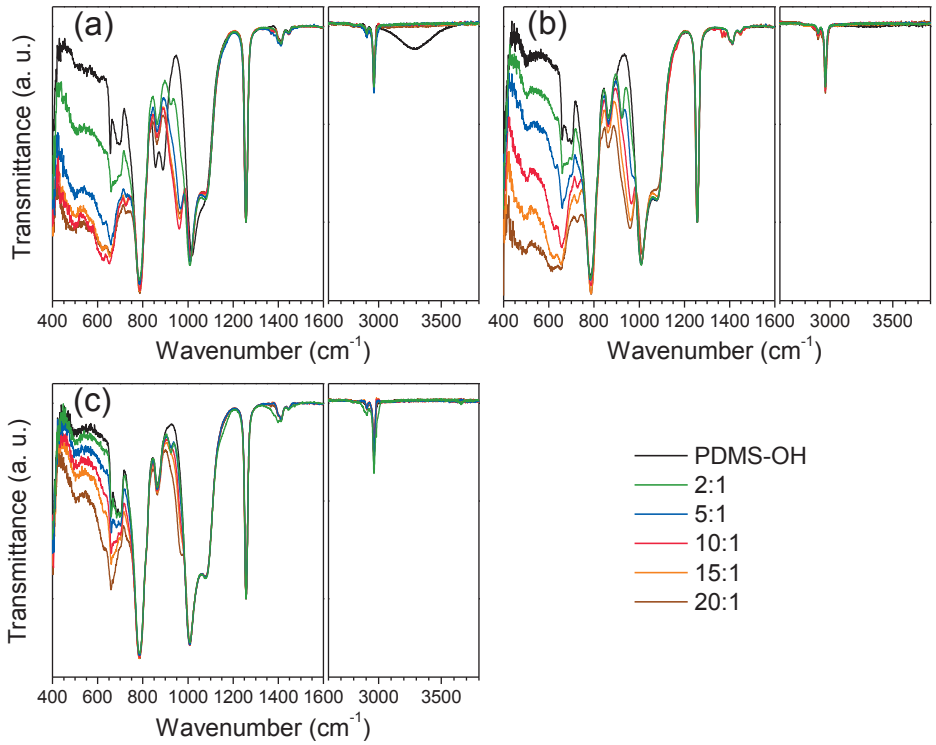

Figure 5.2. Infrared spectra of PDMS-OH precursors and Ti-PDMS hybrid thick films prepared using PDMS-OH with viscosities of (a) 25 cSt, (b) 65 cSt, and (c) 750 cSt for different TIP/PDMS-OH molar ratios. The spectra are normalized to the Si−CH_3 band at 1260 cm^{-1}.

Table 5.1. Assignments of characteristic IR and Raman bands of PDMS-OH precursors and Ti-PDMS hybrid films.

Assignment	Wavenumber (cm^{-1})		Sample	Reference
	IR	Raman		
Si−O−Si (stretch)	n/a	495	All	[236, 237, 331]
Ti−O−Ti	< 700	n/a	Ti-PDMS	[295, 296]
Si−CH_3 (rock)	660-700	690	All	[237, 331-333]
Si−C and CH_3 (rock)	790	790	All	[236, 237, 331, 332]
CH_3 (rock)	860	860	All	[236, 237, 331-334]
Si−OH	890	−	PDMS-OH (strong for 25 cSt)	[332, 334]
Ti−O−Si	920-960	See text	Ti-PDMS	[232, 236, 295, 314, 335]
Si−O−Si (stretch)	1010 and 1080	n/a	All	[236, 237, 295, 331-334]
Si−CH_3	1260	1260	All	[236, 295, 332-334]
CH_3 (bend)	1410 and 1440	1410	All	[236, 237, 295, 331-334]
CH_3 (stretch)	2900 and 2960	−	All	[236, 237, 295, 331-334]
OH	3000-3600	−	PDMS-OH (less visible for 750 cSt)	[295, 332, 334]

Figure 5.3a displays time resolved ambient *in situ* FTIR measurements of the reaction of PDMS-OH (65 cSt) with TIP (TIP/PDMS-OH molar ratio was 20:1), after deposition of a drop of sol on the ATR diamond. The spectra are compared to the spectra of PDMS-OH, isopropanol, and TIP in Figure 5.3b, c, and d, respectively. Due to the solvent evaporation, the relative intensities of the absorption bands from isopropanol and PDMS (Figure 5.3b-c) decrease and increase, respectively, as a function of the time. The two bands at about 1005 and 620 cm^{-1}, corresponding to C−O and Ti−O vibrations in TIP, respectively [31, 336] (Figure 5.3a and d) disappear after a few minutes, confirming the complete hydrolysis of TIP. Despite the sharp intense band of isopropanol at 950 cm^{-1}, additional broad absorption appears in this region, similar to the one observed *ex situ* (Figure 5.2) pointing to rapid formation of Ti−O−Si bonds. However, the absorption in this region continues to increase up to 120 min, implying progressive reaction of TIP as the solvent further evaporates. Similar to the *ex situ* analysis, increased absorption is observed below 700 cm^{-1}, confirming the formation of Ti−O−Ti bonds.

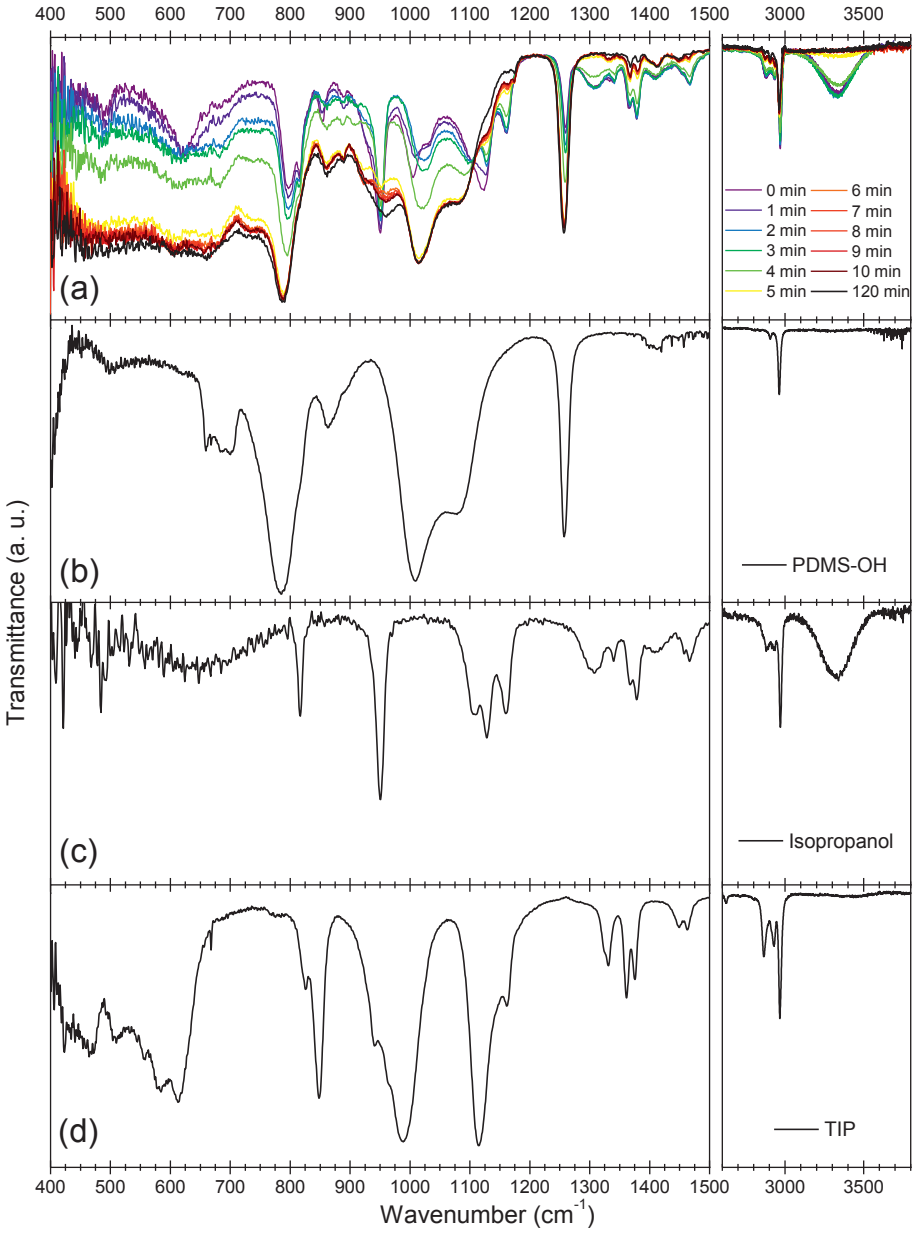

Figure 5.3. (a) *In situ* FTIR analysis of the initial 10 min (by step of 1 min) and after 120 min of the room temperature reaction of TIP and PDMS-OH 65 cSt (20:1 molar ratio). The acquisition was started 1 min before depositing a drop of the sol on the ATR diamond. Infrared spectra (b) PDMS-OH (65 cSt), (c) isopropanol, and (d) TIP are displayed as references.

Raman spectra of the hybrid thick films are displayed in Figure 5.4 and the bands assignments are included in Table 5.1. The spectra were normalized to the Si−O−Si mode at 495 cm^{-1}, resulting in constant intensities of the bands assigned to the PDMS matrix (Table 5.1). Two additional bands appeared at 835 and 1030 cm^{-1} in all materials, and the intensities increase as a function of increased amount of TIP (except for Ti-PDMS-25-20:1, Figure 5.4a). Based on similar analysis of vanadium-PDMS materials [237], as well as calculated values for $Ti\left[OSi(OH)_3\right]_4$ models [337], these new bands are assigned to symmetric and antisymmetric stretching of Ti−O−Si, respectively. In the 25 and 65 cSt series, several weak bands appear as a function of increasing titanium content, which could be the signature of other phases in the samples *e.g.* the weak band at about 600 cm^{-1} for amorphous titania [338]. The band appearing at 440 cm^{-1} has previously been assigned to Si−O−Si mode in a more rigid environment [236].

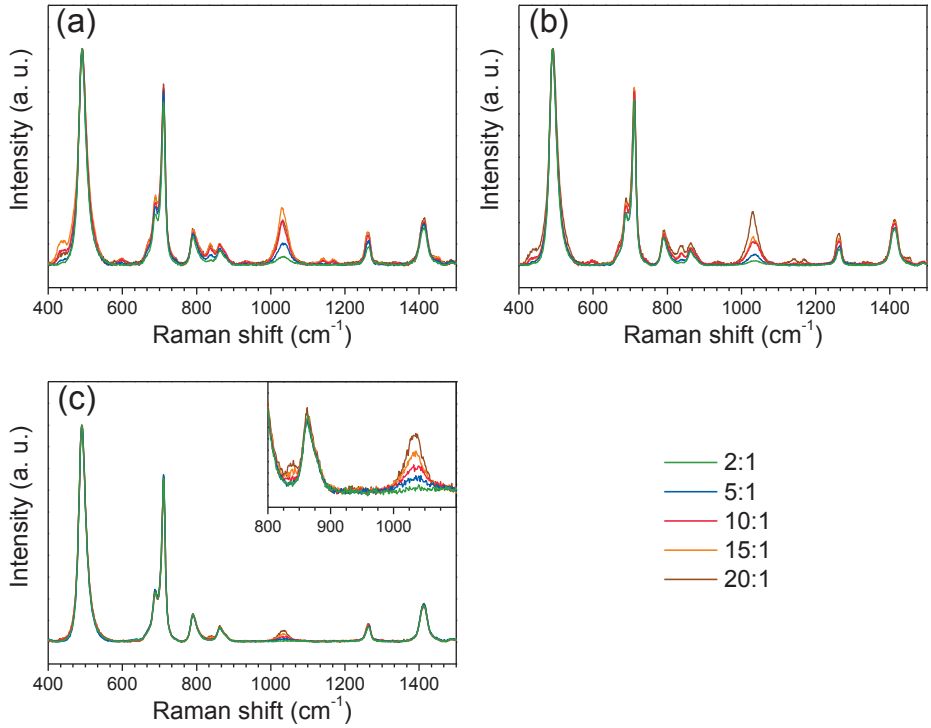

Figure 5.4. Raman spectra of Ti-PDMS hybrid thick films prepared using PDMS-OH with viscosities of (a) 25 cSt, (b) 65 cSt, and (c) 750 cSt for different TIP/PDMS-OH molar ratios. The spectra are normalized to the Si−O−Si band at 495 cm^{-1}.

SAXS scattering profiles of the thick hybrid films are displayed in Figure 5.5. The 2D patterns were similar at all angles demonstrating that the materials are isotropic. All the materials exhibit a peak at high q (about 0.8 $Å^{-1}$), which corresponds to the amorphous halo commonly observed for PDMS-based materials in X-ray diffraction, at about $2\theta = 12°$ under copper radiation [339-342]. The relative intensity of the peak decreases as the amount of incorporated titanium was increased for the three series (less visible for 750 cSt series). The position of the peak (q_{diff}) and the equivalent interplanar spacing (d_{hkl}) are given in Table 5.2. For the three series, the position of the peak shifts towards lower q as the TIP/PDMS-OH molar ratio was increased (Figure 5.6a). Most of the SAXS scattering profiles of the samples display a broad peak in the intermediate q-range which is attributed to correlated inhomogeneities, as previously observed for *in situ* synthesized nanocomposites [221, 222, 235, 236, 339, 343]. The broad peak is attributed to the correlation length between titania-like inorganic domains. The maximum of the broad peak (q_{max}) is related to the correlation length (ζ) between the domains [221, 236, 339]:

$$\zeta = \frac{2\pi}{q_{max}} \tag{5.2}$$

and the values are reported in Table 5.2. For samples Ti-PDMS-750-15:1 and Ti-PDMS-750-20:1, a peak is not clearly defined but a shoulder is visible at about 0.1 $Å^{-1}$ (Figure 5.5c). This value is comparable to the values of q_{max} of the other samples of the series. For Ti-PDMS-750-20:1 sample, an additional shoulder centered at about 0.01 $Å^{-1}$ present which could be assigned to larger scale inhomogeneities ($\zeta \approx 63$ nm) in the material. The fact that different scales of inhomogeneities are observed could indicate that a hierarchical structure is present in the materials where the primary nanoparticles are agglomerated in larger units. Nevertheless, for the other samples (except Ti-PDMS-750-10:1), the correlation length is decreasing when increasing the titanium content (Figure 5.6b).

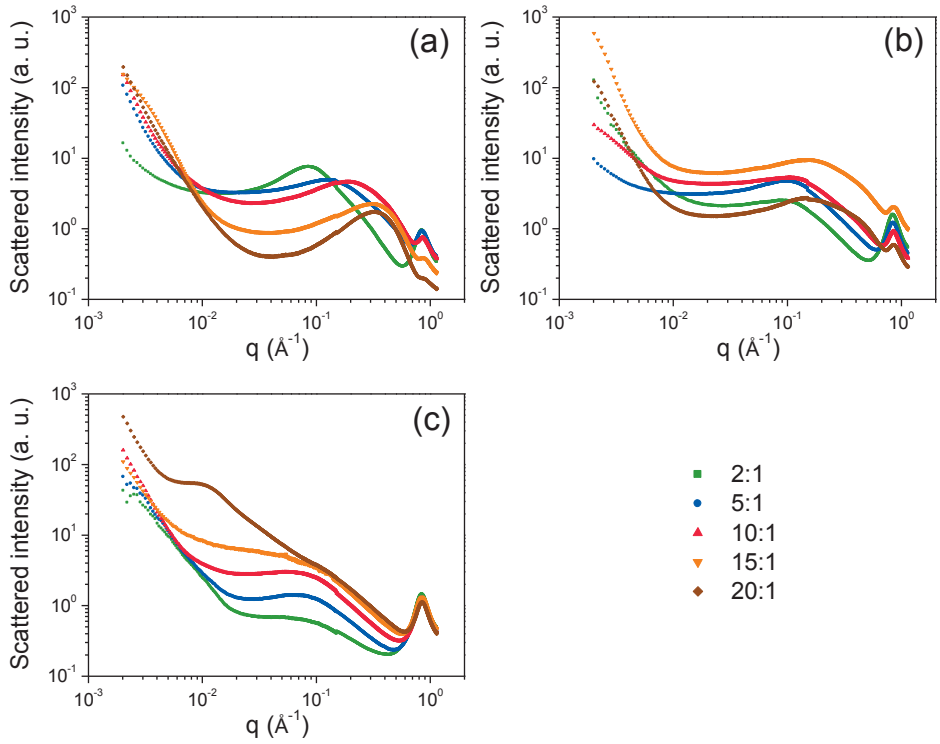

Figure 5.5. SAXS scattering profiles ($\lambda = 1.0332$ Å) of Ti-PDMS hybrid thick films prepared using PDMS-OH with viscosities of (a) 25 cSt, (b) 65 cSt, and (c) 750 cSt for different TIP/PDMS-OH molar ratios.

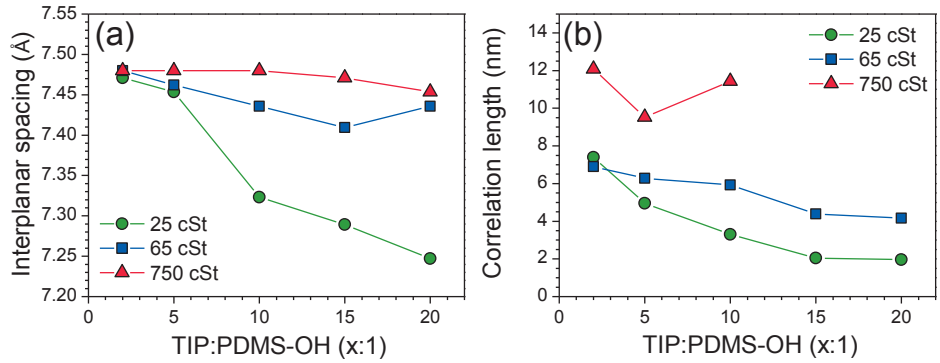

Figure 5.6. (a) Interplanar spacing of the amorphous halo (measured at $q_{diff} \approx 0.8$ Å^{-1}) and (b) correlation length between the inorganic domains (measured at $q_{max} \approx 0.05$-0.32 Å^{-1}) of Ti-PDMS hybrid thick films as a function of the TIP/PDMS-OH molar ratio, calculated from the SAXS data.

Table 5.2. Characteristics of Ti-PDMS hybrid thick films from the SAXS analysis.

PDMS-OH	TIP/PDMS-OH (mol. ratio)	q_{diff}[a] ($Å^{-1}$)	d_{hkl}[b] (Å)	q_{max}[c] ($Å^{-1}$)	ζ[d] (Å)	τ^1[e]	D_m^1[f]	D_s^1[g]	τ^2[h]	D_m^2[i]	D_s^2[j]	R_g[k] (Å)
	2:1	0.841	7.47	0.085	73.92	1.4	1.4	–	2.0	2.0	–	–
	5:1	0.843	7.45	0.127	49.47	2.6	2.6	–	1.6	1.6	–	–
25 cSt	10:1	0.858	7.32	0.190	33.07	2.8	2.8	–	2.5	2.5	–	4.1
	15:1	0.862	7.29	0.308	20.40	2.8	2.8	–	3.0	–	3.0	3.8
	20:1	0.867	7.25	0.321	19.57	2.8	2.8	–	3.6	–	2.4	4.1
	2:1	0.840	7.48	0.091	69.05	1.9	1.9	–	1.5	1.5	–	–
	5:1	0.842	7.46	0.100	62.83	1.2	1.2	–	1.5	1.5	–	–
65 cSt	10:1	0.845	7.44	0.106	59.28	1.4	1.4	–	1.3	1.3	–	–
	15:1	0.848	7.41	0.143	43.94	3.5	–	2.5	1.8	1.8	–	3.2
	20:1	0.845	7.44	0.151	41.61	3.0	–	3.0	2.0	2.0	–	3.3
	2:1	0.840	7.48	0.052	120.83	2.0	2.0	–	0.8	0.8	–	–
	5:1	0.840	7.48	0.066	95.20	2.0	2.0	–	1.2	1.2	–	–
750 cSt	10:1	0.840	7.48	0.055	114.24	2.7	2.7	–	1.4	1.4	–	–
	15:1	0.841	7.47	–	–	2.1	2.1	–	1.4	1.4	–	–
	20:1	0.843	7.45	0.010*	628.32*	2.7	2.7	–	1.4	1.4	–	–

[a] Position of the PDMS amorphous halo (± 0.001 $Å^{-1}$).
[b] Interplanar distance of the PDMS amorphous halo (± 0.01 Å).
[c] Position of the maximum of correlation peak (± 0.001 $Å^{-1}$).
[d] Correlation length (± 0.01 Å).
[e] Slope (± 0.1) at low q-range (< 0.02 $Å^{-1}$).
[f] Mass fractal dimension (± 0.1) at low q-range (< 0.02 $Å^{-1}$).
[g] surface fractal dimension (± 0.1) at low q-range (< 0.02 $Å^{-1}$).
[h] Slope (± 0.1) at high q-range (< 0.8 $Å^{-1}$).
[i] Mass fractal dimension (± 0.1) at high q-range (< 0.8 $Å^{-1}$).
[j] Surface fractal dimension (± 0.1) at high q-range (< 0.8 $Å^{-1}$).
[k] Radius of gyration (± 0.1 Å).
* Higher hierarchical degree (see text).

The dimension of the mass fractal (D_m) or surface fractal (D_s) were calculated from [344, 345]:

$$D_m = \tau \tag{5.3}$$

and

$$D_s = 6 - \tau \tag{5.4}$$

where τ is the power-law scattering exponent or the slope of the linear regions of a Porod plot *i.e.* log(intensity) as a function of log(q) (Figure 5.5) [344, 346, 347]:

$$I(q) \propto q^{-\tau} \tag{5.5}$$

where the measured sample is a mass or surface fractal if $\tau < 3$ or $3 < \tau < 4$, respectively, since the dimension of the space is 3. The exponents and corresponding dimensions of mass fractal or surface fractals calculated for the linear regions at low q-range (< 0.02 $Å^{-1}$) and high q-range (< 0.8 $Å^{-1}$), and labelled with 1 and 2 as superscript, respectively, are included in Table 5.2. The power-law observed beyond the Bragg-like reflection, in the high q-range (< 0.8 $Å^{-1}$) corresponds to diffuse-interface domains [339] between the titania-like heterogeneities and the PDMS matrix. In this region, the first scale objects (or primary particles) are observed. As the amount of incorporated titanium was increased, the fractal dimension increased. For the samples with the highest titanium content (Ti-PDMS-25-15:1 and Ti-PDMS-25-20:1), a surface fractal is observed, which can be assigned to an increased amount of inorganic domains as the titanium alkoxide precursor would be more likely to react with itself [348] and also because of the lower availability of terminal −OH groups from the PDMS-OH precursors. The transition from mass fractal to surface fractal could be assigned to the formation of large scale agglomerate which are close to percolation (*i.e.* the titania-like nanodomains are connected to each other throughout the material) since the correlation length for this samples calculated for these samples is about 2 nm (Table 5.2). For the low q-region, corresponding to larger objects, the calculated fractal for Ti-PDMS-65-15:1 and Ti-PDMS-65-20:1 are surface fractals which correspond to the roughest samples (Figure 5.1). The increased intensity in the low q-range with increased TIP/PDMS-OH is assigned to large scale aggregation of the inorganic titania-like nanodomains of sizes, which could not be assessed in the recorded range or because of overlapping contributions, confirming a hierarchical structure [349, 350].

The radius of gyration (R_g) of the inorganic domains was extracted from the SAXS data by plotting ln(intensity) as a function of q^2 (Figure 5.7) according to Guinier's relation [221, 351, 352]:

$$I(q) \propto \exp\left(-q^2 \frac{R_g^2}{3}\right) \tag{5.6}$$

However, only five samples (those with the highest amount of incorporated titanium) showed linear regions that were well defined enough to be able to apply a linear fitting and calculate the radius of gyration. The calculated values of R_g are included in Table 5.2. Similar values were obtained by Guermeur *et al.* [235] on zirconium-PDMS materials, and the values are consistent with the fact that $R_g \leq \zeta$ [339]. Using Equation (5.7) [352]:

$$d_g = 2R_g\sqrt{5/3} \tag{5.7}$$

the diameter of the nanodomains (d_g) was calculated in the range between 0.8 and 1.1 nm, assuming that they are spherical.

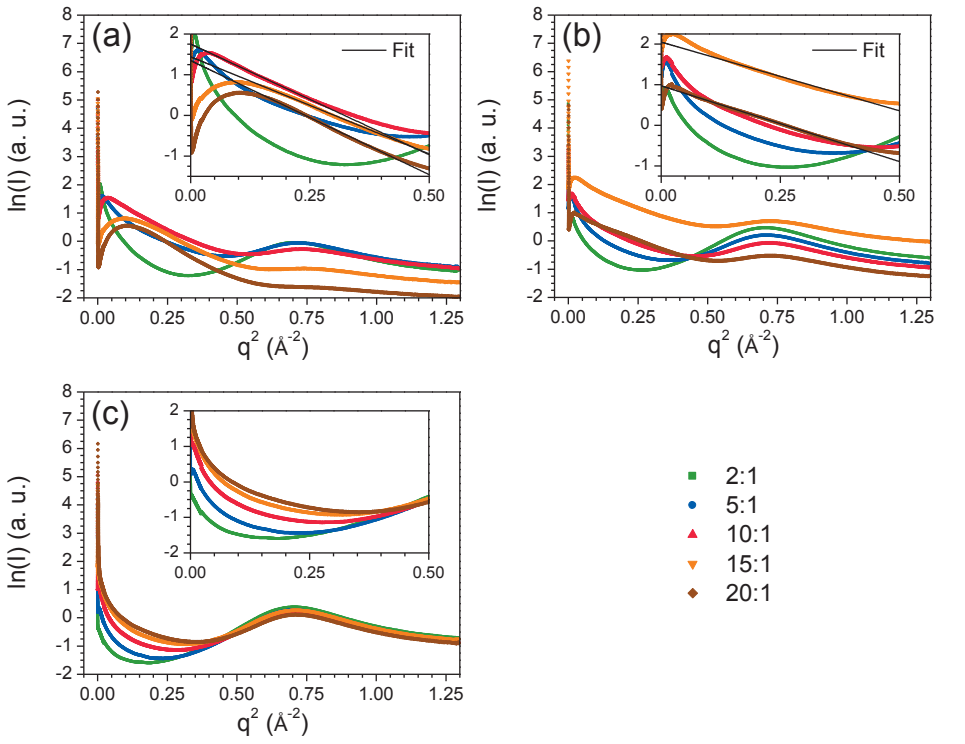

Figure 5.7. Guinier plots of the SAXS data (λ = 1.0332 Å) of Ti-PDMS hybrid thick films prepared using PDMS-OH with viscosities of (a) 25 cSt, (b) 65 cSt, and (c) 750 cSt for different TIP/PDMS-OH molar ratios.

Figure 5.8 shows the contact angle of water measured on the spin-coated films. A gradual decrease of the contact angle of water is observed with increasing TIP/PDMS-OH molar ratios (Figure 5.9), demonstrating the reduced hydrophobicity of the films with increased titanium incorporation. For the same TIP/PDMS-OH molar ratio, as the viscosity (*i.e.* the average molecular weight) of the PDMS-OH precursor was increased, the resulting hybrid material contains a smaller volume fraction of titanium. The highest and the lowest contact angle (about 126° and 91°, respectively) are measured on the samples with the lowest and the highest amount of incorporated titanium (vol.%), Ti-PDMS-750-2:1 and Ti-PDMS-25-20:1, respectively. Similar trends of the contact angle were previously observed on titanium-based hybrid materials [227, 243, 353].

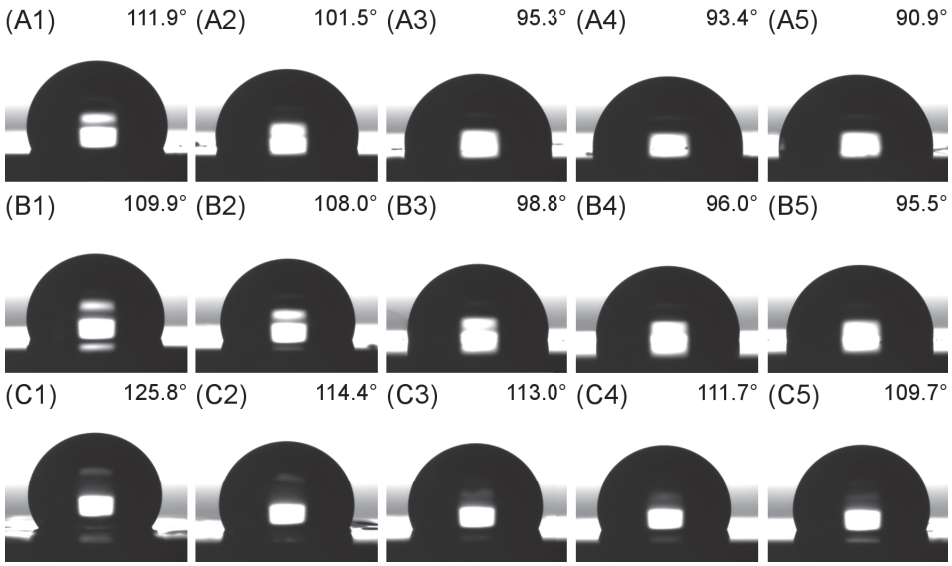

Figure 5.8. Photographs of water droplet contact angles measured on spin-coated Ti-PDMS hybrid films prepared using PDMS-OH with viscosities of (A) 25 cSt, (B) 65 cSt, and (C) 750 cSt; and TIP/PDMS-OH molar ratios of (1) 2:1, (2) 5:1, (3) 10:1, (4) 15:1, and (5) 20:1.

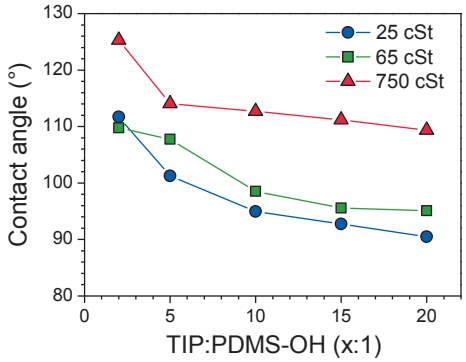

Figure 5.9. Contact angle (± 1°) of water on spin-coated Ti-PDMS hybrid films as a function of the TIP/PDMS-OH molar ratio.

5.1.2. Optical properties

UV-vis spectra recorded in transmission on the thick films are shown in Figure 5.10, which confirm the materials transparency in the visible part of the spectrum (400-800 nm). The transmittance is however significantly reduced when increasing the amount of incorporated titanium, but also due to scattering induced by the relative roughness of the samples, especially samples Ti-PDMS-65-15:1 and Ti-PDMS-65-20:1 (Figure 5.1.B4 and B5, respectively). The transmission of the films follows prediction by the theory (reduced transmittance as the particle size and/or the particle volume fraction is increased, see Chapter 2.3.3). In the UV region, the transmittance is reduced to zero at 320-360 nm. The onset where the transmittance is reduced to zero is red-shifted as the amount of titanium is increased. It results in a partial absorption in the blue region, thus the yellow colorization of the films at higher amount of incorporated titanium. Quantitative trends are difficult to establish due to the difference in thickness and roughness of the samples. Nevertheless, for the 65 cSt and 750 cSt series, the onset gradually shift from 336 to about 362 nm (or 3.69 to 3.42 eV), and 319 to 337 nm (or 3.83 to 3.65 eV), respectively (Figure 5.10b-d).

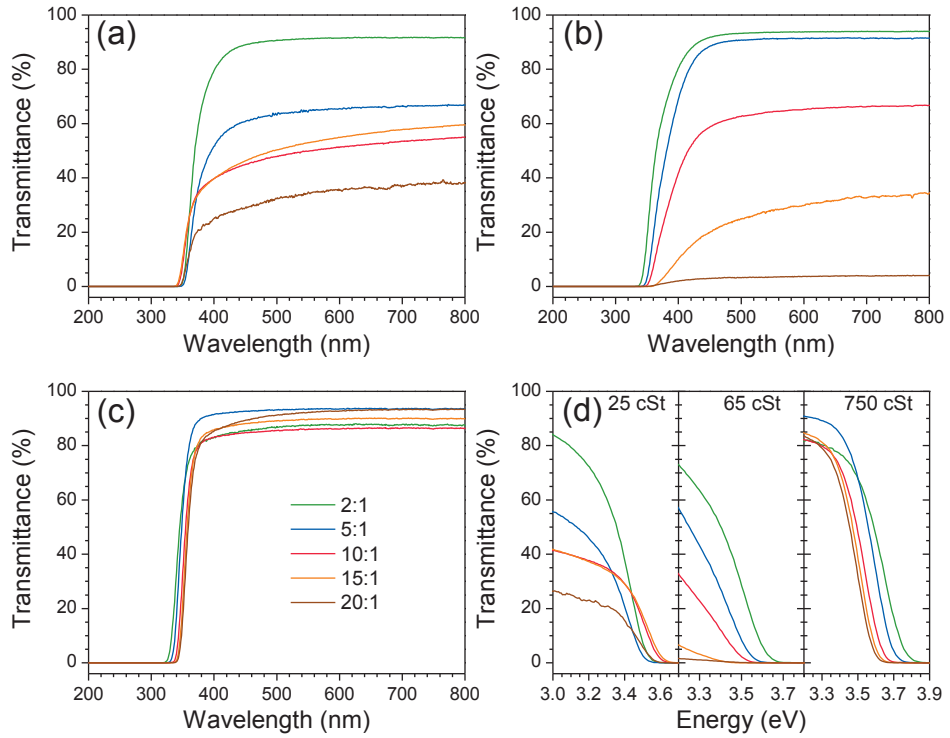

Figure 5.10. UV-vis spectra of Ti-PDMS hybrid thick films (shown in Figure 5.1) prepared using PDMS-OH with viscosities of (a) 25 cSt, (b) 65 cSt, and (c) 750 cSt for different TIP/PDMS-OH molar ratios; (d) onset in eV.

The refractive indices, from the refined ellipsometry measurements, of the spin-coated films from the 25 cSt and the 65 cSt series are displayed Figure 5.11. Phase separation occurred during the spin coating using the 750 cSt PDMS-OH precursor, hence the quality of these films was not sufficient for ellipsometry measurements. The refractive index decreased when the wavelength increases, in accordance with the Cauchy's law, and the refractive index of the hybrid films increased with the TIP/PDMS-OH molar ratio. At constant wavelength (589 nm, Figure 5.12a), the refractive index of both series increases linearly as a function of the TIP/PDMS-OH molar ratio, as previously observed [221, 248, 262, 264, 266, 330]. The 25 cSt samples exhibit higher refractive index than 65 cSt samples at the same TIP/PDMS-OH molar ratio. Including titanium, the refractive index of the PDMS materials was increased from 1.40 to 1.56 (+11 %) at 589 nm. With more titanium incorporation, the wavelength dependence of the refractive index becomes significant, and

the Abbe number (Figure 5.12b) is reduced, demonstrating an increased light dispersion. The Abbe number decreases in an exponential manner for both series. Reduced Abbe number with increased titanium incorporation has previously been reported [221, 264]. The Abbe numbers of the 25 cSt samples is smaller than those of the 65 cSt samples, at equal TIP/PDMS-OH molar ratios.

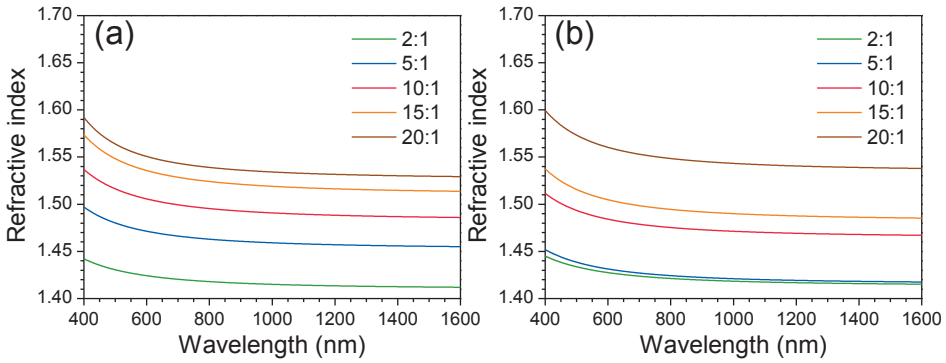

Figure 5.11. Average refractive index of Ti-PDMS hybrid films prepared using PDMS-OH with viscosities of (a) 25 cSt, (b) 65 cSt for different TIP/PDMS-OH molar ratios, measured by ellipsometry.

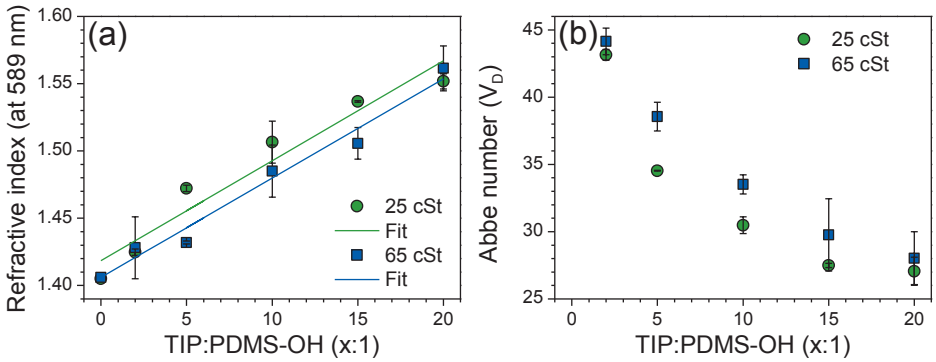

Figure 5.12. (a) Refractive index at 589 nm (value for pure PDMS-OH taken from the provider data sheet) including linear fitting and (b) Abbe number of Ti-PDMS hybrid films as a function of the TIP/PDMS-OH molar ratio, measured by ellipsometry.

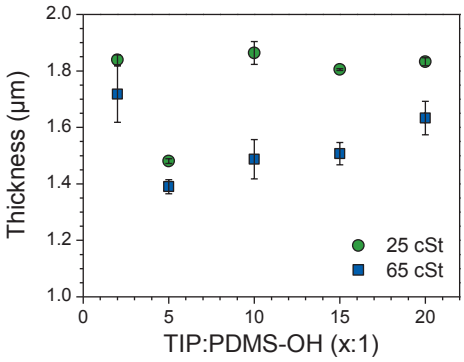

Figure 5.13. Thickness of spin coated Ti-PDMS hybrid films measured by ellipsometry as a function of the TIP/PDMS-OH molar ratio.

The thickness of the spin-coated films extracted from ellipsometry data are plotted Figure 5.13. All the spin-coated films have a thickness comprised between 1.3 and 1.9 µm, and the 25 cSt series resulted in thicker films that the 65 cSt series, regardless of the composition of the materials.

5.1.3. Mechanical properties

The temperature dependence of the shear storage modulus (G') and the loss factor (tan δ) of the composites are displayed in Figure 5.14. For the 25 cSt series, the G' (Figure 5.14a) decreases from −100 °C to about −40 °C and reaches a plateau, except for the samples with TIP/PDMS-OH ratio of 2:1 and 5:1 where the G' increases again. G' increases when the amount of incorporated titanium was increased (from 3 MPa to 220 MPa at 25 °C) except for the 20:1 sample, and G' decreases slightly again above 100 °C. For these two samples, a large decrease (peak in the case of 5:1 sample) in the tan δ curves (Figure 5.14b) is assigned to the glass transition temperature (T_g) [235, 240, 354], below −100 °C and at −68 °C (tan δ = 0.35), respectively. For the 10:1, 15:1, and the 20:1 samples, the tan δ also shows a broader maximum (T_g) at about −70 °C from −100 °C to 50 °C. The amplitude decreased as a function of increasing TIP/PDMS-OH molar ratio. The plateau can thus be attributed to the rubbery region of PDMS. As the titanium amount was increased, the reduced mobility of the chains results in more rigid samples even above the T_g of PDMS.

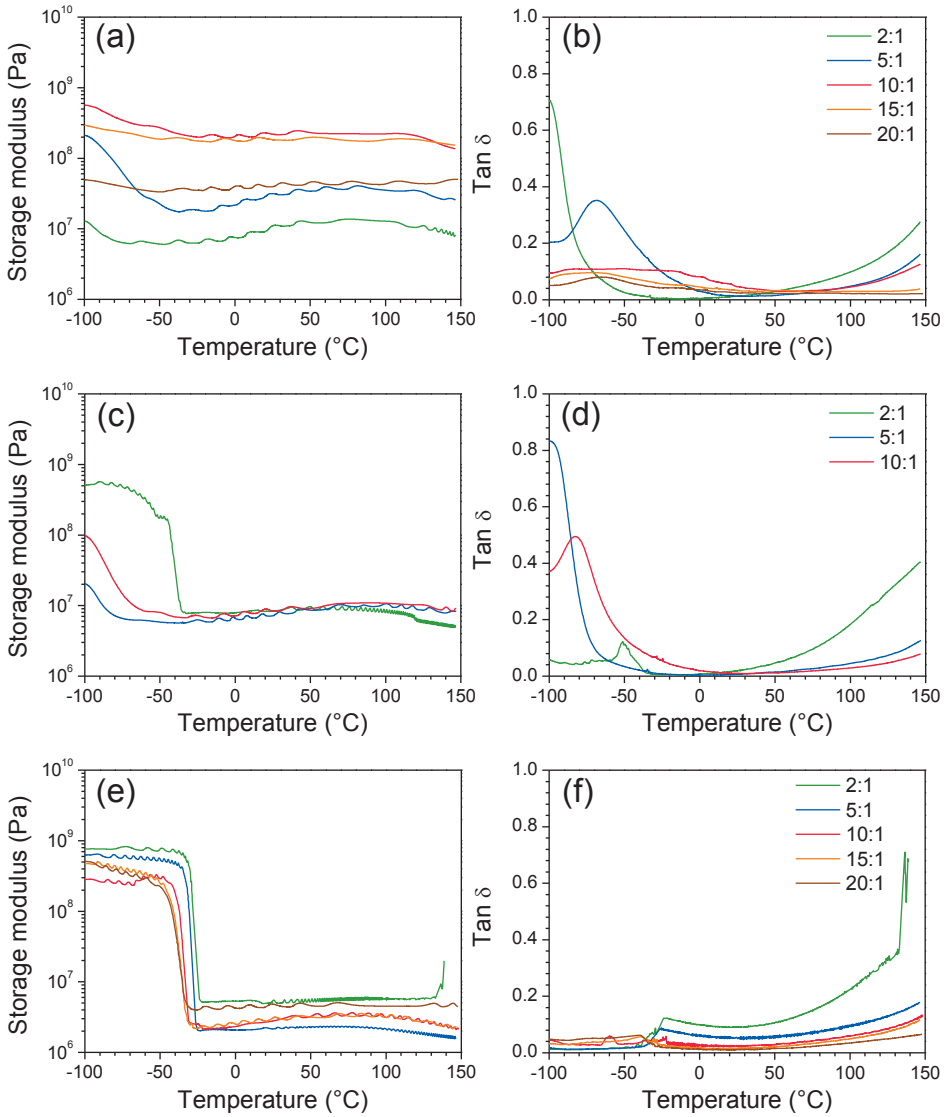

Figure 5.14. Temperature dependence of the shear storage modulus (G', left) and tan δ (right) of Ti-PDMS hybrid thick films (Figure 5.1) prepared using PDMS-OH with viscosities of (a-b) 25 cSt, (c-d) 65 cSt, and (e-f) 750 cSt for different TIP/PDMS-OH molar ratios.

For the 65 cSt series (Figure 5.14c-d), the 5:1 and the 10:1 samples show a similar behavior as the 25 cSt series, exhibiting a T_g at about −100 °C (tan δ = 0.82) and at −83 °C (tan δ = 0.50), respectively. No data were obtained for the Ti-PDMS-65-15:1 and Ti-PDMS-65-20:1 samples due to the mediocre quality of the films (Figure 5.1). Ti-PDMS-65-2:1 sample exhibits a drastic change in the shear storage modulus, resulting in a maximum tan δ (0.12) at −51 °C. From the nature of the change in G' and from the amplitude of tan δ, this transition must be different from the one observed for the previously described samples. However, all samples from the 750 cSt series (Figure 5.14e-f) exhibit similar transitions, with a decrease of G' of about two orders of magnitude. The maximum of tan δ shifts from −40 °C to −23 °C with decreased amount of incorporated titanium. In these samples, less titanium was incorporated and PDMS chains benefit of a higher mobility.

For the three series, the tan δ at elevated temperature is higher with lower amounts of incorporated titanium, and always smaller than 1, demonstrating a non-liquid behavior at any temperature within the range of the measurements (−100 to 150 °C). The origin of the oscillations in the shear storage modulus (also in the shear loss modulus, G'', not shown here) could not be determined, but must be due to the experimental setup and are not assigned to any specific behavior of the samples, as it is observed for all the samples, independently of the temperature and the frequency. However, as tan δ is the ratio between the loss and the storage moduli, the oscillations are not present in tan δ.

5.2. Discussion

5.2.1. Structure of the hybrid films

From a qualitative view (Figure 5.1), the increased rigidity of the films confirms that titanium alkoxide was successfully incorporated as a cross-linking agent of PDMS-OH, which was initially in the liquid state. Incomplete cross-linking in Ti-PDMS-750-2:1 is probably due to the approximations in the estimation of the average molecular weight of the PDMS-OH precursor. The PDMS-OH precursors are most likely not monodispersed (*i.e.* all the chains do not have the same length), thus the molar ratios were not fully accurate. In consequence, the amount of TIP was probably not sufficient to provide the formation of a

continuous network for the 2:1 sample. The cross-linking of the samples was confirmed by the formation of Ti−O−Si bonds from IR and Raman spectroscopy (Figure 5.2-5.4), according to the simplified reaction [31]:

$$\mathrm{Ti\left(OCH\left(CH_3\right)_2\right)_4 + 4HO\left[Si\left(CH_3\right)_2O\right]_nH \xrightarrow[-\,\mathrm{HOCH(CH_3)_2}]{\Delta} Ti\left(O\left[Si\left(CH_3\right)_2O\right]_nH\right)_4} \quad (5.8)$$

On the other hand, the presence of Ti−O−Ti bonds detected by FTIR implies also the formation of titania-like nanodomains, confirmed by the correlation lengths observed in the SAXS analysis (Figure 5.5). The weak band appearing at 600 cm^{-1} in Raman at high TIP/PDMS-OH molar ratios could be the signature of the presence of nanoregions of amorphous titania. This band was probably not detected in all the samples since the titanium content was lower. Because of the low temperature of drying and curing, the titania-like nanodomains are amorphous. The transparency of the thick films (Figure 5.1 and Figure 5.10) also supports the nanometric nature of the titania-like domains. In addition, the fact that using a *simple* Cauchy model was sufficient to analyze the ellipsometry data also confirms high homogeneity of the samples at a micro- and macroscale. Determination of formation route of the nanodomains is challenging, but the nanodomains could result from a combination of intermediate reactions such as, thermal decompositions, ether elimination, and/or reaction with the PDMS-OH precursor [31, 40, 41, 58, 355]. It was also demonstrated that titanium alkoxides could catalyze the condensation reaction of polysiloxane units, *i.e.* longer polymeric chains can be formed during the process, when using dimethyldiethoxysilane as polysiloxane precursor in ethanol and water [234, 356]. In the case described here, the titanium precursor was used in excess with respect to the available terminal −OH groups of the PDMS-OH precursor, thus cross-linking of the PDMS chains by the formation of titania-like nanodomains was desirable. The formation of the titania-like nanodomains can also originate from the hydrophobic nature of the PDMS chains, resulting in partial phase separation.

In the IR region assigned to Ti−O−Si at 920-980 cm^{-1} (Figure 5.2), the materials with the lowest amount of TIP exhibit a band at 925 cm^{-1} as well as a shoulder. As the amount of TIP was increased, the band at 925 cm^{-1} disappear, the shoulder intensity is increased, and a new band can be observed at 960 cm^{-1}. In titanosiloxane oligomers or Ti-PDMS hybrids, the Ti−O−Si band is often observed at around 925 cm^{-1} [232, 248, 335, 357]. However, the position of a band is influenced by the rigidity of the bond and by the environment, as the

Ti−O−Si band was measured and predicted at about 960 cm^{-1} for titanium in a zeolite like structure (tetra-coordinated) [337]. The inorganic domains are amorphous and could thus have various coordination numbers of titanium. The reduced correlation length between the nanodomains (Figure 5.6b) would increase the rigidity of the materials by surrounding the polymer chains. A combination of various coordination number of titanium and increased rigidity could justify the shift of the Ti−O−Si absorption at higher titanium contents, to similar values as titanium in tetra-coordinated environment (*e.g.* zeolite). The increased rigidity is also observed by Raman (Figure 5.4), with *e.g.* the band at 440 cm^{-1} appearing at high TIP amounts, which is a signature of a Si−O−Si mode in a more rigid environment [236]. The increased rigidity could also explain the shift of the amorphous halo observed at high q ($q_{diff} \approx 0.8$ $Å^{-1}$) in SAXS, towards lower d_{hkl} distances (Figure 5.6a). Moreover, the increased rigidity was also confirmed by DMA.

The mechanical properties of the hybrid films (Figure 5.14) are highly dependent on the amount of TIP used during the synthesis. At high titanium incorporation (25 cSt series, Ti-PDMS-65-5:1, and Ti-PDMS-65-10:1), T_g increased even above the value expected for PDMS with infinite chain length, −123 °C (Figure 2.11) [159], probably due to further inhibition of the chain mobility because of the titania-like nanodomains. Increased T_g of hybrid polysiloxane-based materials has been previously observed [235, 343, 358]. For the samples with lower titanium incorporation (750 cSt series and Ti-PDMS-65-2:1), the T_g might be lower than −100 °C and thus not be visible in the analyzed temperature range. Nevertheless, a transition with a different nature is observed and this sharp transition (from −40 °C to −23 °C) can be attributed to the melting of PDMS crystals [354]. In these materials, upon slow cooling, increased mobility of the PDMS chains (compared to materials with high titanium content), and the longer PDMS chains of these materials (compared to the 25 cSt precursor) could result in partial rearrangement of PDMS regions at low temperatures.

The refractive indices of the 25 cSt series (Figure 5.12a) were expected to be higher than the ones measured for the 65 cSt series, as they contain proportionally more titanium. For this series, the drying and curing temperature were lower, reducing shrinkage of the network during solvent evaporation, thus the thickness of the spin-coated samples were larger (Figure 5.13). In consequence, the density is probably lower giving a reduction in the refractive index. However, the thickness is also expected to be different because of the different nature

of the PDMS-OH precursor used for each series. An accurate comparison between the different series remains challenging as the nature of the PDMS-OH precursor and the volume fraction of TIP used are both variable parameters.

5.2.2. General trends via TiO_2 formation hypothesis

Thermogravimetry analysis (TGA) did not allow for accurate measurement of the weight ratios between organics and inorganics components of the Ti-PDMS films, as even after heating up to 1200 °C in air, black and glassy materials resulted from the heat treatment. From the combustion of these nanocomposites, a mixture of TiO_2 and SiO_2 based materials with a white color would be expected (similar to the TiO_2-SiO_2 materials obtained in Chapter 4.2). The black color demonstrates that some carbon remains trapped in the oxide network formed during the combustion. The TGA of the 25 and 65 cSt series, and a picture of the post-treatment products are available in Appendix 8.4.2. However, from the TGA analysis, some trends may still be observed. For both series, the mass loss is reduced when the amount of incorporated TIP is increased, as the hybrids were made of more inorganic material. Similarly, the mass loss of the 25 cSt series is generally lower than for the 65 cSt series, and the difference between each molar ratio is greater in the 25 cSt series. This is consistent with the initial formulation of the films.

However, assuming that TIP has fully reacted to form anatase titanium dioxide in the hybrid materials, a general correlation between all the samples can be achieved. Anatase was selected for these calculations as it is the low density and expected polymorph at nanoscale (ρ_{TiO_2} = 3.89 g cm^{-3}). The calculated weight and volume percentages of hypothetical anatase TiO_2 for each hybrid sample are available in Table 5.3. From these calculations, the TiO_2 volume fraction is ranging from 0.2 vol.% (Ti-PDMS-750-2:1) to 15.5 vol.% (Ti-PDMS-25-20:1), with theoretical Ti/Si molar ratio as high as 0.71. Interestingly, the calculations give the same volume fraction of TiO_2 for Ti-PDMS-65-2:1 and Ti-PDMS-750-10:1, which could thus be more closely compared.

Table 5.3. Calculated weight and volume percentages of TiO_2 and Ti/Si atomic ratios of the Ti-PDMS hybrids, assuming full reaction of TIP to anatase.

PDMS-OH	TIP/PDMS-OH (mol. ratio)	TiO_2 (wt.%)	TiO_2 (vol.%)	Ti/Si (mol. ratio)
25 cSt ($M_n \approx 2100$)	2:1	7.0	1.8	0.07
	5:1	15.9	4.4	0.18
	10:1	27.4	8.4	0.36
	15:1	36.1	12.1	0.54
	20:1	43.0	15.5	0.71
65 cSt ($M_n \approx 4000$)	2:1	3.9	1.0	0.04
	5:1	9.2	2.5	0.09
	10:1	16.8	4.8	0.19
	15:1	23.3	7.0	0.28
	20:1	28.8	9.2	0.38
750 cSt ($M_n \approx 20000$)	2:1	0.8	0.2	0.01
	5:1	2.0	0.5	0.02
	10:1	3.9	1.0	0.04
	15:1	5.8	1.5	0.06
	20:1	7.6	2.0	0.08

The TiO_2 formation hypothesis is confirmed when plotting the relative intensity of the Raman band at 1030 cm^{-1} (assigned to antisymmetric stretching of Ti−O−Si) as a function of the TiO_2 vol.% (Figure 5.15), following a linear relationship, even at a very low amount of incorporated titanium (< 3 vol.%, see inset). At high TIP/PDMS-OH molar ratios, the number of Ti−O−Si should reach a limit due to limited amount of terminal −OH group of the PDMS-OH precursors. Thus, the evolution of the relative intensity of the band may have exhibited a plateau at high TiO_2 vol.%. This could be due to limited self-condensation of the PDMS-OH chains at higher amount of TIP because of *e.g.* steric hindrance or increased kinetics of reaction. Nevertheless, the method could be an efficient tool to quantify the volume fraction of incorporated titanium in PDMS-based nanocomposites, in the condition to have standardized samples.

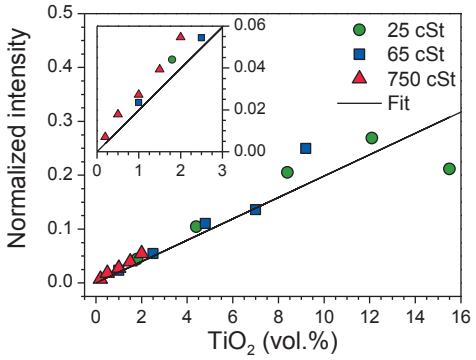

Figure 5.15. Normalized intensity (versus the Si−O−Si band at 495 cm^{-1}) of the Raman band at 1030 cm^{-1} (assigned to antisymmetric stretching of Ti−O−Si) as a function of the estimated TiO_2 vol.% of the hybrid materials and linear regression.

Moreover, in the case of the SAXS data, the interplanar spacing of the amorphous halo (d_{hkl}) attributed to PDMS follows a linear trend, decreasing with increasing the amount of incorporated titanium (Figure 5.16a), which can be due to more densely packed polymeric chains because of the increased number of surrounding inorganic nanodomains. The correlation length between the inorganic nanodomains as a function of the calculated TiO_2 vol.% follows well the behavior described by Equation (2.41), describing average distance between spherical nanodomains of the same size as a function of the volume fraction of the nanodomains. Fitting of the data gives an average nanodomain size of 3.8 nm (Figure 5.16b). The fitted size is slightly above the values estimated from the Guinier plots (Figure 5.7) giving a size between 0.8 and 1.1 nm. This difference is attributed to the fact that using Equation (2.41), the size of the titania-like nanodomains is assumed to be the same for all the samples.

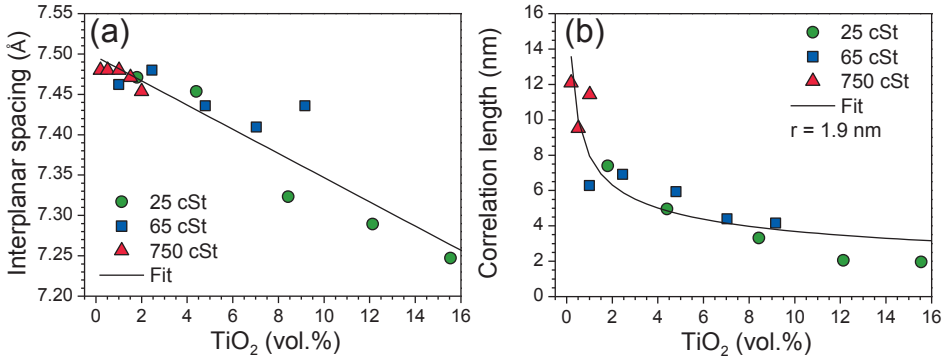

Figure 5.16. (a) Interplanar spacing of the PDMS amorphous halo with linear regression and (b) correlation length of the titania-like inorganic nanodomains from the SAXS data and fitting using Equation (2.41), as a function of the estimated TiO_2 vol.% of the hybrid materials.

The proposed hypothesis for the TiO_2 formation also allows to follow the evolution of the properties of the hybrid materials as a function of the estimated TiO_2 vol.%. The refractive index (at 589 nm) of the hybrid films as a function of the TiO_2 vol.% shows a linear behavior (Figure 5.17), similar to what could be expected from Equation (2.38), using the refractive index of anatase TiO_2 and the reference value given by the provider (1.406 at 589 nm) for the PDMS-OH precursors. Extrapolation to 100 vol.% TiO_2 gives a refractive index of 2.60, close to the one of pure anatase TiO_2 (about 2.49), resulting in a relative error of 4.1 %.

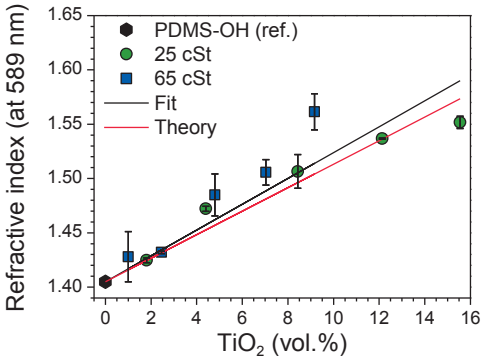

Figure 5.17. Refractive index at 589 nm (the theory line corresponds to Equation (2.38), using $n_p = 2.49$ and $n_m = 1.40$) as a function of the estimated TiO_2 vol.% of the hybrid materials and linear regression.

The contact angle of water (Figure 5.18a) follows a similar behavior as the correlation length (ζ) between the titania-like nanodomains (Figure 5.16b). In the assumption of a constant nanodomain size, the proportion of surface area of PDMS and titania-like phase is directly related to the correlation length between the domains. Within the experimental uncertainty of both analysis, a linear relationship is observed when plotting the contact angle as a function of the correlation length (Figure 5.18b).

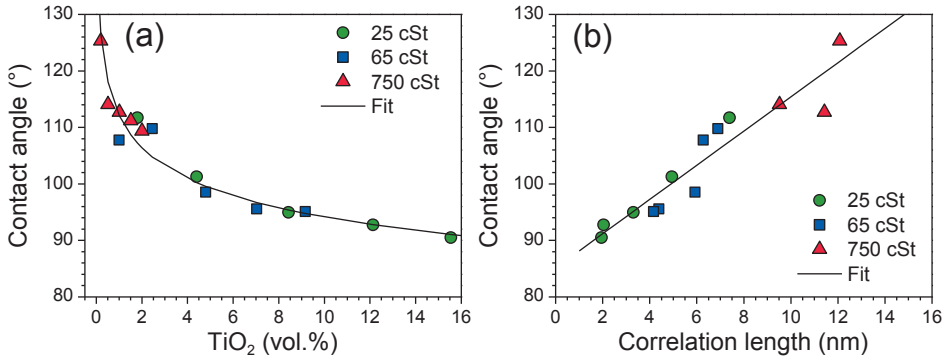

Figure 5.18. Contact angle (± 1°) of water as a function of (a) the estimated TiO_2 vol.% of the hybrid materials with power regression and (b) the correlation length of the titania-like nanodomains measured by SAXS with linear regression.

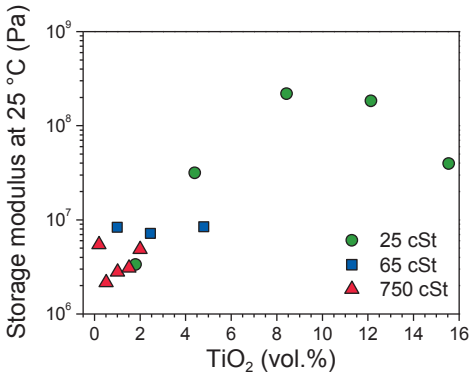

Figure 5.19. Shear storage modulus (*G'*) at 25 °C as a function of the estimated TiO_2 vol.% of the hybrid materials.

The logarithm of the shear storage modulus at room temperature is displayed in Figure 5.19. The shear storage modulus remains in the order of MPa below 4 vol.% incorporated TiO_2, however a large increase is induced at higher titania contents. SAXS data shows surface fractal at high titanium amount, which was assigned large scale aggregation of the titania-like nanodomains. In this case, percolation could have occurred as percolation of the inorganic domains has been shown to possibly lead to drastic changes of the mechanical properties of polymer nanocomposites [350].

Despite the two synthesis methods, the structure and the properties of the materials showed comparable trends (*e.g.* the contact angle of water and the correlation length in Figure 5.18b were measured on the spin-coated and thick films, respectively) which demonstrates that the synthesis routes have a limited effect on the reaction pathways and result in similar materials. However, a lower quantity of sol is used to produce the spin-coated films thus the evaporation time of the solvent (anhydrous isopropanol) is significantly reduced. The reduced reaction time (2 days in the case of the thick films) may be of interest for the industrialization of the process for the production of coatings base on this synthesis route. The relatively low temperatures of drying and curing (maximum 100 °C) also allows for more flexibility with the respect to the substrate and the synthesis condition, as this range of temperature could easily be reach by *e.g.* light-based heat sources.

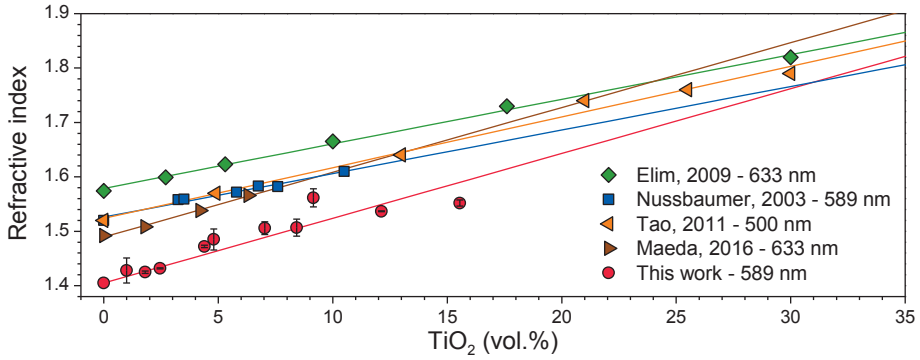

Figure 5.20. Comparison of the linear increase of the refractive index of polymer nanocomposites as a function of TiO_2 vol.% from this work and ref. [161, 167, 168, 172]. The lines are linear regressions of the data points and the wavelengths used for the measurements are labelled in the legend.

Figure 5.20 displays the refractive index of the hybrid films as a function of TiO_2 vol.% with other reported results of TiO_2 based nanocomposites. The reported values are in agreement with previous works, which follow similar trends, despite the fact that different polymer matrices and synthesis routes were used.

The high refractive index and the transparency for visible light make the polymer nanocomposites developed in this work potential materials for coatings [184, 353] or materials for optical applications [13, 329, 359, 360].

5.3. Conclusions

An *in situ* non-aqueous sol-gel route has been used to synthesize transparent PDMS−O−Ti nanocomposites. This synthesis method, initially proposed by Lu and Mullins [266], has the advantage of requiring no inhibitor neither catalyzer, because of the combined use of anhydrous isopropanol and pre-hydrolyzed polysiloxane precursor, respectively. The temperatures of drying and curing have a strong influence on the final morphology of the materials and optimizing the process is key in order to produce transparent materials [235, 240, 329].

Several characterization techniques confirmed cross-linking of the PDMS chains by TIP via the formation of Ti−O−Si bonds and titania-like inorganic nanodomains embedded in the PDMS network. The resulting materials can thus be considered as a class II organic-inorganic nanomaterial and have an average inorganic domain size < 4 nm. The correlation length between the titania-like nanodomains decreased with increased titanium content from 12 to 2 nm. A relationship between nanoscopic (correlation length) and macroscopic properties (hydrophobicity) was established. The hydrophobicity of the films was decreased (contact angle of water reduced from 126 to 91°), the refractive index was increased from 1.40 to 1.56, and the shear storage modulus at room temperature was increased from 2 to 220 MPa when the amount of titanium precursor was increased.

Finally, it was shown that the properties of the nanocomposites can be rationalized by the hypothesis of full reaction of the titanium precursor to anatase TiO_2. For example, the refractive index at 589 nm increased linearly as a function of the estimated TiO_2 vol.% with slope similar to the one predicted by the theory. The refractive index of the nanocomposites could be further increased by including high refractive index groups to the polymer precursor like phenyl groups [173, 361]. The synthesis method can be further extended by using different polymer precursors exhibiting terminal or branched −OH groups and other type of metal alkoxides.

6. Conclusions and outlook

In this work, *in situ* synthesis routes were used to prepare titania and titanium based organic-inorganic nanomaterials, using a common titanium precursor, titanium(IV) isopropoxide and silane coupling agents or hydroxy-terminated polydimethylsiloxane.

In a first part, a single-step hydrothermal synthesis was developed, allowing synthesis and simultaneous surface functionalization of the titanium dioxide nanoparticles, using different types of silane coupling agents as functionalization precursors. The surface properties and the morphology of the nanoparticles could be tuned depending on the synthesis parameters (pH, precursors ratio, and time). The synthesis parameters were thoroughly investigated to study their effect on the final properties of the materials. A combination of *ex situ* analysis, *in situ* XRD, and DFT calculations allowed to describe in detail the phenomena occurring during the growth processes, as well as the kinetics of the crystallization and growth. Furthermore, the synthesis was developed to a two-step synthesis of TiO_2-SiO_2 core-shell nanoparticles via heat treatment of the surface-functionalized TiO_2 nanoparticles. Several potential applications can be investigated for these materials, such as bio-related application (TiO_2-APTES), photocatalysis (TiO_2), or dye-sensitized solar cells (TiO_2-SiO_2), as well as further functionalization for dedicated applications. New and versatile ways to tune nanoparticle properties and simpler synthesis methods are undoubtedly attractive for potential industrial applications of advanced nanomaterials. Attempts to incorporate these titania materials to increase the refractive index of polymers relevant for the poLight application was not successful, and it was concluded that *ex situ* synthesis of the desired nanocomposites was less likely to be a feasible path for commercial applications.

In a second part, PDMS−O−Ti nanocomposites were prepared with a non-aqueous sol-gel approach. The main variables were the nature of the PDMS precursor, the TIP/PDMS-OH molar ratios, and the temperatures of the drying and curing steps. Several characterization techniques allowed to describe precisely the final structure of the nanocomposites. Further investigations would be required to understand thoroughly the reactions mechanisms involved in the formation of the titania-like heterogeneities and/or the

self-condensation of the PDMS chains. It could be evaluated via *e.g.* study of the evaporating species (mass spectroscopy) or more advance *in situ* spectroscopic techniques (nuclear magnetic resonance spectroscopy) [362]. X-ray absorption near edge structure can also be used for measuring proportion of Ti−O−Ti and Ti−O−Si [363]. Answering these questions would be of great interest to be able to adjust the synthesis conditions for the design of nanocomposites. The refractive index of the PDMS materials was successfully increased by incorporation of titania-like nanoparticles via the non-aqueous sol-gel approach. Based on this proof of concept, poLight may adapt this synthesis approach to the current technology of the TLens® and reach better optical performances. The increase of the shear storage modulus and the reduced transmittance obtained at high titanium content can further be optimized by adapting the composition of the current poLight polymer [10]. The yellow appearance can also be computationally corrected for. Nevertheless, the current synthesized materials possess properties which can be further optimized for use as coatings and materials for optics.

7. References

1. Muralt, P. Recent progress in materials issues for piezoelectric MEMS, *J. Am. Ceram. Soc.*, **91** (2008) 1385−1396. doi: 10.1111/j.1551-2916.2008.02421.x

2. Product data sheet - Packaged TLens® Silver – PAF.15.P.001, *poLight AS*, (2011).

3. poLight AS, http://www.polight.com (retrieved: December 14th 2016).

4. Nguyen, C.H.; Farghaly, M.A.; Akram, M.N.; Hanke, U. and Halvorsen, E. Electrode configurations for layered-plate piezoelectric micro-actuators, *Microelectron. Eng.*, **174** (2017) 59−63. doi: 10.1016/j.mee.2017.01.023

5. Nguyen, C.H.; Hanke, U. and Halvorsen, E. Comparison of microactuators based on piezoelectric layered plates with d_{31} and d_{33} coupling, *Proc. SPIE*, **9799** (2016) 97991C. doi: 10.1117/12.2218843

6. Farghaly, M.A.; Akram, M.N. and Halvorsen, E. Modeling framework for piezoelectrically actuated MEMS tunable lenses, *Opt. Express*, **24** (2016) 28889−28904. doi: 10.1364/OE.24.028889

7. Christensen, M.; Einarsrud, M.-A. and Grande, T. Fabrication of lead-free $Bi_{0.5}Na_{0.5}TiO_3$ thin films by aqueous chemical solution deposition, *Materials*, **10** (2017) 213. doi: 10.3390/ma10020213

8. Aksel, E. and Jones, J.L. Advances in lead-free piezoelectric materials for sensors and actuators, *Sensors*, **10** (2010) 1935−1954. doi: 10.3390/s100301935

9. Directive 2011/65/EU of the european parliament and of the council of 8 june 2011 on the restriction of the use of certain hazardous substances in electrical and electronic equipment, *Off. J. Eur. Union*, **L 174** (2011) 88−110.

10. Henriksen, L., poLight AS, *Deformable polymeric lens*, 2014, patent number: EP2781939A1.

11. Jha, G.S.; Seshadri, G.; Mohan, A. and Khandal, R.K. Development of high refractive index plastics, *E-Polymers*, **7** (2007) 1384−1408. doi: 10.1515/epoly.2007.7.1.1384

12. Nicole, L.; Laberty-Robert, C.; Rozes, L. and Sanchez, C. Hybrid materials science: A promised land for the integrative design of multifunctional materials, *Nanoscale*, **6** (2014) 6267−6292. doi: 10.1039/c4nr01788a

13. Parola, S.; Julián-López, B.; Carlos, L.D. and Sanchez, C. Optical properties of hybrid organic-inorganic materials and their applications, *Adv. Funct. Mater.*, **26** (2016) 6506−6544. doi: 10.1002/adfm.201602730

14. Lü, C.L. and Yang, B. High refractive index organic-inorganic nanocomposites: Design, synthesis and application, *J. Mater. Chem.*, **19** (2009) 2884−2901. doi: 10.1039/B816254a

15. Liu, J.G. and Ueda, M. High refractive index polymers: Fundamental research and practical applications, *J. Mater. Chem.*, **19** (2009) 8907−8919. doi: 10.1039/B909690f

16. Kango, S.; Kalia, S.; Celli, A.; Njuguna, J.; Habibi, Y. and Kumar, R. Surface modification of inorganic nanoparticles for development of organic–inorganic nanocomposites—a review, *Prog. Polym. Sci.*, **38** (2013) 1232−1261. doi: 10.1016/j.progpolymsci.2013.02.003

17. Commission recommendation of the 18 october 2011 on the definition of nanomaterial (2011/696/EU), *Off. J. Eur. Union*, **L 275** (2011) 38−40.

18. *International Organization for Standardization*, (2015) ISO/TS 80004-1:2015.

19. Banfield, J.F. and Zhang, H. Nanoparticles in the environment, *Rev. Mineral. Geochem.*, **44** (2001) 1−58. doi: 10.2138/rmg.2001.44.01

20. Binnig, G.; Rohrer, H.; Gerber, C. and Weibel, E. Surface studies by scanning tunneling microscopy, *Phys. Rev. Lett.*, **49** (1982) 57−61. doi: 10.1103/PhysRevLett.49.57

21. Binnig, G. and Rohrer, H. Scanning tunneling microscopy, *IBM J. Res. Dev.*, **30** (1986) 355−369.

22. Binnig, G.; Quate, C.F. and Gerber, C. Atomic force microscope, *Phys. Rev. Lett.*, **56** (1986) 930−933. doi: 10.1103/PhysRevLett.56.930

23. Roduner, E. Size matters: Why nanomaterials are different, *Chem. Soc. Rev.*, **35** (2006) 583−592. doi: 10.1039/b502142c

24. Hanemann, T. and Szabó, D.V. Polymer-nanoparticle composites: From synthesis to modern applications, *Materials*, **3** (2010) 3468−3517. doi: 10.3390/ma3063468

25. Ahmad, M.I. and Bhattacharya, S.S. Size effect on the lattice parameters of nanocrystalline anatase, *Appl. Phys. Lett.*, **95** (2009) 191906. doi: 10.1063/1.3261754

26. Emory, S.R.; Haskins, W.E. and Nie, S. Direct observation of size-dependent optical enhancement in single metal nanoparticles, *J. Am. Chem. Soc.*, **120** (1998) 8009−8010. doi: 10.1021/ja9815677

27. Satoh, N.; Nakashima, T.; Kamikura, K. and Yamamoto, K. Quantum size effect in TiO_2 nanoparticles prepared by finely controlled metal assembly on dendrimer templates, *Nat. Nanotechnol.*, **3** (2008) 106−111. doi: 10.1038/nnano.2008.2

28. de Mello Donegá, C. The nanoscience paradigm: "Size matters!", in *Nanoparticles: Workhorses of nanoscience*, de Mello Donegá, C., Ed., 2014, Springer: Heidelberg, Germany, 1−12. doi: 10.1007/978-3-662-44823-6_1

29. Brinker, C.J. and Scherer, G.W. *Sol-gel science: The physics and chemistry of sol–gel processing*. 1990, Academic Press: San Diego, CA, USA. doi: 10.1016/B978-0-08-057103-4.50001-5

30. Rozes, L.; D'Arras, L.; Hoffman, C.; Potier, F.; Halttunen, N. and Nicole, L. Titania-based hybrid materials: From molecular precursors to the controlled design of hierarchical hybrid materials, in *Chemistry of organo-hybrids: Synthesis and characterization of functional nano-objects*, Charleux, B.; Copéret, C. and Lacôte, E., Eds., 2015, John Wiley & Sons: Hoboken, NJ, USA, 114−167. doi: 10.1002/9781118870068.ch4

31. Bradley, D.C.; Mehrotra, R.C.; Rothwell, I.P. and Singh, A. *Alkoxo and aryloxo derivatives of metals*. 2001, Academic Press: London, UK. doi: 10.1016/B978-0-12-124140-7.50009-8

32. Wen, J. and Wilkes, G.L. Organic/inorganic hybrid network materials by the sol−gel approach, *Chem. Mater.*, **8** (1996) 1667−1681. doi: 10.1021/cm9601143

33. Sanchez, C. and Ribot, F. Design of hybrid organic-inorganic materials synthesized via sol-gel chemistry, *New J. Chem.*, **18** (1994) 1007−1047.

34. Schubert, U. Chemical modification of titanium alkoxides for sol-gel processing, *J. Mater. Chem.*, **15** (2005) 3701−3715. doi: 10.1039/B504269K

35. Sanchez, C.; Livage, J.; Henry, M. and Babonneau, F. Chemical modification of alkoxide precursors, *J. Non-Cryst. Solids*, **100** (1988) 65−76. doi: 10.1016/0022-3093(88)90007-5

36. Livage, J.; Henry, M. and Sanchez, C. Sol-gel chemistry of transition metal oxides, *Prog. Solid State Chem.*, **18** (1988) 259−341. doi: 10.1016/0079-6786(88)90005-2

37. Schmidt, H.; Scholze, H. and Kaiser, A. Principles of hydrolysis and condensation reaction of alkoxysilanes, *J. Non-Cryst. Solids*, **63** (1984) 1−11. doi: 10.1016/0022-3093(84)90381-8

38. Schaefer, D.W. Polymers, fractals, and ceramic materials, *Science*, **243** (1989) 1023−1027. doi: 10.1126/science.243.4894.1023

39. Blanchard, J.; Ribot, F.; Sanchez, C.; Bellot, P.-V. and Trokiner, A. Structural characterization of titanium-oxo-polymers synthesized in the presence of protons or complexing ligands as inhibitors, *J. Non-Cryst. Solids*, **265** (2000) 83−97. doi: 10.1016/S0022-3093(99)00885-6

40. Niederberger, M. and Pinna, N. *Metal oxide nanoparticles in organic solvents*. 2009, Springer: London, UK. doi: 10.1007/978-1-84882-671-7

41. Mutin, P.H. and Vioux, A. Recent advances in the synthesis of inorganic materials via non-hydrolytic condensation and related low-temperature routes, *J. Mater. Chem. A*, **1** (2013) 11504−11512. doi: 10.1039/c3ta12058a

42. Mutin, P.H. and Vioux, A. Nonhydrolytic processing of oxide-based materials: Simple routes to control homogeneity, morphology, and nanostructure, *Chem. Mater.*, **21** (2009) 582−596. doi: 10.1021/cm802348c

43. Rabenau, A. The role of hydrothermal synthesis in preparative chemistry, *Angew. Chem. Int. Ed.*, **24** (1985) 1026−1040. doi: 10.1002/anie.198510261

44. Byrappa, K. and Adschiri, T. Hydrothermal technology for nanotechnology, *Prog. Cryst. Growth Charact. Mater.*, **53** (2007) 117−166. doi: 10.1016/j.pcrysgrow.2007.04.001

45. Einarsrud, M.-A. and Grande, T. 1D oxide nanostructures from chemical solutions, *Chem. Soc. Rev.*, **43** (2014) 2187−2199. doi: 10.1039/c3cs60219b

46. Hayashi, H. and Torii, K. Hydrothermal synthesis of titania photocatalyst under subcritical and supercritical water conditions, *J. Mater. Chem.*, **12** (2002) 3671−3676. doi: 10.1039/B207052A

47. Hayashi, H. and Hakuta, Y. Hydrothermal synthesis of metal oxide nanoparticles in supercritical water, *Materials*, **3** (2010) 3794−3817. doi: 10.3390/ma3073794

48. Pighini, C.; Aymes, D.; Millot, N. and Saviot, L. Low-frequency Raman characterization of size-controlled anatase TiO_2 nanopowders prepared by continuous hydrothermal syntheses, *J. Nanopart. Res.*, **9** (2006) 309−315. doi: 10.1007/s11051-005-9061-6

49. Thomas, G.; Demoisson, F.; Boudon, J. and Millot, N. Efficient functionalization of magnetite nanoparticles with phosphonate using a one-step continuous hydrothermal process, *Dalton Trans.*, **45** (2016) 10821−10829. doi: 10.1039/c6dt01050d

50. Walton, R.I. Subcritical solvothermal synthesis of condensed inorganic materials, *Chem. Soc. Rev.*, **31** (2002) 230−238. doi: 10.1039/b105762f

51. Morris, R.E. Ionothermal synthesis-ionic liquids as functional solvents in the preparation of crystalline materials, *Chem. Commun.*, (2009) 2990−2998. doi: 10.1039/b902611h

52. Taubert, A. and Li, Z. Inorganic materials from ionic liquids, *Dalton Trans.*, (2007) 723−727. doi: 10.1039/b616593a

53. Byrappa, K. and Yoshimura, M. Hydrothermal technology for nanotechnology—a technology for processing of advanced materials, in *Handbook of hydrothermal technology*, Byrappa, K. and Yoshimura, M., Eds., 2013, William Andrew Publishing: Oxford, UK, 615−762. doi: 10.1016/B978-0-12-375090-7.00010-4

54. Danks, A.E.; Hall, S.R. and Schnepp, Z. The evolution of 'sol–gel' chemistry as a technique for materials synthesis, *Mater. Horiz.*, **3** (2016) 91−112. doi: 10.1039/c5mh00260e

55. Claudionico, wikimedia commons, sol-gel scheme, http://commons.wikimedia.org/wiki/File:Sol-Gel_Scheme.svg (retrieved: February 23rd 2017).

56. Sunde, T.O.L.; Grande, T. and Einarsrud, M.-A. Modified Pechini synthesis of oxide powders and thin films, in *Handbook of sol-gel science and technology*, Klein, L.; Aparicio, M. and Jitianu, A., Eds., 2016, Springer: Cham, Switzerland, 1−30. doi: 10.1007/978-3-319-19454-7_130-1

57. Zhou, H.; Einarsrud, M.-A. and Vullum-Bruer, F. PVA-assisted combustion synthesis and characterization of porous nanocomposite Li_2FeSiO_4/C, *Solid State Ionics*, **225** (2012) 585−589. doi: 10.1016/j.ssi.2011.12.008

58. Vioux, A. Nonhydrolytic sol−gel routes to oxides, *Chem. Mater.*, **9** (1997) 2292−2299. doi: 10.1021/cm970322a

59. Thanh, N.T.; Maclean, N. and Mahiddine, S. Mechanisms of nucleation and growth of nanoparticles in solution, *Chem. Rev.*, **114** (2014) 7610−7630. doi: 10.1021/cr400544s

60. Sear, R.P. Quantitative studies of crystal nucleation at constant supersaturation: Experimental data and models, *CrystEngComm*, **16** (2014) 6506−6522. doi: 10.1039/c4ce00344f

61. Myerson, A.S. Concluding remarks, *Faraday Discuss.*, **179** (2015) 543−547. doi: 10.1039/c5fd00042d

62. Xue, X.; Penn, R.L.; Leite, E.R.; Huang, F. and Lin, Z. Crystal growth by oriented attachment: Kinetic models and control factors, *CrystEngComm*, **16** (2014) 1419−1429. doi: 10.1039/C3CE42129E

63. Stølen, S. and Grande, T. *Chemical thermodynamics of materials: Macroscopic and microscopic aspects*. 2003, John Wiley & Sons: Chichester, UK.

64. Huang, F.; Zhang, H. and Banfield, J.F. Two-stage crystal-growth kinetics observed during hydrothermal coarsening of nanocrystalline ZnS, *Nano Lett.*, **3** (2003) 373−378. doi: 10.1021/nl025836+

65. Wagner, C. Theorie der alterung von niederschlägen durch umlösen (Ostwald-reifung), *Z. Elektrochem.*, **65** (1961) 581−591. doi: 10.1002/bbpc.19610650704

66. Kirchner, H.O.K. Coarsening of grain-boundary precipitates, *Metall. Trans.*, **2** (1971) 2861−2864. doi: 10.1007/bf02813264

67. Speight, M.V. Growth kinetics of grain-boundary precipitates, *Acta Metall.*, **16** (1968) 133−135. doi: 10.1016/0001-6160(68)90081-3

68. Ivanov, V.K.; Fedorov, P.P.; Baranchikov, A.Y. and Osiko, V.V. Oriented attachment of particles: 100 years of investigations of non-classical crystal growth, *Russ. Chem. Rev.*, **83** (2014) 1204−1222. doi: 10.1070/RCR4453

69. Niederberger, M. and Cölfen, H. Oriented attachment and mesocrystals: Non-classical crystallization mechanisms based on nanoparticle assembly, *Phys. Chem. Chem. Phys.*, **8** (2006) 3271−3287. doi: 10.1039/b604589h

70. Penn, R.L. and Banfield, J.F. Imperfect oriented attachment: Dislocation generation in defect-free nanocrystals, *Science*, **281** (1998) 969−971. doi: 10.1126/science.281.5379.969

71. Penn, R.L. and Banfield, J.F. Morphology development and crystal growth in nanocrystalline aggregates under hydrothermal conditions: Insights from titania, *Geochim. Cosmochim. Acta*, **63** (1999) 1549−1557. doi: 10.1016/s0016-7037(99)00037-x

72. Penn, R.L. and Banfield, J.F. Oriented attachment and growth, twinning, polytypism, and formation of metastable phases; insights from nanocrystalline TiO_2, *Am. Mineral.*, **83** (1998) 1077−1082. doi: 10.2138/am-1998-9-1016

73. Huang, F.; Zhang, H. and Banfield, J.F. The role of oriented attachment crystal growth in hydrothermal coarsening of nanocrystalline ZnS, *J. Phys. Chem. B*, **107** (2003) 10470−10475. doi: 10.1021/jp035518e

74. Xue, X.; Huang, Y.; Zhuang, Z.; Huang, F. and Lin, Z. Temperature-sensitive growth kinetics and photoluminescence properties of CdS quantum dots, *CrystEngComm*, **15** (2013) 4963−4969. doi: 10.1039/c3ce40478a

75. Zhang, Y.; Li, L.; Zheng, J.; Li, Q.; Zuo, Y.; Yang, E. and Li, G. Two-step grain-growth kinetics of sub-7 nm SnO_2 nanocrystal under hydrothermal condition, *J. Phys. Chem. C*, **119** (2015) 19505−19512. doi: 10.1021/acs.jpcc.5b05282

76. Zhan, H.; Yang, X.; Wang, C.; Liang, C. and Wu, M. Multiple growth stages and their kinetic models of anatase nanoparticles under hydrothermal conditions, *J. Phys. Chem. C*, **114** (2010) 14461−14466. doi: 10.1021/jp1062308

77. Brazeau, A.L. and Jones, N.D. Growth mechanisms in nanocrystalline lead sulfide by stopped-flow kinetic analysis, *J. Phys. Chem. C*, **113** (2009) 20246−20251. doi: 10.1021/jp907270x

78. Penn, R.L. and Soltis, J.A. Characterizing crystal growth by oriented aggregation, *CrystEngComm*, **16** (2014) 1409−1418. doi: 10.1039/C3CE41773E

79. Cölfen, H. and Antonietti, M. Mesocrystals: Inorganic superstructures made by highly parallel crystallization and controlled alignment, *Angew. Chem. Int. Ed.*, **44** (2005) 5576−5591. doi: 10.1002/anie.200500496

80. Yin, Y. and Alivisatos, A.P. Colloidal nanocrystal synthesis and the organic-inorganic interface, *Nature*, **437** (2005) 664−670. doi: 10.1038/nature04165

81. Zhu, T. and Gao, S.-P. The stability, electronic structure, and optical property of TiO_2 polymorphs, *J. Phys. Chem. C*, **118** (2014) 11385−11396. doi: 10.1021/jp412462m

82. Chen, X. and Mao, S.S. Titanium dioxide nanomaterials: Synthesis, properties, modifications, and applications, *Chem. Rev.*, **107** (2007) 2891−2959. doi: 10.1021/cr0500535

83. Fujishima, A. and Honda, K. Electrochemical photolysis of water at a semiconductor electrode, *Nature*, **238** (1972) 37−38. doi: 10.1038/238037a0

84. Diebold, U. The surface science of titanium dioxide, *Surf. Sci. Rep.*, **48** (2003) 53−229. doi: 10.1016/S0167-5729(02)00100-0

85. *Titanium dioxide nanomaterials* special issue, *Chem. Rev.*, **114(19)** (2014) 9281−10216. doi: 10.1021/cr500422r

86. Chen, X.; Liu, L. and Huang, F. Black titanium dioxide (TiO_2) nanomaterials, *Chem. Soc. Rev.*, **44** (2015) 1861−1885. doi: 10.1039/c4cs00330f

87. Schneider, J.; Matsuoka, M.; Takeuchi, M.; Zhang, J.; Horiuchi, Y.; Anpo, M. and Bahnemann, D.W. Understanding TiO_2 photocatalysis: Mechanisms and materials, *Chem. Rev.*, **114** (2014) 9919−9986. doi: 10.1021/cr5001892

88. Zhang, J.; Zhou, P.; Liu, J. and Yu, J. New understanding of the difference of photocatalytic activity among anatase, rutile and brookite TiO_2, *Phys. Chem. Chem. Phys.*, **16** (2014) 20382−20386. doi: 10.1039/c4cp02201g

89. Asahi, R.; Morikawa, T.; Irie, H. and Ohwaki, T. Nitrogen-doped titanium dioxide as visible-light-sensitive photocatalyst: Designs, developments, and prospects, *Chem. Rev.*, **114** (2014) 9824−9852. doi: 10.1021/cr5000738

90. Pan, J.; Liu, G.; Lu, G.Q. and Cheng, H.M. On the true photoreactivity order of {001}, {010}, and {101} facets of anatase TiO_2 crystals, *Angew. Chem. Int. Ed.*, **50** (2011) 2133−2137. doi: 10.1002/anie.201006057

91. Fujishima, A.; Zhang, X. and Tryk, D. TiO_2 photocatalysis and related surface phenomena, *Surf. Sci. Rep.*, **63** (2008) 515−582. doi: 10.1016/j.surfrep.2008.10.001

92. Bai, Y.; Mora-Seró, I.; De Angelis, F.; Bisquert, J. and Wang, P. Titanium dioxide nanomaterials for photovoltaic applications, *Chem. Rev.*, **114** (2014) 10095−10130. doi: 10.1021/cr400606n

93. Barbé, C.J.; Arendse, F.; Comte, P.; Jirousek, M.; Lenzmann, F.; Shklover, V. and Grätzel, M. Nanocrystalline titanium oxide electrodes for photovoltaic applications, *J. Am. Ceram. Soc.*, **80** (2005) 3157−3171. doi: 10.1111/j.1151-2916.1997.tb03245.x

94. Lekphet, W.; Ke, T.-C.; Su, C.; Kathirvel, S.; Sireesha, P.; Akula, S.B. and Li, W.-R. Morphology control studies of TiO_2 microstructures via surfactant-assisted hydrothermal process for dye-sensitized solar cell applications, *Appl. Surf. Sci.*, **382** (2016) 15−26. doi: 10.1016/j.apsusc.2016.04.115

95. Anajafi, Z.; Marandi, M. and Taghavinia, N. Hydrothermal synthesis of TiO_2 nanocrystals in different basic pHs and their applications in dye sensitized solar cells, *Physica E*, **70** (2015) 113−120. doi: 10.1016/j.physe.2015.02.023

96. Kwon, S.J.; Im, H.B.; Nam, J.E.; Kang, J.K.; Hwang, T.S. and Yi, K.B. Hydrothermal synthesis of rutile–anatase TiO_2 nanobranched arrays for efficient dye-sensitized solar cells, *Appl. Surf. Sci.*, **320** (2014) 487−493. doi: 10.1016/j.apsusc.2014.09.110

97. Pan, J.; Wu, X.; Wang, L.; Liu, G.; Lu, G.Q. and Cheng, H.M. Synthesis of anatase TiO_2 rods with dominant reactive {010} facets for the photoreduction of CO_2 to CH_4 and use in dye-sensitized solar cells, *Chem. Commun.*, **47** (2011) 8361−8363. doi: 10.1039/c1cc13034j

98. Nowotny, J.; Bak, T.; Nowotny, M. and Sheppard, L. Titanium dioxide for solar-hydrogen II. Defect chemistry, *Int. J. Hydrogen Energy*, **32** (2007) 2630−2643. doi: 10.1016/j.ijhydene.2006.09.005

99. Adachi, M.; Murata, Y.; Takao, J.; Jiu, J.; Sakamoto, M. and Wang, F. Highly efficient dye-sensitized solar cells with a titania thin-film electrode composed of a network structure of single-crystal-like TiO_2 nanowires made by the "oriented attachment" mechanism, *J. Am. Chem. Soc.*, **126** (2004) 14943−14949. doi: 10.1021/ja048068s

100. Zhang, Y.; Jiang, Z.; Huang, J.; Lim, L.Y.; Li, W.; Deng, J.; Gong, D.; Tang, Y.; Lai, Y. and Chen, Z. Titanate and titania nanostructured materials for environmental and energy applications: A review, *RSC Adv.*, **5** (2015) 79479−79510. doi: 10.1039/c5ra11298b

101. Zhang, J.; Cai, Y.; Hou, X.; Song, X.; Lv, P.; Zhou, H. and Wei, Q. Fabrication of hierarchically porous TiO_2 nanofibers by microemulsion electrospinning and their application as anode material for lithium-ion batteries, *Beilstein J. Nanotechnol.*, **8** (2017) 1297−1306. doi: 10.3762/bjnano.8.131

102. Kubacka, A.; Diez, M.S.; Rojo, D.; Bargiela, R.; Ciordia, S.; Zapico, I.; Albar, J.P.; Barbas, C.; Martins dos Santos, V.A.; Fernandez-Garcia, M. and Ferrer, M. Understanding the antimicrobial mechanism of TiO_2-based nanocomposite films in a pathogenic bacterium, *Sci. Rep.*, **4** (2014) 4134. doi: 10.1038/srep04134

103. Rajh, T.; Dimitrijevic, N.M.; Bissonnette, M.; Koritarov, T. and Konda, V. Titanium dioxide in the service of the biomedical revolution, *Chem. Rev.*, **114** (2014) 10177−10216. doi: 10.1021/cr500029g

104. Xie, J.; Pan, X.; Wang, M.; Yao, L.; Liang, X.; Ma, J.; Fei, Y.; Wang, P.-N. and Mi, L. Targeting and photodynamic killing of cancer cell by nitrogen-doped titanium dioxide coupled with folic acid, *Nanomaterials*, **6** (2016) 113. doi: 10.3390/nano6060113

105. Xie, J.; Pan, X.; Wang, M.; Ma, J.; Fei, Y.; Wang, P.N. and Mi, L. The role of surface modification for TiO_2 nanoparticles in cancer cells, *Colloids Surf., B*, **143** (2016) 148−155. doi: 10.1016/j.colsurfb.2016.03.029

106. Hou, J.; Dong, G.; Ye, Y. and Chen, V. Laccase immobilization on titania nanoparticles and titania-functionalized membranes, *J. Membr. Sci.*, **452** (2014) 229−240. doi: 10.1016/j.memsci.2013.10.019

107. Gao, Z.D.; Guan, F.F.; Li, C.Y.; Liu, H.F. and Song, Y.Y. Signal-amplified platform for electrochemical immunosensor based on TiO_2 nanotube arrays using a HRP tagged antibody-Au nanoparticles as probe, *Biosens. Bioelectron.*, **41** (2013) 771−775. doi: 10.1016/j.bios.2012.10.006

108. Zhuo, Y.; Chai, Y.Q.; Yuan, R.; Mao, L.; Yuan, Y.L. and Han, J. Glucose oxidase and ferrocene labels immobilized at Au/TiO_2 nanocomposites with high load amount and activity for sensitive immunoelectrochemical measurement of ProGRP biomarker, *Biosens. Bioelectron.*, **26** (2011) 3838−3844. doi: 10.1016/j.bios.2011.02.043

109. Yamaguchi, K.; Sugiyama, T.; Kato, S.; Kondo, Y.; Ageyama, N.; Kanekiyo, M.; Iwata, M.; Koyanagi, Y.; Yamamoto, N. and Honda, M. A novel CD4-conjugated ultraviolet light-activated photocatalyst inactivates HIV-1 and SIV efficiently, *J. Med. Virol.*, **80** (2008) 1322−1331. doi: 10.1002/jmv.21235

110. Kwon, D.H.; Kim, K.M.; Jang, J.H.; Jeon, J.M.; Lee, M.H.; Kim, G.H.; Li, X.S.; Park, G.S.; Lee, B.; Han, S.; Kim, M. and Hwang, C.S. Atomic structure of conducting nanofilaments in TiO_2 resistive switching memory, *Nat. Nanotechnol.*, **5** (2010) 148−153. doi: 10.1038/nnano.2009.456

111. Szot, K.; Rogala, M.; Speier, W.; Klusek, Z.; Besmehn, A. and Waser, R. TiO_2–a prototypical memristive material, *Nanotechnology*, **22** (2011) 254001. doi: 10.1088/0957-4484/22/25/254001

112. Strachan, J.P.; Pickett, M.D.; Yang, J.J.; Aloni, S.; David Kilcoyne, A.L.; Medeiros-Ribeiro, G. and Stanley Williams, R. Direct identification of the conducting channels in a functioning memristive device, *Adv. Mater.*, **22** (2010) 3573−3577. doi: 10.1002/adma.201000186

113. Caseri, W.R. Inorganic nanoparticles as optically effective additives for polymers, *Chem. Eng. Commun.*, **196** (2009) 549−572. doi: 10.1080/00986440802483954

114. Szabó, D.V. and Hanemann, T. Polymer nanocomposites for optical applications, in *Advances in polymer nanocomposites: Types and applications*, 2012, Woodhead: Philadelphia, PA, USA, 567−604.

115. Ohko, Y.; Saitoh, S.; Tatsuma, T. and Fujishima, A. Photoelectrochemical anticorrosion and self-cleaning effects of a TiO_2 coating for type 304 stainless steel, *J. Electrochem. Soc.*, **148** (2001) B24−B28. doi: 10.1149/1.1339030

116. Bettini, S.; Boutet-Robinet, E.; Cartier, C.; Comera, C.; Gaultier, E.; Dupuy, J.; Naud, N.; Tache, S.; Grysan, P.; Reguer, S.; Thieriet, N.; Refregiers, M.; Thiaudiere, D.; Cravedi, J.P.; Carriere, M.; Audinot, J.N.; Pierre, F.H.; Guzylack-Piriou, L. and Houdeau, E. Food-grade TiO_2 impairs intestinal and systemic immune homeostasis, initiates preneoplastic lesions and promotes aberrant crypt development in the rat colon, *Sci. Rep.*, **7** (2017) 40373. doi: 10.1038/srep40373

117. Andersson, P.O.; Lejon, C.; Ekstrand-Hammarstrom, B.; Akfur, C.; Ahlinder, L.; Bucht, A. and Osterlund, L. Polymorph- and size-dependent uptake and toxicity of TiO_2 nanoparticles in living lung epithelial cells, *Small*, **7** (2011) 514−523. doi: 10.1002/smll.201001832

118. Jin, C.; Tang, Y.; Yang, F.G.; Li, X.L.; Xu, S.; Fan, X.Y.; Huang, Y.Y. and Yang, Y.J. Cellular toxicity of TiO_2 nanoparticles in anatase and rutile crystal phase, *Biol. Trace Elem. Res.*, **141** (2011) 3−15. doi: 10.1007/s12011-010-8707-0

119. Kuku, G. and Culha, M. Investigating the origins of toxic response in TiO_2 nanoparticle-treated cells, *Nanomaterials*, **7** (2017) 83. doi: 10.3390/nano7040083

120. Song, B.; Zhang, Y.; Liu, J.; Feng, X.; Zhou, T. and Shao, L. Unraveling the neurotoxicity of titanium dioxide nanoparticles: Focusing on molecular mechanisms, *Beilstein J. Nanotechnol.*, **7** (2016) 645−654. doi: 10.3762/bjnano.7.57

121. Zhang, H. and Banfield, J.F. Structural characteristics and mechanical and thermodynamic properties of nanocrystalline TiO_2, *Chem. Rev.*, **114** (2014) 9613−9644. doi: 10.1021/cr500072j

122. Smith, S.J.; Stevens, R.; Liu, S.; Li, G.; Navrotsky, A.; Boerio-Goates, J. and Woodfield, B.F. Heat capacities and thermodynamic functions of TiO_2 anatase and rutile: Analysis of phase stability, *Am. Mineral.*, **94** (2009) 236−243. doi: 10.2138/am.2009.3050

123. Momma, K. and Izumi, F. *VESTA 3* for three-dimensional visualization of crystal, volumetric and morphology data, *J. Appl. Crystallogr.*, **44** (2011) 1272−1276. doi: 10.1107/s0021889811038970

124. Oliver, P.M.; Watson, G.W.; Toby Kelsey, E. and Parker, S.C. Atomistic simulation of the surface structure of the TiO_2 polymorphs rutile and anatase, *J. Mater. Chem.*, **7** (1997) 563−568. doi: 10.1039/A606353E

125. Zhang, H. and F. Banfield, J. Thermodynamic analysis of phase stability of nanocrystalline titania, *J. Mater. Chem.*, **8** (1998) 2073−2076. doi: 10.1039/A802619J

126. Naicker, P.K.; Cummings, P.T.; Zhang, H. and Banfield, J.F. Characterization of titanium dioxide nanoparticles using molecular dynamics simulations, *J. Phys. Chem. B*, **109** (2005) 15243−15249. doi: 10.1021/jp050963q

127. Zhou, Y. and Fichthorn, K.A. Microscopic view of nucleation in the anatase-to-rutile transformation, *J. Phys. Chem. C*, **116** (2012) 8314−8321. doi: 10.1021/jp301228x

128. Ranade, M.R.; Navrotsky, A.; Zhang, H.Z.; Banfield, J.F.; Elder, S.H.; Zaban, A.; Borse, P.H.; Kulkarni, S.K.; Doran, G.S. and Whitfield, H.J. Energetics of nanocrystalline TiO_2, *Proc. Natl. Acad. Sci. U.S.A.*, **99** (2002) 6476−6481. doi: 10.1073/pnas.251534898

129. Mitsuhashi, T. and Kleppa, O.J. Transformation enthalpies of the TiO_2 polymorphs, *J. Am. Ceram. Soc.*, **62** (1979) 356−357. doi: 10.1111/j.1151-2916.1979.tb19077.x

130. Castro, R.H.R. On the thermodynamic stability of nanocrystalline ceramics, *Mater. Lett.*, **96** (2013) 45−56. doi: 10.1016/j.matlet.2013.01.007

131. Levchenko, A.A.; Li, G.; Boerio-Goates, J.; Woodfield, B.F. and Navrotsky, A. TiO_2 stability landscape: Polymorphism, surface energy, and bound water energetics, *Chem. Mater.*, **18** (2006) 6324−6332. doi: 10.1021/cm061183c

132. Castro, R.H.R. and Wang, B. The hidden effect of interface energies in the polymorphic stability of nanocrystalline titanium dioxide, *J. Am. Ceram. Soc.*, **94** (2011) 918−924. doi: 10.1111/j.1551-2916.2010.04164.x

133. Barnard, A.S.; Zapol, P. and Curtiss, L.A. Anatase and rutile surfaces with adsorbates representative of acidic and basic conditions, *Surf. Sci.*, **582** (2005) 173−188. doi: 10.1016/j.susc.2005.03.014

134. Barnard, A.S. and Curtiss, L.A. Prediction of TiO_2 nanoparticle phase and shape transitions controlled by surface chemistry, *Nano Lett.*, **5** (2005) 1261−1266. doi: 10.1021/nl050355m

135. Barnard, A.S. and Xu, H. An environmentally sensitive phase map of titania nanocrystals, *ACS Nano*, **2** (2008) 2237−2242. doi: 10.1021/nn800446w

136. Finnegan, M.P.; Zhang, H. and Banfield, J.F. Phase stability and transformation in titania nanoparticles in aqueous solutions dominated by surface energy, *J. Phys. Chem. C*, **111** (2007) 1962−1968. doi: 10.1021/jp063822c

137. Bourikas, K.; Hiemstra, T. and Van Riemsdijk, W.H. Ion pair formation and primary charging behavior of titanium oxide (anatase and rutile), *Langmuir*, **17** (2001) 749−756. doi: 10.1021/la000806c

138. Kumar, S.G. and Rao, K.S. Polymorphic phase transition among the titania crystal structures using a solution-based approach: From precursor chemistry to nucleation process, *Nanoscale*, **6** (2014) 11574−11632. doi: 10.1039/c4nr01657b

139. Cheng, H.; Ma, J.; Zhao, Z. and Qi, L. Hydrothermal preparation of uniform nanosize rutile and anatase particles, *Chem. Mater.*, **7** (1995) 663−671. doi: 10.1021/cm00052a010

140. Aruna, S.T.; Tirosh, S. and Zaban, A. Nanosize rutile titania particle synthesis a hydrothermal method without mineralizers, *J. Mater. Chem.*, **10** (2000) 2388−2391. doi: 10.1039/B001718N

141. Yin, H.; Wada, Y.; Kitamura, T.; Kambe, S.; Murasawa, S.; Mori, H.; Sakata, T. and Yanagida, S. Hydrothermal synthesis of nanosized anatase and rutile TiO_2 using amorphous phase TiO_2, *J. Mater. Chem.*, **11** (2001) 1694−1703. doi: 10.1039/b008974p

142. Chae, S.Y.; Park, M.K.; Lee, S.K.; Kim, T.Y.; Kim, S.K. and Lee, W.I. Preparation of size-controlled TiO_2 nanoparticles and derivation of optically transparent photocatalytic films, *Chem. Mater.*, **15** (2003) 3326−3331. doi: 10.1021/cm030171d

143. Kim, C.-S.; Moon, B.K.; Park, J.-H.; Choi, B.-C. and Seo, H.-J. Solvothermal synthesis of nanocrystalline TiO_2 in toluene with surfactant, *J. Cryst. Growth*, **257** (2003) 309−315. doi: 10.1016/S0022-0248(03)01468-4

144. Kolen'ko, Y.V.; Burukhin, A.A.; Churagulov, B.R. and Oleynikov, N.N. Synthesis of nanocrystalline TiO_2 powders from aqueous $TiOSO_4$ solutions under hydrothermal conditions, *Mater. Lett.*, **57** (2003) 1124−1129. doi: 10.1016/S0167-577x(02)00943-6

145. Reyes-Coronado, D.; Rodríguez-Gattorno, G.; Espinosa-Pesqueira, M.E.; Cab, C.; de Coss, R. and Oskam, G. Phase-pure TiO_2 nanoparticles: Anatase, brookite and rutile, *Nanotechnology*, **19** (2008) 145605. doi: 10.1088/0957-4484/19/14/145605

146. Dinh, C.T.; Nguyen, T.D.; Kleitz, F. and Do, T.O. Shape-controlled synthesis of highly crystalline titania nanocrystals, *ACS Nano*, **3** (2009) 3737−3743. doi: 10.1021/nn900940p

147. Darbandi, M. and Dickerson, J.H. Nanoscale engineering of TiO_2 nanoparticles: Evolution of the shape, phase, morphology, and facet orientation, *Mater. Lett.*, **180** (2016) 212−218. doi: 10.1016/j.matlet.2016.05.109

148. Painter, P.C. and Coleman, M.M. *Fundamentals of polymer science: An introductory text, second edition*. 1998, CRC Press: Boca Raton, FL, USA.

149. Stepto, R.F.T. Dispersity in polymer science (IUPAC recommendations 2009), *Pure Appl. Chem.*, **81** (2009) 351−353. doi: 10.1351/pac-rec-08-05-02

150. Fox, T.G. and Flory, P.J. Second-order transition temperatures and related properties of polystyrene. I. Influence of molecular weight, *J. Appl. Phys.*, **21** (1950) 581−591. doi: 10.1063/1.1699711

151. Seyferth, D. Dimethyldichlorosilane and the direct synthesis of methylchlorosilanes. The key to the silicones industry, *Organometallics*, **20** (2001) 4978−4992. doi: 10.1021/om0109051

152. Rochow, E.G. The direct synthesis of organosilicon compounds, *J. Am. Chem. Soc.*, **67** (1945) 963−965. doi: 10.1021/ja01222a026

153. Scott, D.W. Thermal rearrangement of branched-chain methylpolysiloxanes, *J. Am. Chem. Soc.*, **68** (1946) 356−358. doi: 10.1021/ja01207a003

154. Patnode, W. and Wilcock, D.F. Methylpolysiloxanes, *J. Am. Chem. Soc.*, **68** (1946) 358−363. doi: 10.1021/ja01207a004

155. Barry, A.J. Viscometric investigation of dimethylsiloxane polymers, *J. Appl. Phys.*, **17** (1946) 1020−1024. doi: 10.1063/1.1707670

156. Kataoka, T. and Ueda, S. Viscosity–molecular weight relationship for polydimethylsiloxane, *J. Polym. Sci., Part C: Polym. Lett.*, **4** (1966) 317−322. doi: 10.1002/pol.1966.110040503

157. Kuo, A.C.M. Poly(dimethylsiloxane), in *Polymer data handbook (second edition)*, Mark, J.E., Ed., 2009, Oxford University Press: New York, NY, USA, 539−561.

158. de Gennes, P.-G. Entangled polymers, *Phys. Today*, **36** (1983) 33−39. doi: 10.1063/1.2915700

159. Clarson, S.J.; Dodgson, K. and Semlyen, J.A. Studies of cyclic and linear poly(dimethylsiloxanes): 19. Glass transition temperatures and crystallization behaviour, *Polymer*, **26** (1985) 930−934. doi: 10.1016/0032-3861(85)90140-5

160. Fox, T.G. and Flory, P.J. The glass temperature and related properties of polystyrene. Influence of molecular weight, *J. Polym. Sci.*, **14** (1954) 315−319. doi: 10.1002/pol.1954.120147514

161. Nussbaumer, R.J.; Caseri, W.R.; Smith, P. and Tervoort, T. Polymer-TiO_2 nanocomposites: A route towards visually transparent broadband UV filters and high refractive index materials, *Macromol. Mater. Eng.*, **288** (2003) 44−49. doi: 10.1002/mame.200290032

162. Nakayama, N. and Hayashi, T. Preparation and characterization of TiO_2 and polymer nanocomposite films with high refractive index, *J. Appl. Polym. Sci.*, **105** (2007) 3662−3672. doi: 10.1002/App.26451

163. Nakayama, N. and Hayashi, T. Preparation and characterization of TiO_2-ZrO_2 and thiol-acrylate resin nanocomposites with high refractive index via UV-induced crosslinking polymerization, *Composites, Part A*, **38** (2007) 1996−2004. doi: 10.1016/j.compositesa.2007.05.005

164. Demir, M.M.; Koynov, K.; Akbey, U.; Bubeck, C.; Park, I.; Lieberwirth, I. and Wegner, G. Optical properties of composites of PMMA and surface-modified zincite nanoparticles, *Macromolecules*, **40** (2007) 1089−1100. doi: 10.1021/Ma062184t

165. Su, H.-W. and Chen, W.-C. High refractive index polyimide-nanocrystalline-titania hybrid optical materials, *J. Mater. Chem.*, **18** (2008) 1139−1145. doi: 10.1039/B717069F

166. Imai, Y.; Terahara, A.; Hakuta, Y.; Matsui, K.; Hayashi, H. and Ueno, N. Transparent poly(bisphenol a carbonate)-based nanocomposites with high refractive index nanoparticles, *Eur. Polym. J.*, **45** (2009) 630−638. doi: 10.1016/j.eurpolymj.2008.12.031

167. Elim, H.I.; Cai, B.; Kurata, Y.; Sugihara, O.; Kaino, T.; Adschiri, T.; Chu, A.-L. and Kambe, N. Refractive index control and Rayleigh scattering properties of transparent TiO_2 nanohybrid polymer, *J. Phys. Chem. B*, **113** (2009) 10143−10148. doi: 10.1021/jp902598f

168. Tao, P.; Li, Y.; Rungta, A.; Viswanath, A.; Gao, J.; Benicewicz, B.C.; Siegel, R.W. and Schadler, L.S. TiO_2 nanocomposites with high refractive index and transparency, *J. Mater. Chem.*, **21** (2011) 18623−18629. doi: 10.1039/C1JM13093E

169. Yamada, S.; Mouri, E. and Yoshinaga, K. Incorporation of titanium dioxide particles into polymer matrix using block copolymer micelles for fabrication of high refractive and transparent organic-inorganic hybrid materials, *J. Polym. Sci., Part A: Polym. Chem.*, **49** (2011) 712−718. doi: 10.1002/pola.24483

170. Tao, P.; Viswanath, A.; Li, Y.; Siegel, R.W.; Benicewicz, B.C. and Schadler, L.S. Bulk transparent epoxy nanocomposites filled with poly(glycidyl methacrylate) brush-grafted TiO_2 nanoparticles, *Polymer*, **54** (2013) 1639−1646. doi: 10.1016/j.polymer.2013.01.032

171. Tsai, C.M.; Hsu, S.H.; Ho, C.C.; Tu, Y.C.; Tsai, H.C.; Wang, C.A. and Su, W.F. High refractive index transparent nanocomposites prepared by *in situ* polymerization, *J. Mater. Chem. C*, **2** (2014) 2251−2258. doi: 10.1039/c3tc32374a

172. Maeda, S.; Fujita, M.; Idota, N.; Matsukawa, K. and Sugahara, Y. Preparation of transparent bulk TiO_2/PMMA hybrids with improved refractive indices via an in situ polymerization process using TiO_2 nanoparticles bearing PMMA chains grown by surface-initiated atom transfer radical polymerization, *ACS Appl. Mater. Interfaces*, **8** (2016) 34762−34769. doi: 10.1021/acsami.6b10427

173. Zhan, X.; Xing, Q.; Liu, H.; Zhang, J.; Cheng, J. and Lin, X. A facile method for fabrication of titanium-doped hybrid materials with high refractive index, *RSC Adv.*, **4** (2014) 13909−13918. doi: 10.1039/C3RA46359A

174. Schadler, L.S. Polymer-based and polymer-filled nanocomposites, in *Nanocomposite science and technology*, Ajayan, P.M.; Schadler, L.S. and Braun, P.V., Eds., 2003, John Wiley & Sons: Weinheim, Germany, 77−153. doi: 10.1002/3527602127.ch2

175. Judeinstein, P. and Sanchez, C. Hybrid organic–inorganic materials: A land of multidisciplinarity, *J. Mater. Chem.*, **6** (1996) 511−525. doi: 10.1039/jm9960600511

176. Drisko, G.L. and Sanchez, C. Hybridization in materials science - evolution, current state, and future aspirations, *Eur. J. Inorg. Chem.*, **2012** (2012) 5097−5105. doi: 10.1002/ejic.201201216

177. Leroux, F. and Besse, J.-P. Polymer interleaved layered double hydroxide: A new emerging class of nanocomposites, *Chem. Mater.*, **13** (2001) 3507−3515. doi: 10.1021/cm0110268

178. James, S.L. Metal-organic frameworks, *Chem. Soc. Rev.*, **32** (2003) 276−288. doi: 10.1039/b200393g

179. Sanchez, C.; Julián, B.; Belleville, P. and Popall, M. Applications of hybrid organic–inorganic nanocomposites, *J. Mater. Chem.*, **15** (2005) 3559−3592. doi: 10.1039/b509097k

180. Hussain, F.; Hojjati, M.; Okamoto, M. and Gorga, R.E. Review article: Polymer-matrix nanocomposites, processing, manufacturing, and application: An overview, *J. Compos. Mater.*, **40** (2006) 1511−1575. doi: 10.1177/0021998306067321

181. Usuki, A.; Kawasumi, M.; Kojima, Y.; Okada, A.; Kurauchi, T. and Kamigaito, O. Swelling behavior of montmorillonite cation exchanged for ω-amino acids by ε-caprolactam, *J. Mater. Res.*, **8** (1993) 1174−1178. doi: 10.1557/jmr.1993.1174

182. Dolez, P.I. Nanomaterials definitions, classifications, and applications, in *Nanoengineering*, Dolez, P.I., Ed., 2015, Elsevier: Amsterdam, Netherlands, 3−40. doi: 10.1016/B978-0-444-62747-6.00001-4

183. Caseri, W.R. In situ synthesis of polymer-embedded nanostructures, in *Nanocomposites: In situ synthesis of polymer-embedded nanostructures*, Nicolais, L. and Carotenuto, G., Eds., 2014, John Wiley & Sons: Hoboken, NJ, USA, 45−72. doi: 10.1002/9781118742655.ch2

184. Faure, B.; Salazar-Alvarez, G.; Ahniyaz, A.; Villaluenga, I.; Berriozabal, G.; De Miguel, Y.R. and Bergström, L. Dispersion and surface functionalization of oxide nanoparticles for transparent photocatalytic and UV-protecting coatings and sunscreens, *Sci. Tech. Adv. Mater.*, **14** (2013) 023001. doi: 10.1088/1468-6996/14/2/023001

185. Hiemenz, P.C. and Rajagopalan, R. *Principles of colloid and surface chemistry*. 1997, CRC Press: Boca Raton, FL, USA.

186. Bernhard, Y.; Winckler, P.; Perrier-Cornet, J.-M. and Decreau, R.A. Harnessing medically relevant metals onto water-soluble subphthalocyanines: Towards bimodal imaging and theranostics, *Dalton Trans.*, **44** (2015) 3200−3208. doi: 10.1039/c4dt03536d

187. Boles, M.A.; Ling, D.; Hyeon, T. and Talapin, D.V. The surface science of nanocrystals, *Nat. Mater.*, **15** (2016) 141−153. doi: 10.1038/nmat4526

188. Pujari, S.P.; Scheres, L.; Marcelis, A.T. and Zuilhof, H. Covalent surface modification of oxide surfaces, *Angew. Chem. Int. Ed.*, **53** (2014) 6322−6356. doi: 10.1002/anie.201306709

189. Mallakpour, S. and Madani, M. A review of current coupling agents for modification of metal oxide nanoparticles, *Prog. Org. Coat.*, **86** (2015) 194−207. doi: 10.1016/j.porgcoat.2015.05.023

190. Qu, Q.; Geng, H.; Peng, R.; Cui, Q.; Gu, X.; Li, F. and Wang, M. Chemically binding carboxylic acids onto TiO_2 nanoparticles with adjustable coverage by solvothermal strategy, *Langmuir*, **26** (2010) 9539−9546. doi: 10.1021/la100121n

191. Sakeye, M. and Smått, J.-H. Comparison of different amino-functionalization procedures on a selection of metal oxide microparticles: Degree of modification and hydrolytic stability, *Langmuir*, **28** (2012) 16941−16950. doi: 10.1021/la303925x

192. Leroux, F.; Dalod, A.; Hennous, M.; Sisti, L.; Totaro, G.; Celli, A.; Coehlo, C. and Verney, V. X-ray diffraction and rheology cross-study of polymer chain penetrating surfactant tethered layered double hydroxide resulting into intermixed structure with polypropylene, poly(butylene)succinate and poly(dimethyl)siloxane, *Appl. Clay Sci.*, **100** (2014) 102−111. doi: 10.1016/j.clay.2014.05.006

193. Shin, Y.; Lee, D.; Lee, K.; Ahn, K.H. and Kim, B. Surface properties of silica nanoparticles modified with polymers for polymer nanocomposite applications, *J. Ind. Eng. Chem.*, **14** (2008) 515−519. doi: 10.1016/j.jiec.2008.02.002

194. Shirai, Y.; Kawatsura, K. and Tsubokawa, N. Graft polymerization of vinyl monomers from initiating groups introduced onto polymethylsiloxane-coated titanium dioxide modified with alcoholic hydroxyl groups, *Prog. Org. Coat.*, **36** (1999) 217−224. doi: 10.1016/s0300-9440(99)00046-6

195. Plueddemann, E.P. *Silane coupling agents*. 1991, Springer: New York, NY, USA. doi: 10.1007/978-1-4899-2070-6

196. Chen, Q. and Yakovlev, N.L. Adsorption and interaction of organosilanes on TiO_2 nanoparticles, *Appl. Surf. Sci.*, **257** (2010) 1395−1400. doi: 10.1016/j.apsusc.2010.08.036

197. Milanesi, F.; Cappelletti, G.; Annunziata, R.; Bianchi, C.L.; Meroni, D. and Ardizzone, S. Siloxane−TiO_2 hybrid nanocomposites. The structure of the hydrophobic layer, *J. Phys. Chem. C*, **114** (2010) 8287−8293. doi: 10.1021/jp1014669

198. Zhao, J.; Milanova, M.; Warmoeskerken, M.M.C.G. and Dutschk, V. Surface modification of TiO_2 nanoparticles with silane coupling agents, *Colloids Surf., A*, **413** (2012) 273−279. doi: 10.1016/j.colsurfa.2011.11.033

199. Porter, M.D.; Bright, T.B.; Allara, D.L. and Chidsey, C.E.D. Spontaneously organized molecular assemblies. 4. Structural characterization of n-alkyl thiol monolayers on gold by optical ellipsometry, infrared spectroscopy, and electrochemistry, *J. Am. Chem. Soc.*, **109** (1987) 3559−3568. doi: 10.1021/ja00246a011

200. Helmy, R. and Fadeev, A.Y. Self-assembled monolayers supported on TiO_2: Comparison of $C_{18}H_{37}SiX_3$ (X = H, Cl, OCH_3), $C_{18}H_{37}Si(CH_3)_2Cl$, and $C_{18}H_{37}PO(OH)_2$, *Langmuir*, **18** (2002) 8924−8928. doi: 10.1021/la0262506

201. Fadeev, A.Y.; Helmy, R. and Marcinko, S. Self-assembled monolayers of organosilicon hydrides supported on titanium, zirconium, and hafnium dioxides, *Langmuir*, **18** (2002) 7521−7529. doi: 10.1021/la020178u

202. Liu, Y.; Li, Y.; Li, X.M. and He, T. Kinetics of (3-aminopropyl)triethoxylsilane (APTES) silanization of superparamagnetic iron oxide nanoparticles, *Langmuir*, **29** (2013) 15275−15282. doi: 10.1021/la403269u

203. Meroni, D.; Lo Presti, L.; Di Liberto, G.; Ceotto, M.; Acres, R.G.; Prince, K.C.; Bellani, R.; Soliveri, G. and Ardizzone, S. A close look at the structure of the TiO_2-APTES interface in hybrid nanomaterials and its degradation pathway: An experimental and theoretical study, *J. Phys. Chem. C*, **121** (2017) 430−440. doi: 10.1021/acs.jpcc.6b10720

204. Iijima, M.; Kobayakawa, M. and Kamiya, H. Tuning the stability of TiO_2 nanoparticles in various solvents by mixed silane alkoxides, *J. Colloid Interface Sci.*, **337** (2009) 61−65. doi: 10.1016/j.jcis.2009.05.007

205. Wang, C.; Mao, H.; Wang, C. and Fu, S. Dispersibility and hydrophobicity analysis of titanium dioxide nanoparticles grafted with silane coupling agent, *Ind. Eng. Chem. Res.*, **50** (2011) 11930−11934. doi: 10.1021/ie200887x

206. Mallakpour, S. and Barati, A. Efficient preparation of hybrid nanocomposite coatings based on poly(vinyl alcohol) and silane coupling agent modified TiO_2 nanoparticles, *Prog. Org. Coat.*, **71** (2011) 391−398. doi: 10.1016/j.porgcoat.2011.04.010

207. Kassir, M.; Roques-Carmes, T.; Hamieh, T.; Razafitianamaharavo, A.; Barres, O.; Toufaily, J. and Villiéras, F. Surface modification of TiO_2 nanoparticles with AHAPS aminosilane: Distinction between physisorption and chemisorption, *Adsorption*, **19** (2013) 1197−1209. doi: 10.1007/s10450-013-9555-y

208. Sabzi, M.; Mirabedini, S.M.; Zohuriaan-Mehr, J. and Atai, M. Surface modification of TiO_2 nano-particles with silane coupling agent and investigation of its effect on the properties of polyurethane composite coating, *Prog. Org. Coat.*, **65** (2009) 222−228. doi: 10.1016/j.porgcoat.2008.11.006

209. Xuan, L.; Han, G.; Wang, D.; Cheng, W.; Gao, X.; Chen, F. and Li, Q. Effect of surface-modified TiO_2 nanoparticles on the anti-ultraviolet aging performance of foamed wheat straw fiber/polypropylene composites, *Materials*, **10** (2017) 456. doi: 10.3390/ma10050456

210. Teleki, A.; Bjelobrk, N. and Pratsinis, S.E. Continuous surface functionalization of flame-made TiO_2 nanoparticles, *Langmuir*, **26** (2010) 5815−5822. doi: 10.1021/la9037149

211. Koziej, D.; Fischer, F.; Kränzlin, N.; Caseri, W.R. and Niederberger, M. Nonaqueous TiO_2 nanoparticle synthesis: A versatile basis for the fabrication of self-supporting, transparent, and UV-absorbing composite films, *ACS Appl. Mater. Interfaces*, **1** (2009) 1097−1104. doi: 10.1021/am9000584

212. Sunkara, H.B.; Jethmalani, J.M. and Ford, W.T. Composite of colloidal crystals of silica in poly(methyl methacrylate), *Chem. Mater.*, **6** (1994) 362−364. doi: 10.1021/cm00040a006

213. Nguyen, V.S.; Rouxel, D. and Vincent, B. Dispersion of nanoparticles: From organic solvents to polymer solutions, *Ultrason. Sonochem.*, **21** (2014) 149−153. doi: 10.1016/j.ultsonch.2013.07.015

214. Zhao, H. and Li, R.K.Y. A study on the photo-degradation of zinc oxide (ZnO) filled polypropylene nanocomposites, *Polymer*, **47** (2006) 3207−3217. doi: 10.1016/j.polymer.2006.02.089

215. Evans, B.A.; Fiser, B.L.; Prins, W.J.; Rapp, D.J.; Shields, A.R.; Glass, D.R. and Superfine, R. A highly tunable silicone-based magnetic elastomer with nanoscale homogeneity, *J. Magn. Magn. Mater.*, **324** (2012) 501−507. doi: 10.1016/j.jmmm.2011.08.045

216. Tsuzuki, T. Abnormal transmittance of refractive-index-modified ZnO/organic hybrid films, *Macromol. Mater. Eng.*, **293** (2008) 109−113. doi: 10.1002/mame.200700326

217. Althues, H.; Henle, J. and Kaskel, S. Functional inorganic nanofillers for transparent polymers, *Chem. Soc. Rev.*, **36** (2007) 1454−1465. doi: 10.1039/b608177k

218. Mammeri, F.; Bourhis, E.L.; Rozes, L. and Sanchez, C. Mechanical properties of hybrid organic-inorganic materials, *J. Mater. Chem.*, **15** (2005) 3787−3811. doi: 10.1039/B507309J

219. Sanchez, C.; Ribot, F.; Rozes, L. and Alonso, B. Design of hybrid organic-inorganic nanocomposites synthesized via sol-gel chemistry, *Mol. Cryst. Liq. Cryst. Sci. Technol., Sect. A*, **354** (2000) 143−158. doi: 10.1080/10587250008023609

220. Wei, Y.; Bakthavatchalam, R. and Whitecar, C.K. Synthesis of new organic-inorganic hybrid glasses, *Chem. Mater.*, **2** (1990) 337−339. doi: 10.1021/cm00010a001

221. Xiong, M.; Zhou, S.; Wu, L.; Wang, B. and Yang, L. Sol–gel derived organic–inorganic hybrid from trialkoxysilane-capped acrylic resin and titania: Effects of preparation conditions on the structure and properties, *Polymer*, **45** (2004) 8127−8138. doi: 10.1016/j.polymer.2004.09.066

222. Xiong, M.; You, B.; Zhou, S. and Wu, L. Study on acrylic resin/titania organic–inorganic hybrid materials prepared by the sol–gel process, *Polymer*, **45** (2004) 2967−2976. doi: 10.1016/j.polymer.2004.02.043

223. Agag, T.; Tsuchiya, H. and Takeichi, T. Novel organic–inorganic hybrids prepared from polybenzoxazine and titania using sol–gel process, *Polymer*, **45** (2004) 7903−7910. doi: 10.1016/j.polymer.2004.09.022

224. Müh, E.; Stieger, M.; Klee, J.E.; Frey, H. and Mülhaupt, R. Organic-inorganic hybrid networks by the sol-gel process and subsequent photopolymerization, *J. Polym. Sci., Part A: Polym. Chem.*, **39** (2001) 4274−4282. doi: 10.1002/pola.10079

225. Zhang, J.U.N.; Luo, S. and Gui, L. Poly(methyl methacrylate)–titania hybrid materials by sol–gel processing, *J. Mater. Sci.*, **32** (1997) 1469−1472. doi: 10.1023/a:1018553901058

226. Wu, C.-S. In situ polymerization of titanium isopropoxide in polycaprolactone: Properties and characterization of the hybrid nanocomposites, *J. Appl. Polym. Sci.*, **92** (2004) 1749−1757. doi: 10.1002/app.20135

227. Sangermano, M.; Amerio, E.; Priola, A.; Di Gianni, A. and Voit, B. Preparation and characterization of acrylic resin/titania hybrid nanocomposite coatings by photopolymerization and sol–gel process, *J. Appl. Polym. Sci.*, **102** (2006) 4659−4664. doi: 10.1002/app.24707

228. Martinelli, M.; de Luca, M.A.; Bechi, D.M. and Mitidieri, S. Hybrid films based on hydroxylated castor oil and titanium (IV) isopropoxide, *J. Sol-Gel Sci. Technol.*, **52** (2009) 202−209. doi: 10.1007/s10971-009-2044-9

229. Andrianov, K.A. and Zhdanov, A.A. Synthesis of new polymers with inorganic chains of molecules, *J. Polym. Sci.*, **30** (1958) 513−524. doi: 10.1002/pol.1958.1203012141

230. Andrianov, K.A.; Golubkov, G.E.; Yelinek, V.I.; Kurasheva, N.A.; Manucharova, I.F.; Litvinova, L.F. and Artemyev, B.K. Synthesis and properties of polytitanodimethylsiloxanes, *Polym. Sci. U.S.S.R.*, **7** (1965) 752−760. doi: 10.1016/0032-3950(65)90130-9

231. Andrianov, K.A.; Golubkov, G.E.; Yelinek, V.I.; Kurasheva, N.A.; Manucharova, I.F.; Litvinova, L.F. and Artemyev, B.K. X-ray studies of polytitanodimethylsiloxanes, *Polym. Sci. U.S.S.R.*, **7** (1965) 760−769. doi: 10.1016/0032-3950(65)90131-0

232. Andrianov, K.A.; Kurasheva, N.A.; Lavrukhin, B.D. and Kuteinikova, L.I. The condensation reaction of titanium tetrabutoxide with α,ω-dihydroxypolydimethylsiloxanes, *Polym. Sci. U.S.S.R.*, **14** (1972) 2857−2865. doi: 10.1016/0032-3950(72)90215-8

233. Glaser, R.H. and Wilkes, G.L. Structure property behavior of polydimethylsiloxane and poly(tetramethylene oxide) modified TEOS based sol-gel materials, *Polym. Bull.*, **19** (1988) 51−57. doi: 10.1007/BF00255023

234. Diré, S.; Babonneau, F.; Carturan, G. and Livage, J. Synthesis and characterization of siloxane-titania materials, *J. Non-Cryst. Solids*, **147−148** (1992) 62−66. doi: 10.1016/s0022-3093(05)80594-0

235. Guermeur, C.; Lambard, J.; Gerard, J.-F. and Sanchez, C. Hybrid polydimethylsiloxane-zirconium oxo nanocomposites. Part 1 characterization of the matrix and the siloxane-zirconium oxo interface, *J. Mater. Chem.*, **9** (1999) 769−778. doi: 10.1039/a807310d

236. Julián, B.; Gervais, C.; Cordoncillo, E.; Escribano, P.; Babonneau, F. and Sanchez, C. Synthesis and characterization of transparent PDMS−metal-oxo based organic−inorganic nanocomposites, *Chem. Mater.*, **15** (2003) 3026−3034. doi: 10.1021/cm031054l

237. Alonso, B. and Sanchez, C. Structural investigation of polydimethylsiloxane–vanadate hybrid materials, *J. Mater. Chem.*, **10** (2000) 377−386. doi: 10.1039/a908032e

238. Matkovskii, A.K.; Yurchenko, G.R.; Zub, Y.L. and Roesky, H.W. Preparation and properties of porous polytitano- and polyzirconomethylsiloxane xerogels, *Inorg. Mater.*, **41** (2005) 888−891. doi: 10.1007/s10789-005-0231-9

239. Foussaier, O.; Menetrier, M.; Videau, J.-J. and Duguet, E. Polydimethylsiloxane-based ORMOSIL microstructure: Correlation with compressive behavior, *Mater. Lett.*, **42** (2000) 305−310. doi: 10.1016/s0167-577x(99)00203-7

240. Yamada, N.; Yoshinaga, I. and Katayama, S. Synthesis and dynamic mechanical behaviour of inorganic-organic hybrids containing various inorganic components, *J. Mater. Chem.*, **7** (1997) 1491−1495. doi: 10.1039/A700793K

241. Yamada, N.; Yoshinaga, I. and Katayama, S. Processing and properties of inorganic/organic hybrid materials, *Nippon Steel Technical Report*, **77–78** (1998) 90−94.

242. Yoshinaga, I.; Yamada, N. and Katayama, S. Effect of metal alkoxide complexes on condensation reactions of hydrolyzed phenyltriethoxysilane, *J. Sol-Gel Sci. Technol.*, **28** (2003) 65−70. doi: 10.1023/a:1025637103740

243. Shindou, T.; Katayama, S.; Yamada, N. and Kamiya, K. Effect of composition on surface properties of polydimethylsiloxane-based inorganic/organic hybrid films, *J. Sol-Gel Sci. Technol.*, **30** (2004) 229−237. doi: 10.1023/B:JSST.0000039528.70437.fe

244. Yamada, N.; Yoshinaga, I. and Katayama, S. Processing and properties of inorganic-organic hybrids containing various inorganic components, *J. Sol-Gel Sci. Technol.*, **13** (1998) 445−449. doi: 10.1023/a:1008629529581

245. Katayama, S.; Kubo, Y. and Yamada, N. Characterization and mechanical properties of flexible dimethylsiloxane-based inorganic/organic hybrid sheets, *J. Am. Ceram. Soc.*, **85** (2002) 1157−1163. doi: 10.1111/j.1151-2916.2002.tb00238.x

246. Yamada, N.; Yoshinaga, I. and Katayama, S. Effect of inorganic phase dimension on structure and mechanical properties of inorganic-organic hybrids prepared from metal alkoxides and polydimethylsiloxane, *J. Ceram. Soc. Jpn.*, **107** (1999) 1160−1165. doi: 10.2109/jcersj.107.1160

247. Almeida, J.C.; Castro, A.G.B.; Miranda Salvado, I.M.; Margaça, F.M.A. and Vaz Fernandes, M.H. A new approach to the preparation of PDMS–SiO_2 based hybrids – a structural study, *Mater. Lett.*, **128** (2014) 105−109. doi: 10.1016/j.matlet.2014.04.135

248. Yamada, N.; Yoshinaga, I. and Katayama, S. Formation behavior and optical properties of transparent inorganic-organic hybrids prepared from metal alkoxides and polydimethylsiloxane, *J. Sol-Gel Sci. Technol.*, **17** (2000) 123−130. doi: 10.1023/a:1008787200364

249. Almeida, J.C.; Wacha, A.; Bóta, A.; Almásy, L.; Vaz Fernandes, M.H.; Margaça, F.M.A. and Miranda Salvado, I.M. PDMS-SiO_2 hybrid materials – a new insight into the role of Ti and Zr as additives, *Polymer*, **72** (2015) 40−51. doi: 10.1016/j.polymer.2015.06.053

250. Almeida, J.C.; Castro, A.G.B.; Lancastre, J.J.H.; Miranda Salvado, I.M.; Margaça, F.M.A.; Fernandes, M.H.V.; Ferreira, L.M. and Casimiro, M.H. Structural characterization of PDMS–TEOS–CaO–TiO_2 hybrid materials obtained by sol–gel, *Mater. Chem. Phys.*, **143** (2014) 557−563. doi: 10.1016/j.matchemphys.2013.09.032

251. Kim, Y.B.; Cho, D. and Park, W.H. Fabrication and characterization of TiO_2/poly(dimethyl siloxane) composite fibers with thermal and mechanical stability, *J. Appl. Polym. Sci.*, **116** (2010) 449−454. doi: 10.1002/app.31480

252. Jenkins, F.A. and White, H.E. *Fundamentals of optics*. 1976, McGraw-Hill: Auckland.

253. Rao, C.N.R. and Gopalakrishnan, J. *New directions in solid state chemistry*. 1997, Cambridge University Press: Cambridge, UK. doi: 10.1017/cbo9780511623141

254. Rysselberghe, P.V. Remarks concerning the Clausius-Mossotti law, *J. Phys. Chem.*, **36** (1931) 1152−1155. doi: 10.1021/j150334a007

255. Yang, C.-J. and Jenekhe, S.A. Group contribution to molar refraction and refractive index of conjugated polymers, *Chem. Mater.*, **7** (1995) 1276−1285. doi: 10.1021/cm00055a002

256. Caseri, W.R. Nanocomposites of polymers and inorganic particles: Preparation, structure and properties, *Mater. Sci. Technol.*, **22** (2006) 807−817. doi: 10.1179/174328406x101256

257. Lide, D.R. *CRC handbook of chemistry and physics*. 2005, CRC Press: Boca Raton, FL, USA.

258. Zimmermann, L.; Weibel, M.; Caseri, W.; Suter, U.W. and Walther, P. Polymer nanocomposites with "ultralow" refractive index, *Polym. Adv. Technol.*, **4** (1993) 1−7. doi: 10.1002/pat.1993.220040101

259. Chandrasekhar, S. Stochastic problems in physics and astronomy, *Rev. Mod. Phys.*, **15** (1943) 1−89. doi: 10.1103/RevModPhys.15.1

260. Bansal, P.P. and Ardell, A.J. Average nearest-neighbor distances between uniformly distributed finite particles, *Metallography*, **5** (1972) 97−111. doi: 10.1016/0026-0800(72)90048-1

261. Liu, Y.; Lü, C.; Li, M.; Zhang, L. and Yang, B. High refractive index organic–inorganic hybrid coatings with TiO_2 nanocrystals, *Colloids Surf., A*, **328** (2008) 67−72. doi: 10.1016/j.colsurfa.2008.06.026

262. Chau, J.L.H.; Liu, H.W. and Su, W.F. Fabrication of hybrid surface-modified titania-epoxy nanocomposite films, *J. Phys. Chem. Solids*, **70** (2009) 1385−1389. doi: 10.1016/j.jpcs.2009.08.011

263. Sullalti, S.; Totaro, G.; Askanian, H.; Celli, A.; Marchese, P.; Verney, V. and Commereuc, S. Photodegradation of TiO_2 composites based on polyesters, *J. Photochem. Photobiol. A*, **321** (2016) 275−283. doi: 10.1016/j.jphotochem.2015.11.007

264. Chang, C.-C. and Chen, W.-C. High-refractive-index thin films prepared from aminoalkoxysilane-capped pyromellitic dianhydride-titania hybrid materials, *J. Polym. Sci., Part A: Polym. Chem.*, **39** (2001) 3419−3427. doi: 10.1002/pola.1323

265. Chang, C.-C. and Chen, W.-C. Synthesis and optical properties of polyimide-silica hybrid thin films, *Chem. Mater.*, **14** (2002) 4242−4248. doi: 10.1021/cm0202310

266. Lu, Q. and Mullins, M.E. In situ synthesis of high refractive index PDMS/metal oxide nanocomposites, *MRS Proc.*, **1400** (2012). doi: 10.1557/opl.2012.17

267. Park, S.K.; Kang, B.-K.; Shin, J.-W.; Joo, C.W.; Moon, J.; Cho, D.-H.; Yu, B.; Chu, H.Y. and Lee, J.-I. Triethylene glycol–titanium oxide hydrate hybrid films with high refractive index and surface evenness, *J. Mater. Chem. C*, **2** (2014) 4468−4475. doi: 10.1039/c3tc32200a

268. Kresse, G. and Hafner, J. Ab initio molecular dynamics for liquid metals, *Phys. Rev. B*, **47** (1993) 558−561. doi: 10.1103/PhysRevB.47.558

269. Kresse, G. and Furthmüller, J. Efficiency of ab-initio total energy calculations for metals and semiconductors using a plane-wave basis set, *Comput. Mater. Sci.*, **6** (1996) 15−50. doi: 10.1016/0927-0256(96)00008-0

270. Kresse, G. and Furthmüller, J. Efficient iterative schemes for ab initio total-energy calculations using a plane-wave basis set, *Phys. Rev. B*, **54** (1996) 11169−11186. doi: 10.1103/PhysRevB.54.11169

271. Kresse, G. and Joubert, D. From ultrasoft pseudopotentials to the projector augmented-wave method, *Phys. Rev. B*, **59** (1999) 1758−1775. doi: 10.1103/PhysRevB.59.1758

272. Perdew, J.P.; Ruzsinszky, A.; Csonka, G.I.; Vydrov, O.A.; Scuseria, G.E.; Constantin, L.A.; Zhou, X. and Burke, K. Restoring the density-gradient expansion for exchange in solids and surfaces, *Phys. Rev. Lett.*, **100** (2008) 136406. doi: 10.1103/PhysRevLett.100.136406

273. Zucker, R.V.; Chatain, D.; Dahmen, U.; Hagège, S. and Carter, W.C. New software tools for the calculation and display of isolated and attached interfacial-energy minimizing particle shapes, *J. Mater. Sci.*, **47** (2012) 8290−8302. doi: 10.1007/s10853-012-6739-x

274. Skjærvø, S.L.; Sommer, S.; Nørby, P.; Bøjesen, E.D.; Grande, T.; Iversen, B.B. and Einarsrud, M.-A. Formation mechanism and growth of $MNbO_3$, M=K, Na by in situ X-ray diffraction, *J. Am. Ceram. Soc.*, (2017) in press. doi: 10.1111/jace.14932

275. Becker, J.; Bremholm, M.; Tyrsted, C.; Pauw, B.; Jensen, K.M.Ø.; Eltzholt, J.; Christensen, M. and Iversen, B.B. Experimental setup for in situ X-ray SAXS/WAXS/PDF studies of the formation and growth of nanoparticles in near- and supercritical fluids, *J. Appl. Crystallogr.*, **43** (2010) 729−736. doi: 10.1107/s0021889810014688

276. Jensen, K.M.Ø.; Christensen, M.; Juhas, P.; Tyrsted, C.; Bøjesen, E.D.; Lock, N.; Billinge, S.J.L. and Iversen, B.B. Revealing the mechanisms behind SnO_2 nanoparticle formation and growth during hydrothermal synthesis: An in situ total scattering study, *J. Am. Chem. Soc.*, **134** (2012) 6785−6792. doi: 10.1021/ja300978f

277. Dyadkin, V.; Pattison, P.; Dmitriev, V. and Chernyshov, D. A new multipurpose diffractometer PILATUS@SNBL, *J. Synchrotron Radiat.*, **23** (2016) 825−829. doi: 10.1107/S1600577516002411

278. Rietveld, H.M. A profile refinement method for nuclear and magnetic structures, *J. Appl. Crystallogr.*, **2** (1969) 65−71. doi: 10.1107/s0021889869006558

279. Evans, J.S.O. Advanced input files & parametric quantitative analysis using Topas, *Mater. Sci. Forum*, **651** (2010) 1−9. doi: 10.4028/www.scientific.net/MSF.651.1

280. Pease, R.S. An X-ray study of boron nitride, *Acta Crystallogr.*, **5** (1952) 356−361. doi: 10.1107/s0365110x52001064

281. Topas wiki (Durham university): *Anisotropic_hkl*, http://topas.dur.ac.uk/topaswiki/doku.php?id=anisotropic_hkl (retrieved: August 1st 2016).

282. Jensen, G.V.; Bremholm, M.; Lock, N.; Deen, G.R.; Jensen, T.R.; Iversen, B.B.; Niederberger, M.; Pedersen, J.S. and Birkedal, H. Anisotropic crystal growth kinetics of anatase TiO_2 nanoparticles synthesized in a nonaqueous medium, *Chem. Mater.*, **22** (2010) 6044−6055. doi: 10.1021/cm100469y

283. Hummer, D.R.; Heaney, P.J. and Post, J.E. Thermal expansion of anatase and rutile between 300 and 575 K using synchrotron powder X-ray diffraction, *Powder Diffr.*, **22** (2007) 352−357. doi: 10.1154/1.2790965

284. Brunauer, S.; Emmett, P.H. and Teller, E. Adsorption of gases in multimolecular layers, *J. Am. Chem. Soc.*, **60** (1938) 309−319. doi: 10.1021/ja01269a023

285. Barrett, E.P.; Joyner, L.G. and Halenda, P.P. The determination of pore volume and area distributions in porous substances. I. Computations from nitrogen isotherms, *J. Am. Chem. Soc.*, **73** (1951) 373−380. doi: 10.1021/ja01145a126

286. German, R.M. and Park, S.J. *Handbook of mathematical relations in particulate materials processing*, in *Wiley series on processing of engineering materials*. 2008, John Wiley & Sons: Hoboken, NJ, USA.

287. David, G. and Pérez, J. Combined sampler robot and high-performance liquid chromatography: A fully automated system for biological small-angle X-ray scattering experiments at the synchrotron SOLEIL SWING beamline, *J. Appl. Crystallogr.*, **42** (2009) 892−900. doi: 10.1107/s0021889809029288

288. Girardot, R.; Viguier, G.; Pérez, J. and Ounsy, M. FOXTROT: A JAVA-based application to reduce and analyze SAXS and WAXS piles of 2D data at synchrotron SOLEIL. 14-16 April 2015, canSAS-VIII, Tokai, Japan.

289. Dalod, A.R.M.; Henriksen, L.; Grande, T. and Einarsrud, M.-A. Functionalized TiO_2 nanoparticles by single-step hydrothermal synthesis: The role of the silane coupling agents, *Beilstein J. Nanotechnol.*, **8** (2017) 304−312. doi: 10.3762/bjnano.8.33

290. Dalod, A.R.M.; Grendal, O.G.; Skjærvø, S.L.; Inzani, K.; Selbach, S.M.; Henriksen, L.; van Beek, W.; Grande, T. and Einarsrud, M.-A. Controlling oriented attachment and in situ functionalization of TiO_2 nanoparticles during hydrothermal synthesis with APTES, *J. Phys. Chem. C*, **121** (2017) 11897−11906. doi: 10.1021/acs.jpcc.7b02604

291. Grendal, O.G. *Hydrothermal synthesis of in situ functionalized TiO_2 nanoparticles with amino silane*. 2015, Specialization project report at NTNU, Norwegian University of Science and Technology: Trondheim, Norway.

292. Grendal, O.G. *Development of polymer-nanoparticle composite with high refractive index*. 2016, Master Thesis at NTNU, Norwegian University of Science and Technology: Trondheim, Norway.

293. Ribeiro, C.; Barrado, C.M.; de Camargo, E.R.; Longo, E. and Leite, E.R. Phase transformation in titania nanocrystals by the oriented attachment mechanism: The role of the pH value, *Chem. Eur. J.*, **15** (2009) 2217−2222. doi: 10.1002/chem.200801019

294. Viana, M.M.; Soares, V.F. and Mohallem, N.D.S. Synthesis and characterization of TiO_2 nanoparticles, *Ceram. Int.*, **36** (2010) 2047−2053. doi: 10.1016/j.ceramint.2010.04.006

295. Socrates, G. *Infrared and Raman characteristic group frequencies: Tables and charts*. 2001, John Wiley & Sons: Chichester, UK.

296. Xu, T.; Hou, W.; Shen, X.; Wu, H.; Li, X.; Wang, J. and Jiang, Z. Sulfonated titania submicrospheres-doped sulfonated poly(ether ether ketone) hybrid membranes with enhanced proton conductivity and reduced methanol permeability, *J. Power Sources*, **196** (2011) 4934−4942. doi: 10.1016/j.jpowsour.2011.02.017

297. Matinlinna, J.P.; Laajalehto, K.; Lassila, L.V.J.; Yli-Urpo, A. and Vallittu, P.K. FT-IR and XPS surface characterization of allyltrimethoxysilane and 3-methacryloxypropyltrimethoxysilane mixture adsorbed onto titanium substrate, in *Silanes and other coupling agents*, vol. **3**, Mittal, K.L., Ed., 2004, CRC Press: Boca Raton, FL, USA, 21−37. doi: 10.1201/b12184-5

298. Plodinec, M.; Gajović, A.; Iveković, D.; Tomašić, N.; Zimmermann, B.; Macan, J.; Haramina, T.; Su, D.S. and Willinger, M. Study of thermal stability of (3-aminopropyl)trimethoxy silane-grafted titanate nanotubes for application as nanofillers in polymers, *Nanotechnology*, **25** (2014) 435601. doi: 10.1088/0957-4484/25/43/435601

299. Czarnobaj, K. Sol–gel-processed silica/polydimethylsiloxane/calcium xerogels as polymeric matrices for metronidazole delivery system, *Polym. Bull.*, **66** (2011) 223−237. doi: 10.1007/s00289-010-0332-8

300. Polleux, J.; Pinna, N.; Antonietti, M. and Niederberger, M. Ligand-directed assembly of preformed titania nanocrystals into highly anisotropic nanostructures, *Adv. Mater.*, **16** (2004) 436−439. doi: 10.1002/adma.200306251

301. Yang, X.H.; Li, Z.; Sun, C.; Yang, H.G. and Li, C. Hydrothermal stability of {001} faceted anatase TiO_2, *Chem. Mater.*, **23** (2011) 3486−3494. doi: 10.1021/cm2008768

302. Vashist, S.K.; Lam, E.; Hrapovic, S.; Male, K.B. and Luong, J.H.T. Immobilization of antibodies and enzymes on 3-aminopropyltriethoxysilane-functionalized bioanalytical platforms for biosensors and diagnostics, *Chem. Rev.*, **114** (2014) 11083−11130. doi: 10.1021/cr5000943

303. Gärtner, M.; Dremov, V.; Müller, P. and Kisch, H. Bandgap widening of titania through semiconductor support interactions, *ChemPhysChem*, **6** (2005) 714−718. doi: 10.1002/cphc.200400185

304. Kirillova, S.A.; Almjashev, V.I. and Gusarov, V.V. Phase relationships in the SiO_2-TiO_2 system, *Russ. J. Inorg. Chem.*, **56** (2011) 1464−1471. doi: 10.1134/s0036023611090117

305. Boulay, E.; Nakano, J.; Turner, S.; Idrissi, H.; Schryvers, D. and Godet, S. Critical assessments and thermodynamic modeling of BaO–SiO_2 and SiO_2–TiO_2 systems and their extensions into liquid immiscibility in the BaO–SiO_2–TiO_2 system, *Calphad*, **47** (2014) 68−82. doi: 10.1016/j.calphad.2014.06.004

306. Tobaldi, D.M.; Tucci, A.; Škapin, A.S. and Esposito, L. Effects of SiO_2 addition on TiO_2 crystal structure and photocatalytic activity, *J. Eur. Ceram. Soc.*, **30** (2010) 2481−2490. doi: 10.1016/j.jeurceramsoc.2010.05.014

307. Hirano, M.; Ota, K. and Iwata, H. Direct formation of anatase (TiO_2)/silica (SiO_2) composite nanoparticles with high phase stability of 1300°C from acidic solution by hydrolysis under hydrothermal condition, *Chem. Mater.*, **16** (2004) 3725−3732. doi: 10.1021/cm040055q

308. Tizjang, V.; Montazeri-Pour, M.; Rajabi, M.; Kari, M. and Moghadas, S. Surface modification of sol–gel synthesized TiO_2 photo-catalysts for the production of core/shell structured TiO_2–SiO_2 nano-composites with reduced photo-catalytic activity, *J. Mater. Sci.: Mater. Electron.*, **26** (2015) 3008−3019. doi: 10.1007/s10854-015-2791-z

309. Anderson, C. and Bard, A.J. Improved photocatalytic activity and characterization of mixed TiO_2/SiO_2 and TiO_2/Al_2O_3 materials, *J. Phys. Chem. B*, **101** (1997) 2611−2616. doi: 10.1021/jp9626982

310. Fu, X.; Clark, L.A.; Yang, Q. and Anderson, M.A. Enhanced photocatalytic performance of titania-based binary metal oxides: TiO_2/SiO_2 and TiO_2/ZrO_2, *Environ. Sci. Technol.*, **30** (1996) 647−653. doi: 10.1021/es950391v

311. Anderson, C. and Bard, A.J. An improved photocatalyst of TiO_2/SiO_2 prepared by a sol-gel synthesis, *J. Phys. Chem.*, **99** (1995) 9882−9885. doi: 10.1021/j100024a033

312. Cojocariu, A.M.; Mutin, P.H.; Dumitriu, E.; Fajula, F.; Vioux, A. and Hulea, V. Non-hydrolytic synthesis of mesoporous silica-titania catalysts for the mild oxidation of sulfur compounds with hydrogen peroxide, *Chem. Commun.*, (2008) 5357−5359. doi: 10.1039/b811668g

313. Balachandran, K.; Venckatesh, R.; Sivaraj, R.; Hemalatha, K.V. and Mariappan, R. Enhancing power conversion efficiency of DSSC by doping SiO_2 in TiO_2 photo anodes, *Mater. Sci. Semicond. Process.*, **35** (2015) 59−65. doi: 10.1016/j.mssp.2015.02.071

314. Do, Y.-J.; Kim, J.-H.; Park, J.-H.; Park, S.-S.; Hong, S.-S.; Suh, C.-S. and Lee, G.-D. Photocatalytic decomposition of 4-nitrophenol on Ti-containing MCM-41, *Catal. Today*, **101** (2005) 299−305. doi: 10.1016/j.cattod.2005.03.009

315. Rasalingam, S.; Peng, R. and Koodali, R.T. Removal of hazardous pollutants from wastewaters: Applications of TiO_2-SiO_2 mixed oxide materials, *J. Nanomater.*, **2014** (2014) 617405. doi: 10.1155/2014/617405

316. Palomares, E.; Clifford, J.N.; Haque, S.A.; Lutz, T. and Durrant, J.R. Control of charge recombination dynamics in dye sensitized solar cells by the use of conformally deposited metal oxide blocking layers, *J. Am. Chem. Soc.*, **125** (2003) 475−482. doi: 10.1021/ja027945w

317. Tong, H.; Enomoto, N.; Inada, M.; Tanaka, Y. and Hojo, J. Hydrothermal synthesis of mesoporous TiO_2-SiO_2 core-shell composites for dye-sensitized solar cells, *Electrochim. Acta*, **130** (2014) 329−334. doi: 10.1016/j.electacta.2014.03.032

318. Gholami, T.; Bazarganipour, M.; Salavati-Niasari, M. and Bagheri, S. Photocatalytic degradation of methylene blue on $TiO_2@SiO_2$ core/shell nanoparticles: Synthesis and characterization, *J. Mater. Sci.: Mater. Electron.*, **26** (2015) 6170−6177. doi: 10.1007/s10854-015-3198-6

319. Nussbaum, M. and Paz, Y. Ultra-thin SiO_2 layers on TiO_2: Improved photocatalysis by enhancing products' desorption, *Phys. Chem. Chem. Phys.*, **14** (2012) 3392−3399. doi: 10.1039/c2cp23202b

320. Yu, J.; Yu, J.C.; Leung, M.K.-P.; Ho, W.; Cheng, B.; Zhao, X. and Zhao, J. Effects of acidic and basic hydrolysis catalysts on the photocatalytic activity and microstructures of bimodal mesoporous titania, *J. Catal.*, **217** (2003) 69−78. doi: 10.1016/s0021-9517(03)00034-4

321. Mi, J.-L.; Clausen, C.; Bremholm, M.; Lock, N.; Jensen, K.M.Ø.; Christensen, M. and Iversen, B.B. Rapid hydrothermal preparation of rutile TiO_2 nanoparticles by simultaneous transformation of primary brookite and anatase: An in situ synchrotron PXRD study, *Cryst. Growth Des.*, **12** (2012) 6092−6097. doi: 10.1021/cg301230w

322. Eltzholtz, J.R.; Tyrsted, C.; Jensen, K.M.Ø.; Bremholm, M.; Christensen, M.; Becker-Christensen, J. and Iversen, B.B. Pulsed supercritical synthesis of anatase TiO_2 nanoparticles in a water-isopropanol mixture studied by in situ powder X-ray diffraction, *Nanoscale*, **5** (2013) 2372−2378. doi: 10.1039/c3nr33127j

323. Zhang, H.; Chen, B. and Banfield, J.F. The size dependence of the surface free energy of titania nanocrystals, *Phys. Chem. Chem. Phys.*, **11** (2009) 2553−2558. doi: 10.1039/b819623k

324. Barnard, A.S.; Zapol, P. and Curtiss, L.A. Modeling the morphology and phase stability of TiO_2 nanocrystals in water, *J. Chem. Theory Comput.*, **1** (2005) 107−116. doi: 10.1021/ct0499635

325. Zhao, Z.; Li, Z. and Zou, Z. Surface properties and electronic structure of low-index stoichiometric anatase TiO_2 surfaces, *J. Phys.: Condens. Matter*, **22** (2010) 175008. doi: 10.1088/0953-8984/22/17/175008

326. Martsinovich, N. and Troisi, A. How TiO_2 crystallographic surfaces influence charge injection rates from a chemisorbed dye sensitiser, *Phys. Chem. Chem. Phys.*, **14** (2012) 13392−13401. doi: 10.1039/c2cp42055d

327. Mi, J.-L.; Jensen, K.M.Ø.; Tyrsted, C.; Bremholm, M. and Iversen, B.B. In situ total X-ray scattering study of the formation mechanism and structural defects in anatase TiO_2 nanoparticles under hydrothermal conditions, *CrystEngComm*, **17** (2015) 6868−6877. doi: 10.1039/c5ce00544b

328. Sun, Y. and Ren, Y. In situ synchrotron X-ray techniques for real-time probing of colloidal nanoparticle synthesis, *Part. Part. Syst. Charact.*, **30** (2013) 399−419. doi: 10.1002/ppsc.201300033

329. Yamada, N.; Yoshinaga, I. and Katayama, S. Processing and optical properties of patternable inorganic–organic hybrid films, *J. Appl. Phys.*, **85** (1999) 2423−2427. doi: 10.1063/1.369560

330. Katayama, S.; Yoshinaga, I. and Yamada, N. Processing of transparent inorganic/organic hybrids using metal alkoxides and polydimethylsiloxane, *Proc. SPIE*, **3136** (1997) 134−142. doi: 10.1117/12.284143

331. Cai, D.; Neyer, A.; Kuckuk, R. and Heise, H.M. Raman, mid-infrared, near-infrared and ultraviolet–visible spectroscopy of PDMS silicone rubber for characterization of polymer optical waveguide materials, *J. Mol. Struct.*, **976** (2010) 274−281. doi: 10.1016/j.molstruc.2010.03.054

332. Lin-Vien, D.; Colthup, N.B.; Fateley, W.G. and Grasselli, J.G. *The handbook of infrared and Raman characteristic frequencies of organic molecules*. 1991, Academic Press: London, UK. doi: 10.1016/B978-0-08-057116-4.50001-8

333. Smith, A.L. and Anderson, D.R. Vibrational spectra of Me_2SiCl_2, Me_3SiCl, $Me_3SiOSiMe_3$, $(Me_2SiO)_3$, $(Me_2SiO)_4$, $(Me_2SiO)_x$, and their deuterated analogs, *Appl. Spectrosc.*, **38** (1984) 822−834. doi: 10.1366/0003702844554549

334. Téllez, L.; Rubio, J.; Rubio, F.; Morales, E. and Oteo, J.L. FT-IR study of the hydrolysis and polymerization of tetraethyl orthosilicate and polydimethyl siloxane in the presence of tetrabutyl orthotitanate, *Spectrosc. Lett.*, **37** (2004) 11−31. doi: 10.1081/sl-120028420

335. Zeitler, V.A. and Brown, C.A. The infrared spectra of some Ti−O−Si, Ti−O−Ti and Si−O−Si compounds, *J. Phys. Chem.*, **61** (1957) 1174−1177. doi: 10.1021/j150555a010

336. Barraclough, C.G.; Bradley, D.C.; Lewis, J. and Thomas, I.M. The infrared spectra of some metal alkoxides, trialkylsilyloxides, and related silanols, *J. Chem. Soc.*, (1961) 2601−2605. doi: 10.1039/jr9610002601

337. Ricchiardi, G.; Damin, A.; Bordiga, S.; Lamberti, C.; Spanò, G.; Rivetti, F. and Zecchina, A. Vibrational structure of titanium silicate catalysts. A spectroscopic and theoretical study, *J. Am. Chem. Soc.*, **123** (2001) 11409−11419. doi: 10.1021/ja010607v

338. Chang, H. and Huang, P.J. Thermo-Raman studies on anatase and rutile, *J. Raman Spectrosc.*, **29** (1998) 97−102. doi: 10.1002/(sici)1097-4555(199802)29:2<97::aid-jrs198>3.0.co;2-e

339. Beaucage, G.; Ulibarri, T.A.; Black, E.P. and Schaefer, D.W. Multiple size scale structures in silica–siloxane composites studied by small-angle scattering, *ACS Symp. Ser.*, **585** (1995) 97−111. doi: 10.1021/bk-1995-0585.ch009

340. Andrianov, K.A.; Slonimski, G.L.; Zhdanov, A.A.; Yu. Levin, V.; Godovski, Y.K. and Moskalenko, V.A. Some physical properties of polyorganosiloxanes. I. Linear polyorganosiloxanes, *J. Polym. Sci., Part A: Polym. Chem.*, **10** (1972) 1−22. doi: 10.1002/pol.1972.150100101

341. Zhang, D.; Liu, Y.; Shi, Y. and Huang, G. Effect of polyhedral oligomeric silsesquioxane (POSS) on crystallization behaviors of POSS/polydimethylsiloxane rubber nanocomposites, *RSC Adv.*, **4** (2014) 6275−6283. doi: 10.1039/c3ra46711b

342. Ferreira, P.; Carvalho, A.; Correia, T.R.; Antunes, B.P.; Correia, I.J. and Alves, P. Functionalization of polydimethylsiloxane membranes to be used in the production of voice prostheses, *Sci. Tech. Adv. Mater.*, **14** (2013) 055006. doi: 10.1088/1468-6996/14/5/055006

343. Surivet, F.; Thanh My, L.; Pascault, J.P. and Mai, C. Organic-inorganic hybrid materials. 2. Compared structures of polydimethylsiloxane and hydrogenated polybutadiene based ceramers, *Macromolecules*, **25** (1992) 5742−5751. doi: 10.1021/ma00047a027

344. Cherny, A.Y.; Anitas, E.M.; Osipov, V.A. and Kuklin, A.I. Scattering from surface fractals in terms of composing mass fractals, *J. Appl. Crystallogr.*, **50** (2017) 919−931. doi: 10.1107/s1600576717005696

345. Chen, Y.; Zhou, S.; Gu, G. and Wu, L. Microstructure and properties of polyester-based polyurethane/titania hybrid films prepared by sol–gel process, *Polymer*, **47** (2006) 1640−1648. doi: 10.1016/j.polymer.2005.12.073

346. Schmidt, P. Interpretation of small-angle scattering curves proportional to a negative power of the scattering vector, *J. Appl. Crystallogr.*, **15** (1982) 567−569. doi: 10.1107/S002188988201259X

347. Schaefer, D.W. and Keefer, K.D. Fractal aspects of ceramic synthesis, *MRS Proc.*, **73** (1986) 277−288. doi: 10.1557/proc-73-277

348. Betrabet, C.S. and Wilkes, G.L. Effect on microstructure of acid-catalyzed PTMO/TEOS and PTMO/TIOPR hybrids when aged in neutral and alkaline aqueous solutions, *Chem. Mater.*, **7** (1995) 535−545. doi: 10.1021/cm00051a015

349. Schaefer, D.W. and Justice, R.S. How nano are nanocomposites?, *Macromolecules*, **40** (2007) 8501−8517. doi: 10.1021/ma070356w

350. Baeza, G.P.; Genix, A.-C.; Degrandcourt, C.; Petitjean, L.; Gummel, J.; Couty, M. and Oberdisse, J. Multiscale filler structure in simplified industrial nanocomposite silica/SBR systems studied by SAXS and TEM, *Macromolecules*, **46** (2013) 317−329. doi: 10.1021/ma302248p

351. Guinier, A. La diffraction des rayons X aux très petits angles : Application à l'étude de phénomènes ultramicroscopiques, *Ann. Phys.*, **11** (1939) 161−237. doi: 10.1051/anphys/193911120161

352. Yano, S.; Iwata, K. and Kurita, K. Physical properties and structure of organic-inorganic hybrid materials produced by sol-gel process, *Mater. Sci. Eng., C*, **6** (1998) 75−90. doi: 10.1016/s0928-4931(98)00043-5

353. Wu, L.Y.L.; Tan, G.H.; Zeng, X.T.; Li, T.H. and Chen, Z. Synthesis and characterization of transparent hydrophobic sol-gel hard coatings, *J. Sol-Gel Sci. Technol.*, **38** (2006) 85−89. doi: 10.1007/s10971-006-5917-1

354. Bosq, N.; Guigo, N.; Persello, J. and Sbirrazzuoli, N. Melt and glass crystallization of PDMS and PDMS silica nanocomposites, *Phys. Chem. Chem. Phys.*, **16** (2014) 7830−7840. doi: 10.1039/c4cp00164h

355. Litzov, I. and Brabec, C. Development of efficient and stable inverted bulk heterojunction (BHJ) solar cells using different metal oxide interfaces, *Materials*, **6** (2013) 5796−5820. doi: 10.3390/ma6125796

356. Babonneau, F. Hybrid siloxane-oxide materials via sol-gel processing: Structural characterization, *Polyhedron*, **13** (1994) 1123−1130. doi: 10.1016/s0277-5387(00)80249-1

357. Hoebbel, D.; Nacken, M.; Schmidt, H.; Huch, V. and Veith, M. X-ray and NMR spectroscopic characterisation of cyclic titanodiphenylsiloxanes and examination of the hydrolytic stability of their Si–O–Ti bonds, *J. Mater. Chem.*, **8** (1998) 171−178. doi: 10.1039/a702644g

358. Huang, H.H.; Orler, B. and Wilkes, G.L. Structure-property behavior of new hybrid materials incorporating oligomeric species into sol-gel glasses. 3. Effect of acid content, tetraethoxysilane content, and molecular weight of poly(dimethylsiloxane), *Macromolecules*, **20** (1987) 1322−1330. doi: 10.1021/ma00172a026

359. Jeong, S. and Moon, J. Fabrication of inorganic–organic hybrid films for optical waveguide, *J. Non-Cryst. Solids*, **351** (2005) 3530−3535. doi: 10.1016/j.jnoncrysol.2005.08.029

360. Kuznetsov, A.I.; Kameneva, O.; Bityurin, N.; Rozes, L.; Sanchez, C. and Kanaev, A. Laser-induced photopatterning of organic-inorganic TiO_2-based hybrid materials with tunable interfacial electron transfer, *Phys. Chem. Chem. Phys.*, **11** (2009) 1248−1257. doi: 10.1039/b814494j

361. Chen, M.; Zhang, G.; Liang, X.; Zhang, W.; Zhou, L.; He, B.; Song, P.; Yuan, X.; Zhang, C.; Zhang, L.; Yu, H. and Yang, H. Thermally stable transparent sol–gel based active siloxane–oligomer materials with tunable high refractive index and dual reactive groups, *RSC Adv.*, **6** (2016) 70825−70831. doi: 10.1039/c6ra13164f

362. Delattre, L. and Babonneau, F. ^{17}O solution NMR characterization of the preparation of sol−gel derived SiO_2/TiO_2 and SiO_2/ZrO_2 glasses, *Chem. Mater.*, **9** (1997) 2385−2394. doi: 10.1021/cm970372f

363. Kim, W.B.; Choi, S.H. and Lee, J.S. Quantitative analysis of Ti−O−Si and Ti−O−Ti bonds in Ti−Si binary oxides by the linear combination of XANES, *J. Phys. Chem. B*, **104** (2000) 8670−8678. doi: 10.1021/jp000042+

8. Appendices

8.1. Example of Rietveld refinement code from TOPAS

Legend: Description
Name/directory
Refined parameter (value_error)
Example

```
'Global fitting results
r_exp  1.6387229 r_exp_dash  2.3637761 r_wp  1.06318863 r_wp_dash  1.53359661 r_p  0.844431879
r_p_dash  1.41718803 weighted_Durbin_Watson  0.00706555239 gof  0.648790979
iters 100000
do_errors
'Refinement conditions
xdd "C:\Users\...\TiO2-quench.xy"
   r_exp  1.6387229 r_exp_dash  2.3637761 r_wp  1.06318863 r_wp_dash  1.53359661 r_p  0.844431879
   r_p_dash  1.41718803 weighted_Durbin_Watson  0.00706555239 gof  0.648790979
   x_calculation_step 0.02
   bkg @ 1571.57236`_65.0891724  1240.17023`_65.7142412  233.702509`_18.4463084 -
   561.909742`_43.0524605  117.14421`_21.6584844  158.263695`_5.7766385 -5.95730102`_10.5959962 -
   53.5243192`_5.27269512
   start_X  4.9
   finish_X  42.1
   LP_Factor( 90_LIMIT_MIN_0.0001)
   Zero_Error(Zer,  0.00928`_0.00131)

'Instrument parameters: arbitrary functions refined with LaB6 (peak function FP, Pawley refinement)
   Rp 600
   Rs 600
   User_Defined_Dependence_Convolution(lor_fwhm,  Tan(Th)   , , 0.000100000033_LIMIT_MIN_0.0001)
   User_Defined_Dependence_Convolution(one_on_x_conv,  1/Cos(Th)   , , 0.008974582542)
   User_Defined_Dependence_Convolution(circles_conv,  1/Cos(Th)   , , 0.009276279691)
   User_Defined_Dependence_Convolution(lor_fwhm, , , 0.002137617527)
   User_Defined_Dependence_Convolution(lor_fwhm,  1/Cos(Th) , , 0.0001000000204_LIMIT_MIN_0.0001)
   User_Defined_Dependence_Convolution(one_on_x_conv,  1/Cos(Th)   , , 0.008959113127)
   User_Defined_Dependence_Convolution(exp_conv_const, , , 0.04736146589)
   User_Defined_Dependence_Convolution(gauss_fwhm, , , 0.03396894257)
```

```
'Wavelength was 0.699900 Å
lam
   ymin_on_ymax  0.001
   la  1 lo  0.6999 lh  0.01_LIMIT_MAX_5

'Anatase Rietveld
str
   r_bragg  0.372433894
   phase_MAC  14.7759085
   phase_name "anatase"
   weight_percent anatase_percent 0
   MVW( 319.463, 137.300`_0.026, 86.989`_1.411)
   scale @  0.00133090928`_9.755e-006
   space_group I41/amd
   Phase_LAC_1_on_cm( 57.08915`_0.01074)
   Phase_Density_g_on_cm3( 3.86366`_0.00073)
   Tetragonal(a_anatase  3.799058`_0.000312,c_anatase  9.513036`_0.000876)
   site Ti num_posns  4 occ Ti+4  1 beq  1 x  0 y  0 z  0
   site O num_posns  8 occ O-2  1 beq  1 x  0 y  0 z  0.20806

'Anisotropic crystallite size calculations
   prm lor1_h00  200.00000`_0.64879_LIMIT_MIN_0.3 min .3
   prm lor1_0k0  14.05646`_0.39226 min .3
   prm lor1_00l  11.98785`_0.32089 min .3
   prm lor1_hk0  11.14043`_0.70435_LIMIT_MIN_0.3 min .3
   prm lor1_h0l  200.00000`_0.64879_LIMIT_MIN_0.3 min .3
   prm lor1_0kl  16.09746`_0.39512 min .3
   prm lor1_hkl  16.68187`_0.72488 min .3
   prm gauss1_h00  200.00000`_0.64879_LIMIT_MIN_0.3 min .3
   prm gauss1_0k0  13.96198`_0.34916 min .3
   prm gauss1_00l  43.61188`_9.16135_LIMIT_MIN_0.3 min .3
   prm gauss1_hk0  19.21690`_2.83204_LIMIT_MIN_0.3 min .3
   prm gauss1_h0l  200.00000`_0.64879_LIMIT_MIN_0.3 min .3
   prm gauss1_0kl  14.01353`_0.19164 min .3
   prm gauss1_hkl  11.63672`_0.26930 min .3
'Calculation of crystallite sizes IB and FWHM
   'LVol_H00
   prm LVol_H00 = 1 / IB_from_CS(gauss1_h00, lor1_h00); :  89.79020`_0.20791
   'L_FWHM_H00
   prm L_FWHM_H00 = 0.89 / Voigt_FWHM_from_CS(gauss1_h00, lor1_h00); :  108.49815`_0.25061
   'LVol_0K0
   prm LVol_0K0 = 1 / IB_from_CS(gauss1_0k0, lor1_0k0); :  6.29229`_0.12063
   'L_FWHM_0K0
   prm L_FWHM_0K0 = 0.89 / Voigt_FWHM_from_CS(gauss1_0k0, lor1_0k0); :  7.59674`_0.14149
   'LVol_00L
   prm LVol_00L = 1 / IB_from_CS(gauss1_00l, lor1_00l); :  7.29212`_0.22017
   'L_FWHM_00L
   prm L_FWHM_00L = 0.89 / Voigt_FWHM_from_CS(gauss1_00l, lor1_00l); :  9.93897`_0.35380
```

```
   'LVol_HK0
   prm LVol_HK0 = 1 / IB_from_CS(gauss1_hk0, lor1_hk0); :  6.01800`_0.36145
   'L_FWHM_HK0
   prm L_FWHM_HK0 = 0.89 / Voigt_FWHM_from_CS(gauss1_hk0, lor1_hk0); :  7.76219`_0.51556
   'LVol_H0L
   prm LVol_H0L = 1 / IB_from_CS(gauss1_h0l, lor1_h0l); :  89.79020`_0.20791
   'L_FWHM_H0L
   prm L_FWHM_H0L = 0.89 / Voigt_FWHM_from_CS(gauss1_h0l, lor1_h0l); :  108.49815`_0.25061
   'LVol_0KL
   prm LVol_0KL = 1 / IB_from_CS(gauss1_0kl, lor1_0kl); :  6.78671`_0.09791
   'L_FWHM_0KL
   prm L_FWHM_0KL = 0.89 / Voigt_FWHM_from_CS(gauss1_0kl, lor1_0kl); :  8.05604`_0.10279
   'LVol_HKL
   prm LVol_HKL = 1 / IB_from_CS(gauss1_hkl, lor1_hkl); :  6.28279`_0.14766
   'LVol_FWHM_HKL
   prm LVol_FWHM = 0.89 / Voigt_FWHM_from_CS(gauss1_hkl, lor1_hkl); :  7.25149`_0.15343
'hkl
   lor_fwhm =
   (0.1 Rad Lam / Cos(Th)) /
   IF And(H == 0, L == 0) THEN
   lor1_0k0
   ELSE IF And(K == 0, L == 0) THEN
   lor1_h00
   ELSE IF And(H == 0, K == 0) THEN
   lor1_00l
   ELSE IF And(H == 0) THEN
   lor1_0kl
   ELSE IF And(K == 0) THEN
   lor1_h0l
   ELSE IF And(L == 0) THEN
   lor1_hk0
   ELSE
   lor1_hkl
   ENDIF
   ENDIF
   ENDIF
   ENDIF
   ENDIF
   ENDIF   ;
   gauss_fwhm =
   (0.1 Rad Lam / Cos(Th)) /
   IF And(H == 0, L == 0) THEN
   gauss1_0k0
   ELSE IF And(K == 0, L == 0) THEN
   gauss1_h00
   ELSE IF And(H == 0, K == 0) THEN
   gauss1_00l
   ELSE IF And(H == 0) THEN
```

```
   gauss1_0kl
   ELSE IF And(K == 0) THEN
   gauss1_h0l
   ELSE IF And(L == 0) THEN
   gauss1_hk0
   ELSE
   gauss1_hkl
   ENDIF
   ENDIF
   ENDIF
   ENDIF
   ENDIF
   ENDIF   ;

'Brookite Rietveld
str
   LVol_FWHM_CS_G_L( 1, 3.19553`_0.38892, 0.89, 4.46738`_0.54372,,,@, 5.01953`_0.61092_LIMIT_MIN_5
   min =5; max =50;)
   r_bragg  0.450845809
   phase_MAC  14.7759085
   phase_name "brookite"
   weight_percent brookite_percent 0
   MVW( 638.926, 257.632, 13.011`_1.411)
   scale @  5.30436245e-005`_6.606e-006
   space_group Pcab
   Phase_LAC_1_on_cm( 60.84927)
   Phase_Density_g_on_cm3( 4.11814)
   a  5.4558
   b  9.1819
   c  5.1429
   site Ti num_posns  8 occ Ti+4  1 beq  1 x  0.0972 y  0.129 z  0.8629
   site O1 num_posns  8 occ O-2  1 beq  1 x  0.8514 y  0.9899 z  0.8176
   site O2 num_posns  8 occ O-2  1 beq  1 x  0.113 y  0.2304 z  0.5371

'Peak locked between 2theta = 12 - 15 for water (in situ)
xo_Is
   xo @  12.2952853`_0.00907462975 min =12; max =15;
   LVol_FWHM_CS_G_L( 1, 0.32709`_0.00513, 0.89, 0.45727`_0.00718,,,@, 0.51379`_0.00807)
   I @  791.24266`_37.54825
   peak_type fp

'Peak locked between 2theta = 19 - 20 for water (in situ)
xo_Is
   xo @  18.380816`_0.0119668571 min =18; max =20;
   LVol_FWHM_CS_G_L( 1, 0.42990`_0.00621, 0.89, 0.60101`_0.00868,,,@, 0.67529`_0.00975)
   I @  600.78839`_20.75015
   peak_type fp
```

```
'Export of data: Y observed, Y calculated and difference for each refined .xy file
Out_Yobs_Ycalc_and_Difference("C:\Users\...\TiO2-quench.txt")

'Export of data: refined parameters for all diffractograms as a single table in a text file
out "TiO2-ani.txt" append
   Out_String("TiO2-quench.xy")                          'name                 TiO2-quench.xy
   Out(Get (r_exp), " %11.5f")                           'Rexp                 1.64 %
   Out(Get (r_wp), " %11.5f")                            'Rwp                  1.06 %
   Out(Get (r_p), " %11.5f")                             'Rp                   0.84 %
   Out(Get (gof), " %11.5f")                             'GOF                  0.65
   Out(scale_A, "  %11.7f", " %11.7f")                   'scale anatase        0.00133(1)
   Out(anatase_percent, " %11.5f", " %11.5f")            '%anatase             86(1) %
   Out(scale_B, "  %11.7f", " %11.7f")                   'scale brookite       0.000053(7)
   Out(brookite_percent,  " %11.5f", " %11.5f")          '%brookite            13(1) %
   Out(a_anatase, " %11.5f", " %11.5f")                  'a_anatase            3.7990(3) Å
   Out(c_anatase, " %11.5f", " %11.5f")                  'c_anatase            9.5130(9) Å
   Out(LVol_0K0," %11.5f", " %11.5f")                    'LVol_0K0             6.29(12) nm
   Out(LVol_00L," %11.5f", " %11.5f")                    'LVol_00L             7.29(22) nm
   Out(LVol_HK0," %11.5f", " %11.5f")                    'LVol_HK0             6.01(36) nm
   Out(LVol_0KL," %11.5f", " %11.5f")                    'LVol_0KL             6.78(10) nm
   Out(LVol_HKL," %11.5f", " %11.5f")                    'LVol_HKL             6.28(15) nm
   Out(Zer, " %11.5f", " %11.5f\n")                      'zero_error           0.009(1) °
```

8.2. Comparison of Rietveld refinement models

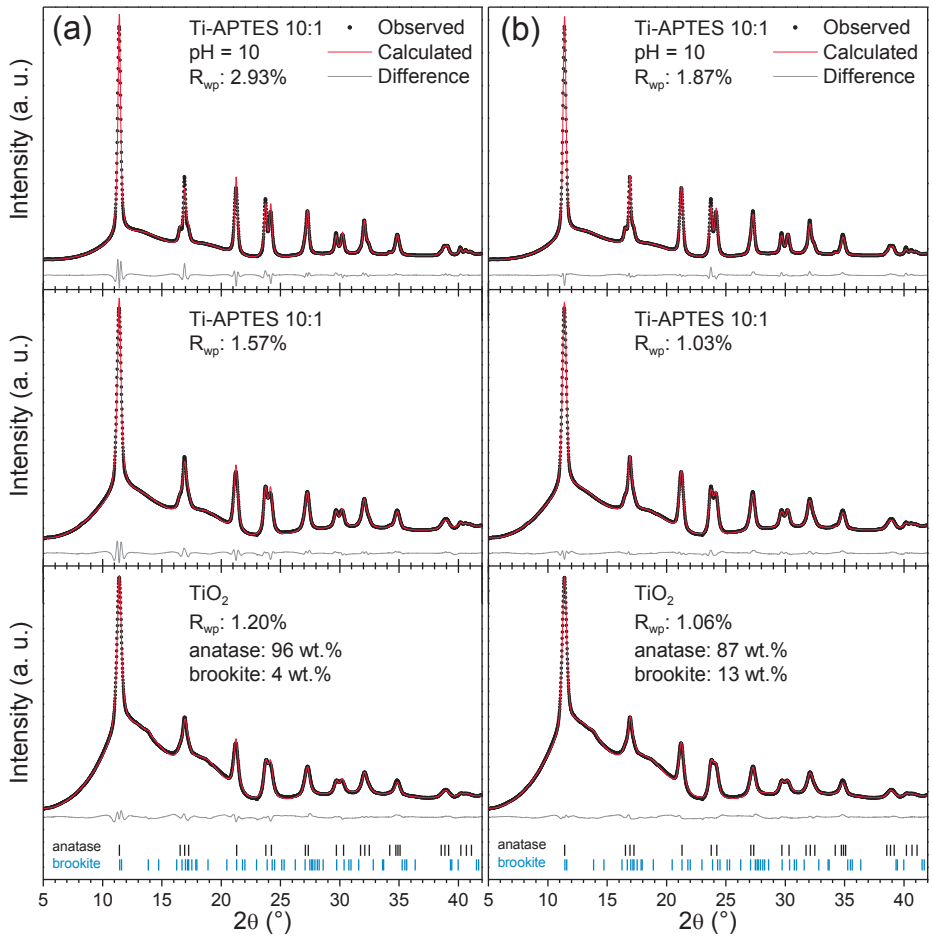

Figure 8.1. Comparison of Rietveld refinements on the room temperature diffractograms obtained from *in situ* XRD ($\lambda = 0.6999$ Å): (a) standard, (b) with the correction for anisotropic peak broadening.

8.3. Initial tests on Ti-DTES

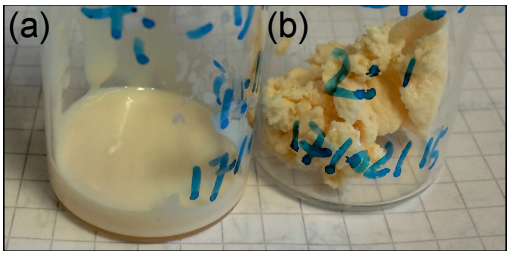

Figure 8.2. Photographs of Ti-DTES initial test samples with TIP/DTES molar ratio of (a) 1:1 and (b) 2:1. The gel-like appearance demonstrates cross-linking of the DTES precursor.

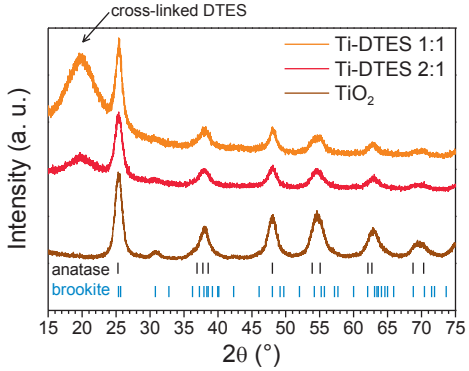

Figure 8.3. Diffractograms (λ = 1.5406 Å) of Ti-DTES 1:1 and 2:1 initial test samples. The broad line at 20° is increasing with increasing DTES amount implies that it originates from the DTES precursors. The presence of anatase and brookite reflections, similar to that of pure TiO_2, indicates that the nanoparticles are embedded in the polymeric-like material.

8.4. Additional information on the Ti-PDMS materials

8.4.1. Ellipsometry

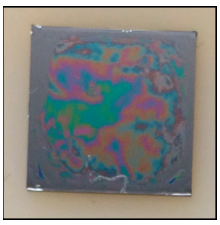

Figure 8.4. Example of spin-coated film (Ti-PDMS-65-2:1).

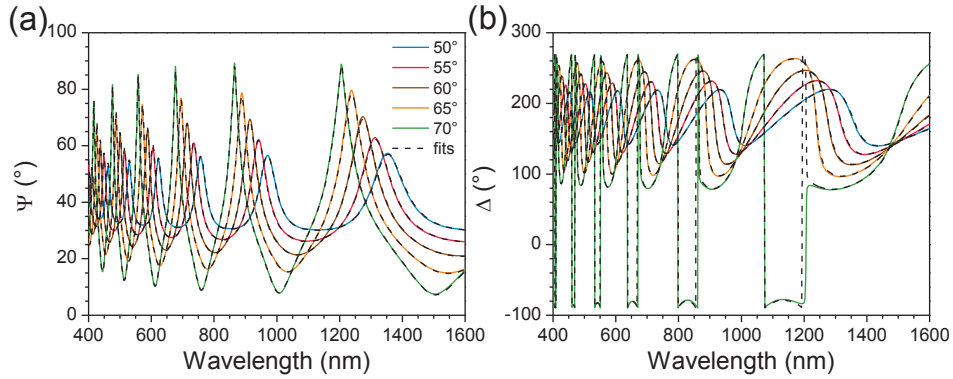

Figure 8.5. Example of ellipsometry raw data and fits from Ti-PDMS-65-2:1 sample.

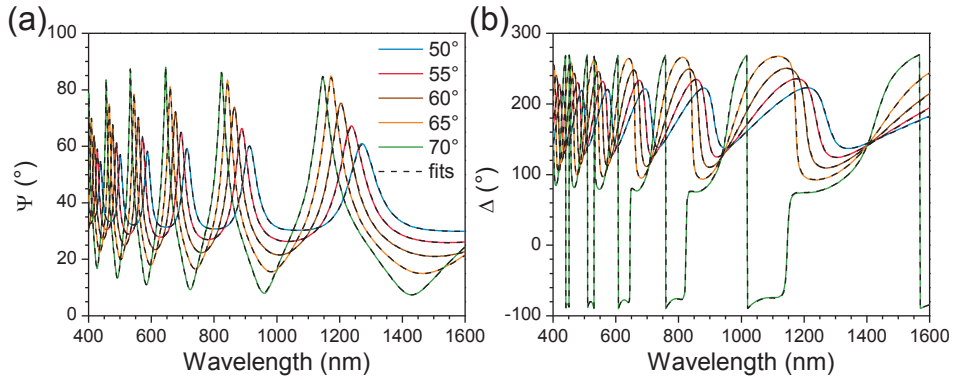

Figure 8.6. Example of ellipsometry raw data and fits from Ti-PDMS-25-5:1 sample.

8.4.2. Thermogravimetry

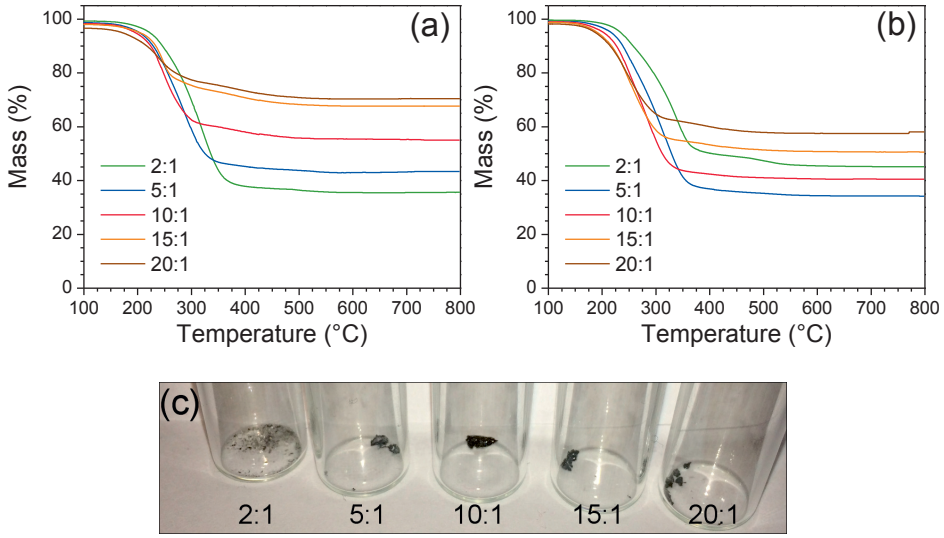

Figure 8.7. Thermogravimetry analysis on Ti-PDMS prepared using PDMS with viscosities of (a) 25 cSt and (b) 65 cSt for different TIP/PDMS-OH molar ratios; (c) picture of the residual products of the 65 cSt series after the analysis.

8.5. Scientific papers

Paper 1.

Dalod, A.R.M.; Henriksen, L.; Grande, T. and Einarsrud, M.-A. Functionalized TiO_2 nanoparticles by single-step hydrothermal synthesis: the role of the silane coupling agents. *Beilstein J. Nanotechnol.*, **8** (2017) 304−312. doi: 10.3762/bjnano.8.33

Paper 2.

Dalod, A.R.M.; Grendal, O.G.; Skjærvø, S.L.; Inzani, K.; Selbach, S.M.; Henriksen, L.; van Beek, W.; Grande, T. and Einarsrud, M.-A. Controlling oriented attachment and *in situ* functionalization of TiO_2 nanoparticles during hydrothermal synthesis with APTES.

J. Phys. Chem. C, **121** (2017) 11897−11906. doi: 10.1021/acs.jpcc.7b02604

BEILSTEIN JOURNAL OF NANOTECHNOLOGY

Functionalized TiO_2 nanoparticles by single-step hydrothermal synthesis: the role of the silane coupling agents

Antoine R. M. Dalod[1], Lars Henriksen[2], Tor Grande[1] and Mari-Ann Einarsrud[*1,§]

Full Research Paper

Open Access

Address:
[1]Department of Materials Science and Engineering, NTNU, Norwegian University of Science and Technology, NO-7491 Trondheim, Norway and [2]poLight AS, Kongeveien 77, NO-3188 Horten, Norway

Email:
Mari-Ann Einarsrud[*] - mari-ann.einarsrud@ntnu.no

* Corresponding author
§ Telephone: +47 73 59 40 02

Keywords:
core–shell nanoparticles; functionalized nanoparticles; hydrothermal synthesis; oriented attachment; silane coupling agent

Beilstein J. Nanotechnol. **2017,** *8,* 304–312.
doi:10.3762/bjnano.8.33

Received: 23 August 2016
Accepted: 16 December 2016
Published: 31 January 2017

This article is part of the Thematic Series "Hybrid nanomaterials: from the laboratory to the market".

Guest Editor: A. Taubert

Abstract

A simple, robust and versatile hydrothermal synthesis route to in situ functionalized TiO_2 nanoparticles was developed using titanium(IV) isopropoxide as Ti-precursor and selected silane coupling agents (3-aminopropyltriethoxysilane (APTES), 3-(2-aminoethylamino)propyldimethoxymethylsilane (AEAPS), and *n*-decyltriethoxysilane (DTES)). Spherical nanoparticles (ca. 9 nm) with narrow size distribution were obtained by using DTES or by synthesis performed without silane coupling agents. Rod-like nanoparticles along with 9 nm spherical nanoparticles were formed using aminosilane coupling agents because of a combination of oriented attachment of nanoparticles and specific adsorption of the aminosilane on crystallographic faces of anatase nanoparticles. The nanoparticles were functionalized in situ and became hydrophobic as silanes reacted to form covalent bonds on the surface of TiO_2. The versatility of the aqueous synthesis route was demonstrated, and by selecting the type of silane coupling agent the surface properties of the TiO_2 nanoparticles could be tailored. This synthesis route has been further developed into a two-step synthesis to TiO_2–SiO_2 core–shell nanoparticles. Combustion of the silane coupling agents up to 700 °C leads to the formation of a nanometric amorphous SiO_2 layer, preventing growth and phase transition of the in situ functionalized nanoparticles.

Introduction

Because of the high surface-to-volume ratio, the intrinsic properties of titanium dioxide (TiO_2) nanoparticles have led to exploitation in many fields such as in photocatalysis [1], solar cells [2], and in biomedical applications [3]. The naturally occurring phases of TiO_2 are rutile (thermodynamically stable polymorph), brookite, and anatase [4]. Due to the differences in surface energy, anatase and brookite are more stable than rutile at nanosize, and anatase is more stable than brookite at even smaller sizes (generally below 15–30 nm) [5-7]. Surface modification of TiO_2 nanoparticles, via core–shell structures or grafted nanoparticles [8], has resulted in new applications such as nanofiller for polymer nanocomposites [9,10], coatings [11],

and biosensors [3,12]. Classical synthesis routes for surface-functionalized particles are following two steps: particles synthesis followed by a post-functionalization process [9,10,13].

Post-functionalization of TiO_2 nanoparticles with silane coupling agents was obtained via reflux in aqueous solution [14,15]. Chen et al. investigated interactions of 3-aminopropyltrimethoxysilane (APTMS) and phenyltrimethoxysilane with commercially available TiO_2 nanoparticles (Degussa P-25) [14]. They concluded that the silane coupling agents covalently bond onto the surface of TiO_2 nanoparticles. Using a mixture of isomeric octyltriethoxysilanes (OTES), Milanesi et al. focused on the structure of the hydrophobic layer and proposed that cross-linking (via Si–O–Si bonds) and chemical bonding (via Ti–O–Si bonds) of silanes onto TiO_2 nanoparticles occurred [16]. Later, Zhao et al. detailed the cross-linking and chemical bonding mechanisms of APTMS and 3-isocyanatopropyltrimethoxysilane on TiO_2 nanoparticles [15]. A contact angle of about 150° for water was measured demonstrating hydrophobic nanoparticles. Wang et al. functionalized commercial TiO_2 nanoparticles in aqueous solution via ultrasonic treatment at room temperature with 3-(trimethoxysilyl)propyl methacrylate [17]. The resulting particles exhibited hydrophobic behavior. Another study reported room-temperature surface functionalization of commercial TiO_2 nanoparticles in ethanol using *n*-(6-aminohexyl)aminopropyltrimethoxysilane [18].

Nanoparticle synthesis with in situ surface functionalization has the advantage to reduce the number of reaction steps and is thus of greater interest for potential industrial applications. Teleki et al. developed a route for the continuous production of surface-functionalized TiO_2 via flame spray pyrolysis where the particles were directly functionalized after synthesis with OTES [19]. Depending on the conditions, they obtained surface-functionalized TiO_2 nanoparticles with an average size of 40 nm and they determined a maximum surface coverage of about 2.6 OTES molecules per square nanometer. Niederberger et al. developed a room-temperature non-aqueous in situ functionalization process of TiO_2 nanoparticles with 4-*tert*-butylcatechol and dopamine [20]. A brittle brown solid and a dark red powder was obtained for 4-*tert*-butylcatechol and dopamine surface functionalized samples, respectively. More recently, Gao and Cui reported a sol–gel method in which TiO_2 nanoparticles functionalized with chlorinated alcohols through hydrogen bonding were produced [21]. However, sol–gel synthesis often leads to poorly crystalline particles [22].

Hydrothermal synthesis [23] is simple and cost efficient [24] and allows for improved crystallinity compared to sol–gel methods [22] giving improved TiO_2 characteristics for applications such as photocatalysis and solar cell applications [2,25,26]. Typically used precursors are titanium alkoxides where the formation of anatase nanocrystals occurs through hydrolysis and condensation [22]. To our knowledge there is only one work where in situ functionalization of TiO_2 nanoparticles using solvothermal synthesis is reported. Koziej et al. used trimethoxy(7-octen-1-yl)silane (7-OTS) and 3-(trimethoxysilyl)propyl methacrylate coupling agents during TiO_2 nanoparticle synthesis from titanium isopropoxide in anhydrous benzyl alcohol [27]. The particles however needed further post functionalization with 7-OTS for better compatibility with organic solvent and PMMA.

Here, we report on a novel and versatile in situ aqueous hydrothermal synthesis route to surface-functionalized TiO_2 nanoparticles using selected silane coupling agents. The nanoparticles were characterized with respect to crystal structure, size, size distribution, specific surface area, surface coverage, and hydrophobicity. Tuning the surface properties of the nanoparticles for different applications by selecting the silane coupling agent is discussed. We further report the effect of heat treatment of the nanoparticles for the formation of core–shell TiO_2–SiO_2 nanoparticles.

Experimental

Synthesis

The synthesis of the non-functionalized TiO_2 nanoparticles was based on a hydrothermal route previously described by Hayashi and Torii, using titanium(IV) isopropoxide (TIP) as precursor [28]. The synthesis method was further developed for in situ surface functionalization using selected silane coupling agents: 3-aminopropyltriethoxysilane (Sigma-Aldrich, 99%), 3-(2-aminoethylamino)propyldimethoxymethylsilane (Fluka, ≥95%), and *n*-decyltriethoxysilane (ABCR, 97%); abbreviated APTES, AEAPS, and DTES, respectively.

TIP (28 mmol, Sigma-Aldrich, ≥97%) was mixed with distilled water, to which the silane coupling agent (TIP/silane molar ratio equal to 10:1) was initially added to give a filling factor of 70% in the autoclave. The solutions were vigorously stirred for 10 min prior to transfer into a PTFE-lined autoclave (Parr, 125 mL) and heated for 2 h at 200 °C. After cooling to room temperature, the products were centrifuged (10000 rpm, 10 min) and washed with distilled water. This process was repeated three times. The obtained slurries were dried for about 12 h at 100 °C for analysis.

TiO_2 samples in situ surface-functionalized with APTES, AEAPS, and DTES are labeled Ti-APTES, Ti-AEAPS, and Ti-DTES, respectively. Heat-treated samples at 700 °C in synthetic air during thermogravimetric analysis (see details below) were further investigated and are labeled adding the suffix

"-HT" to the original sample name, i.e., TiO_2-HT, Ti-APTES-HT, Ti-AEAPS-HT, and Ti-DTES-HT.

Characterization

Powder X-ray diffraction (XRD) was performed on a Bruker D8 Advance DAVINCI working in Bragg–Brentano (θ/2θ) geometry. Diffractograms were recorded under Cu Kα radiation, with a step size of 0.013°, an integration time of 0.4 s, and using variable divergent slits. Rietveld refinements and crystallite sizes were obtained using TOPAS (Bruker AXS version 4.2).

Scanning electron microscopy (SEM) images were recorded on an in-lens cold-field-emission S(T)EM Hitachi S-5500. The acceleration voltage was set at 7 kV and secondary electrons were detected. For the preparation of the samples, a drop of particles in water obtained after the centrifugation steps was placed on an aluminum sample holder which was set to dry overnight. The line-intercept method was used to calculate average particle sizes, using sample pictures containing more than 300 intercepts.

Transmission electron microscopy (TEM) images were recorded on a JEOL 2100 equipped with Oxford X-Max 80 SDD detector for energy-dispersive X-ray spectroscopy (EDS) analysis. The acceleration voltage was set at 200 kV. For the preparation of the samples, the nanoparticles were dispersed in anhydrous 2-propanol (Sigma-Aldrich, 99.5%) by sonication for 15 min. A droplet of the suspension was then placed on a carbon-coated copper TEM grid, which was set to rest until evaporation of the solvent. The d_{hkl} distances were measured by extracting an area of interest from the HR-TEM images with fast Fourier transform analysis, and calculating the average distance over more than ten consecutive *hkl* planes, using DigitalMicrograph (Gatan Inc. version 3.01).

Specific surface area (BET method [29]) and pore size distribution (BJH method [30]) were measured by nitrogen adsorption on a Micrometrics Tristar 3000. Samples were degassed for 12 h at 180 °C in vacuum prior to analysis. Particle sizes were estimated from the surface area assuming non-porous and spherical particles.

Fourier-transform infrared (FTIR) spectra were acquired on a Bruker Vertex 80v FTIR equipped with Bruker Platinum ATR diamond system from 400 to 4000 cm^{-1}, under medium vacuum (280 Pa). A background was collected under medium vacuum, without sample. Between each analysis, the ATR diamond was cleaned with isopropanol, for which vacuum provides fast evaporation and no specific adsorption bands of isopropanol were observed. A total of 128 scans were acquired for each sample at a resolution of 1 cm^{-1}.

Thermogravimetric analysis (TGA) was acquired on a Netzsch Jupiter STA 449 C using an alumina crucible. The nanoparticles were firstly heat-treated from 25 to 150 °C (10 °C·min^{-1}), maintained at 150 °C for 30 min, cooled down to room temperature, and heat-treated again from 25 to 200 °C (2 °C·min^{-1}) in order to remove adsorbed water. The samples were finally heat-treated from 100 to 700 °C (2 °C·min^{-1}). All treatments were performed under synthetic air.

Results and Discussion

Structure, particle size and morphology

XRD patterns of TiO_2 and in situ surface-functionalized TiO_2 nanoparticles, presented in Figure 1, show anatase as main phase with around 25 wt % of brookite in the case of pure TiO_2 and Ti-DTES samples (for Rietveld refinements see Figure S1 of Supporting Information File 1). The broad diffraction lines demonstrate small crystallite sizes, which were determined by refinement to be between 4.7 and 9.1 nm (Table 1). The HR-TEM image of the pure TiO_2 sample (Figure 2a) demonstrates that anatase and brookite nucleate as individual monocrystalline nanoparticles. The electron diffraction patterns also show anatase and brookite in the case of TiO_2 (Figure 2b) while Ti-APTES (Figure 2d) is purely anatase.

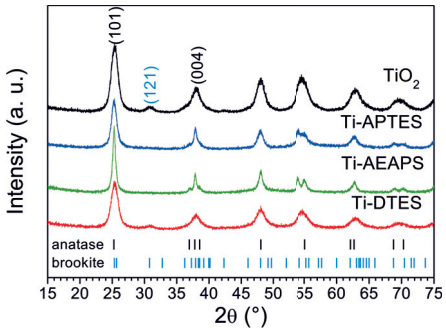

Figure 1: XRD patterns of TiO_2 and in situ surface-functionalized TiO_2 nanoparticles (the bars show diffraction lines of anatase from ICDD card #00-021-1272 and brookite from ICDD card #00-029-1360).

SEM images of TiO_2 and in situ surface-functionalized TiO_2 nanoparticle agglomerates are displayed Figure 3. The measured particle sizes are included in Table 1. TiO_2 (Figure 3a), and Ti-DTES (Figure 3b) samples consist of non-porous spherical nanoparticles with an average diameter of 9 nm and a narrow size distribution. Samples functionalized with aminosilane (Figure 3c,d) exhibit similar nanoparticles, but also larger rod-like nanoparticles. Similar crystallite size and roughness of the rod-like nanostructures suggest that they are formed by oriented attachment [31] of the nanoparticles. HR-TEM image of Ti-APTES (Figure 2c) shows {004} planes

Table 1: Properties of TiO_2 and in situ surface-functionalized TiO_2 nanoparticles from nitrogen adsorption, XRD, SEM, and TGA analysis.

sample	S_{BET}[a] ($m^2 \cdot g^{-1}$)	d_{BET}[b] (nm)	d_{BJH}[c] (nm)	d_{XRD}[d] (nm)	d_{SEM}[e] (nm)	organic mass loss (%)	surface coverage (nm^{-2})
TiO_2	195	7.9	7.9	5.7	9.0 ± 0.6	n/a	n/a
Ti-APTES	178	8.7	9.2	6.0	16.4 ± 1.4	5.8	3.4
Ti-AEAPS	149	10.3	11.8	9.1	20.9 ± 3.2	6.7	2.3
Ti-DTES	114	13.5	9.7	4.7	9.2 ± 0.9	10.8	4.0

[a]BET specific surface area from nitrogen adsorption measurements; [b]particle size estimated from BET specific surface area; [c]average pore diameter from BJH desorption calculations; [d]crystallite size from Rietveld refinement of XRD measurements; [e]particle size from SEM observations.

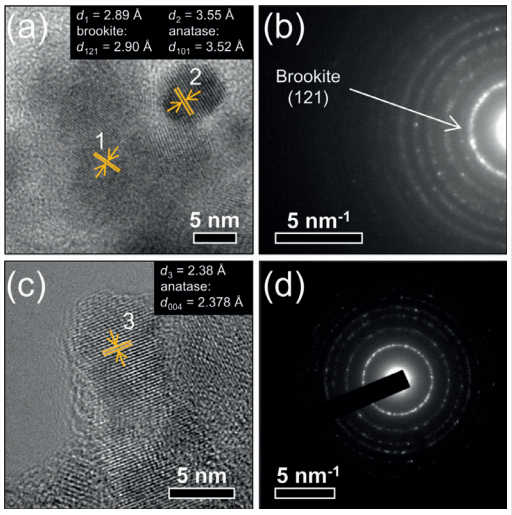

Figure 2: (a) HR-TEM image showing two individual nanoparticles of (1) brookite and (2) anatase and (b) electron diffraction pattern of pure TiO_2 (top); (c) HR-TEM image of a rod-like nanoparticle and (d) electron diffraction pattern of Ti-APTES (bottom).

oriented perpendicularly to the elongation direction of a rod-like nanoparticle indicating growth along the [001] crystallographic direction, as previously reported for hydrothermally formed anatase [32]. This is also confirmed by the narrower FWHM of the (004) diffraction line at 37.80° (Figure 1 and Figure S1 of Supporting Information File 1) compared to other reflections. The rod-like nanoparticles are longer in the Ti-AEAPS sample (50–200 nm) compared to the Ti-APTES sample (50–100 nm) and they are not observed with the alkylsilane functionalization agent (DTES). Ahmad et al. [33] reported that different crystallographic faces of anatase exhibit different polarity and Kassir et al. [18] demonstrated that aminosilanes do not react homogeneously on the different faces of TiO_2 nanoparticles. Thus, we propose that as the nanoparticles growth and functionalization occur simultaneously, rod-like nanoparticles originate from aminosilanes that guide the growth of the nanoparticles along the [001] crystallographic direction of anatase. The aminosilane-functionalized TiO_2 nanoparticles are also the only ones that are purely anatase (Figure 1 and Figure S1 of Supporting Information File 1). Particle size and surface energy are some of the main factors for phase stability crossovers in nanotitania [5-7] and specific adsorption of aminosilanes could reduce the surface energy of the forming nanoparticles, promoting anatase nucleation during the synthesis, even if the crystallite and particle sizes are in this case larger than those measured for pure TiO_2 (Table 1).

The measured BET specific surface area and the corresponding calculated size of the nanoparticles are included in Table 1. The particle sizes are consistent with the SEM and TEM observations and the crystallite sizes determined by XRD, which suggest only weakly agglomeration in the powders after drying.

The nitrogen adsorption and desorption isotherms of TiO_2 and in situ surface-functionalized TiO_2 nanoparticles demonstrate the hysteresis profile similar to mesoporous materials (Figure 4a). Since particle sizes from SEM and surface area are similar, porosity is associated with inter-particle volume of the agglomerates and can be directly correlated with the particle sizes [34]. Figure 4b displays the pore size distribution from desorption isotherms of TiO_2 and in situ surface-functionalized TiO_2 nanoparticles. The pore size distribution is centered between 4 and 7 nm for TiO_2 and Ti-DTES, while for the aminosilane-functionalized samples, the size distribution is broader and shifted towards larger pores and two features are observed. The first feature centered between 4 and 7 nm is assigned to interstitial volume of the spherical nanoparticles and the second broader feature is assigned to interstitial volume of the rod-like particles. Coherently with SEM observations, as less spherical nanoparticles are observed in Ti-AEAPS, the volume of the feature between 4 and 7 nm is decreasing (relative comparison to Ti-APTES), and as rod-like particles are larger, the feature at 10 nm is shifted towards larger pores. The average pore diameters from BJH desorption curves are included in Table 1.

Functionalization and hydrophobicity

Thermogravimetric analysis of TiO_2 and the in situ surface-functionalized TiO_2 nanoparticles are presented in Figure 5a. In

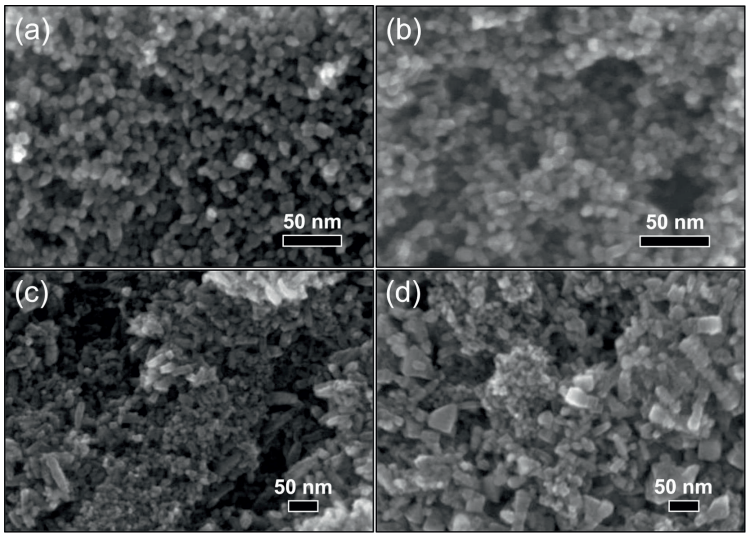

Figure 3: SEM images of (a) TiO_2 and in situ surface-functionalized TiO_2 nanoparticles, (b) Ti-DTES, (c) Ti-APTES, and (d) Ti-AEAPS.

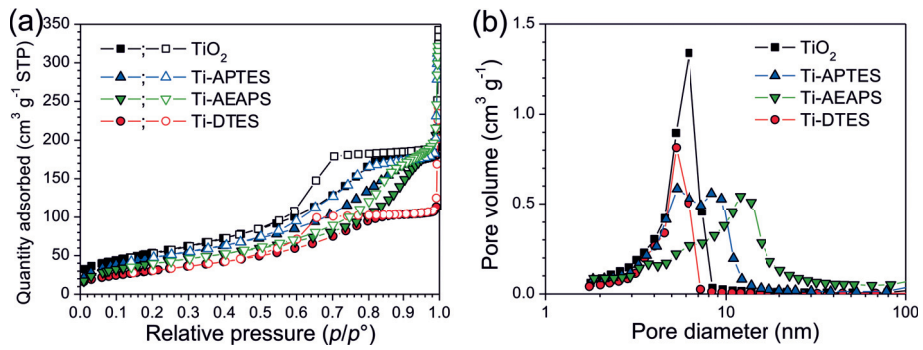

Figure 4: (a) Adsorption (solid symbols) and desorption (open symbols) isotherms and (b) BJH desorption d*V*/dlog(*D*) pore volume, from nitrogen adsorption measurements, of TiO_2 and in situ surface-functionalized TiO_2 nanoparticles.

case of pure TiO_2, a significant mass loss assigned to hydroxy groups was observed until 400 °C. For the in situ surface-functionalized samples, the mass loss (at 230–460 °C) was assigned to the combustion of the organic part of the silane. The average surface coverages (molecules per square nanometer) of the nanoparticles were calculated based on the specific surface area and the mass loss due to combustion of the organic part, considering loss of C, H, and N of the silanes [35] (Table 1).

The FTIR spectra of TiO_2 and in situ surface-functionalized TiO_2 nanoparticles are shown in Figure 5b (see Table S1 of Supporting Information File 1 for the assignments of the absorption bands). No specific bands from isopropanol were observed indicating full reaction of the TIP precursor and high purity of the nanoparticles. In the case of in situ surface-functionalized samples, Si–O–Si bands at 1020 and 1120 cm^{-1} and the Ti–O–Si shoulder at 910 cm^{-1} confirmed that the silanes react via a condensation mechanism, cross-link, and covalently bond on the surface of the TiO_2 nanoparticles [15,16,36]. The degree of order in the organic monolayer can be qualitatively estimated by comparing the CH_2 stretching modes in crystalline (highly ordered) and liquid (highly disordered) states [36,37]. For Ti-DTES sample, the CH_2 stretching modes at 2852 and 2921 cm^{-1} are close to those measured for crystalline polymethylene and for $CH_3(CH_2)_9SH$ adsorbed on gold [37] indicating well-ordered organic monolayers. In case of the aminosilane-

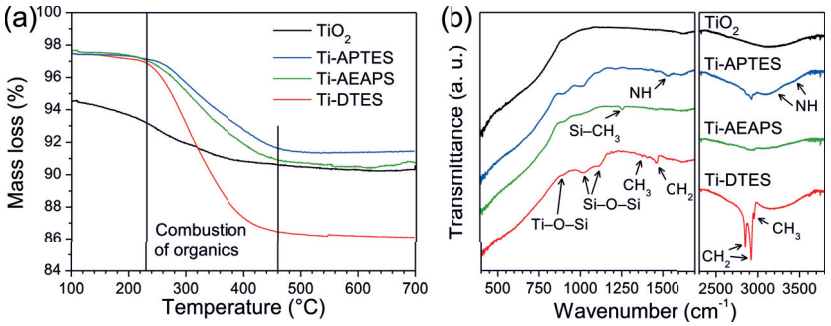

Figure 5: (a) TGA curves and (b) FTIR spectra of TiO_2 and in situ surface-functionalized TiO_2 nanoparticles.

functionalized samples, the low signal/noise ratios do not allow for an accurate measurement of the band positions. Additionally, because of possible surface contamination (from the carbon-coated grid) and/or optical aberration, the HR-TEM observation of Ti-APTES (Figure 2c) did not show clear evidence of the organic layer, confirming the nanometric nature of the organic coating.

A photo of TiO_2 and in situ surface-functionalized TiO_2 nanoparticles in a mixed solution of diethyl ether and water is displayed in Figure 6. Pure TiO_2 entirely dispersed in the water phase and formed a blurred suspension, showing hydrophilic behavior. The Ti-APTES sample dispersed in both phases, indicating partial hydrophobic behavior. The Ti-AEAPS and Ti-DTES samples completely dispersed in the diethyl ether phase, demonstrating the hydrophobic behavior of these materials. The resulting hydrophobic properties of the nanoparticles depend on organic chain length and surface coverage [17], and are comparable to results reported by Iijima and co-workers on TiO_2 nanoparticles post-modified with decyltrimethoxysilane and APTMS in mixed solutions of toluene and methanol [38].

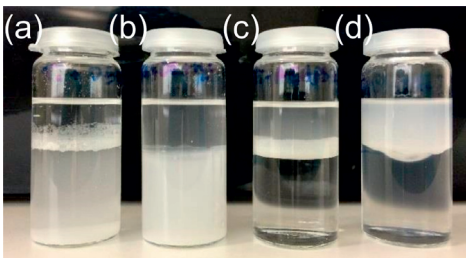

Figure 6: Photograph showing the behavior of (a) TiO_2 and in situ surface-functionalized TiO_2 nanoparticles, (b) Ti-APTES, (c) Ti-AEAPS, and (d) Ti-DTES in a mixed solutions of diethyl ether (top) and water (bottom).

Heat treatment

XRD patterns of heat-treated TiO_2 and the in situ surface-functionalized TiO_2 nanoparticles are shown Figure 7a, and these patterns were also refined (Figure S2 of Supporting Informa-

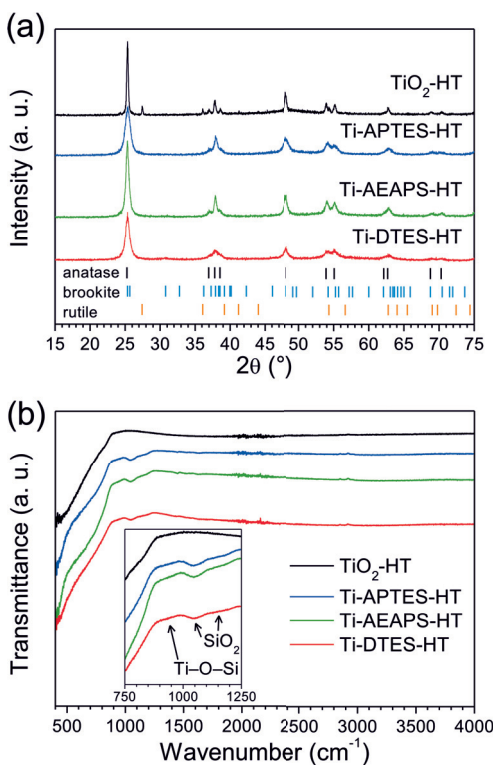

Figure 7: (a) XRD patterns (bars show diffraction lines of anatase from ICDD card #00-021-1272, brookite from ICDD card #00-029-1360, and rutile from ICDD card #00-021-1276) and (b) FTIR spectra of heat-treated TiO_2 and in situ surface-functionalized TiO_2 nanoparticles.

tion File 1). While the pure TiO_2 sample exhibits crystallites growth (from 5.7 to 28.8 nm), the functionalized nanoparticles with silane coupling agents showed only negligible growth of the crystallites after the heat treatment. Calculated crystallite sizes of the heat-treated samples are listed in Table 2. Additionally, in TiO_2-HT, the heat treatment induced a partial phase transition from brookite and anatase to rutile, the thermodynamically stable polymorph of TiO_2 [4]. In the case of in situ surface-functionalized TiO_2 nanoparticles, the heat treatment has negligible effects on the crystallographic structure of the samples.

Table 2: Properties of heat-treated TiO_2 and in situ surface-functionalized TiO_2 nanoparticles from XRD and SEM analysis.

sample	d_{XRD}[a] (nm)	d_{SEM}[b] (nm)
TiO_2-HT	28.8	30.0 ± 2.9
Ti-APTES-HT	7.8	15.5 ± 2.1
Ti-AEAPS-HT	10.4	23.7 ± 2.2
Ti-DTES-HT	8.9	12.0 ± 0.6

[a]crystallite size from Rietveld refinement of XRD measurements; [b]particle size from SEM observations.

The SEM images of heat-treated nanoparticles (Figure 8) confirmed the conclusions regarding both the morphology and the particles sizes (Table 2) showing the growth of the TiO_2-HT nanoparticles.

The FTIR investigations of the heat-treated nanoparticles (Figure 7b) show absorption bands at 1050 and 1150 cm^{-1}, which were assigned to Si–O–Si vibrations in silica [39] and a weak shoulder centered at 930 cm^{-1} was assigned to Ti–O–Si vibrations, in addition of the large absorption band below 900 cm^{-1} due to Ti–O–Ti vibrations.

The EDS maps of the Ti-APTES-HT nanoparticles (Figure 9) show that silicon is homogeneously distributed over the particles. EDS spectra over relatively large areas of the heat-treated in situ surface-functionalized nanoparticles and the pure TiO_2 samples (Figure S3 of Supporting Information File 1) confirm the presence and the absence of silicon, respectively.

Removal of the organic part of the silane coupling agent during the heat treatment induces the formation of a SiO_2 layer on the surface of the TiO_2 nanoparticles. The nature of the amorphous SiO_2 layer could not be fully determined by TEM observation (Figure S4 of Supporting Information File 1), but it indicated nanometric thickness of the layer. The amorphous SiO_2 layer inhibits surface diffusion of titanium, which prevents growth and phase transition of the nanoparticles, even at relatively high

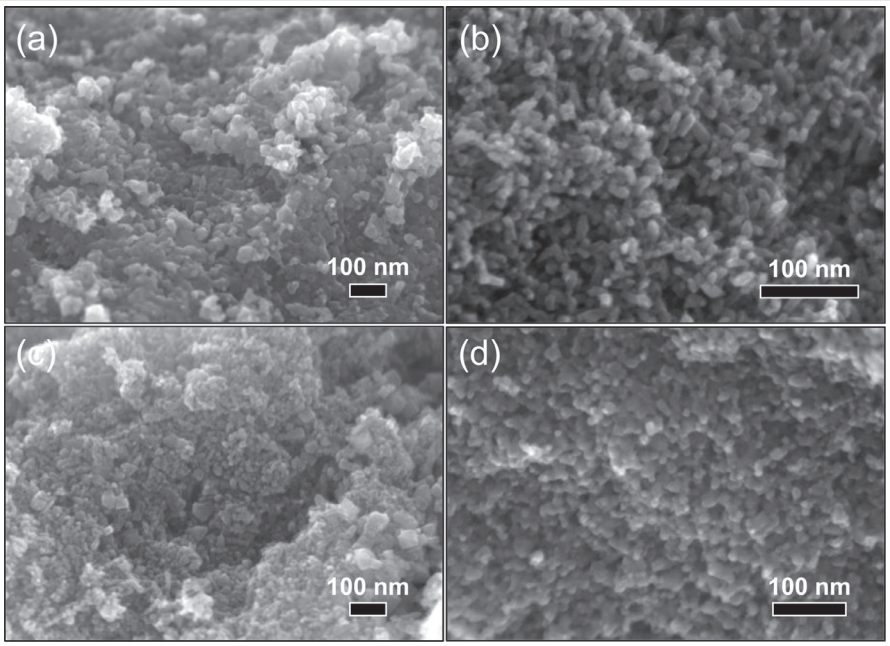

Figure 8: SEM images of (a) TiO_2-HT and heat-treated in situ surface-functionalized TiO_2 nanoparticles, (b) Ti-APTES-HT, (c) Ti-AEAPS-HT, and (d) Ti-DTES-HT.

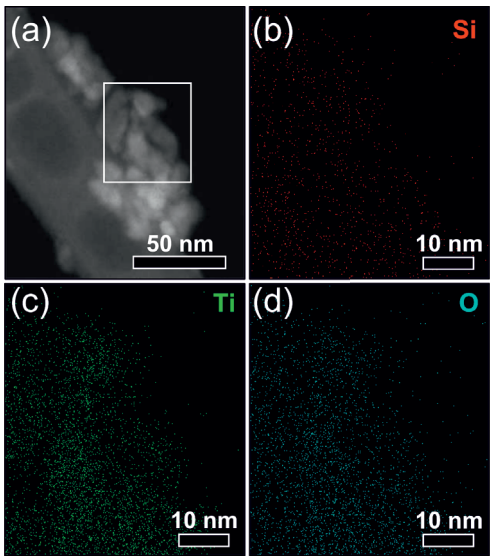

Figure 9: (a) Scanning electron image of Ti-APTES-HT with localization of the mapping (white rectangle) and EDS maps of (b) Si $K\alpha_1$, (c) Ti $K\alpha_1$, and (d) O $K\alpha_1$ signals.

temperatures. Reduced crystallite growth and retarded phase transition have also been observed when firing mixtures of TiO_2 and SiO_2 powders [40].

Conclusion

A new simple hydrothermal route to in situ surface-functionalized TiO_2 nanoparticles has successfully been developed. Spherical hydrophobic TiO_2 nanoparticles with a size of about 9 nm were prepared using silane coupling agents to functionalize the surface. Using aminosilane, the TiO_2 nanoparticles showed oriented attachment along the [001] crystallographic direction of anatase to form rod-like nanostructures with a diameter close to the one of the spherical particles and a length in the range 50–200 nm dependent on the type of silane coupling agent. Surface coverage of the nanoparticles was measured to be between 2.3 and 4.0 molecules per square nanometer. The one-step aqueous synthesis reported here reduces time, the number of steps needed, and the complexity of production of surface-functionalized TiO_2 nanoparticles. Despite the hydrothermal conditions, the synthesis is simple, robust, and reproducible. The numerous varieties of silane coupling agents offer versatility for tuning the surface properties of the TiO_2 nanoparticles that are required for selected applications. Further modifications of the synthesis route are also possible for tuning the properties towards various types of applications. For example, applying the nanoparticles as filler in polymer nanocomposites, hydrophobicity is a parameter of utmost importance [10,27].

Heat treatment of the in situ surface-functionalized nanoparticles at 700 °C revealed neither crystallite growth nor phase transition of TiO_2 because of the formation of an amorphous SiO_2 layer, originating from the silane coupling agents, and leading to TiO_2–SiO_2 core–shell nanoparticles.

Supporting Information

Supporting Information features Rietveld refinements of diffractograms of in situ functionalized and heat-treated nanoparticles, EDS spectra, additional TEM images, and assignments of the FTIR absorption bands.

Supporting Information File 1

Additional experimental data.
[http://www.beilstein-journals.org/bjnano/content/supplementary/2190-4286-8-33-S1.pdf]

Acknowledgements

Financial support from The Research Council of Norway to the project "Beat the Human Eye" (number 235210) and for the support to NTNU NanoLab through the Norwegian Micro- and Nano-Fabrication Facility, NorFab (197411/V30), is gratefully acknowledged. The TEM work was carried out on the NORTEM JEOL 2100 instrument, TEM Gemini Centre, NTNU, Norway, and we want to acknowledge Dr. Ragnhild Sæterli for help in operating the TEM.

References

1. Schneider, J.; Matsuoka, M.; Takeuchi, M.; Zhang, J.; Horiuchi, Y.; Anpo, M.; Bahnemann, D. W. *Chem. Rev.* **2014,** *114,* 9919–9986. doi:10.1021/cr5001892
2. Bai, Y.; Mora-Seró, I.; De Angelis, F.; Bisquert, J.; Wang, P. *Chem. Rev.* **2014,** *114,* 10095–10130. doi:10.1021/cr400606n
3. Rajh, T.; Dimitrijevic, N. M.; Bissonnette, M.; Koritarov, T.; Konda, V. *Chem. Rev.* **2014,** *114,* 10177–10216. doi:10.1021/cr500029g
4. Smith, S. J.; Stevens, R.; Liu, S.; Li, G.; Navrotsky, A.; Boerio-Goates, J.; Woodfield, B. F. *Am. Mineral.* **2009,** *94,* 236–243. doi:10.2138/am.2009.3050
5. Levchenko, A. A.; Li, G.; Boerio-Goates, J.; Woodfield, B. F.; Navrotsky, A. *Chem. Mater.* **2006,** *18,* 6324–6332. doi:10.1021/cm061183c
6. Zhang, H.; Banfield, J. F. *J. Phys. Chem. B* **2000,** *104,* 3481–3487. doi:10.1021/jp000499j
7. Zhang, H.; Banfield, J. F. *Chem. Rev.* **2014,** *114,* 9613–9644. doi:10.1021/cr500072j
8. Tao, P.; Viswanath, A.; Li, Y.; Siegel, R. W.; Benicewicz, B. C.; Schadler, L. S. *Polymer* **2013,** *54,* 1639–1646. doi:10.1016/j.polymer.2013.01.032
9. Lü, C.; Yang, B. *J. Mater. Chem.* **2009,** *19,* 2884–2901. doi:10.1039/B816254a

10. Kango, S.; Kalia, S.; Celli, A.; Njuguna, J.; Habibi, Y.; Kumar, R. *Prog. Polym. Sci.* **2013,** *38,* 1232–1261. doi:10.1016/j.progpolymsci.2013.02.003
11. Faure, B.; Salazar-Alvarez, G.; Ahniyaz, A.; Villaluenga, I.; Berriozabal, G.; De Miguel, Y. R.; Bergström, L. *Sci. Technol. Adv. Mater.* **2013,** *14,* 023001. doi:10.1088/1468-6996/14/2/023001
12. Vashist, S. K.; Lam, E.; Hrapovic, S.; Male, K. B.; Luong, J. H. T. *Chem. Rev.* **2014,** *114,* 11083–11130. doi:10.1021/cr5000943
13. Mallakpour, S.; Madani, M. *Prog. Org. Coat.* **2015,** *86,* 194–207. doi:10.1016/j.porgcoat.2015.05.023
14. Chen, Q.; Yakovlev, N. L. *Appl. Surf. Sci.* **2010,** *257,* 1395–1400. doi:10.1016/j.apsusc.2010.08.036
15. Zhao, J.; Milanova, M.; Warmoeskerken, M. M. C. G.; Dutschk, V. *Colloids Surf., A* **2012,** *413,* 273–279. doi:10.1016/j.colsurfa.2011.11.033
16. Milanesi, F.; Cappelletti, G.; Annunziata, R.; Bianchi, C. L.; Meroni, D.; Ardizzone, S. *J. Phys. Chem. C* **2010,** *114,* 8287–8293. doi:10.1021/jp1014669
17. Wang, C.; Mao, H.; Wang, C.; Fu, S. *Ind. Eng. Chem. Res.* **2011,** *50,* 11930–11934. doi:10.1021/ie200887x
18. Kassir, M.; Roques-Carmes, T.; Hamieh, T.; Razafitianamaharavo, A.; Barres, O.; Toufaily, J.; Villiéras, F. *Adsorption* **2013,** *19,* 1197–1209. doi:10.1007/s10450-013-9555-y
19. Teleki, A.; Bjelobrk, N.; Pratsinis, S. E. *Langmuir* **2010,** *26,* 5815–5822. doi:10.1021/la9037149
20. Niederberger, M.; Garnweitner, G.; Krumeich, F.; Nesper, R.; Cölfen, H.; Antonietti, M. *Chem. Mater.* **2004,** *16,* 1202–1208. doi:10.1021/cm031108r
21. Gao, X.; Cui, H. *J. Sol-Gel Sci. Technol.* **2014,** *70,* 355–360. doi:10.1007/s10971-014-3289-5
22. Cargnello, M.; Gordon, T. R.; Murray, C. B. *Chem. Rev.* **2014,** *114,* 9319–9345. doi:10.1021/cr500170p
23. Rabenau, A. *Angew. Chem., Int. Ed. Engl.* **1985,** *24,* 1026–1040. doi:10.1002/anie.198510261
24. Einarsrud, M.-A.; Grande, T. *Chem. Soc. Rev.* **2014,** *43,* 2187–2199. doi:10.1039/c3cs60219b
25. Kwon, S. J.; Im, H. B.; Nam, J. E.; Kang, J. K.; Hwang, T. S.; Yi, K. B. *Appl. Surf. Sci.* **2014,** *320,* 487–493. doi:10.1016/j.apsusc.2014.09.110
26. Anajafi, Z.; Marandi, M.; Taghavinia, N. *Physica E* **2015,** *70,* 113–120. doi:10.1016/j.physe.2015.02.023
27. Koziej, D.; Fischer, F.; Kränzlin, N.; Caseri, W. R.; Niederberger, M. *ACS Appl. Mater. Interfaces* **2009,** *1,* 1097–1104. doi:10.1021/am9000584
28. Hayashi, H.; Torii, K. *J. Mater. Chem.* **2002,** *12,* 3671–3676. doi:10.1039/B207052A
29. Brunauer, S.; Emmett, P. H.; Teller, E. *J. Am. Chem. Soc.* **1938,** *60,* 309–319. doi:10.1021/ja01269a023
30. Barrett, E. P.; Joyner, L. G.; Halenda, P. P. *J. Am. Chem. Soc.* **1951,** *73,* 373–380. doi:10.1021/ja01145a126
31. Niederberger, M.; Cölfen, H. *Phys. Chem. Chem. Phys.* **2006,** *8,* 3271–3287. doi:10.1039/b604589h
32. Penn, R. L.; Banfield, J. F. *Geochim. Cosmochim. Acta* **1999,** *63,* 1549–1557. doi:10.1016/s0016-7037(99)00037-x
33. Ahmad, M. A.; Prelot, B.; Razafitianamaharavo, A.; Douillard, J. M.; Zajac, J.; Dufour, F.; Durupthy, O.; Chaneac, C.; Villiéras, F. *J. Phys. Chem. C* **2012,** *116,* 24596–24606. doi:10.1021/jp307707h
34. Viana, M. M.; Soares, V. F.; Mohallem, N. D. S. *Ceram. Int.* **2010,** *36,* 2047–2053. doi:10.1016/j.ceramint.2010.04.006
35. García-González, C. A.; Fraile, J.; López-Periago, A.; Domingo, C. *J. Colloid Interface Sci.* **2009,** *338,* 491–499. doi:10.1016/j.jcis.2009.06.035
36. Helmy, R.; Fadeev, A. Y. *Langmuir* **2002,** *18,* 8924–8928. doi:10.1021/la0262506
37. Porter, M. D.; Bright, T. B.; Allara, D. L.; Chidsey, C. E. D. *J. Am. Chem. Soc.* **1987,** *109,* 3559–3568. doi:10.1021/ja00246a011
38. Iijima, M.; Kobayakawa, M.; Kamiya, H. *J. Colloid Interface Sci.* **2009,** *337,* 61–65. doi:10.1016/j.jcis.2009.05.007
39. Gärtner, M.; Dremov, V.; Müller, P.; Kisch, H. *ChemPhysChem* **2005,** *6,* 714–718. doi:10.1002/cphc.200400185
40. Tobaldi, D. M.; Tucci, A.; Škapin, A. S.; Esposito, L. *J. Eur. Ceram. Soc.* **2010,** *30,* 2481–2490. doi:10.1016/j.jeurceramsoc.2010.05.014

License and Terms

THE JOURNAL OF PHYSICAL CHEMISTRY C

Article

pubs.acs.org/JPCC

Controlling Oriented Attachment and in Situ Functionalization of TiO_2 Nanoparticles During Hydrothermal Synthesis with APTES

Antoine R. M. Dalod,[†] Ola G. Grendal,[†] Susanne L. Skjærvø,[†] Katherine Inzani,[†] Sverre M. Selbach,[†] Lars Henriksen,[‡] Wouter van Beek,[§] Tor Grande,[†] and Mari-Ann Einarsrud*[,†]

[†]Department of Materials Science and Engineering, NTNU, Norwegian University of Science and Technology, 7491 Trondheim, Norway

[‡]poLight AS, Kongeveien 77, 3188 Horten, Norway

[§]Swiss-Norwegian Beamlines at European Synchrotron Research Facility, 38043 Grenoble, France

Supporting Information

ABSTRACT: Understanding growth mechanisms and the role of surface functionalization is of key importance to control shape and morphology of nanoparticles and their properties. Here, we describe the growth mechanism and the effect of hydrothermal synthesis parameters (pH, time, and precursor/functionalization agent ratio) during in situ functionalization of anatase TiO_2 nanoparticles with 3-aminopropyltriethoxysilane. Elongated crystallographically oriented TiO_2 nanoparticles were formed by oriented attachment mechanism in addition to spherical nanoparticles. The growth mechanism is determined by a combination of ex situ techniques such as high-resolution transmission electron microscopy combined with in situ synchrotron X-ray diffraction and density functional theory calculations. Oriented attachment induced by the functionalization agent is shown to be the origin of the elongation of the nanoparticles, as only spherical nanoparticles were formed in the absence of surface functionalization. Finally, it was shown that the amount and the size of the elongated nanoparticles can be tuned by adjusting pH.

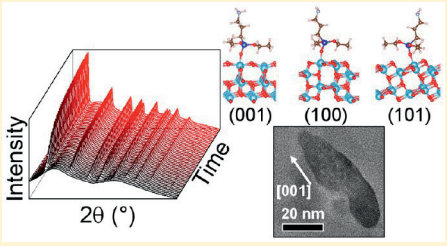

1. INTRODUCTION

Controlling the particle size, morphology, and crystallinity (including the type of polymorph) of titanium dioxide (TiO_2) nanoparticles has attracted a lot of interest with respect to tailored materials dedicated to applications such as in the energy or in the biomedical fields.[1,2] With respect to controlling these parameters, solvothermal and hydrothermal syntheses[3] are intensively investigated in order to obtain efficient anatase TiO_2 nanomaterials for, for example, photocatalysis[4,5] and photovoltaics,[6] but also because of the intrinsic advantages of the method, simplicity and cost efficiency.[7] Surface functionalization of nanoparticles with organic molecules such as silane coupling agents,[8−12] brings additional properties and better dispersion in organic solvents and polymers.[12−15]

The effect of the synthesis conditions on the morphology of TiO_2 nanoparticles has been the focus of numerous works. Dinh et al. studied solvothermal synthesis of anatase TiO_2 in ethanol reporting different shapes such as rhombic, truncated rhombic, spherical, and dog-bone, by tuning the oleic acid and oleylamine surfactants molar ratio.[16] Correspondingly, Jun et al. tuned the surface selective surfactant (lauric acid) and the surface nonselective surfactant (trioctylphospine oxide) during nonhydrolytic synthesis of TiO_2 nanoparticles, leading to morphologic evolution from spheres to diamond, rod, and branched rod shapes.[17] In both reports, the anatase nanoparticles were elongated along the [001] direction. Anisotropic growth of TiO_2 nanoparticles synthesized by solvothermal reaction of $TiCl_4$ in benzyl alcohol was also reported.[18] Recently, asparagus, wire, cube, eggplant, and tetragon shapes were obtained via solvothermal synthesis in cyclohexane.[19] Elongation along [001] direction was considerably reduced with addition of sodium oleate from which it was deduced that it strongly adsorbs on {001} facets. Sugimoto et al. observed a change from cube shaped to ellipsoidal shape of TiO_2 nanoparticles synthesized via a combination of sol−gel and hydrothermal treatments, using triethanolamine as surface selective surfactant and pH above 11.[20] Similar effects were observed using different primary amines.[21] Li et al. reported a combined solvothermal/hydrothermal synthesis with tunable shapes of anatase nanoparticles from spherical to rodlike shapes, elongated along the [101] direction, as a function of the increasing temperature.[4] Oriented attachment is now a well-known phenomenon in which nanoparticles self-organize spontaneously, sharing a common crystallographic plane and resulting in monocrystalline particles.[22,23] Oriented attachment of anatase nanoparticles to form [001] elongated nanoparticles has been observed in earlier studies.[24−26]

Received: March 20, 2017
Revised: May 1, 2017
Published: May 2, 2017

DOI: 10.1021/acs.jpcc.7b02604
J. Phys. Chem. C 2017, 121, 11897−11906

We have previously reported an in situ hydrothermal route to functionalize TiO_2 nanoparticles with silane coupling agents.[27] Whereas spherical nanoparticles were observed in the case of pure TiO_2 and TiO_2 in situ functionalized with *n*-decyltriethoxysilane, [001] oriented rods were also formed along with spheres in the case of functionalization with aminosilanes. We proposed that the formation of the rods was due to a combination of specific adsorption or surface selective adsorption of the aminosilane and oriented attachment mechanism, as the functionalization and the growth occur simultaneously, and both spheres and rods were formed.

Here we report on the growth mechanism of elongated particles and the role of the surface functionalization during hydrothermal synthesis with focus on in situ functionalization of TiO_2 with 3-aminopropyltriethoxysilane (APTES). We applied a unique combination of in situ X-ray diffraction during the hydrothermal synthesis and ex situ studies on the process parameters influencing the formation of rodlike nanoparticles to determine the growth mechanism of the [001] oriented nanoparticles. The simultaneous growth and functionalization of the anatase TiO_2 nanoparticles are discussed with particular attention to the role of the surface functionalization on the phase purity and the morphology of the nanoparticles. The conclusions on the growth mechanism were supported by density functional theory calculations.

2. METHODS

2.1. Synthesis. The syntheses were based on the in situ functionalization of TiO_2 nanoparticles with silane coupling agents as previously described,[27] using titanium(IV) isopropoxide (TIP, Sigma-Aldrich, ≥ 97%) as titanium precursor and APTES (Sigma-Aldrich, 99%) as functionalization agent. TIP (28 mmol) was added to distilled water and APTES (TIP/APTES molar ratio equal to 10:1 and 15:1) to obtain a filling factor of 70% in the autoclave. The solutions were stirred for 10 min prior to transfer into a 125 mL PTFE-lined autoclave (Parr) and heated for selected duration time (1, 15, 30, 60, and 120 min) at 200 °C. After cooling to room temperature, the products were centrifuged (10 000 rpm, 10 min) and washed with distilled water. This process was repeated 3 times. The obtained slurries were dried for about 12 h at 100 °C for analysis. The effect of changing the pH was investigated for the 120 min synthesis time using ammonium hydroxide (Sigma-Aldrich, 30−33%) and nitric acid (Sigma-Aldrich, 65%) to give pH values of about 10 and 2, respectively. Table 1 summarizes the synthesis conditions and the labels of the samples.

The slurries used for in situ X-ray diffraction (XRD) measurements were prepared three times more concentrated than the synthesis in autoclave in order to obtain a good diffraction signal during the acquisition. Typically, 9.55 mmol of TIP was added to distilled water to get a total volume of 10 mL. When the synthesis was performed to produce in situ functionalized TiO_2 with APTES, the necessary volume of water is substituted to APTES. The temperature and the pressure were 213 °C and 250 bar, respectively, for all in situ experiments.

2.2. Computational. Density functional theory (DFT) calculations were performed using the Vienna ab initio Simulation Package (VASP) with projector augmented wave (PAW) pseudopotentials, the exchange-correlation functional PBEsol, and an energy cutoff of 700 eV.[28−32] A slab model was employed for calculation of (001), (100), and (101) surface energies and binding energies with single-sided absorption of APTES. Meroni et al. investigated the geometrical configuration of APTES on the fully hydroxylated (101) anatase surface by a combined experimental and theoretical study, finding that single molecules or dimers could chemisorb with feasible geometries but high bond strain limited extensive cross-linking.[33] Adsorption was modeled via Ti−O−Si bonding to 25% hydroxylated surface Ti with removal of one C_2H_5 branch from the APTES molecule. This situation can be considered as an intermediate stage of the reaction. More computational details are given in the Supporting Information.

Table 1. Sample Names and Parameters of the 120 min Hydrothermal Synthesis of TiO_2 and APTES in Situ Functionalized TiO_2 Nanoparticles

sample name	TIP/APTES (mol ratio)	pH	in situ XRD
TiO_2-A	n/a	2.7	no
TiO_2	n/a	4.5	yes[a]
TiO_2-B	n/a	9.3	no
10:1-A	10:1	2.2	no
10:1	10:1	6.3	yes[a]
10:1-B	10:1	10.1	yes[b]
15:1-A	15:1	2.2	no
15:1	15:1	6.3	no
15:1-B	15:1	9.7	no

[a]pH was not measured and not modified. [b]pH was increased to about 10 with ammonium hydroxide.

2.3. Characterization. Powder X-ray diffraction (XRD) was performed on a Bruker D8 Advance Da-Vinci working in Bragg−Brentano ($\theta/2\theta$) geometry and equipped with LynxEye detector. Diffractograms were recorded with CuK_α radiation (λ = 1.5406 Å) with a step size of 0.013°, an integration time of 0.4 s, and using variable divergent slits. The in situ XRD measurements were carried out at the Swiss-Norwegian Beamlines (BM01A) at the European Synchrotron Radiation Facility (ESRF), Grenoble, France. The diffraction data were collected in transmission mode (λ = 0.6999 Å) using the PILATUS@SNBL platform.[34] The experimental setup consisted of a single crystal sapphire capillary (1.15 ± 0.1 and 0.8 ± 0.08 mm outer and inner diameters, respectively) connected to a high-pressure liquid chromatography pump at one end and closed at the other end, and a heat blower was placed above the capillary as heat source, as previously described.[35−37] The blower was pointed toward the sample once desired temperature and pressure were reached and data collection was started. The slurries were gently ground in a mortar to facilitate injection in the capillary with a plastic syringe. Rietveld refinements were performed in batches using TOPAS (Bruker AXS version 5) operating in launch mode, and jEdit with macros for TOPAS.[38] More details about the diffraction data acquisition and analysis are given in the Supporting Information.

Scanning electron microscope (SEM) images were recorded on an in-lens cold field emission S(T)EM Hitachi S-5500. The acceleration voltage was 7 kV and secondary electrons were detected. Samples were prepared by dropping an aqueous suspension of the particles obtained after the centrifugation on an aluminum sample holder, which was set to dry overnight. The linear intercept method was used to calculate average particle sizes, using images containing more than 100 particle intercepts.

Transmission electron microscope (TEM) images were recorded on a JEOL 2100 equipped with Oxford X-Max 80

DOI: 10.1021/acs.jpcc.7b02604
J. Phys. Chem. C 2017, 121, 11897−11906

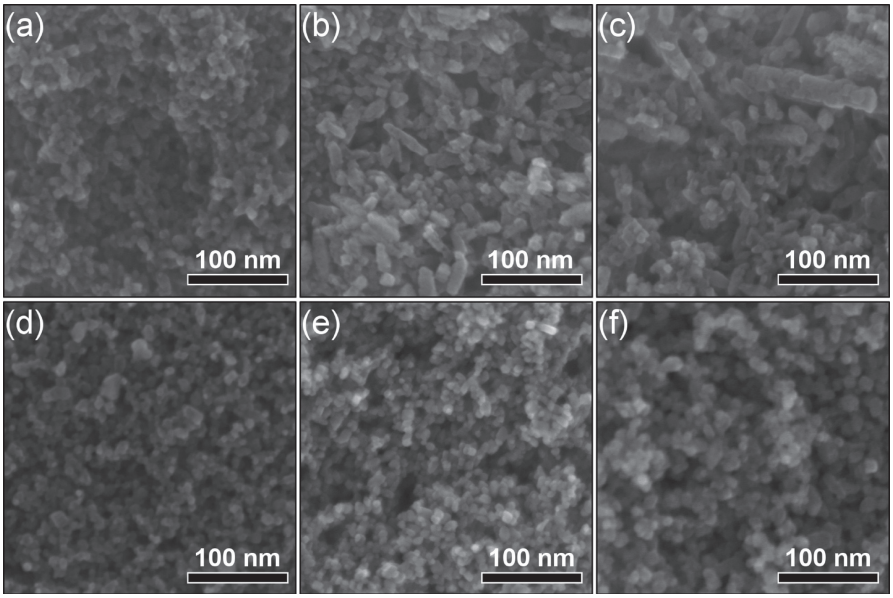

Figure 1. SEM micrographs of (a) 10:1-A, (b) 10:1, (c) 10:1-B, (d) TiO_2-A, (e) TiO_2, and (f) TiO_2-B samples.

Table 2. Nanoparticles Characteristics from Nitrogen Adsorption, XRD, SEM, and TGA Analysis

sample	d_{XRD}[a] (nm)	d_{SEM}[b] (nm)	d_{BET}[c] (nm)	d_{BJH}[d] (nm)	S_{BET}[e] (m^2 g^{-1})	organic mass loss (%)	surface coverage (nm^{-2})
TiO_2-A	4.6 ± 0.1	7.9 ± 0.6	7.6 ± 0.1	7.3 ± 0.1	203 ± 1	n/a	n/a
TiO_2	4.8 ± 0.1	9.3 ± 0.1	9.0 ± 0.1	7.3 ± 0.1	171 ± 1	n/a	n/a
TiO_2-B	6.1 ± 0.1	9.1 ± 0.6	9.7 ± 0.1	5.7 ± 0.1	158 ± 1	n/a	n/a
10:1-A	5.9 ± 0.2	8.3 ± 0.5	8.7 ± 0.1	14.6 ± 0.1	177 ± 1	5.0 ± 0.5	2.9 ± 0.3
10:1	5.4 ± 0.1	11.6 ± 1.0	7.2 ± 0.1	11.3 ± 0.1	213 ± 1	8.2 ± 0.5	4.0 ± 0.3
10:1-B	8.4 ± 0.1	13.7 ± 3.0	6.3 ± 0.1	6.6 ± 0.1	243 ± 1	7.0 ± 0.5	3.0 ± 0.2
15:1-A	4.9 ± 0.1	10.0 ± 0.9	8.1 ± 0.1	6.6 ± 0.1	190 ± 1	3.4 ± 0.5	1.9 ± 0.3
15:1	5.5 ± 0.1	12.2 ± 1.2	8.5 ± 0.1	5.5 ± 0.1	182 ± 1	6.0 ± 0.5	3.4 ± 0.3
15:1-B	7.4 ± 0.1	10.5 ± 0.7	8.4 ± 0.1	8.0 ± 0.1	183 ± 1	5.1 ± 0.5	2.9 ± 0.3

[a]Average crystallite size from Rietveld refinement of XRD measurements. [b]Particle size from SEM observations. [c]Particle size estimated from BET specific surface area. [d]Average pore diameter from BJH desorption calculations. [e]BET specific surface area from nitrogen adsorption measurements.

SDD detector for energy-dispersive X-ray spectroscopy (EDS) analysis. The acceleration voltage was 200 kV. For the preparation of the TEM samples, the nanoparticles were dispersed in anhydrous propan-2-ol (Sigma-Aldrich, 99.5%) dropped on a carbon-coated copper TEM grid (Lacey). The high-resolution TEM (HR-TEM) images were analyzed using DigitalMicrograph (Gatan Inc. version 3.01).

Specific surface area (Brunauer–Emmett–Teller (BET) method[39]) and pore size distribution (Barrett–Joyner–Halenda (BJH) method[40]) were measured by nitrogen adsorption on a Micrometrics Tristar 3000. Samples were degassed for 12 h at 180 °C in vacuum prior to analysis. Particle sizes were estimated from the specific surface area assuming nonporous and spherical particles.

Fourier transform infrared (FTIR) spectra were acquired on a Bruker Vertex 80v FTIR equipped with Bruker Platinum ATR diamond system from 600 to 4000 cm^{-1}. A total of 32 scans were acquired for each sample at a resolution of 1 cm^{-1}.

Thermogravimetric analysis (TGA) was acquired on a Netzsch Jupiter STA 449 C using an alumina crucible. The nanoparticles were first heat treated from 25 to 150 °C (10 °C min^{-1}), maintained at 150 °C for 30 min, cooled to room temperature, and heat treated again from 25 to 200 °C (2 °C min^{-1}) in order to remove adsorbed water. The samples were finally heat treated from 100 to 700 °C (2 °C min^{-1}). All treatments were performed under synthetic air.

3. RESULTS

3.1. Particle Size, Morphology, and Functionalization.

Selected SEM images of the nanoparticles are presented in Figure 1. The nonfunctionalized samples consist of particles with a size of about 10 nm. Significantly larger rodlike particles with lengths from 50 to 200 nm were formed for samples functionalized with APTES in addition to spherical nanoparticles. The average particle sizes are presented in Table 2. For the functionalized samples, shorter reaction time resulted in a smaller average particle (Figure S2 and Table S3 in Supporting Information) and basic reaction conditions promote the formation of rods, while acidic conditions considerably reduce the rod formation (Figure 1a–c). Sample 10:1-B consists of the largest and highest number of rodlike nanoparticles (Figures 1c and 2a). HR-TEM images of an

DOI: 10.1021/acs.jpcc.7b02604
J. Phys. Chem. C 2017, 121, 11897–11906

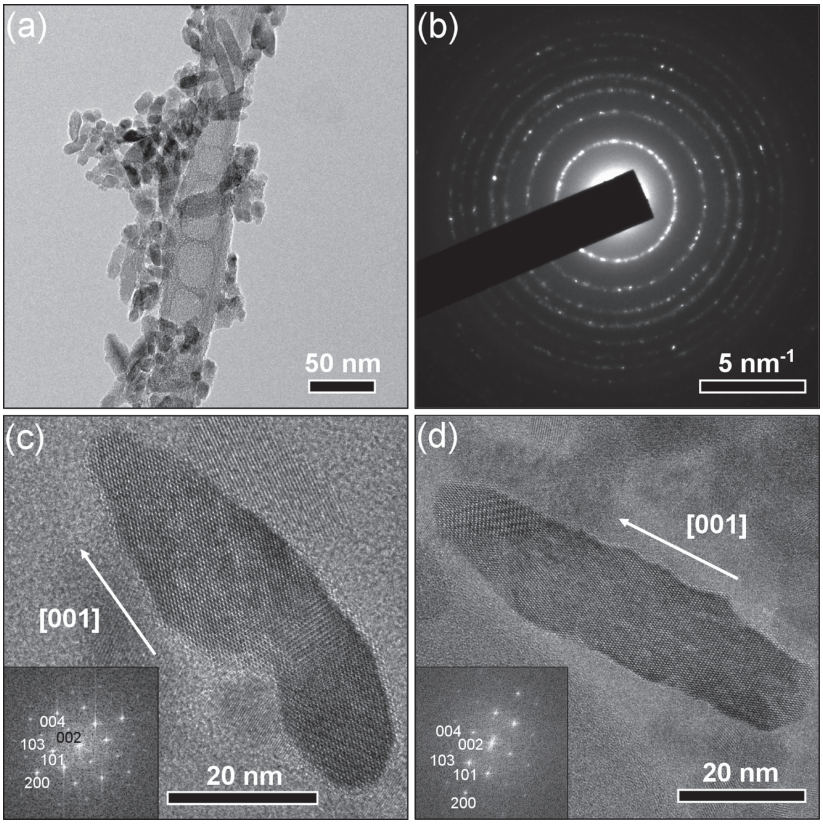

Figure 2. TEM images of 10:1-B sample: (a) overview (b) electron diffraction pattern assigned to anatase, (c) a rodlike nanoparticle formed from attached nanoparticles, (d) a rodlike nanoparticle; insets show fast Fourier transform of a selected area within the particle.

[001] elongated single crystal from this sample is shown in Figure 2c. From the shape of this particle, it is likely that at least two individual crystals have merged via oriented attachment mechanism because the curved surface at the center of the particle would be energetically unfavored during a conventional growth mechanism. Another typical single crystal rodlike anatase nanoparticle is displayed in Figure 2d, also presenting an elongation along the [001] crystallographic direction. The pH has negligible influence on the particle size and morphology in absence of the surface functionalization (Figure 1d–f).

Surface area and particle size calculated from BET specific surface area, as well as average pore size distribution from BJH desorption are included in Table 2 (Figure S2 in Supporting Information). The average particle sizes estimated from these measurements are in accordance with the size observed by SEM. The differences when comparing acidic or basic reaction conditions could be assigned to a different degree of agglomeration of the particles in these samples. The surface coverage (ranging from 1.7 to 4.0 silane nm^{-2}) was calculated from the mass loss measured during TGA analysis from 230 to 460 °C (Figure S3 in Supporting Information) and BET specific surface area and are included in Table 2.[27] With respect to reaction time, the mass loss is fairly constant but is considerably lower for the samples with 15:1 compared to 10:1 molar ratio (TIP/APTES). FTIR spectra confirm that APTES is covalently bonded to the surface of the nanoparticles via formation of Ti–O–Si bonds and cross-linked at the surface of the particles via formation of Si–O–Si bonds (Figure S4 and Table S4 in Supporting Information).[9,11,27,33] TEM analysis (Figures 2 and S5 in Supporting Information) does not show clear evidence of an amorphous coating, confirming the nanometric nature of the functionalization layer.

Surface energies calculated by DFT, given in Table 3, are in agreement with previously published results.[41,42] These surface energies result in a square truncated bipyramid Wulff construction, replicating the known equilibrium anatase nanoparticle shape (Figure 3a).[43] The surface energy of all facets is lowered by APTES adsorption but the ratio of surface energies between the facets remains similar, such that the Wulff construction is not strongly changed (Figure 3b). This indicates that the equilibrium nanoparticle shape is not strongly affected by APTES adsorption. The (100) surfaces are not predicted to

Table 3. Bare and APTES Adsorbed Surface Energies, and Binding Energies of APTES to (001), (100), and (101) Anatase Surfaces

	(001)	(100)	(101)
bare surface energy ($J\ m^{-2}$)	1.170	0.712	0.609
APTES adsorbed surface energy ($J\ m^{-2}$)	0.567	0.400	0.338
binding energy (eV)	2.145	1.413	1.315

DOI: 10.1021/acs.jpcc.7b02604
J. Phys. Chem. C 2017, 121, 11897–11906

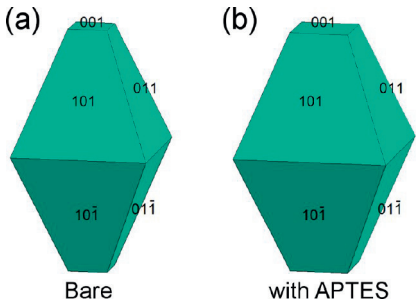

Figure 3. Wulff constructions of anatase equilibrium shapes with (a) bare surfaces and (b) APTES adsorption, based on DFT-calculated surface energies.

appear in the Wulff plots of either the bare surfaces or the APTES-functionalized surfaces. The binding energy is positive and reasonably large for all three surfaces, indicating that APTES absorption is favorable and likely on all surfaces.

3.2. X-ray Diffraction Analysis. X-ray diffractograms presented in Figure 4a show that all the functionalized samples are phase pure anatase. The nonfunctionalized samples are mainly anatase with 28, 22, and 14 wt % brookite in acidic, neutral, and basic reaction conditions, respectively (Figure S6 in Supporting Information). In the case of in situ functionalized samples, the average crystallite sizes are found to be below 10 nm from the Rietveld refinements (Figure S7 in Supporting Information) and are included in Table 2. The small sizes are consistent with the broad reflections. The crystallite sizes decrease with decreasing reaction time (Table S3 in Supporting Information). For the samples functionalized with APTES, the (004) reflection is considerably narrower than the other reflections, pointing to anisotropic crystallite sizes due to the presence of the [001] oriented rodlike nanoparticles. Implementing anisotropic size broadening in the Rietveld refinements (see details in the Supporting Information) was necessary to improve the fit of all the diffractograms of functionalized nanoparticles as similarly done by Jensen et al. in the case of the synthesis of pure TiO_2 in benzyl alcohol.[18] The anisotropic size broadening also allows to extract the average crystallite size (avg size) as well as the crystallite sizes along *a*-axis and *c*-axis of anatase ($size_a$ and $size_c$, respectively). The size anisotropy (expressed as a percentage) was calculated, as previously reported,[18] using eq 1. It must be noted that the functionalized materials contain both spheres and rods, thus the size anisotropy also reflects the average of their respective contributions. The size anisotropy diminishes under acidic conditions and increases when basic reaction conditions are used. This is also reflected in the refined crystallite sizes, where 10:1-B (having the narrowest (004) reflection) have the largest crystallite sizes and anisotropy (Figure 5). The crystallite sizes of 10:1 samples are larger than the 15:1 samples, at any pH conditions.

$$\text{Size anisotropy} = \frac{\text{Size}_c - \text{Size}_a}{\text{Size}_c} \quad (1)$$

The diffractograms of the final reaction products after cooling to room temperature are shown in Figure 4b. Table 4 summarizes the results from Rietveld refinements (Figure S8 in Supporting Information). The in situ synthesis of pure TiO_2 resulted in 13 wt % brookite according to the Rietveld refinement, but the exactitude of the amount must be taken cautiously due to overlap with the solution background. The only distinguishable diffraction peak (121) is at 13.86°.

The XRD contour plots of the first 40 min of the reactions of the three syntheses are displayed in Figure 6. Nucleation of anatase occurs rapidly (within tens of seconds after the initial heating) without the formation of any intermediate phase. The broadening of the reflections is largest for pure TiO_2 (Figure 6a), reflecting a smaller crystallite size. The size broadening is smaller when the synthesis is performed with APTES (Figure 6b) and even smaller with APTES in basic conditions (Figure 6c). This reduction in the broadening is also visible from Figure 7 that shows the initial 15 min evolution of the (004) (*c*-parameter) and (200) (*a*-parameter) reflections.

The relative full width at half-maximum of the (004) and (200) reflections in Figure 7 reveals the anisotropic growth of the particles when the synthesis is performed with APTES, particularly at basic conditions. Figure 8 shows crystallite sizes along the anatase cell parameter directions and the size anisotropy as a function of time from the diffraction data refinements. The crystal growth occurs within the first minutes of reaction and increases continuously for the growth along the *a*-axis. The size difference is larger along the *c*-axis in the case of APTES functionalized samples. Two phases of growth are distinguishable (separated at about 5 min of reaction). The growth rate of the crystallite size along the *c*-axis decreases more rapidly than the one along the *a*-axis. Thus, the size anisotropy is evident from the initial moments of the reactions

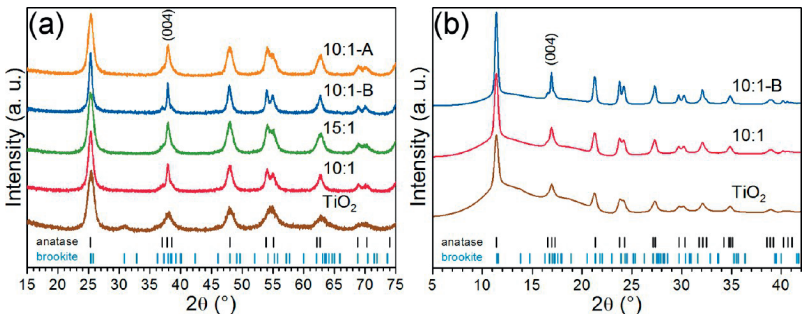

Figure 4. Normalized diffractograms collected (a) ex situ (λ = 1.5406 Å) and (b) in situ (λ = 0.6999 Å) at room temperature and after reaction (vertical bars show diffraction lines of anatase from ICDD card #00-021-1272 and brookite from ICDD card #00-029-1360).

DOI: 10.1021/acs.jpcc.7b02604
J. Phys. Chem. C 2017, 121, 11897−11906

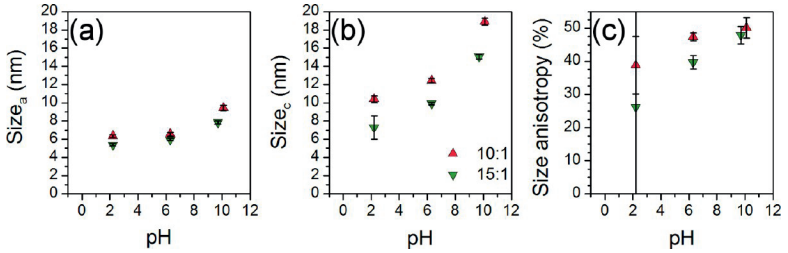

Figure 5. Crystallite sizes along the (a) *a*-axis and (b) *c*-axis, and (c) size anisotropy evolution as a function of the pH of the synthesis of 10:1 and 15:1 samples (from ex situ XRD).

Table 4. Results of Rietveld Refinements of Long Exposure Diffractograms of End Reaction Products Collected in Situ at Room Temperature

			lattice parameters (Å)		crystallite sizes (nm)			
sample	duration of reaction (h)	R_{wp} (%)	*a*	*c*	avg. size	size$_a$	size$_c$	size anisotropy (%)
TiO_2	1.75	1.06	3.7991(3)	9.5130(9)	6.28(15)	6.29(12)	7.29(22)	14 ± 7
10:1	1.58	1.03	3.7977(2)	9.5204(5)	7.44(11)	7.22(9)	9.11(17)	21 ± 2
10:1-B	9[a]	1.87	3.7969(1)	9.5236(4)	10.20(14)	9.52(12)	14.11(27)	32 ± 1

[a]Limited evolution after about 100 min of reaction.

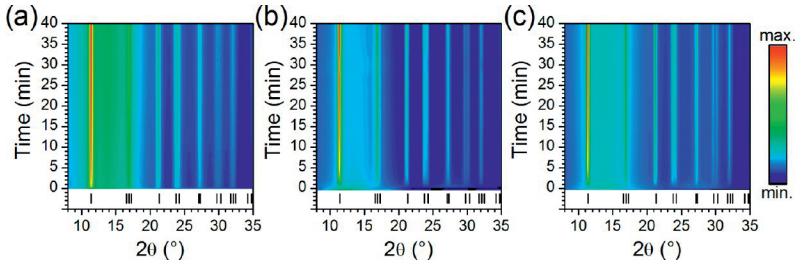

Figure 6. Time-resolved XRD contour plots (λ = 0.6999 Å) of (a) TiO_2, (b) 10:1, and (c) 10:1-B samples collected during the syntheses at 213 °C and 250 bar (the color scale represents the intensity and the vertical bars show diffraction lines of anatase from ICDD card #00-021-1272).

and reach a maximum of 38% and 26% for 10:1-B and 10:1 samples, respectively, and decreases constantly to reach the values reported in Table 4. The same trends are observed in the case of ex situ analysis (Figure S9 in Supporting Information), but the calculated size anisotropy is larger (up to 48%) even though the pH was not modified. The size anisotropy is more pronounced in the case of 10:1 samples than the 15:1 samples.

The time evolution of the cell parameters is reported Figure 9. The *a*-parameter converges rapidly during the in situ measurements to 3.802 Å (slightly above in the case of pure TiO_2), via expansion (10:1) and contraction (TiO_2 and 10:1-B). In all cases, the *c*-parameter increases, but it remains well below the bulk value in the case of TiO_2, and it converges rapidly to values above calculated bulk value at 213 °C (9.535 and 9.539 Å for 10:1 and 10:1-B samples, respectively). Similar evolutions were also observed in previous studies of pure TiO_2.[44,45] The divergence of the cell parameters from the bulk values during in situ XRD is also visible from the position of the (004) and (200) Bragg reflections in Figure 7. The cell parameters for the pure TiO_2 nanocrystalline sample diverge the most from bulk TiO_2. These observations are contrasted with the ex situ measurements (Figure S10 in Supporting Information) where the *a*-parameter converges slowly to the bulk value via contraction and the *c*-parameter expands but remains well below the bulk value for both TIP/APTES ratios. However, in all cases the *c*/*a* ratio shows similar trend, increasing and stabilizing at values below the bulk value.

4. DISCUSSION

The similarity of the diffractograms from the ex situ and in situ measurements (Figure 4) provides solid evidence of the robustness and the reproducibility of the synthesis conditions that can be reliably reproduced in situ. The in situ measurements are hence not biased and can be considered as representative for the reaction pathways.

In the case of pure TiO_2, the amount of brookite decreased when the pH was increased as previously observed.[46,47] Nanoparticles of about 10 nm in size were obtained for all TiO_2 samples (Figure 1d–f). From the SEM images, the morphology was not affected in contrast to previous hydrothermal studies where a strong dependence of the particles morphology with pH was reported, often leading to elongated nanoparticles in basic conditions.[20,21,48] With respect to the cell parameters and crystallite size, the values reported here follow the trend from previously reported in situ studies of hydrothermal synthesis of TiO_2 at different temperatures.[45] The kinetics of the crystallite growth (Figure 8a,b) follows a power-law type of function (eq 2), where *d* is the crystallite size at the time *t*, d_0 is the average size at $t = 0$, k_{OR} is a temperature-dependent rate constant, and *n* is an integer exponent when the

DOI: 10.1021/acs.jpcc.7b02604
J. Phys. Chem. C 2017, 121, 11897–11906

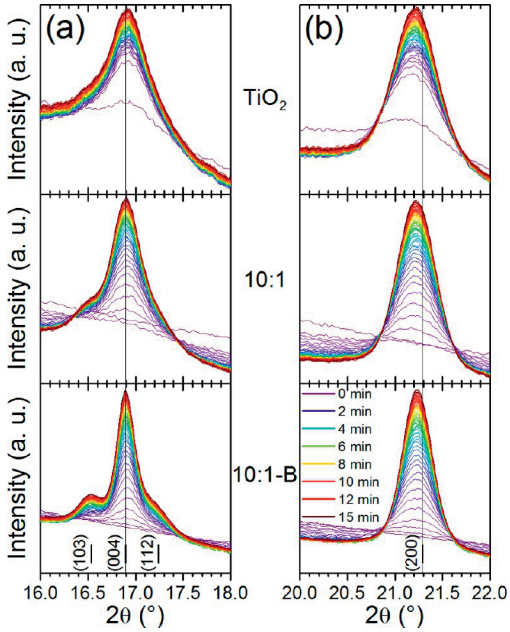

Figure 7. Time evolution of (a) (004) and (b) (200) diffraction lines (λ = 0.6999 Å) during the first 15 min of the hydrothermal synthesis of TiO_2 (top), 10:1 (middle), and 10:1-B (bottom) samples (vertical bars show recalculated bulk diffraction line positions of anatase at 213 °C).

growth can be attributed to Ostwald ripening mechanism.[49,50] The fitted parameters using eq 2 on the crystallite size of TiO_2 during in situ XRD measurements are available in Table 5 and the fitted plots in Figure S11 in Supporting Information. The best fits were obtained for n = 4, indicating that growth is controlled by dissolution kinetics at the particle−matrix interface.[50]

$$d - d_0 = k_{OR} t^{1/n} \quad (2)$$

When TiO_2 nanoparticles are in situ functionalized with APTES, the differences in phase purity, morphology and growth mechanisms are attributed to APTES, as the conditions were the same as during the synthesis performed without APTES. The differences result from a combination of several effects, since the growth and the functionalization of the nanoparticles occur simultaneously. The nucleation of the TiO_2 nanoparticles is most likely to occur first due to the much higher reactivity of titanium alkoxides compared to their silicon counterparts in aqueous media.[51] After nucleation, as the binding energy of APTES is large and positive (>1.3 eV) for all facets (Table 3), aminosilanes probably adsorb regardless of facet. The similarity in equilibrium shape predicted by DFT with and without APTES adsorption (Figure 3) supports the theory that oriented attachment is occurring. This differs from the pH affect shown by Barnard et al.,[43] where the surface energy of the (100) faces is lowered by highly basic conditions and the shape of the nanoparticles is elongated along the *c*-axis. Such a result would support a preferential growth mechanism. In the case shown here, however, the surface energy of the (100) faces remains too high to be stable, hence preferential growth is not favored, and a relative roughness of the surfaces parallel to the elongation direction can be observed in Figure 2d. The adsorption of APTES provides the building blocks for oriented attachment mechanism reaction (Figure 2c) within the few first minutes of the synthesis. Yet, the highest binding energy is on the (001) faces, which are also the faces with the highest surface energy (Table 3), so if there is preferential adsorption of APTES on the (001) faces then this would likely attract the nanoparticles in this direction due to the polarity effect (hydrogen bonding of amino groups and hydrophobicity of the silanes), causing oriented attachment along the *c*-axis. Attraction of the building blocks facing (001) facets could desorb APTES molecules, increasing the total entropy of the system and providing the alignment of the nanoblocks for oriented attachment. Thus, the anisotropy of the particle along the preferential [001] or *c*-axis (Figures 2c,d and Figure 8) is observed. At longer reaction time, cross-linking of APTES on the surface of the nanoparticles (which is kinetically slower than the growth of the particles, see Si−O−Si FTIR band intensity as a function of the time in Figure S4 in Supporting Information) does not allow for more drastic changes in the nanoparticle morphology. These competing phenomena (growth and functionalization) result in the mixture of spheres and rods. On the other hand, the role of APTES is also demonstrated when the amount is reduced (15:1 samples) leading to reduced amount and size of rodlike nanoparticles. During the second phase of the growth, when a slower evolution of the cell parameters and crystallite sizes is observed, ongoing cross-linking of APTES on the surface of the nanoparticles prevents further growth of the particles along the *c*-axis. However, surface diffusion might still occur to reach an equilibrium morphology (Figure 3b), thus the slow increase of the crystallite size along the *a*-axis and the slow decrease of the anisotropy (Figure 8c) resulting in partially faceted nanorods (Figure 2c,d). To confirm, the in situ diffractogram

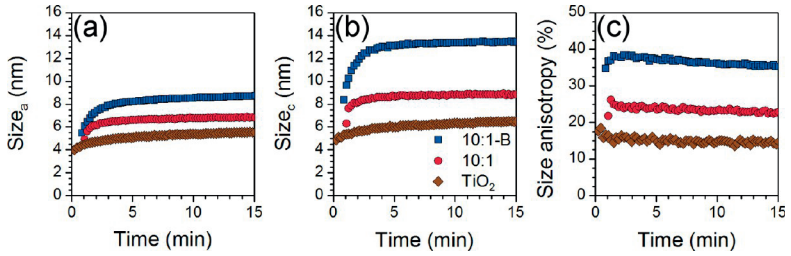

Figure 8. Time evolution of the crystallite sizes along the (a) *a*-axis and (b) *c*-axis, and (c) size anisotropy from in situ XRD.

DOI: 10.1021/acs.jpcc.7b02604
J. Phys. Chem. C 2017, 121, 11897−11906

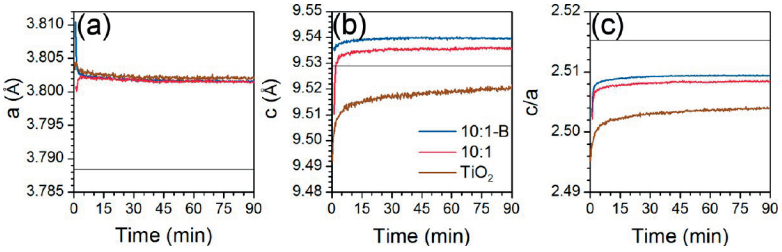

Figure 9. Time evolution of the (a) *a*-parameter, (b) *c*-parameter, and (c) *c*/*a* from in situ XRD (horizontal lines show bulk references of anatase recalculated at 213 °C).

Table 5. Fitted Parameters for the Kinetics of Crystallite Growth Obtained from in Situ XRD

sample	variable	d_0 (nm)	k_{OR} (nm $min^{-1/n}$)	k_{OA} (min^{-1})	m	R^2
TiO_2	$size_a$	3.9	0.80	n/a	n/a	0.98
	$size_c$	4.6	0.95	n/a	n/a	0.98
10:1	$size_a$	4.3	n/a	0.65	1.7	0.81
	$size_c$	2.7	n/a	2.55	3.3	0.66
10:1-B	$size_a$	3.9	n/a	0.77	2.4	0.97
	$size_c$	2.2	n/a	2.60	6.3	0.88

of 10:1-B (Figure 4b) was taken after 9 h of reaction and limited evolution was observed after about 100 min of reaction.

The kinetics of crystallite growth of the functionalized samples for both in situ (Figure 8a,b) and ex situ data (Figure S9 in Supporting Information) could not be fitted to a power-law type of function as presented in eq 2. However, the fitting could be done using eq 3, describing an oriented attachment mechanism, where m was defined as the aggregation factor and k_{OA} as the rate constant for oriented attachment.[52] The fitted parameters using eq 3 for the growth of the functionalized nanoparticles are available in Table 5 (see Table S5 and Figure S11 in Supporting Information for ex situ XRD data and fitted plots). The rate of growth of pure TiO_2 is similar in both crystallographic directions while in the case of functionalized samples, the rate of growth along the *c*-axis is 2 to 4 times higher than along the *a*-axis, depending on the synthesis conditions. Additionally, it can be observed that the aggregation factor is also more important along the *c*-axis and increases when increasing pH and APTES values. These observations are consistent with electron microscope observations (Figures 1 and 2).

$$d = d_0 \frac{1 + mk_{OA}t}{1 + k_{OA}t} \quad (3)$$

The functionalization of the TiO_2 nanoparticles increases the stability of the nanoparticles by reducing the deviation from the bulk of the cell parameters (Figure 9b), and results in phase pure anatase TiO_2. Functionalization of the nanoparticles reduces the finite size effect which is usually observed for anatase nanoparticles,[53,54] by creating covalent bonds with the silane coupling agent (passivation of the dangling bonds), reducing the surface stress and surface energy of the nanoparticles (Table 3). The variations of the cell parameters as a function of the pH are relatively small thus the difference in the particle size does not seem to be the origin of this difference between pure TiO_2 and the in situ functionalized sample. However, the variations of pH toward more acidic or more basic conditions strongly influence the anisotropy (Figure 1a–c). The surface state of TiO_2 nanoparticles, the attractive forces, and the reactivity of titanium alkoxides and silane coupling agents are affected by the variations of the pH. A more homogeneous system and a kinetically faster functionalization (increasing the extent of cross-linking that can be achieved before oriented attachment takes place) would lead toward more spherically shaped nanoparticles. These observations justify previous results in which in situ functionalization of TiO_2 with *n*-decyltriethoxysilane (nonpolar) and 3-(2-aminoethylamino)propyldimethoxymethylsilane (two amino groups) resulted in the observations of only spheres, and a mixture of spheres and larger rods (compared to functionalization with APTES), respectively.[27]

To summarize, in the case of the hydrothermal synthesis of TiO_2 a classical Ostwald ripening process was observed (Figure 10a). When APTES was introduced (Figure 10b), the adsorption of the aminosilane coupling agent favors the anatase polymorph and an oriented attachment process is observed via the anisotropic broadening of the Bragg reflections, HR-TEM imaging, kinetic modeling, and DFT calculations. Functionalization and cross-linking of APTES on the surface of TiO_2 nanoparticles also contributes to reduce the rate of growth at longer reaction times.

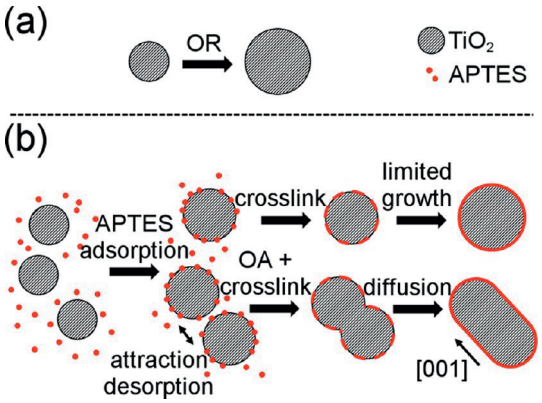

Figure 10. Schematics of the growth processes during the hydrothermal synthesis of (a) TiO_2 and (b) TiO_2 in situ functionalized with APTES (OR, Ostwald ripening; OA, oriented attachment).

DOI: 10.1021/acs.jpcc.7b02604
J. Phys. Chem. C 2017, 121, 11897–11906

5. CONCLUSION

The effect of pH, precursor/functionalization agent ratio, and time during the hydrothermal synthesis of TiO_2 and APTES functionalized TiO_2 was investigated in detail by ex situ and in situ techniques. While nanoparticles of about 10 nm in size were obtained for pure TiO_2, additional [001] oriented rodlike nanoparticles were formed due to an oriented attachment mechanism in the presence of APTES. The amount and the size of the rodlike nanoparticles was shown to increase with increasing pH and decrease with a lower amount of APTES. Comparison of ex situ and in situ XRD showed that the in situ results were representative for the reaction. In situ XRD allowed one to follow the growth kinetics of the synthesis, despite the extreme conditions of the synthesis (213 °C and 250 bar). DFT calculations supported an oriented attachment mechanism as the elongated nanoparticle was shown to not be the stable shape after functionalization. The hydrothermal synthesis of functionalized TiO_2 has the main advantage of being a single-step method and understanding the phenomenon and the reaction processes are essential in order to gain control over the product of the synthesis. This method opens further possibilities for green synthesis of in situ functionalized nano-oxides with desired size, shape, phase, and surface properties.

■ ASSOCIATED CONTENT

Supporting Information

The Supporting Information is available free of charge on the ACS Publications website at DOI: 10.1021/acs.jpcc.7b02604.

Experimental details for in situ diffraction analysis and Rietveld refinement, detailed computational calculations description, ex situ analysis on the synthesis time, nitrogen adsorption, and desorption isotherms, BJH pore size distribution, thermogravimetry data, Fourier transform infrared spectra, additional HR-TEM images and EDS spectrum, Rietveld fits, time evolution of parameters from ex situ XRD, and kinetic fits (PDF)

■ AUTHOR INFORMATION

Corresponding Author

*E-mail: mari-ann.einarsrud@ntnu.no. Telephone: +47 73 59 40 02.

ORCID

Mari-Ann Einarsrud: 0000-0002-3017-1156

Notes

The authors declare no competing financial interest.

■ ACKNOWLEDGMENTS

Financial support from the Research Council of Norway to the project "Beat the Human Eye" (number 235210) and for the support to NTNU NanoLab through the Norwegian Micro- and Nano-Fabrication Facility, NorFab (197411/V30) is gratefully acknowledged. K.I. and S.M.S. were supported by NTNU and the Research Council of Norway through project number 240466/F20. Computational resources were provided by Sigma2 Uninett, through the project nn9264k. We acknowledge SNBL at ESRF, Grenoble, France for the granted beamtime. The TEM work was carried out on the NORTEM JEOL 2100 instrument, TEM Gemini Centre, NTNU, Norway, and we want to acknowledge Dr. Ragnhild Sæterli for help in operating the TEM. Dr. Julian R. Tolchard (SINTEF Materials and Chemistry) is acknowledged for the help with the Rietveld analysis.

■ REFERENCES

(1) Zhang, Y.; Jiang, Z.; Huang, J.; Lim, L. Y.; Li, W.; Deng, J.; Gong, D.; Tang, Y.; Lai, Y.; Chen, Z. Titanate and Titania Nanostructured Materials for Environmental and Energy Applications: A Review. *RSC Adv.* **2015**, *5*, 79479−79510.

(2) Liu, G.; Yang, H. G.; Pan, J.; Yang, Y. Q.; Lu, G. Q.; Cheng, H. M. Titanium Dioxide Crystals with Tailored Facets. *Chem. Rev.* **2014**, *114*, 9559−9612.

(3) Rabenau, A. The Role of Hydrothermal Synthesis in Preparative Chemistry. *Angew. Chem., Int. Ed. Engl.* **1985**, *24*, 1026−1040.

(4) Li, X.; Zheng, W.; He, G.; Zhao, R.; Liu, D. Morphology Control of TiO_2 Nanoparticle in Microemulsion and Its Photocatalytic Property. *ACS Sustainable Chem. Eng.* **2014**, *2*, 288−295.

(5) Bian, Z.; Zhu, J.; Li, H. Solvothermal Alcoholysis Synthesis of Hierarchical TiO_2 with Enhanced Activity in Environmental and Energy Photocatalysis. *J. Photochem. Photobiol., C* **2016**, *28*, 72−86.

(6) Lekphet, W.; Ke, T.-C.; Su, C.; Kathirvel, S.; Sireesha, P.; Akula, S. B.; Li, W.-R. Morphology Control Studies of TiO_2 Microstructures Via Surfactant-Assisted Hydrothermal Process for Dye-Sensitized Solar Cell Applications. *Appl. Surf. Sci.* **2016**, *382*, 15−26.

(7) Einarsrud, M.-A.; Grande, T. 1D Oxide Nanostructures from Chemical Solutions. *Chem. Soc. Rev.* **2014**, *43*, 2187−2199.

(8) Fadeev, A. Y.; Helmy, R.; Marcinko, S. Self-Assembled Monolayers of Organosilicon Hydrides Supported on Titanium, Zirconium, and Hafnium Dioxides. *Langmuir* **2002**, *18*, 7521−7529.

(9) Milanesi, F.; Cappelletti, G.; Annunziata, R.; Bianchi, C. L.; Meroni, D.; Ardizzone, S. Siloxane−TiO_2 Hybrid Nanocomposites. The Structure of the Hydrophobic Layer. *J. Phys. Chem. C* **2010**, *114*, 8287−8293.

(10) Chen, Q.; Yakovlev, N. L. Adsorption and Interaction of Organosilanes on TiO_2 Nanoparticles. *Appl. Surf. Sci.* **2010**, *257*, 1395−1400.

(11) Zhao, J.; Milanova, M.; Warmoeskerken, M. M. C. G.; Dutschk, V. Surface Modification of TiO_2 Nanoparticles with Silane Coupling Agents. *Colloids Surf., A* **2012**, *413*, 273−279.

(12) Plodinec, M.; Gajović, A.; Iveković, D.; Tomašić, N.; Zimmermann, B.; Macan, J.; Haramina, T.; Su, D. S.; Willinger, M. Study of Thermal Stability of (3-Aminopropyl)Trimethoxy Silane-Grafted Titanate Nanotubes for Application as Nanofillers in Polymers. *Nanotechnology* **2014**, *25*, 435601.

(13) Iijima, M.; Kobayakawa, M.; Kamiya, H. Tuning the Stability of TiO_2 Nanoparticles in Various Solvents by Mixed Silane Alkoxides. *J. Colloid Interface Sci.* **2009**, *337*, 61−65.

(14) Faure, B.; Salazar-Alvarez, G.; Ahniyaz, A.; Villaluenga, I.; Berriozabal, G.; De Miguel, Y. R.; Bergström, L. Dispersion and Surface Functionalization of Oxide Nanoparticles for Transparent Photocatalytic and UV-Protecting Coatings and Sunscreens. *Sci. Technol. Adv. Mater.* **2013**, *14*, 023001.

(15) Kango, S.; Kalia, S.; Celli, A.; Njuguna, J.; Habibi, Y.; Kumar, R. Surface Modification of Inorganic Nanoparticles for Development of Organic−Inorganic Nanocomposites—a Review. *Prog. Polym. Sci.* **2013**, *38*, 1232−1261.

(16) Dinh, C. T.; Nguyen, T. D.; Kleitz, F.; Do, T. O. Shape-Controlled Synthesis of Highly Crystalline Titania Nanocrystals. *ACS Nano* **2009**, *3*, 3737−3743.

(17) Jun, Y. W.; Casula, M. F.; Sim, J. H.; Kim, S. Y.; Cheon, J.; Alivisatos, A. P. Surfactant-Assisted Elimination of a High Energy Facet as a Means of Controlling the Shapes of TiO_2 Nanocrystals. *J. Am. Chem. Soc.* **2003**, *125*, 15981−15985.

(18) Jensen, G. V.; Bremholm, M.; Lock, N.; Deen, G. R.; Jensen, T. R.; Iversen, B. B.; Niederberger, M.; Pedersen, J. S.; Birkedal, H. Anisotropic Crystal Growth Kinetics of Anatase TiO_2 Nanoparticles Synthesized in a Nonaqueous Medium. *Chem. Mater.* **2010**, *22*, 6044−6055.

(19) Darbandi, M.; Dickerson, J. H. Nanoscale Engineering of TiO_2 Nanoparticles: Evolution of the Shape, Phase, Morphology, and Facet Orientation. *Mater. Lett.* **2016**, *180*, 212−218.
(20) Sugimoto, T.; Zhou, X.; Muramatsu, A. Synthesis of Uniform Anatase TiO_2 Nanoparticles by Gel−Sol Method 3. Formation Process and Size Control. *J. Colloid Interface Sci.* **2003**, *259*, 43−52.
(21) Sugimoto, T.; Zhou, X.; Muramatsu, A. Synthesis of Uniform Anatase TiO_2 Nanoparticles by Gel−Sol Method 4. Shape Control. *J. Colloid Interface Sci.* **2003**, *259*, 53−61.
(22) Penn, R. L.; Banfield, J. F. Imperfect Oriented Attachment: Dislocation Generation in Defect-Free Nanocrystals. *Science* **1998**, *281*, 969−971.
(23) Niederberger, M.; Cölfen, H. Oriented Attachment and Mesocrystals: Non-Classical Crystallization Mechanisms Based on Nanoparticle Assembly. *Phys. Chem. Chem. Phys.* **2006**, *8*, 3271−3287.
(24) Penn, R. L.; Banfield, J. F. Morphology Development and Crystal Growth in Nanocrystalline Aggregates under Hydrothermal Conditions: Insights from Titania. *Geochim. Cosmochim. Acta* **1999**, *63*, 1549−1557.
(25) Polleux, J.; Pinna, N.; Antonietti, M.; Niederberger, M. Ligand-Directed Assembly of Preformed Titania Nanocrystals into Highly Anisotropic Nanostructures. *Adv. Mater.* **2004**, *16*, 436−439.
(26) Dalmaschio, C. J.; Leite, E. R. Detachment Induced by Rayleigh-Instability in Metal Oxide Nanorods: Insights from TiO_2. *Cryst. Growth Des.* **2012**, *12*, 3668−3674.
(27) Dalod, A. R. M.; Henriksen, L.; Grande, T.; Einarsrud, M.-A. Functionalized TiO_2 Nanoparticles by Single-Step Hydrothermal Synthesis: The Role of the Silane Coupling Agents. *Beilstein J. Nanotechnol.* **2017**, *8*, 304−312.
(28) Kresse, G.; Hafner, J. Ab Initio Molecular Dynamics for Liquid Metals. *Phys. Rev. B: Condens. Matter Mater. Phys.* **1993**, *47*, 558−561.
(29) Kresse, G.; Furthmüller, J. Efficiency of Ab-Initio Total Energy Calculations for Metals and Semiconductors Using a Plane-Wave Basis Set. *Comput. Mater. Sci.* **1996**, *6*, 15−50.
(30) Kresse, G.; Furthmüller, J. Efficient Iterative Schemes for Ab Initio Total-Energy Calculations Using a Plane-Wave Basis Set. *Phys. Rev. B: Condens. Matter Mater. Phys.* **1996**, *54*, 11169−11186.
(31) Kresse, G.; Joubert, D. From Ultrasoft Pseudopotentials to the Projector Augmented-Wave Method. *Phys. Rev. B: Condens. Matter Mater. Phys.* **1999**, *59*, 1758−1775.
(32) Perdew, J. P.; Ruzsinszky, A.; Csonka, G. I.; Vydrov, O. A.; Scuseria, G. E.; Constantin, L. A.; Zhou, X.; Burke, K. Restoring the Density-Gradient Expansion for Exchange in Solids and Surfaces. *Phys. Rev. Lett.* **2008**, *100*, 136406.
(33) Meroni, D.; Lo Presti, L.; Di Liberto, G.; Ceotto, M.; Acres, R. G.; Prince, K. C.; Bellani, R.; Soliveri, G.; Ardizzone, S. A Close Look at the Structure of the TiO_2-APTES Interface in Hybrid Nanomaterials and Its Degradation Pathway: An Experimental and Theoretical Study. *J. Phys. Chem. C* **2017**, *121*, 430−440.
(34) Dyadkin, V.; Pattison, P.; Dmitriev, V.; Chernyshov, D. A New Multipurpose Diffractometer PILATUS@SNBL. *J. Synchrotron Radiat.* **2016**, *23*, 825−829.
(35) Becker, J.; Bremholm, M.; Tyrsted, C.; Pauw, B.; Jensen, K. M. Ø.; Eltzholt, J.; Christensen, M.; Iversen, B. B. Experimental Setup for in situ X-Ray SAXS/WAXS/PDF Studies of the Formation and Growth of Nanoparticles in near- and Supercritical Fluids. *J. Appl. Crystallogr.* **2010**, *43*, 729−736.
(36) Jensen, K. M. Ø.; Christensen, M.; Juhas, P.; Tyrsted, C.; Bøjesen, E. D.; Lock, N.; Billinge, S. J. L.; Iversen, B. B. Revealing the Mechanisms Behind SnO_2 Nanoparticle Formation and Growth During Hydrothermal Synthesis: An in situ Total Scattering Study. *J. Am. Chem. Soc.* **2012**, *134*, 6785−6792.
(37) Skjærvø, S. L.; Sommer, S.; Nørby, P.; Bøjesen, E. D.; Grande, T.; Iversen, B. B.; Einarsrud, M.-A. Formation Mechanism and Growth of $MNbO_3$, M = K, Na by in situ X-Ray Diffraction. *J. Am. Ceram. Soc.* **2017**, DOI: 10.1111/jace.14932.
(38) Evans, J. S. O. Advanced Input Files & Parametric Quantitative Analysis Using Topas. *Mater. Sci. Forum* **2010**, *651*, 1−9.
(39) Brunauer, S.; Emmett, P. H.; Teller, E. Adsorption of Gases in Multimolecular Layers. *J. Am. Chem. Soc.* **1938**, *60*, 309−319.
(40) Barrett, E. P.; Joyner, L. G.; Halenda, P. P. The Determination of Pore Volume and Area Distributions in Porous Substances. I. Computations from Nitrogen Isotherms. *J. Am. Chem. Soc.* **1951**, *73*, 373−380.
(41) Zhao, Z.; Li, Z.; Zou, Z. Surface Properties and Electronic Structure of Low-Index Stoichiometric Anatase TiO_2 Surfaces. *J. Phys.: Condens. Matter* **2010**, *22*, 175008.
(42) Martsinovich, N.; Troisi, A. How TiO_2 Crystallographic Surfaces Influence Charge Injection Rates from a Chemisorbed Dye Sensitiser. *Phys. Chem. Chem. Phys.* **2012**, *14*, 13392−13401.
(43) Barnard, A. S.; Curtiss, L. A. Prediction of TiO_2 Nanoparticle Phase and Shape Transitions Controlled by Surface Chemistry. *Nano Lett.* **2005**, *5*, 1261−1266.
(44) Mi, J.-L.; Jensen, K. M. Ø.; Tyrsted, C.; Bremholm, M.; Iversen, B. B. In Situ Total X-Ray Scattering Study of the Formation Mechanism and Structural Defects in Anatase TiO_2 Nanoparticles under Hydrothermal Conditions. *CrystEngComm* **2015**, *17*, 6868−6877.
(45) Eltzholtz, J. R.; Tyrsted, C.; Jensen, K. M. Ø.; Bremholm, M.; Christensen, M.; Becker-Christensen, J.; Iversen, B. B. Pulsed Supercritical Synthesis of Anatase TiO_2 Nanoparticles in a Water-Isopropanol Mixture Studied by in situ Powder X-Ray Diffraction. *Nanoscale* **2013**, *5*, 2372−2378.
(46) Reyes-Coronado, D.; Rodríguez-Gattorno, G.; Espinosa-Pesqueira, M. E.; Cab, C.; de Coss, R.; Oskam, G. Phase-Pure TiO_2 Nanoparticles: Anatase, Brookite and Rutile. *Nanotechnology* **2008**, *19*, 145605.
(47) Zhang, H.; Banfield, J. F. Structural Characteristics and Mechanical and Thermodynamic Properties of Nanocrystalline TiO_2. *Chem. Rev.* **2014**, *114*, 9613−9644.
(48) Ribeiro, C.; Barrado, C. M.; de Camargo, E. R.; Longo, E.; Leite, E. R. Phase Transformation in Titania Nanocrystals by the Oriented Attachment Mechanism: The Role of the pH Value. *Chem. - Eur. J.* **2009**, *15*, 2217−2222.
(49) Xue, X.; Penn, R. L.; Leite, E. R.; Huang, F.; Lin, Z. Crystal Growth by Oriented Attachment: Kinetic Models and Control Factors. *CrystEngComm* **2014**, *16*, 1419−1429.
(50) Huang, F.; Zhang, H.; Banfield, J. F. Two-Stage Crystal-Growth Kinetics Observed During Hydrothermal Coarsening of Nanocrystalline ZnS. *Nano Lett.* **2003**, *3*, 373−378.
(51) Rozes, L.; D'Arras, L.; Hoffman, C.; Potier, F.; Halttunen, N.; Nicole, L. In *Chemistry of Organo-Hybrids: Synthesis and Characterization of Functional Nano-Objects*; Charleux, B., Copéret, C., Lacôte, E., Eds.; John Wiley & Sons: Hoboken, NJ, 2015; pp 114−167.
(52) Zhan, H.; Yang, X.; Wang, C.; Liang, C.; Wu, M. Multiple Growth Stages and Their Kinetic Models of Anatase Nanoparticles under Hydrothermal Conditions. *J. Phys. Chem. C* **2010**, *114*, 14461−14466.
(53) Ahmad, M. I.; Bhattacharya, S. S. Size Effect on the Lattice Parameters of Nanocrystalline Anatase. *Appl. Phys. Lett.* **2009**, *95*, 191906.
(54) Zhang, H.; Chen, B.; Banfield, J. F. The Size Dependence of the Surface Free Energy of Titania Nanocrystals. *Phys. Chem. Chem. Phys.* **2009**, *11*, 2553−2558.

DOI: 10.1021/acs.jpcc.7b02604
J. Phys. Chem. C 2017, 121, 11897−11906